Measurements of HCFC-22 in the upper troposphere and lower stratosphere from the MIPAS-E instrument

Thesis submitted to the University of Leicester for the degree of Doctor of Philosophy

by

David Philip Moore BSc

Department of Physics and Astronomy

University of Leicester

November 2005

ProQuest LLC
789 East Eisenhower Parkway
P.O. Box 1346
Ann Arbor, MI 48106-1346

Declaration

I hereby declare that no part of this thesis has been submitted to this or any other University as part of the requirements for a higher degree. The work described here was conducted by the undersigned except for the contributions of colleagues indicated in the text.

David Philip Moore

November 2005

Measurements of HCFC-22 in the upper troposphere and lower stratosphere from the MIPAS-E instrument

David Philip Moore, November 2005

Abstract

The potential for retrieval of HCFC-22 volume mixing ratios in the upper troposphere and lower stratosphere (UTLS) from a spaceborne infrared limb-sounding spectrometer is assessed.

Hydrochlorofluorocarbon-22 (HCFC-22) is an important trace constituent in the atmosphere through its role as a greenhouse gas and its potential influence on stratospheric ozone chemistry. Current estimates of its vertical distribution are limited to infrequent and sparse balloon and aircraft campaigns, giving poor spatial coverage.

Atmospheric limb-emission spectra measured by the Michelson Interferometer for Passive Atmospheric Sounding onboard the ENVISAT satellite (MIPAS-E) have been successfully used to detect and retrieve HCFC-22 volume mixing ratios (vmrs) between 9 and 15 km. Global and seasonal means are presented from 2003.

An OPtimal Estimation Retrieval Algorithm (OPERA) was developed and designed specifically to invert measurements from MIPAS-E data to trace gas concentrations. The scheme performs a joint retrieval of the target gas and total extinction from clouds or aerosols. High extinctions are observed globally at 9 km.

In January 2003, global mean HCFC-22 vmr data at 9 km agreed to within 8 % of the measured mean surface value. Mean agreement for all seasons in 2003 was 15 %. Indications are that mean HCFC-22 data at 9 km are accurate to better than 10 %. Vertical profiles were measured between 9 and 15 km.

OPERA CFC-12 retrievals were used as a consistency check on the likely accuracy of HCFC-22 data. These data were validated against independent measurements. Agreement with HAGAR measurements in spring 2003 was better than 7 %.

This work demonstrates that HCFC-22 (and CFC-12) can be detected and retrieved from MIPAS-E data in the UTLS based on current concentrations. In addition, they show the potential to obtain other vertical profiles of particle extinction on a global basis throughout the UTLS.

Acknowledgements

There are so many people I want to thank for helping me through the rollercoaster ride of the past four years...

Firstly, thank you to my supervisor, John Remedios, for giving me the opportunity to carry out this project and all the help he has given me along the way. Thank you also to Alison Waterfall, Reinhold Spang and John Greenhough for all of the constructive comments you've given me at various times during the project. I want to also thank NERC for funding me.

A big thank you to all of the great people I've met and become good friends with in the Earth Observation Science Group in Leicester. An especially big thank you (in no particular order you understand) to Scott, Glen, Neil, Nige(l), Roland, Grant(y), Simon, Lizzie, Harj, Louisa and Gary. Thank you also to the physics 5-a-side football players.

I can't forget to thank both Burton Albion and Stapenhill football clubs for the many "enjoyable" Saturday afternoons you've given me over the past years...

Above all I want to thank my family for all the help you have given me in getting me where I am today. An especially big thank you to my parents and my sister Rachel. You are all fantastic!

Chapter 1

Halocarbons in the Upper Troposphere and Lower Stratosphere

1 Introduction

Life on Earth is sustainable due to the relatively thin atmosphere (approximately 120 km deep) that envelopes it. The major constituent is nitrogen (78 %) followed by oxygen (21 %), argon (0.9 %), carbon dioxide (0.3 %) and then a large number of less abundant trace gases (including ozone and water vapour). The atmosphere regulates the surface temperature of the Earth and also provides protection from the space environment through which it passes.

The ultimate source of energy that gives life on Earth is the Sun. The radiation balance of the Earth is shown schematically in Figure 1.1. About half of the incoming radiation is in the visible short-wave part of the electromagnetic part of the spectrum, with most of the other half in the near-infrared and the remainder in the ultraviolet. From a study by Kiehl and Trenberth [1997], the annual average incoming solar radiation (insolation) at the top of the Earth's atmosphere is 342 Wm^{-2}. At any given location and time the insolation depends on latitude and the annual mean top of atmosphere insolation varies from 160 Wm^{-2} at the poles to 500 Wm^{-2} in the tropics. Approximately 30 % of this radiation is reflected straight back into space by clouds, the atmosphere and the surface. The majority of the remaining 235 Wm^{-2} warms the Earth's surface (land and ocean) but some (67 Wm^{-2}) is absorbed by the atmosphere itself. The Earth's surface returns that heat to the atmosphere, partly as infrared radiation, partly as sensible heat and as water vapour which releases its latent heat when it condenses higher up in the atmosphere. This exchange of heat energy between surface and atmosphere maintains a global mean temperature near the surface of 287 K,

decreasing rapidly with height and reaching a minimum of 215 K at the top of the troposphere.

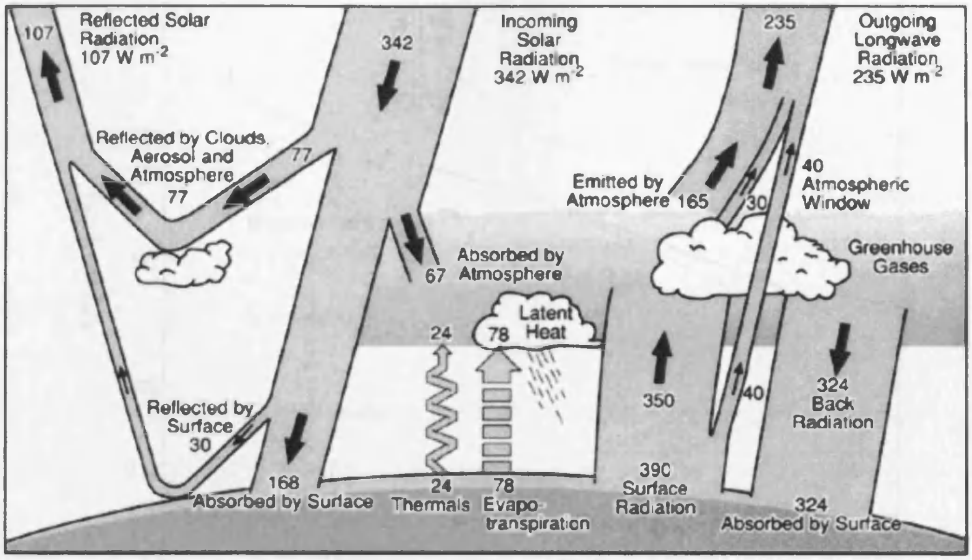

Figure 1.1 The Earth's radiation and energy balance. The net incoming solar radiation of 342 Wm^{-2} is partially reflected by clouds and the atmosphere, or at the surface, but 49% is absorbed by the surface. Some of that heat is returned to the atmosphere as sensible heating and most as evapotranspiration that is realised as latent heat in precipitation. The remainder is radiated as thermal infrared radiation with the majority of that absorbed by the atmosphere which in turn emits radiation, producing a greenhouse effect, as the radiation lost to space comes from cloud tops and parts of the atmosphere much colder than the surface. The partitioning of the annual global mean energy budget and the accuracy of the values are given in Kiehl and Trenberth [1997]. Source: www.climatechangedebate.org

The atmosphere is divided into layers (Figure 1.2) which are based on its temperature structure. The lowest layer is the troposphere which extends from the surface to between 8 and 17 km, depending on latitude and season. This layer contains most of the "weather" experienced at the surface. Temperature decreases with altitude in the troposphere due to solar radiation absorption by the surface and re-emission at infrared wavelengths, thus heating the atmosphere from below. This is coupled with cooling from atmospheric gases themselves. Directly above the troposphere is the stratosphere, extending to altitudes of approximately 50 km. In this layer, temperature increases with height due to the absorption by ozone of solar radiation at ultraviolet wavelengths. This layer contains the "ozone layer" which protects the surface from short-wave ultraviolet radiation. Above the stratosphere is the mesosphere which extends up to altitudes of 90 km. Temperatures decrease in this layer due to radiative cooling by predominantly carbon dioxide (CO_2).

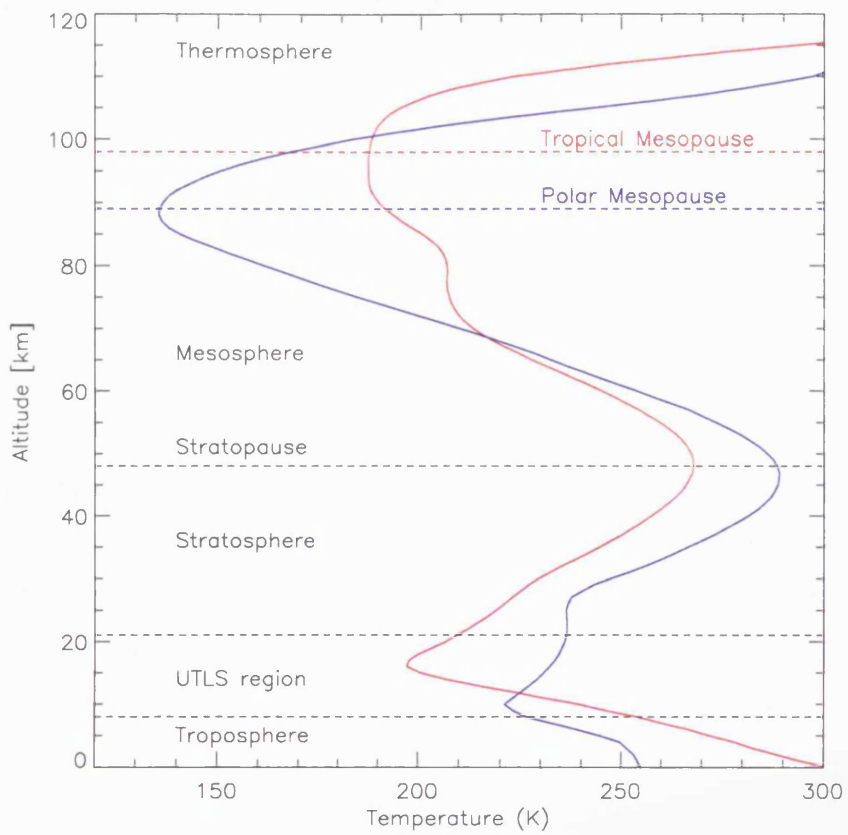

Figure 1.2 The vertical temperature structure of the Earth's atmosphere, typical of both tropical (red) and polar (blue) conditions, showing the three distinct levels of the atmosphere considered in this thesis. The troposphere extends from the surface up to 18 km in the tropics and 8 km at the Earth's poles. The stratosphere is directly above, extending up to 50 km. The mesosphere caps the stratosphere and above this layer is the thermosphere. Also shown is the Upper Troposphere and Lower Stratosphere (UTLS) which is the focus of this thesis, a region that generally extends between 8 and 21 km.

The upper troposphere and lower stratosphere region (UTLS), indicated in Figure 1.2, can be thought of as a layer extending across the tropopause between approximately 8 and 21 km. It is characterised by steep vertical gradients in temperature and concentration of a variety of trace gases including for example ozone, water vapour and anthropogenic halocarbons. The subject of this thesis is the halocarbons which are present in the atmosphere almost entirely due to human activity. In the stratosphere, the presence of halocarbons leads to the catalytic destruction of ozone, increasing levels of harmful ultraviolet radiation able to penetrate the atmosphere and reach the surface. In the troposphere halocarbons act as greenhouse gases as a result of their strong absorption and emission lines in the infrared region of the electromagnetic spectrum.

1.1 Dynamics of the atmosphere

The troposphere and stratosphere are the two layers in the atmosphere where halocarbons are predominantly found. The characteristics (for example the static stability) of the two layers are fundamentally different and transport of air masses between the two layers is of great interest. The tropopause separates the layers, a region which has numerous definitions. The World Meteorological Organisation [1996] defines the tropopause as the lowest level at which the temperature lapse rate averaged between this level and any level within the next 2 km does not exceed 2 K km^{-1}. In the tropics this corresponds to a 380 K potential temperature surface (θ) which is located at a height between 15 and 18 km [Holton *et al.*, 1995]. Towards the poles it slopes down to heights of between 6 and 8 km corresponding to a potential temperature of 290-320 K. A tropopause defined by a surface of 2 PVU (potential vorticity units) is often used in the mid-latitudes as the quantity of potential vorticity emphasizes the material surface nature of the tropopause. For example, tropopause folds can occur behind cold-fronts in extratropical cyclones, which appear as multiple stable layers in vertical temperature profiles but these layers are actually represent the same folded discontinuity surface.

The complex transport of air masses across the tropopause is referred to as Stratosphere-Troposphere Exchange (STE), and represents exchange from global spatial scales down to local turbulent mixing. Globally, the mean meridional circulation in the upper troposphere and stratosphere can be described by the Brewer-Dobson circulation [Brewer, 1949] which transports air from the upper troposphere to the stratosphere in the tropics. The air is then carried to the extratropics in the stratosphere, followed by a downwelling of mass flux in middle and high latitudes (Figure 1.3).

The Brewer-Dobson circulation exists due to breaking of gravity and Rossby waves which exerts a drag force on the westerly wintertime stratospheric jet. Through thermal wind balance warm air is driven poleward, creating a thermal imbalance at the poles. As a consequence, the polar stratosphere radiatively cools, the air becomes denser and sinks, leading to a downwards mass flux towards the troposphere. The mass balance is maintained by upward motion across the tropical tropopause.

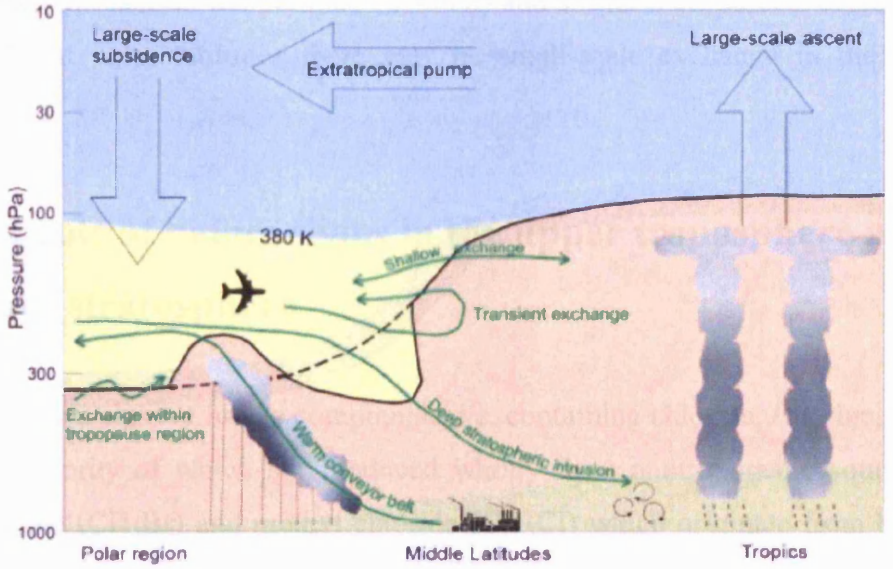

Figure 1.3 Global aspects of Stratosphere-Troposphere Exchange (STE) from Holton *et al.* [1995] adapted by Stohl *et al.* [2003]. The thick black line indicates the average position of the tropopause. The blue shaded region is the "overworld", the yellow region is the lowermost stratosphere, the pink region the free troposphere and the brown region is the atmospheric boundary layer. Arrows show transport by the global-scale circulation and the green trajectories indicate small scale aspects of STE.

Strong surface heating in the tropics initiates deep convection, lifting moist air from the boundary layer into the upper troposphere, with some of this air transported into the stratosphere. Exchange is mainly from the troposphere to the stratosphere, although the details of how tropospheric air enters the stratosphere in the tropics and the scales involved are still heavily debated and discussed in detail for example in Stohl *et al.* [2003]. One of the favoured mechanisms involves mixing in a transition zone between the top of the convective outflow and the stratospheric Brewer-Dobson circulation above the cold point over a single tropopause surface [Highwood and Hoskins, 1998].

In the extra-tropics, transport occurs mainly from the stratosphere to the troposphere due to synoptic-scale and meso-scale processes. Cut-off lows [Ebel *et al.*, 1991] and tropospheric folds in the vicinity of subtropical jets [Baray *et al.*, 2000] provide mechanisms for this transport as they are associated with great latitudinal displacement of the tropopause on isentropic surfaces. Often the tropopause fold is formed during the development of a cut-off low. At midlatitudes, warm conveyor belts (airstreams ahead of cold fronts associated with extratropical cyclones) initiate strong diabatic heating by latent heat release (Browning, 1990) rapidly transferring lower tropospheric air into the lower stratosphere. Deep penetration into the stratosphere is not possible by radiative heating alone (due to the

large potential increase of temperature required) and so these air parcels cannot reach the "overworld". At polar latitudes there may be small-scale exchange in the tropopause region.

1.2 The role of halocarbons in the upper troposphere and lower stratosphere

Halocarbons are a class of halide compounds, i.e. containing chlorine, fluorine, bromine or iodine, the majority of which are produced wholly from anthropogenic sources (except methyl bromide (CH_3Br) and methyl chloride (CH_3Cl) which originate from both natural and anthropogenic sources). The most abundant of these compounds in the atmosphere are the chlorofluorocarbons (including CFC-11 and CFC-12) and the hydrochlorofluorocarbons (including HCFC-22). None of these synthesised compounds existed in the atmosphere before the 20th century [Butler *et al.*, 1999].

YEAR	MONTH	HALOCARBON					
		CFC-12			HCFC-22		
		Global (pptv)	NH (pptv)	SH (pptv)	Global (pptv)	NH (pptv)	SH (pptv)
2002	January	535	536	534	151	159	144
	April	534	536	532	152	159	144
	July	535	536	532	152	159	145
	October	534	536	532	155	162	147
2003	January	535	538	533	155	163	148
	April	535	537	533	156	164	149
	July	536	538	533	159	167	150
	October	536	537	534	160	168	152
2004	January	536	537	534	160	167	153

Table 1.1 Averages of surface CFC-12 and HCFC-22 concentrations; globally and in both the Northern Hemisphere (NH) and Southern Hemisphere (SH). The data are courtesy of the NOAA Earth System Research Laboratory (ESRL). The data measurement technique and earlier results can be found in Montzka *et al.*, 1993. Website: **www.cmdl.noaa.gov**

Chlorofluorocarbons (CFCs) are non-toxic, non-flammable chemicals formerly used in the manufacture of aerosol sprays, solvents, refrigerants and in blowing agents for foams. The unique numbering system for these compounds indicates the number of carbon, hydrogen,

fluorine and chlorine atoms each molecule contains. The first number indicates the number of carbon atoms (C) the molecule contains minus one (if equal to zero the number is not written), the second is the number of hydrogen atoms (H) plus one and the third represents the number of fluorine atoms (F). To calculate the number of chlorine atoms (Cl) in a CFC molecule requires the solution of the equation: $Cl = 2(C+1) - H - F$ (e.g. CFC-11 describes the compound CCl_3F, CFC-12 depicts CCl_2F_2 and HCFC-22 expresses $CHClF_2$).

CFCs were first manufactured in 1928 by Thomas Midgley, Jr. of General Motors for refrigerators used in large commercial applications as safer alternatives to previously used ammonia (NH_3) and sulphur dioxide (SO_2). In 1932, the world's first self-contained home air-conditioning unit, using CFC-11, was produced. By 1935, 8 million refrigerators in the United States of America were using CFC-12 as a coolant. After World War 2, CFCs were used as propellants for insect sprays, paints, hair sprays and other health products.

In 1974, Molina and Rowland showed that CFCs could be a major source of inorganic chlorine in the stratosphere following their photolytic decomposition by ultraviolet radiation. This is discussed in further detail in section 1.3. Hydrochlorofluorocarbons (HCFCs) were developed in the 1970s as a replacement option for CFCs. These new gases have the same properties as CFCs but pose less of a threat to the ozone layer. They were designed to be shorter lived in the atmosphere and be predominantly destroyed in the troposphere. The atmospheric lifetimes of these new HCFCs are still decadal, long enough for these compounds to be transported into the stratosphere and release chlorine, meaning that even they were seen as only a temporary replacement. To limit the production of CFCs the Montreal Protocol on Substances that deplete the Ozone layer [1987] was internationally agreed and stipulated, amongst other gases, that CFCs should be phased out in developed countries by 2000 and their use curtailed in developing nations with consumption phased-out by 2010. The Protocol also recognises the effect that HCFCs have on stratospheric ozone depletion and their consumption is due to be phased-out in developed countries by 2030 and in developing nations by 2040.

In the troposphere, CFCs are chemically inert and therefore are well mixed within the layer. According to the IPCC report of 2001, the tropospheric lifetime of CFC-12 is 100 years. However this long residence time coupled with the fact that CFCs have strong emission lines in the infrared means that these compounds contribute to the greenhouse effect.

Ground-based measurements are performed regularly by the Earth System Research Laboratory (ESRL) network [Montzka *et al.*, 1993] and Figure 1.4 indicates current global trends (since 1995) in CFC-12 tropospheric volume mixing ratios. Average surface data from both hemispheres and the global average during 2003 and 2004 are also shown in Table 1.1. The average global tropospheric concentration of CFC-12 by the beginning of 2004 was 536 pptv and increasing at a rate of 0.6 pptv/yr. This measured trend for CFC-12 represents a dramatic change since the IPCC report of 2001 which reported a globally increasing trend of CFC-12 in 1998 of 4.4 pptv/yr.

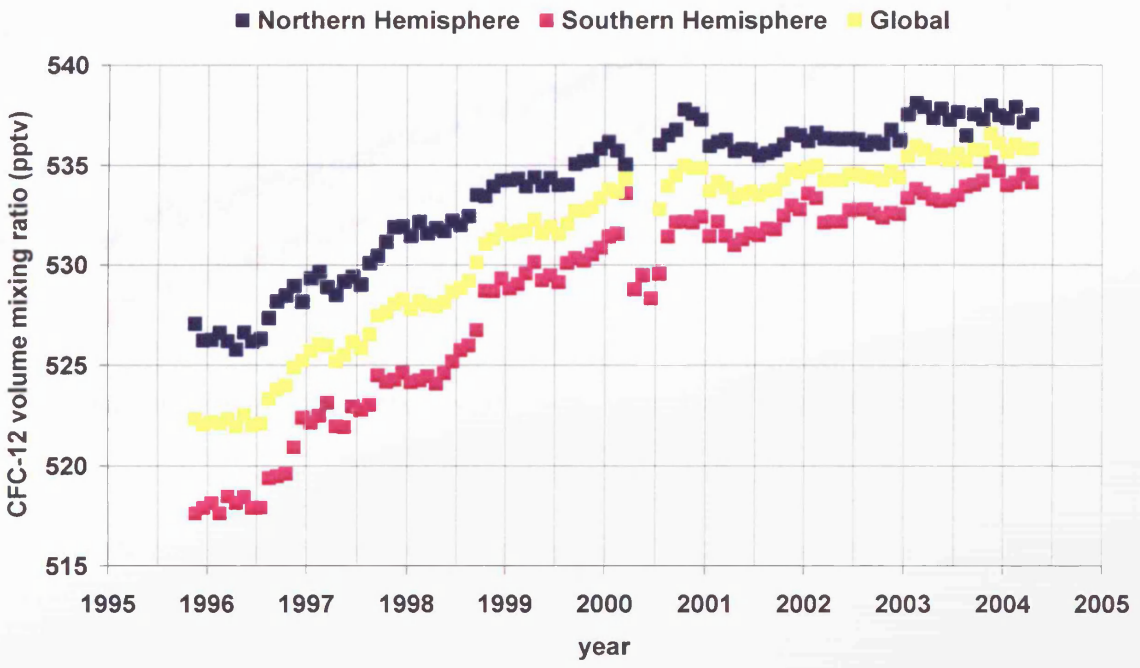

Figure 1.4 The tropospheric trend of CFC-12 between 1995 and 2004. Dark blue squares indicate average Northern Hemispheric concentrations and the pink squares show the average Southern Hemisphere concentrations. The yellow squares represent average global CFC-12 concentrations. (Data courtesy of the Earth System Research Laboratory: www.cmdl.noaa.gov).

The reduction of the increasing trend of tropospheric CFC-12 concentrations is as a direct result of its discontinuation as a coolant in new refrigeration units. Its temporary replacement, the hydrochlorofluorocarbon HCFC-22 (so-called because of the extra hydrogen atom contained within each molecule), is increasing rapidly within the troposphere. HCFC-22 also absorbs strongly in the infrared and so is also classified as a greenhouse gas. The average lifetime of the compound in the atmosphere (11.8 years [IPCC, 2001]) is much shorter than that of CFC-12. Although much of the released HCFC-22 is destroyed in the troposphere, if transported to the stratosphere its residence

time is much longer at up to 214 years [Kanakidou *et al.*, 1995]. However, global concentrations of HCFC-22 are growing linearly in the troposphere at a rate of approximately 5.2 pptv/yr (Figure 1.5). The mean tropospheric HCFC-22 concentration at the beginning of 2004 was 160 pptv.

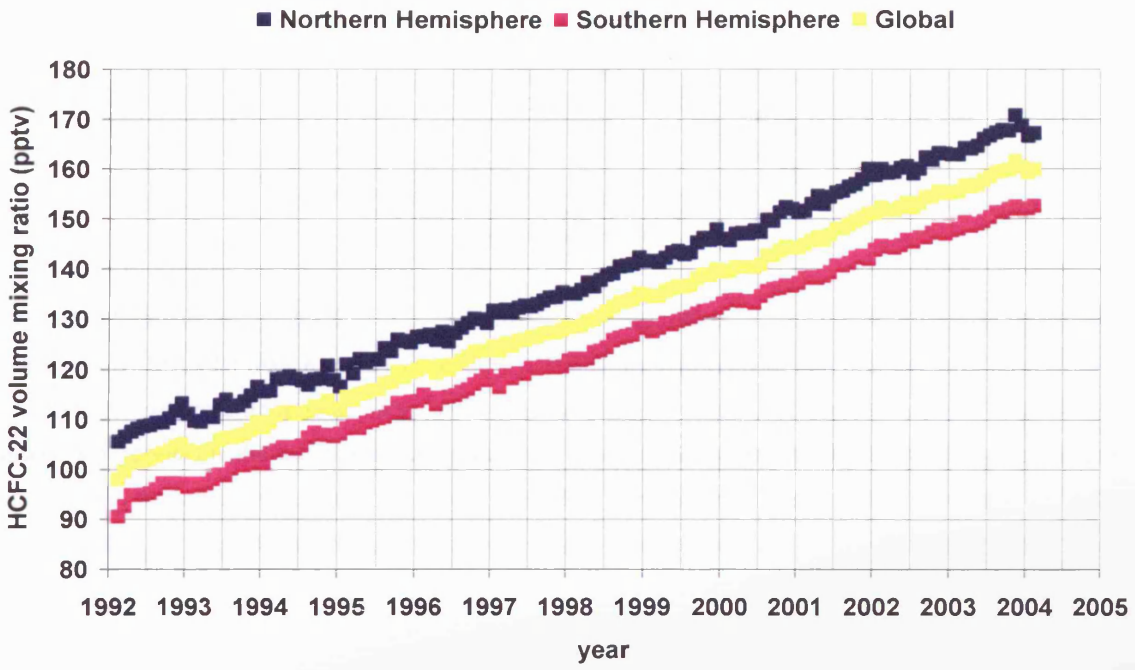

Figure 1.5 The tropospheric trend of HCFC-22 between 1992 and 2004. Dark blue squares indicate average Northern Hemispheric concentrations and the pink squares show the average Southern Hemisphere concentrations. The yellow squares represent average global HCFC-22 concentrations. (Data courtesy of the Earth System Research Laboratory: **www.cmdl.noaa.gov**)

The upper troposphere and lower stratosphere is a very complex layer where many important and inextricably linked chemical and dynamical processes occur and affect the atmospheric radiative balance. The role of halocarbons in the stratosphere is important particularly in the chemistry of ozone, although measurements of their concentrations can also act as a tracer of dynamical motions. It is critical, therefore, that the distributions of the most abundant halocarbons (such as CFC-12 and HCFC-22) are well understood and quantified. Unfortunately, due to the relative inaccessibility of the UTLS, measurements of many radiatively important gases, such as the halocarbons, are sparse and limited to infrequent measurement campaigns. Figure 1.6 and Figure 1.7 show profiles of CFC-12 and HCFC-22 measured by a Fourier Transform Spectrometer (section 3.2.1) instrument which has been deployed on a balloon platform (MIPAS-B).

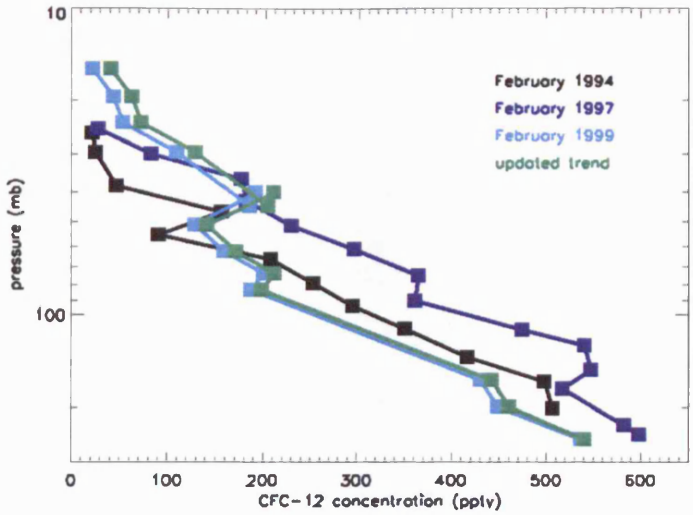

Figure 1.6 Stratospheric CFC-12 volume mixing ratios measured by a balloonborne version of the MIPAS instrument (MIPAS-B) over Kiruna (68 N, 20 E). The green line represents a prediction of current CFC-12 stratospheric concentrations (February 2005) calculated here. CFC-12 has recently been increasing very slowly (0.6 pptv/yr) in the troposphere but previously much more rapidly than this (4.4 pptv/yr) at the time of the results in the last IPCC report, 2001, from 1998. The trend accounts for age of air [Andrews *et al.*, 2001] with values in the upper troposphere (200 mb) predicted to have increased by approximately 5 pptv between 1999 and 2005 (assuming mixing on scales much less than a year). In the lower stratosphere (100mb), assuming an age of air of two years, concentrations are predicted to have increased by 12 pptv. In the middle stratosphere (20mb), assuming an age of air of 4 years, CFC-12 concentrations are predicted to have increased by around 19 pptv.

The gradient of all three compounds is very sharp and their concentrations reduce rapidly with height. Dynamically, a temperature inversion in the stratosphere, induced by absorption of sunlight by ozone, suppresses convection and vertical mixing is much slower than in the troposphere. Chemically, the compounds are exposed to increasing ultra violet radiation levels as they are transported higher. The combination of both factors accounts for the sharp gradients observed.

Tropospheric CFC-12 concentrations were slowly rising at less than 1 pptv/yr (in 2005) but the Kiruna results in Figure 1.6 contradict the expected rise, suggesting there are also important dynamical considerations between the two measurement periods. Although the HCFC-22 profiles measured in 1997 and 1999 are similar in both shape and measured concentrations, there is a marked stratospheric concentration increase (up to 33 pptv at 80 mb) between the 1994 and 1999 measurements, consistent with an increase expected from globally averaged ground based-measurements shown in Figure 1.5.

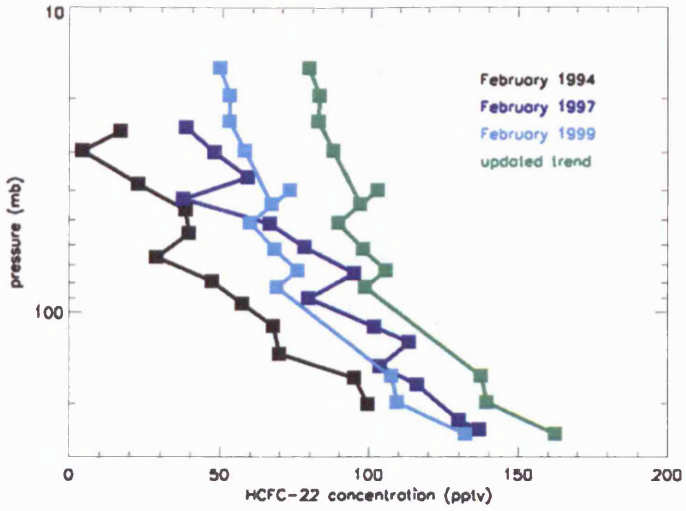

Figure 1.7 Stratospheric HCFC-22 volume mixing ratios measured by a balloonborne version of the MIPAS instrument (MIPAS-B) over Kiruna (68 N, 20 E). The green line represents a prediction of current HCFC-22 stratospheric concentrations (February 2005) based on a linearly decreasing trend in the troposphere of 5 pptv/yr (ESRL) applied to the February 1999 data.

1.3 Halocarbon Chemistry

It is estimated that 90 % or more of all the purely anthropogenic CFC-11 and CFC-12 produced up to 1996 has been released to the atmosphere [Wayne, 2000]. It was recognised by Jim Lovelock and collaborators in 1973 that halocarbons were present in the troposphere. Within experimental error, it was also realised that the quantity of CFCs were equal to the total amount ever produced confirming the tropospheric inertness of the compounds. Transport to the stratosphere and photochemical destruction is the only sink for CFCs but more generally destruction of halocarbons (also including HCFCs) is initiated by one of three processes: photolysis, reaction with the hydroxyl radical (OH) or reaction with excited state oxygen atoms ($O(^1D)$). The altitude at which a halocarbon will be destroyed is dependent chiefly on its chemical composition. Generally, more Cl atoms in the molecule shift its ultraviolet absorption spectrum to longer wavelengths, photolysis can occur at lower altitudes and results in a decrease in the atmospheric lifetime.

Photochemical destruction of CFCs in the stratosphere releases chlorine atoms. The reaction path CFC-12 can be characterised:

$$CF_2Cl_2 + h\nu \rightarrow CF_2Cl + Cl \quad (1)$$
$$CF_2Cl + O_2 + M \rightarrow CF_2ClO_2 + M \quad (2)$$
$$CF_2ClO_2 + NO \rightarrow CF_2ClO + NO_2 \quad (3)$$
$$CF_2ClO + M \rightarrow COF_2 + Cl + M \quad (4)$$

In the short wave photolysis ($\lambda \leq 320$ nm) of stratospheric ozone an excited electronic state oxygen atom, $O(^1D)$, is produced. Reaction of an $O(^1D)$ atom with CFCs proceeds along a series of channels for CFC-12:

$$O(^1D) + CF_2Cl_2 \rightarrow CF_2Cl + ClO$$
$$\rightarrow O(^3P) + CF_2Cl_2$$
$$\rightarrow CF_2ClO + Cl$$
$$\rightarrow COF_2 + Cl_2$$

Production of ClO is probably the dominant path (60 %), with quenching of $O(^1D)$ to $O(^3P)$ the minor channel (15 to 20 %). Concentrations of $O(^1D)$ increase rapidly with altitude, and hence CFC-12 destruction via reaction with $O(^1D)$ increases. Recent concentration estimates of $O(^1D)$ in the atmosphere are 10 atom cm^{-3} at 15 km, 100 atom cm^{-3} at 25 km and 1000 atom cm^{-3} at 35 km [Brasseur, 1999]. The concentration increase of $O(^1D)$ with altitude almost parallels the increase of the photolysis rate of CFC-12 with altitude over the 20 to 35 km range. Statistically, reaction with $O(^1D)$ contributes about 30 % of the CFC-12 loss in the atmosphere. Reaction with OH is not a significant loss mechanism for CFCs.

For halocarbons that contain hydrogen atoms (for example the HCFCs), reaction with OH in the troposphere provides the main route for their atmospheric destruction:

$$OH + CX_3H \rightarrow H_2O + CX_3$$

where X refers to H, F, Cl, Br, or I. For example the reaction for HCFC-22 is:

$$OH + CHClF_2 \rightarrow H_2O + CClF_2$$

The reaction rate of the compounds is slow meaning that significant fractions of these compounds are transported to the stratosphere. In the stratosphere, all three pathways are then possible for the removal of these gases, i.e. photolysis, reaction with OH and reaction with $O(^1D)$.

1.3.1 Stratospheric ozone destruction by halocarbons

Chlorofluorocarbons, along with other chlorine and bromine containing compounds accelerate ozone depletion in the Earth's stratosphere. A complex scenario of solar radiation, chemical reactions and atmospheric dynamics explained the discovery of a polar springtime ozone "hole" over Antarctica in 1985 [Farman *et al.*, 1985]. This whole process is initiated by the onset of the polar winter where high latitudes remain in complete darkness throughout the winter months. The air above the pole cools rapidly forming a vortex (usually most pronounced in the Antarctic winter) which isolates the colder region from lower latitudes. The vortex formation provides the necessary conditions for depletion of ozone by catalytic cycles (a series of reactions in which a particular chemical species is depleted, but the catalyst is unaffected). The released chlorine atoms, from reservoir species $ClONO_2$ and HCl, formed from the destruction of CFCs, react with ozone to form the following catalytic cycle:

$$Cl + O_3 \rightarrow ClO + O_2$$
$$ClO + O \rightarrow Cl + O_2$$

resulting in $Cl + O_3 + O \rightarrow Cl + 2O_2$. The cycle initially removes chlorine by reaction with ozone to form chlorine monoxide, but this chlorine is released again through reaction of chlorine monoxide with an oxygen atom. The same amount of chlorine is present before and after the reaction. For the lower stratosphere this chain reaction is only thought to be responsible for 5 % of the portion of total ozone loss that is due to halogens in general [Finlayson-Pitts, 1999] at 15 km and approximately 25 % at 21 km.

Most of the ozone loss associated with ClO_x (and also BrO_x) at lower stratospheric altitudes is due to the cycle:

$$Cl + O_3 \rightarrow ClO + O_2$$
$$ClO + HO_2 \rightarrow HOCl + O_2$$
$$HOCl + h\nu \rightarrow Cl + OH$$
$$OH + O_3 \rightarrow HO_2 + O_2$$

resulting in the net: $2O_3 \rightarrow 3O_2$ which accounts for approximately 30 % of the ozone loss here. The corresponding cycle for bromine constitutes 20-30 % of the ozone loss between 15 and 21 km. Reaction of ClO with HO_2 produces HOCl + O_2 with a yield $\geq$ 95 % at

temperatures from 210 to 300 K. At the lower end of this temperature range HCl may react with ozone, with a yield of < 5 %, which may be significant in the net ozone destruction both in polar regions and mid-latitudes (Finkbeiner *et al.*, 1995).

The reaction chain of OH with ClO may also play an important role and is characterised by:

$$OH + ClO \rightarrow HO_2 + Cl$$
$$\rightarrow HCl + O_2$$

Lipson *et al.*, 1997 report a yield of 5 ± 2 %.

Halocarbon	Chemical Formula	Atmospheric lifetime (yr)[a]	Ozone Depletion Potential (ODP)	Release rate (106 kg yr-1)		Contribution to Ozone Loss[b]	
				1990	1998	1990	1998
CFC-11	$CFCl_3$	53	[1.0]	250	103	22.6	21.0
CFC-12	CF_2Cl_2	100	0.82	371	186	27.5	31.2
CFC-113	$C_2F_2Cl_3$	83	0.90	236	44	19.2	8.1
HCFC-22	CHF_2Cl	11.8	0.04	178	282	0.6	2.3

Table 1.2 Estimated Ozone Depletion Potentials (ODPs) of the primary halocarbons in the atmosphere. (a) Scientific assessment of stratospheric ozone: 1998, World Meteorological Organization, Geneva, 1999, Lifetimes from CSIRO model. (b) Percentages, calculated from only those halogen compounds listed in the table. The remaining 30.1 % for 1990 and 37.4 % for 1998 is constituted CFC-113, CF_3Br, CF_2BrCl, CH_3CCl_3, CCl_4 and CH_3Br. [The table is adapted from the Wayne, 2000].

The Montreal Protocol on substances that deplete the ozone layer [1991] recognised the need firstly to phase-out CFCs, and secondly to eliminate their HCFC substitutes. To categorise the contribution by individual compounds to ozone depletion, an ozone depletion potential (ODP) has been defined. It is the ratio of the global loss of ozone (i.e. an integration over latitude, altitude and time) from that compound at steady state per unit mass emitted relative to the loss of ozone due to emission of unit mass of a reference compound, usually CFC-11. This ODP represents the overall impact of a compound on ozone destruction in the long-term. Table 1.2 presents the ODP for the most abundant HCFC, HCFC-22, and compares it to that of the major CFCs. The ODP is at least twenty times lower for HCFC than that for the CFCs, but the impact of unregulated use on ozone layer destruction is still sufficient to initiate action to curb their production.

1.4 Radiative effects of halocarbons

A method of assessing the contribution of the greenhouse gases (including halocarbons) towards global warming to quantify this by calculating their radiative forcing (RF). The RF is defined as the change in net radiative flux at the tropopause, after the climate has been perturbed (for example by an increasing/decreasing gas amount), and after allowing the stratosphere to come into equilibrium with the perturbation.

The RF is calculated after equilibrium in the stratosphere is observed because the timescale for stratospheric adjustment to a change is a few months, unlike the surface and troposphere for which this can be decades. Temperature changes in the stratosphere are therefore counted as part of the forcing and not the response, meaning that the tropopause is the ideal place to calculate the RF. A positive (negative) forcing is a process that will result in a warming (cooling) at the surface.

Gas	Chemical Formula	Radiative Forcing (Wm^{-2} $ppbv^{-1}$)	Lifetime (Years)	100-year GWP
CFC-11	$CFCl_3$	0.242	45	4,500
CFC-12	CF_2Cl_2	0.321	100	10,600
HCFC-123	$CHCl_2CF_3$	0.141	1.4	80
HCFC-124	$CHClFCF_3$	0.193	6.1	540
HCFC-141b	CH_3CFCl_2	0.130	9.2	650
HCFC-142b	CH_3CF_2Cl	0.163	18.5	1900
HCFC-21	$CHFCl_2$	0.140	2	170
HCFC-225ca	$CF_3CF_2CHCl_2$	0.202	2.1	130
HCFC-225cb	$CF_2ClCF_2CHCl_F$	0.280	6.2	540
HCFC-22	CHF_2Cl	0.208	11.8	1,800

Table 1.3 Table containing estimates of radiative forcing/100-year GWP of principle HCFCs and two primary CFCs for comparison. [Table adapted from the IPCC report in 2001]

The radiative forcing concept provides a simplified means of comparing the various radiative factors that are believed to influence the climate system to one another. Global Warming Potentials (GWPs) are another important concept used to compare the relative climatic effects of an increase of one unit mass of a greenhouse gas compared to a one unit mass increase of carbon dioxide over a period of time. Since these potentials are usually based on global/annual mean estimates, the effects of applying vertical profiles and spatial distributions, [Freckleton *et al*, 1998], are important particularly for (H)CFCs.

Impacts of greenhouse gas emissions upon the atmosphere are related not only to the radiative properties of a gas but also to the time scale characterising the removal of substances from the atmosphere. This is accounted for in the GWP by the time horizon. The choice of the time horizon depends on whether short or long term processes need to be emphasized, e.g. shorter times for speed of climate impacts, longer times for magnitude of impact. Current estimates can be found in Table 1.3.

It is noted that the radiative forcing of HCFC-22 is nearly as strong as CFC-12 (the compound it was designed to replace). Due to the major sink of HCFC-22 in the troposphere, its GWP is six times lower than that of CFC-12, but it is still significant nonetheless.

1.5 Summary

Halocarbons act as chlorine reservoirs and consequently accurate measurement of their stratospheric temporal and spatial distribution is key to our understanding of future stratospheric ozone depletion as a consequence of halocarbon release. The compounds are also very efficient greenhouse gases, contributing directly to the global warming effect, and regular, accurate global atmospheric measurements are also required in model calculations to quantify the halocarbon global warming potential.

Halocarbons are purely anthropogenic compounds (except for methyl bromide and methyl chloride for which there are natural sources) with atmospheric lifetimes ranging from years to centuries, intrinsically implying that they are very well-mixed in the troposphere, but the high static stability of the stratosphere limits their vertical diffusion leading to gradients with height. Mean tropospheric values of CFC-11 and CFC-12 in early 2004 were 236 pptv and 537 pptv respectively and the mean for HCFC-22 was 160 pptv (all based on globally averaged CMDL surface measurements). Tropospheric CFC-12 concentrations were rising only very slowly (0.6 pptv/yr) and are expected to begin decreasing over the next few years. Tropospheric HCFC-22 concentrations were rising at 5.2 pptv/yr and the trend is not expected to change dramatically over the next few years until the compound is phased out more readily by 2030 as part of the Montreal Protocol.

New possibilities for infrared remote sensing, giving global measurement capability independently of day or night, have recently been made available by the launch of

Michelson Interferometer for Passive Atmospheric Sounding (MIPAS) on the European Space Agency (ESA) ENVISAT satellite and the Tropospheric Emission Spectrometer (TES) on NASA's EOS-AURA satellite. A Fourier Transform Spectrometer (FTS) has also been deployed on the Canadian Atmospheric Chemistry Experiment (ACE) satellite to investigate the chemical processes involved in the distribution of ozone in the atmosphere and was launched in August 2003.

Retrieval of trace gas information from satellite measurements requires detection of the gas in the measured spectra and the development of an accurate retrieval scheme to maximise the information on the gas gained from the measurement. These results then require thorough validation against independent sources. This thesis aims to detect HCFC-22 signals in MIPAS-E spectra, characterise suitable regions for the retrieval of the gas, develop an accurate retrieval scheme to invert the spectral measurements into gas volume mixing ratio and validate these results. The final aim of this project is to provide global, seasonal datasets of HCFC-22 vertical profiles from a spaceborne FTS for the first time. The thesis was also extended to retrieve global CFC-12 in order to verify the retrieval scheme and provide confidence in MIPAS-E retrievals.

Chapter 2

2 Remote Sounding of the Atmosphere

Remote sensing of the atmosphere provides one method of measuring atmospheric trace gas concentrations. In contrast to *in situ* measurements where the quantity of interest is directly sampled, remote sensing techniques measure the electromagnetic radiation from a region of the atmosphere and invert these measurements, through mathematical techniques, into the quantity of interest such as gas concentration, pressure or temperature. The major advantage of remotely sensed measurements, particularly when they are deployed in space, is their ability to provide global coverage from only one sensor system over a period of time. These are both important criteria for climate studies.

Remotely sensed data from the MIPAS-E (chapter 3) is considered in this thesis and is used to detect and retrieve HCFC-22 profile concentrations in the upper troposphere and lower stratosphere (UTLS). The Atmospheric Trace MOlecule Spectroscopy experiment (ATMOS) instrument (section 5.3) has previously measured HCFC-22 concentrations in the UTLS using solar occultation remote sensing techniques, but the technique and the mission were limited as it took three years and three separate missions to obtain global coverage of important halocarbons including HCFC-22. The average tropospheric value of HCFC-22 over this time would have increased by over 15 pptv.

All molecules interact with electromagnetic radiation and emit and absorb this radiation at discrete frequencies and this information is used to provide information of their atmospheric concentration. In particular, halocarbons are strong absorbers in the infrared part of the electromagnetic spectrum and as such are strong greenhouse gases. Recent advances in remote-sensing of atmospheric thermal infrared emission has led to exciting new possibilities of using a continuous source of radiation, independent of day or night, to provide gas concentration information. Table 2.1 lists some of the current infrared missions that have been deployed in space to measure trace gases in the UTLS.

This chapter reviews the current theory of the propagation of radiation of radiation through the atmosphere (radiative transfer) and the infrared spectroscopy of halocarbons. A

mathematical technique to invert spectral measurements into gas concentrations (retrieval theory) is also described.

Instrument	Platform	Measurement quantity	Launch
MIPAS-E	The European Space Agency (ESA) ENVIronmental SATellite (ENVISAT)	Atmospheric Limb Emission (4.15-14.6 μm)	March 2002
ACE-FTS	The Canadian Space Agency SCISAT-1 satellite	Solar Occultation (2-13 μm)	August 2003
TES	The EOS-AURA satellite (NASA)	Atmospheric Limb Emission (3.2-15.4 μm)	July 2004
ATMOS	NASA space shuttle	Solar Occultation (2.1-16.6 μm)	Four missions between 1985 and 1994

Table 2.1 Selected high-resolution limb sounding spectrometers capable of measuring trace gases in the upper troposphere and lower stratosphere (UTLS).

2.1 Limb Sounding

Limb sounding instruments view a slice through the atmosphere, measuring emission from a point tangential to the Earth's surface at height *h,* a point where the line of sight of the instrument intersects a line of circumference centred on the Earth (Figure 2.1). This viewing geometry is ideal for measuring gases with very low atmospheric concentrations as the long horizontal path through which the instrument measures maximises the signal received. Although horizontal resolution is generally no better than a few hundred kilometres, limb sounding does provide vertical measurements to a high-resolution of 1 to 3 km.

There are two ways to measure the limb signal; either by measuring the absorption of solar radiation by the atmosphere (solar occultation- both ACE-FTS and ATMOS) or directly measuring the cold atmospheric emission against deep-space (MIPAS on ENVISAT and the Tropospheric Emission Spectrometer (TES)). Measurements are not limited to the UTLS region and can also be made up to the mesosphere and beyond to look at non-LTE effects and to measure the optical depth of noctilucent clouds.

The path taken by the radiation varies with viewing angle with measurements of the lower atmosphere having a longer tangent path than measurements of the upper atmosphere. Atmospheric density decreases rapidly with increasing altitude and as a consequence, the majority of observed radiation by the instrument, for any viewing angle, originates from the tangent point, *h*. There is an added complication as the varying density also produces a varying refractive index along the tangent path. The "true" tangent height observed is curved but for a specified state of the atmosphere the effect can be modelled. The contribution of the signal emanating from the layers directly above the tangent point increases as the tangent height decreases, so by the upper troposphere a large amount of measured signal is due to higher layers in the tangent path. Fortunately, in limb geometry the region of the atmosphere below the line of sight (and associated field of view) at the tangent does not contribute to the measured spectra, meaning that emission from the surface and lower atmosphere can be neglected (assuming no scattering). The theory of radiative transfer and forward modelling is described in sections 2.2 and 2.4 respectively).

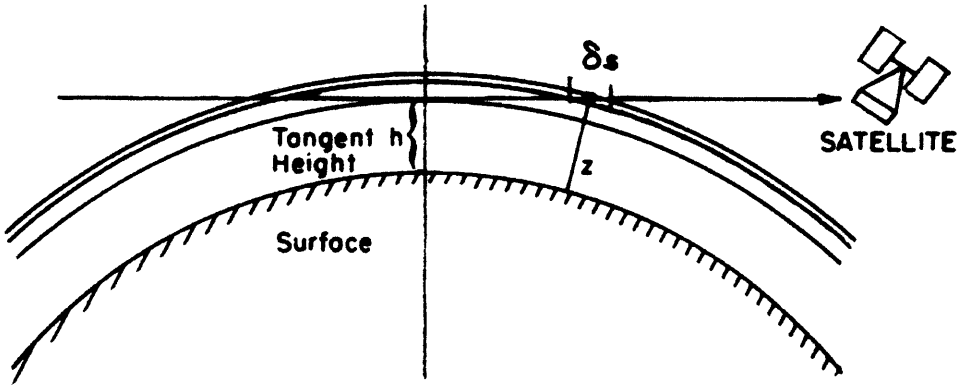

Figure 2.1 Limb viewing geometry of MIPAS-E. The satellite instrument scans through the atmosphere along the limb at a tangent height h. Radiance is received from segments δs of the path at height z.

2.2 Radiative transfer

Radiative transfer is the most fundamental concept in the study of atmospheric radiation. Indeed, remote sensing observations are only possible due to the transfer of radiation through the atmosphere to the instrument. The radiation arriving at an observing instrument is the sum of the radiation entering the atmosphere in the field of view of the instrument and that emitted or scattered by trace gases such as H_2O, O_3, aerosols or by clouds into the beam of radiation. This radiation will be modified by absorption and

scattering processes out of the beam as it passes through the atmosphere. The intensity, or radiance, of a beam of energy originating from a point can be defined as the flux of energy in a given direction per second per unit frequency (or wavelength) range per unit solid angle per unit area perpendicular to the given direction.

As mentioned in the previous chapter, there are two kinds of interactions between radiation and matter; extinction processes (those which decrease the energy in the radiation field by either scattering or absorption) and emission processes (those which increase the energy). The Beer-Lambert law states that the rate of change (reduction) of the radiance in passing through matter is proportional to the amount of radiation, I_ν, and the amount of matter. This decrease of radiance when travelling through a medium is:

$$dI_\nu = -e_\nu n_a I_\nu ds \tag{2.1}$$

where e_ν is the molecular extinction coefficient constant that characterises the radiation-matter interaction (including both absorption and scattering), and n_a is the number density of absorbing atoms or molecules. In a path ds in emission, the increase in radiance travelling through the path ds is given by:

$$dI_\nu = j_\nu n_a ds \tag{2.2}$$

where j_ν is the emission coefficient constant, which characterises the emission properties of the molecules in the path.

Assuming that the atmospheric layer is in local thermodynamic equilibrium (LTE) [Goody and Yung, 1989] at a given temperature, T, then Kirchoff's law states that the emission and absorption coefficients, j_ν and e_ν, are related by a universal function depending only on temperature:

$$\frac{j_\nu}{e_\nu} = f_\nu(T) \tag{2.3}$$

The general source function can be defined as:

$$J_\nu = \frac{j_\nu}{e_\nu} \tag{2.4}$$

and hence Equation 2.2 can be rewritten and expressed as:

$$dI_\nu = e_\nu n_a J_\nu ds \tag{2.5}$$

Extinction and emission must combine to give a change in radiance. This change is expressed by:

$$\frac{dI_\nu(P,\mathbf{s})}{ds} = -e_\nu n_a [I_\nu(P,\mathbf{s}) - J_\nu(P,\mathbf{s})] \tag{2.6}$$

where $I_\nu(P,s)$ defines the radiance at a point P in an arbitrary direction s. This is Schwarzchild's radiative transfer equation, originally derived in the early 20th century.

In the absorption process, a photon excites the matter into one of its internal energy modes, while in emission, the reverse process, an excited state is deactivated by emitting a photon. Absorption is often followed by energy transfer of the excited internal energy mode to translational energy in a subsequent matter-matter interaction. Energy of a photon may be re-emitted, or simply transferred to some other internal state of the same molecule or one of its collision partners.

The effects of simple scattering are usually negligible in infrared atmospheric radiative transfer for limb sounding, so ignoring simple scattering implies that the extinction coefficient is the same as the absorption coefficient:

$$e_\nu = k_\nu \tag{2.7}$$

and so the emission term is given by:

$$e_\nu n_a J_\nu = k_\nu n_a J_\nu \tag{2.8}$$

where J_ν excludes "simple scattering". Both absorption and emission are assumed to be isotropic (i.e. there is no dependence of k_ν and J_ν on the angular distribution of photons).

To apply the radiative transfer equation (Equation 2.6) to remote sensing problems firstly consider the optical path of radiation from source to the instrument in Figure 2.2.

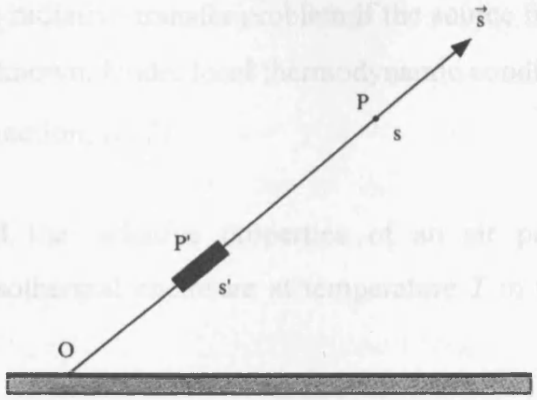

Figure 2.2 Optical path

The optical thickness $\bar{\tau}_\nu$ describes the total optical path length in a medium, here the atmosphere, between two points s' and s (Figure 4.2) along the direction **s** defined by:

$$\bar{\tau}_\nu(s',s) = \int_{s'}^{s} k_\nu(s'')n_a(s'')ds'' \tag{2.9}$$

The radiative transfer equation (2.6) at the point P' at a distance s' can be written as:

$$\frac{dI_\nu(s',\mathbf{s})}{d\bar{\tau}_\nu} = [I_\nu(s',\mathbf{s}) - J_\nu(s',\mathbf{s})] \tag{2.10}$$

where $\bar{\tau}_\nu$ is defined as a positive quantity as $s > s'$.

As Equation 2.10 is a linear first-order differential equation with constant coefficients, the necessary integrating factor is $\exp(-\bar{\tau}_\nu)$. Multiplying Equation 2.10 by this factor gives:

$$\frac{d[I_\nu(s',\mathbf{s})\exp(-\bar{\tau}_\nu)]}{d\bar{\tau}_\nu} = -\exp(-\bar{\tau}_\nu)J_\nu(s',\mathbf{s}) \tag{2.11}$$

Integrating from s, where $\bar{\tau}_\nu$ =0, to the origin s_0

$$I_\nu(s,\mathbf{s}) = I_\nu(s_0,\mathbf{s})\exp[-\tau_\nu(s_0,s)] + \int_0^{\tau_\nu(s_0,s)} J_\nu(s',\mathbf{s})\exp[-\tau_\nu(s',s)]d\tau_\nu \tag{2.12}$$

Equation 2.12 solves the radiative transfer problem if the source function at a point P' and direction $\mathbf{s}$, $J_\nu(P',\mathbf{s})$, is known. Under local thermodynamic conditions the source function is given by the Planck function, $B_\nu(T)$.

Kirchoff first described the radiative properties of an air parcel in thermodynamic equilibrium, inside an isothermal enclosure at temperature T in the late 19th century. He discovered:

- The radiation inside the enclosure is homogeneous, unpolarized and isotropic
- The source function is equal to the radiance
- The radiance is a universal function of the temperature within the enclosure

Planck found an analytical formula to quantify the radiant energy, the Planck function:

$$B_\nu(T) = \frac{2h\nu^3}{c^2}\frac{1}{[\exp(h\nu/kT)-1]} \tag{2.13}$$

with h as the Planck constant, and k the Boltzmann constant. Equation 2.13 gives an expression for the source function $J_\nu(T)$ for a system in thermodynamic equilibrium. At a given frequency, the source function depends only on temperature, T, if the gas is in thermodynamic equilibrium. Different gas properties emitting and absorbing radiation at frequency ν are contained in their absorption coefficient, k_ν.

For measurements of limb thermal emission, $I_\nu(s_0, \mathbf{s})$, is the emission of cold space and, in the infrared, can be considered negligible. Equation 2.12 can be re-written as:

$$I_\nu(s,\mathbf{s}) = \int_0^{\bar{\tau}_\nu(s_0,s)} B_\nu(s',\mathbf{s})\exp\left[-\bar{\tau}(s',s)\right]d\bar{\tau}_\nu \tag{2.14}$$

2.3 Infrared Spectroscopy

Forward modelling of the emission, and as a consequence the retrieval of atmospheric parameters, requires accurate reference spectral data from which to calculate the radiative

transfer. Infrared spectral line shapes and line widths have to be measured beforehand in a laboratory environment at various pressures and temperatures representative of the atmosphere. An added complication is that even over very small spectral ranges the measured atmospheric radiance is a function of the emission from multiple gases, so accurate reference data is required for all these gases and not just the gas of interest if the retrieval is to have any degree of accuracy. The spectroscopy of halocarbons relevant to this thesis, namely CFC-12 and HCFC-22, is described in the following sections.

2.3.1 Theory

Molecular energy is exchanged in transitions between quantum states and this is accompanied by the absorption or emission of photons (quanta of electromagnetic radiation energy). This thesis studies radiance emissions in the mid-infrared and photon energies involved in such transitions between energy levels corresponding to mainly simultaneous molecular vibrational and rotational transitions. In the atmosphere both of these transitions occur simultaneously forming infrared bands centred on a vibrational transition frequency, displaying lines or a rotational fine structure. In addition, various physical mechanisms can cause overlap or broadening of the spectral lines, by collisions or Doppler effects.

2.3.2 Rotation of Molecules

All molecules can be segregated into types depending on their moments of inertia about three perpendicular axes through their centre of gravity. These are conventionally labelled I_A, I_B and I_C where $I_A \leq I_B \leq I_C$. Molecules are divided into one of four groups depending on their symmetry:

- Linear molecules have one moment of inertia equal to zero, whilst the other two are equal ($I_A = 0$ and $I_B = I_C$). One example is carbon dioxide (CO_2).

- Symmetric top molecules with two equal and the third different and not equal to zero. Further subdivision of this group leads to the prolate symmetric top ($I_A < I_B = C$) and the oblate symmetric top ($I_A = I_B < I_C$). An example of a

symmetric top molecule (or rotor molecules as they are sometimes called) is ammonia (NH_3).

- Spherical tops have all three moments of inertia equal ($I_A = I_B = I_C$). An example is sulphur hexafluoride (SF_6) or methane (CH_4)

- Asymmetric tops have none of the three moments of inertia equal ($I_A \neq I_B \neq I_C$). Many halocarbons are of this type and the majority of molecules belong to this fourth class.

Energy of a pure rotational transition lies in the microwave region of the electromagnetic spectrum and in principle the rotational energy levels can be calculated from Schrödinger's equation.

2.3.3 Molecular Vibrations

The number of degrees of freedom of the molecule determines the number of fundamental vibrations of a molecule. A molecule comprising N atoms will have 3N degrees of freedom of which three are needed to describe the translational motions of the molecule. For non-linear molecules a further three are required to describe their rotational motion and this is reduced to two for linear molecules. Ultimately for non-linear molecules there are 3N-6 vibrational degrees of freedom and for linear molecules there are 3N-5.

In the infrared, vibrational transitions occur and if the motion can be assumed to be simple harmonic, then the energy levels of each vibrational state are:

$$E_{\upsilon}(\upsilon_i) = hc\left(\upsilon_i + \frac{1}{2}\right)\tilde{\nu}_i \qquad (2.15)$$

where $\tilde{\nu}_i$ is the wavenumber (defined as the reciprocal of wavelength) of the normal vibrational mode and υ_i is the vibrational quantum number (greater than or equal to zero). The usual vibrational transition selection rule at lower temperatures is given by $\Delta\upsilon = \pm 1$ (where +1 represents absorption and −1 emission). In the ground state only absorption by the molecule (a positive transition) is permitted. The strongest band is between the

transition from the ground state ($\upsilon = 0$) and $\upsilon = 1$ due to the fact that relative populations of the levels decrease towards higher energy states according to the Boltzmann distribution:

$$\frac{N_\upsilon}{N_0} = \exp\left(-\frac{E_\upsilon}{kT}\right) \tag{2.16}$$

where N_υ describes the population of higher vibrational states relative to the ground state, N_0 at a temperature T. Spacing between vibrational levels is large and the majority of molecules occupy the ground state at standard atmospheric temperatures. With a temperature increase, the population of higher energy states increases, allowing transitions between higher vibrational states ($\upsilon > 0$); these are known as "hot" bands. Additionally, each vibrational state may have other harmonics or overtones associated with it and so $\Delta\upsilon = \pm 2, 3, 4$, etc leading to overtone bands ($2\nu_1$, $2\nu_2$), combination bands (e.g. $\upsilon_1 + \upsilon_3$) and difference bands (e.g. $\upsilon_3 - \upsilon_1$), which can be seen in the mid-infrared.

2.3.4 Vibration-Rotation Bands

Vibrational energy levels in a rotating molecule are split into rotational energy levels a fact described by the Born-Oppenheimer approximation. This assumes energy associated with vibrational and rotational (and also electronic and nuclear) states are independent and the total energy of a molecule is the sum of energies of vibrational and rotational motion. Interactions between the two motions are not insignificant meaning that this is only an approximation. Rotational transitions require much smaller amounts of energy than vibrational ones and so occur simultaneously with vibrational transitions.

Selection rules for vibration-rotation bands are molecule dependent, and are defined by whether vibration causes a parallel or perpendicular change in the electric dipole moment to the axis of symmetry. For linear molecules, the dipole moment change occurs parallel to the major axis of symmetry (parallel bands) with the selection rules of $\Delta J = \pm 1$. If the change occurs perpendicular to the axis of symmetry (perpendicular bands), which happens for many halocarbons, $\Delta J = 0$ is allowed in addition to $\Delta J = \pm 1$. Since all three types of rotational transitions are allowed for asymmetric top molecules (of which many halocarbons are included), the most common form of a vibration-rotation band is the 'PQR' band. In this situation, the P-branch corresponds to $\Delta J = -1$, the Q-branch to $\Delta J = 0$ and the R-branch to $\Delta J = +1$. The Q-branch is usually the most intense feature of the band

in the mid-infrared and corresponds to the purely vibrational transition energy. The P-branch is observed at lower frequencies to the Q-branch and the R-branch is observed at higher frequencies compared to the Q-branch.

2.3.5 Line Intensities

The intensity of each spectral line (S) is as important to know as the position of the line itself. S is calculated by:

$$S = \int k(\tilde{\nu}) d\tilde{\nu} \tag{2.17}$$

where $k(\tilde{\nu})$ is the absorption coefficient. The Einstein coefficient for induced absorption and stimulated emission, dependent on the population of the states between which the transition takes place and the transition probability can be used to derive $k(\tilde{\nu})$. For a vibration-rotation line for a state i to state j transition, the line intensity of a single molecule is given by:

$$S_{line} = \frac{8\pi^3 \nu_{ji}}{4\pi\varepsilon_0 3hcQ} \exp\left(\frac{-E_i}{kT}\right)\left(1 - \exp\left(\frac{-hc\tilde{\nu}_{ij}}{kT}\right)\right) S_{ij} \tag{2.18}$$

where Q is the partition function, T is the temperature in Kelvin, E_i is the energy of the lower state, and S_{ij} is the line strength, defined as the square of the transition moment relative to a fixed an axis fixed in space.

2.3.6 Line Widths

Spectral lines can be broadened (that is the line width increased) by many physical mechanisms including natural, Doppler and collisional broadening. Natural broadening is the smallest of the three mechanisms and is a direct result of the Heisenberg Uncertainty Principle. In the atmosphere both Doppler and collisional broadening are important where the lineshape may involve a combination of the two effects. One example is the Voigt lineshape. On MIPAS-E measurements there is also a lineshape imposed on real spectral lines, characteristic of the instrument itself.

Doppler broadening is caused by the particles moving towards or away from the point of measurement inducing a frequency shift of the spectral line emitted by the particle. The net result is broadening of the line as observed in the atmosphere. This is most important in the atmosphere at altitudes above 80 km. Collision broadening is the most important line-broadening mechanism below 30 km in the atmosphere.

The varying influence of these broadening mechanisms on molecules can be parameterised using line shapes in the forward modelling of atmospheric spectra.

2.3.6.1 The Voigt lineshape

In the mid infrared, spectral line widths due to Doppler and pressure broadening become equal at around 30 km. A radiative transfer model has to consider the spectral lineshape of line sources from surrounding altitudes to model the most accurate representation of the true atmosphere. The Voigt lineshape [Armstrong, 1967] adequately describes the combined behaviour of both mechanisms in atmospheric applications. This provides a convolution of the Doppler and pressure-broadened (Lorentz) lineshapes:

$$k(\tilde{\nu}) = \frac{S}{\alpha_D \sqrt{\pi}} \frac{y}{\pi} \int_{-\infty}^{\infty} \frac{e^{-t^2}}{y^2 + (x-t)^2} dt \tag{2.19}$$

where $k(\tilde{\nu})$ is the absorption coefficient at some wavenumber $\tilde{\nu}$. S is the line intensity at some reference line centre, ν_0 and t is the duration of emission. Also, x and y defined as:

$$x = \frac{\alpha_L}{\alpha_D} \tag{2.20}$$

$$y = \frac{\tilde{\nu} - \tilde{\nu}_0}{\alpha_D} \tag{2.21}$$

where α_L and α_D are the Lorentz and Doppler half-widths respectively.

2.3.7 Heavy Molecules

For heavy molecules such as the halocarbons, the spacing of lines are such that individual lines cannot be distinguished. This is caused by the large moment of inertia of the molecules, causing the energy and hence the spectral spacing of rotational transition lines to be very small. The rotational constant, B, where:

$$B = \frac{h^2}{2I} \tag{2.22}$$

and I is the moment of inertia, is related to the spacing of the rotational energy levels by:

$$E_J = BJ(J+1) \tag{2.23}$$

where J is the rotational quantum number and is a positive integer. Hence, as the moment of inertia increases then the spacing of the rotational levels decreases. Even at the highest spectral resolutions possible the lines within a typical band may overlap due to Doppler and Lorentz broadening (section 2.3.6). The overlapping of features results in broadband spectral features. Therefore measurements at very high spectral resolutions will not yield significant additional information about individual line parameters.

As the spectra of heavy molecules are complex, determination of line parameters for heavy molecules has not been attempted. Instead reference spectral data for heavy molecules are reported as absorption cross-sectional data, where the absorption cross-section per molecule is a function of wavenumber. These absorption cross-sections are derived from the Beer-Lambert law (equation 2.12) along a homogeneous path for negligible emission and scattering:

$$I(\nu) = I_0(\nu)\exp(-n\sigma(\nu)x) \tag{2.24}$$

where $I_0(\nu)$ is the intensity of source radiation as a function of wavenumber, $I(\nu)$ is the transmitted intensity of radiation through some sample of pathlength x with molecular number density, or concentration, n. The absorption cross-section per molecule, $\sigma(\nu)$, is conventionally given in units of cm^2 $molecule^{-1}$.

Then, measurements of transmittance spectra $[I(\nu)/I_0(\nu)]$ of a gas in the laboratory can be used to calculate the absorption cross-section from equation 2.24. The cross-section may also depend on temperature and pressure. Therefore reference cross-sections for heavy molecules must be made over a number of temperature and pressure states representative of atmospheric conditions. The HITRAN database [Rothman *et al.*, 1998] contains cross-sectional data for some heavy molecules including CFC-12 and HCFC-22.

2.4 Forward Modelling

2.4.1 The Oxford reference forward model

The spectra observed by the MIPAS instrument can be modelled and identified using a forward model. The Oxford reference forward model (RFM) is a line-by-line model developed at Oxford University (http://www-atm.physics.ox.ac.uk/RFM/) under a European Space Agency (ESA) contract to provide reference spectral calculations for the MIPAS-E. The RFM has the ability to calculate the appropriate atmospheric limb emission/transmission spectra that will subsequently be used in the retrieval process to atmospheric concentrations. The model works in the infrared and has the capability to include all the gases needed for this study.

2.4.1.1 Input Files

In order to calculate the signal observed by the MIPAS satellite instrument it is necessary to know about:

- Atmospheric parameters
    - Concentration of the gas
    - Its temperature and pressure
- Spectroscopy of the gases
    - Frequencies of the transition
    - Line strengths or cross-sections
    - Broadening parameters
    - Non-Voigt behaviour
- Viewing Geometry

- Instrument line of sight
- Refraction of the atmosphere
- Field of View

- Instrument type
  - Limb emission/Occultation
  - Spectrometer/radiometer
  - Instrument lineshape

These will be discussed in turn in the following sections.

2.4.1.1.1 Atmospheric parameters

The RFM uses reference atmospheres, or climatologies, as input to represent a mean atmospheric state. In this study, reference atmospheres were employed [Remedios, 1999] for four different latitude bands, including tropical, polar summer, polar winter and the mid-latitudes (for which there are two distinct files for day and night to represent the diurnal behaviour of species in the stratosphere). Each file contains mean information on temperature and pressure between 0 and 120 km. Corresponding to each height, there is volume mixing ratio information for 30 radiatively important gases which could be significant emitters in the MIPAS-E spectral range. There is also the possibility to update the input atmosphere files in such a way as to also use retrievals of contaminant gases from other measurements by the instrument of interest.

2.4.1.1.2 Spectroscopic Information

The forward model allows three options for spectral calculations, using:

- HITRAN [Rothman *et. al*, 1998] line data
- HITRAN cross-section data (or data in this form)
- Look-up tables compressed by singular value decomposition (SVD)

The RFM allows both line data and absorption cross-sections to be employed. Usually, line data are preferred where available but for heavier molecules, such as CFCs and HCFCs, this is usually not possible due to the broad spectra without distinguishable lines (see section below for HCFC-22).

For line data, the calculation uses a two-pass system with an initial coarse grid (0.5 cm^{-1}) calculation for the interpolation of line wings up to 25 cm^{-1} from line centre. This is followed by a fine mesh calculation (which can be modified but is typically 0.0005cm^{-1}) for modelling fine details of the shape of lines within 1 to 2 cm^{-1} from line centre. Total internal partition sums and molecular cross-section data are those associated with the HITRAN-MIPAS, basically HITRAN 2000 reduced to MIPAS spectral range, with best available updates for each significant molecule [Flaud *et al.*, 2003]. Voigt line shapes (see below) are calculated using a version of the Humlicek algorithm. For cross-section data a triangulation is used which directly interpolates the associated pressure temperature grid. The benefit of this method is the avoidance of any intermediate interpolation to resample the pressure and temperature coordinates into a uniform spacing. Other effects observed in the atmosphere such as line-coupling and non-LTE can be accounted for in the RFM and continua for H_2O, CO_2, O_2 and N_2.

The RFM usually treats spectral lineshapes in the Voigt formulation. The Voigt line shape is a convolution of nearly independent Lorentzian and Doppler line broadening mechanisms (section 2.3.6). Gases such as CO_2 exhibit non-Voigt characteristics; particularly in the 4.3 μm band. This means that there is an impact of time dependence of collisions on the line shapes itself and this can be considered by empirical functions, or chi-factors. These account for the sub-Lorentzian behaviour that CO_2 exhibits in this region. The RFM allows the use of non-Voigt line shapes, in the form of Chi-factor implementation. This multiplicative factor increases or lowers the lineshape values at a specified distance from the line centre.

2.4.1.1.3 Viewing Geometry

Ray paths can be defined in terms of elevation angle, geometric or refracted tangent altitudes to represent various scenarios. The RFM assumes a constant radius of curvature or a local spherical symmetry for each path calculation but includes a local Earth radius option. The ray tracing technique has alternative algorithms according to whether the atmosphere specified is one or two-dimensional. For one dimension, as in the case of this study, the FASCODE (Smith *et. al*, 1978) algorithm is used with altitude as the integrated co-ordinate. A transformation has to be performed to avoid singularity in the proximity of the tangent height.

The field of view (FOV) of the MIPAS can be incorporated into the RFM calculations. The thermal radiation entering the aperture of the instrument is not from a point source, rather a collection of photons from a finite area. The FOV function file that is specified, convolved with the monochromatic RFM spectra, yields a realistic approximation to the spectra observed by the MIPAS (section 3.2.2).

2.4.1.1.4 Instrument type

Another important characteristic to be considered when calculating the signal that the instrument measures is that the signal depends on the type of instrument. All instruments impose some spectral response on the atmospheric spectrum observed. For a Fourier transform spectrometer such as the MIPAS-E, the relevant factor is the instrument line shape (ILS) of the instrument itself. The RFM can incorporate this instrumental response by specifying an ILS file. This file is calculated from known spectrometer parameters, such as maximum optical path difference, field of view and apodization function. The FOV and ILS are treated independently from one another and the RFM performs the convolutions sequentially in an arbitrary order.

2.4.1.2 Output Files

The output files from the RFM depend on the particular case, but the main purpose of the RFM is to generate spectra. These files can be radiance, transmission, absorption or optical depth spectra. For the MIPAS case, the measurements obtained are in radiance form and hence this mode of the RFM, where the line-by-line radiance calculations are convolved with the MIPAS FOV and ILS, forms the basis in which results from the radiative model can be compared with measurements of the atmosphere.

Another important calculation in the retrieval process is the ability of the forward model to estimate Jacobians accurately. In the RFM, these calculations represent the difference in, for example, radiance caused by a perturbation to the atmospheric profile. The perturbation sizes for the Jacobians are 1 % for volume mixing ratio, 1 K for temperature, and 1×10^{-4} ext/km for extinction. For a "set" of altitudes, the perturbations for each Jacobian are effectively triangular, centred on each altitude and decreasing linearly (in K or percentage) to zero at the adjacent altitudes. The MIPAS has a finite field of view and

measures the radiation over a finite layer. It is usually assumed that the intensity of radiation observed across the layer is uniform.

2.5 Retrieval Theory

To obtain vertical profiles of atmospheric temperature, pressure and constituents from remote sensing instruments, such as the MIPAS-E, retrievals are performed from the measured radiance spectra. Radiance measurements are a complicated function of the parameters required. The problem of inverting these measured spectra into the parameters required is introduced here. An explanation of the terminology and definitions is given along with the approach used to finding a "best" solution from the measurements and also a full error analysis and characterisation of these solutions. The theory shown follows largely from Rodgers, 1976, 1990, 1993 and 2000.

2.5.1 Definitions

2.5.1.1 The state and measurement vectors

Consider the set-up of the MIPAS-E, which makes m radiance measurements at different limb altitudes. A set of n parameters (the state vector $\mathbf{x}$) are determined from this set of measurements ($\mathbf{y}$). The aim of the retrieval is to gain as much information about $\mathbf{x}$ given $\mathbf{y}$. The associated random error of the measurements, or measurement noise, is denoted by the vector $\boldsymbol{\varepsilon}$.

2.5.1.2 The forward model

The relationship between the state vector and the measurement vector are related to a forward model, $\mathbf{F(x)}$, which attempts to approximate the atmospheric physics involved.

Assuming a perfect model:

$$\mathbf{y} = \mathbf{F}(\mathbf{x}) + \boldsymbol{\varepsilon} \tag{2.25}$$

In principle, the forward model incorporates knowledge of how the instrument works, coupled with how the measured quantity from the instrument (radiance for MIPAS-E) is related to the desired quantity. To gain atmospheric information about vertical gas concentrations (such as HCFC-22), the forward model has to represent the relationship between the measured radiance and gas concentration. As atmospheric gas concentration is a function of pressure and temperature, the model would also need to incorporate information about pressure and temperature distributions, which could be done initially using a climatology, from independent measurements or from pressure and temperature retrievals from other measurements by the instrument of interest.

2.5.1.3 The weighting function matrix

The general remote sensing problem is non-linear so simplifying assumptions are made to reduce the problem to a linear one, providing that $\mathbf{F}(\mathbf{x})$ is linear within the bounds of the retrieval. This is done by linearising equation (2.25) about some reference state $\mathbf{x_0}$:

$$\mathbf{y} - \mathbf{F}(\mathbf{x}_0) = \frac{\partial \mathbf{F}(\mathbf{x})}{\partial \mathbf{x}}(\mathbf{x} - \mathbf{x}_0) + \boldsymbol{\varepsilon} \tag{2.26}$$

where the partial derivative $\partial\mathbf{F}/\partial\mathbf{x}$ denotes the sensitivity of the forward model (i.e. the change in radiance) to a change in the state vector. This quantity is known as the weighting function, a matrix (usually represented by $\mathbf{K}$) of m forward model elements with respect to n state vector elements. Equation 2.26 can be rewritten as:

$$\mathbf{y} - \mathbf{F}(\mathbf{x}_0) = \mathbf{K}(\mathbf{x} - \mathbf{x}_0) + \boldsymbol{\varepsilon} \tag{2.27}$$

Other terms commonly used for the weighting function matrix $\mathbf{K}$ include the adjoint, the kernel matrix (hence $\mathbf{K}$) or, as it shall be referred to hereafter, the Jacobian matrix.

2.5.2 Solution with prior data

The retrieval problem is often non-linear and ill-posed, which can lead to an unstable solution with associated large errors. Addition of "*a priori* information" can be used to constrain the problem to one that is well-posed. This information often comes from previous measurements that have been collated into a climatology of a former state. The

variation expected in these previously measured values is characterised in the *a priori* covariance matrix. It is a combination of the new measurements and the *a priori* information that are used to find a best estimate of the atmospheric state.

Define $\mathbf{x}$ and $\mathbf{y}$ as vector random variables. A vector random variable is described by its probability density function (pdf). The vector $\mathbf{x}$ has a pdf written as $P(\mathbf{x})$ and $\mathbf{y}$ has a pdf $P(\mathbf{y})$. Once the measurement, $\mathbf{y}$, is made the pdf of $\mathbf{x}$ is then $P(\mathbf{x}\,|\,\mathbf{y})$. From Bayes' theorem:

$$P(\mathbf{x}\,|\,\mathbf{y}) = \frac{P(\mathbf{y}\,|\,\mathbf{x})P(\mathbf{x})}{P(\mathbf{y})} \tag{2.28}$$

The term $P(\mathbf{y}\,|\,\mathbf{x})$ can be calculated using the forward model and the known noise of the instrument. Equation 2.28 is not much use as it stands as an estimate of the profile is required rather than a pdf. One obvious solution method is to try to find the profile $\hat{\mathbf{x}}$ for which $P(\mathbf{x}\,|\,\mathbf{y})$ has the largest possible value. In turn, this is the most probable value for $\mathbf{x}$. A technique that finds such a value is called a maximum *a posteriori* (MAP) method. The pdfs are assumed to have a Gaussian distribution symmetric about its maximum. For a random vector, $\mathbf{v}$, the normal distribution takes the form:

$$P(\mathbf{v}) = \frac{1}{(2\pi)^{\frac{n}{2}}|\mathbf{S}|^{\frac{1}{2}}}\exp\left(-\frac{1}{2}(\mathbf{v}-\bar{\mathbf{v}})^T\mathbf{S}^{-1}(\mathbf{v}-\bar{\mathbf{v}})\right) \tag{2.29}$$

where $\bar{\mathbf{v}}$ is the mean value of $\mathbf{v}$ and $\mathbf{S}$ is its covariance matrix. Taking the natural logarithm of equation (2.29) $P(\mathbf{v})$ can be expressed as:

$$-2\ln P(\mathbf{v}) = (\mathbf{v}-\bar{\mathbf{v}})^T\mathbf{S}^{-1}(\mathbf{v}-\bar{\mathbf{v}}) + c_1 \tag{2.30}$$

with c_1 a constant which does not depend on $\mathbf{v}$. Writing the various terms of Bayes' theorem (equation 2.28) in this form it can be shown that:

$$(\mathbf{x}-\hat{\mathbf{x}})^T\hat{\mathbf{S}}^{-1}(\mathbf{x}-\hat{\mathbf{x}}) + c_2 = (\mathbf{x}-\mathbf{x}_a)^T\mathbf{S}_a^{-1}(\mathbf{x}-\mathbf{x}_a) + (\mathbf{y}-\mathbf{K}\mathbf{x})^T\mathbf{S}_y^{-1}(\mathbf{y}-\mathbf{K}\mathbf{x}) \tag{2.31}$$

where c_2 is a constant, $\mathbf{x}_a$ is the chosen *a priori* value of $\mathbf{x}$ with associated covariance $\mathbf{S}_a$.The term $\mathbf{S}_y$ represents the covariance of the measurements, $\mathbf{y}$. Multiplying out equation (2.31) and equating quadratic terms in $\mathbf{x}$ gives:

$$\mathbf{x}^T\hat{\mathbf{S}}^{-1}\mathbf{x} = \mathbf{x}^T\mathbf{S}_a^{-1}\mathbf{x} + \mathbf{x}^T\mathbf{K}^T\mathbf{S}_y^{-1}\mathbf{K}\mathbf{x} \tag{2.32}$$

and hence:

$$\hat{\mathbf{S}}^{-1} = \mathbf{S}_a^{-1} + \mathbf{K}^T\mathbf{S}_y^{-1}\mathbf{K} \tag{2.33}$$

From equating the terms linear in $\mathbf{x}^T$ in equation 2.31 it can be shown that:

$$\hat{\mathbf{x}} = \left(\mathbf{S}_a^{-1} + \mathbf{K}^T\mathbf{S}_y^{-1}\mathbf{K}\right)^{-1}\left(\mathbf{S}_a^{-1}\mathbf{x}_a + \mathbf{K}'\mathbf{S}_y^{-1}\mathbf{y}\right) \tag{2.34}$$

Equation (2.34) can be re-written in many forms; two of the most useful are

$$\hat{\mathbf{x}} = \mathbf{x}_a + \mathbf{S}_a\mathbf{K}^T\left(\mathbf{K}\mathbf{S}_a\mathbf{K}^T + \mathbf{S}_y\right)^{-1}\left(\mathbf{y} - \mathbf{K}\mathbf{x}_a\right) \tag{2.35}$$

$$\hat{\mathbf{x}} = \mathbf{x}_a + \left(\mathbf{S}_a^{-1} + \mathbf{K}^T\mathbf{S}_y^{-1}\right)^{-1}\mathbf{K}^T\mathbf{S}_y^{-1}\left(\mathbf{y} - \mathbf{K}\mathbf{x}_a\right) \tag{2.36}$$

Equation 2.35 is the *m*-form of the equation as the matrix to be inverted is an $m \times m$ matrix – for underconstrained problems this is easier to do than inverting the $n \times n$ matrices in equation 2.36.

2.5.2.1 Gain Matrix

The measurement gain matrix, **G**, or contribution function matrix as it is sometimes otherwise known, is defined as:

$$\mathbf{G} = \frac{\partial\hat{\mathbf{x}}}{\partial\mathbf{y}} \tag{2.37}$$

So in the case with *a priori* data;

$$\mathbf{G} = \left(\mathbf{K}^T\mathbf{S}_y^{-1}\mathbf{K} + \mathbf{S}_a^{-1}\right)^{-1}\mathbf{K}^T\mathbf{S}_y^{-1} \tag{2.38}$$

$$= \mathbf{S}_a\mathbf{K}^T\left(\mathbf{K}\mathbf{S}_a\mathbf{K}^T + \mathbf{S}_y\right)^{-1} \tag{2.39}$$

The contribution function represents how the solution is affected by a change in **y**, since:

$$\hat{\mathbf{x}} = \mathbf{x}_a + \mathbf{G}\left(\mathbf{y} - \mathbf{K}\mathbf{x}_a\right) \tag{2.40}$$

$$= \mathbf{G}\mathbf{y} + \left(\mathbf{I}_n - \mathbf{G}\mathbf{K}\right)\mathbf{x}_a \tag{2.41}$$

The *a priori* contribution function as the name suggests estimates the contribution to the retrieval from the *a priori*:

$$\mathbf{G}_a = \frac{\partial\hat{\mathbf{x}}}{\partial\mathbf{x}_a} = \mathbf{I}_n - \mathbf{G}\mathbf{K} \tag{2.42}$$

2.5.2.2 Averaging kernel

The averaging kernel matrix gives an indication of how the true profile is smoothed by the retrieval and is defined as:

$$\mathbf{A} = \frac{\partial\hat{\mathbf{x}}}{\partial\mathbf{x}} \tag{2.43}$$

The retrieved profile is a combination of both the *a priori* climatology and the true atmospheric state, with the averaging kernel as a weight:

$$\hat{\mathbf{x}} = \mathbf{G}\mathbf{y} + \left(\mathbf{I}_n - \mathbf{G}\mathbf{K}\right)\mathbf{x}_a = \mathbf{G}\mathbf{K}\mathbf{x} + \left(\mathbf{I}_n - \mathbf{G}\mathbf{K}\right)\mathbf{x}_a \tag{2.44}$$

So in turn;

$$\mathbf{A} = \mathbf{G}\mathbf{K} \tag{2.45}$$

and therefore:

$$\hat{\mathbf{x}} = \mathbf{A}\mathbf{x} + (\mathbf{I} - \mathbf{A})\mathbf{x}_a \tag{2.46}$$

The rows of matrix **A** are the 'smoothing functions' or averaging kernels with the width representing a measure of the resolution of the retrieval (e.g. height). Where the area of the averaging kernel is one, the retrieval utilises the measurement information from the measurement strongly. In effect, the averaging kernel is a measure of the fraction of the retrieval that comes from the measurements as opposed to the *a priori*. Therefore, an ideal observing system would have δ-function averaging kernels and no noise.

2.5.3 Information content of a measurement

There are numerous ways of describing the information gained from a measurement. Described in this section are two: Shannon information content and degrees of freedom of signal.

2.5.3.1 Shannon Information content

Arising from information theory [Shannon and Weaver, 1949] developed in the 1940's, the concept of Shannon information content is related to the information gained from a measurement. The quantity is defined in terms of entropy, closely related to thermodynamic entropy, of the probability density functions (pdfs). In the thermodynamic context, entropy is the logarithm of the number of distinct internal states of a thermodynamic system consistent with a measured macro-state (i.e. pressure or temperature). Information is concerned with the change of knowledge of the system resulting from a measurement as opposed to what was known before the measurement was made. For a continuous pdf, the entropy can be defined as:

$$S(P) = -\int P(\mathbf{x}) \log_2 [P(\mathbf{x}) / M(\mathbf{x})]\, dx \tag{2.47}$$

where M is a measure function which is chosen to make P/M dimensionless and so $P = M$ corresponds to a state of no knowledge of $\mathbf{x}$.

Assuming $P_1(\mathbf{x})$ describes knowledge before a measurement, and $P_2(\mathbf{x})$ describes it afterwards, then the reduction in entropy expresses the information content, H, of the measurement:

$$H = S(P_1) - S(P_2) \tag{2.48}$$

Rodgers [2000] shows that when Gaussian statistics are assumed, $S(P) = \frac{1}{2}\ln|\mathbf{S}|$ so the information content is:

$$H = \frac{1}{2}\ln|\mathbf{S}_a| - \frac{1}{2}\ln|\hat{\mathbf{S}}| \tag{2.49}$$

$$= \frac{1}{2}\ln|\hat{\mathbf{S}}^{-1}\mathbf{S}_a| \tag{2.50}$$

where $\hat{\mathbf{S}}$ is the covariance of the solution and $\mathbf{S}_a$ is the *a priori* covariance and H represents the information content of the measurement in state space.

The averaging kernel matrix (section 2.5.2.2) is related to the information content. From equations 2.45 and 2.38:

$$\mathbf{A} = \mathbf{GK} = \left(\mathbf{K}^T\mathbf{S}_y^{-1}\mathbf{K} + \mathbf{S}_a^{-1}\right)^{-1}\mathbf{K}^T\mathbf{S}_y^{-1}\mathbf{K} \tag{2.51}$$

and therefore:

$$\mathbf{I} - \mathbf{A} = \left(\mathbf{K}^T\mathbf{S}_y^{-1}\mathbf{K} + \mathbf{S}_a^{-1}\right) = \hat{\mathbf{S}}\mathbf{S}_a^{-1} \tag{2.52}$$

$$H = -\frac{1}{2}\ln|\mathbf{I}_n - \mathbf{A}| \tag{2.53}$$

2.5.3.2 Degrees of freedom for signal

The degrees of freedom for signal, d_s, is the trace of the averaging kernel matrix:

$$d_s = tr(\mathbf{A}) \tag{2.54}$$

Therefore the diagonal of the matrix $\mathbf{A}$ is a measure of the number of degrees of freedom per height level, in the case of the MIPAS-E, and its reciprocal as the number of levels per degree of freedom, a measure of height resolution.

2.5.4 Error analysis

Errors can be classified into two classes, systematic and random, depending on whether they are identical between separate measurements, or vary randomly between them. Other terms that are related to the exactness of measurement that will be referred to later in this thesis are not to be confused with one another are precision (the variability between repeated measurements of the same state) and accuracy (the total difference between the measurement and the truth). From practical measurements the difference between the two can be indistinct, depending on the variability of the error over time. An error which is systematic on one scale may be totally random on another.

There are four major sources of error in the retrieval considered in this section. They are:

Retrieval Noise: a totally random quantity, with no correlation over time.

Model parameter: may be truly systematic (i.e. in the spectral data) or could vary from day to day (i.e. calibration parameters). But even the random component of the model parameter error may be constant over minutes or hours.

Forward model error: estimate of how well the model represents the physics of the system.

Smoothing error: the loss of fine structure in the retrieval due to the observing system

Written formally, the error in $\hat{\mathbf{x}}$ can be defined as:

$$\begin{aligned}
\hat{\mathbf{x}} - \mathbf{x} = {} & \mathbf{G}_y \varepsilon && \text{retrieval noise} \\
& + \mathbf{G}_y \mathbf{K}_b \left(\mathbf{b} - \hat{\mathbf{b}} \right) && \text{model parameter error} \\
& + \mathbf{G}_y \Delta \mathbf{f}(\mathbf{x}, \mathbf{b}, \mathbf{b}') && \text{forward model error} \\
& + (\mathbf{A} - \mathbf{I}_n)(\mathbf{x} - \mathbf{x}_a) && \text{smoothing error}
\end{aligned}$$

2.5.4.1 Retrieval noise

This is generally the easiest component to evaluate. Measurement noise itself, ε, is usually random, generally unbiased and often uncorrelated between channels. It also has a known covariance matrix. The covariance of the retrieval noise is:

$$\mathbf{S}_m = \mathbf{G}_y \mathbf{S}_y \mathbf{G}_y^T \tag{2.55}$$

2.5.4.2 Forward model parameter error

The error in the retrieval due to forward model parameter errors is $\mathbf{G}_y\mathbf{K}_b\left(\mathbf{b}-\hat{\mathbf{b}}\right)$. Evaluation of $\mathbf{G}_y$ and $\mathbf{K}_b$ can be performed by perturbation from the inverse method and forward model respectively. If the forward model parameters have been estimated properly and assuming that the model is linear as far as they are concerned then their individual errors will be unbiased and the expected error will be zero.

2.5.4.3 Forward model error

This error source is defined as $\mathbf{G}_y\Delta\mathbf{f} = \mathbf{G}_y\left[\mathbf{f}(\mathbf{x},\mathbf{b},\mathbf{b}')-\mathbf{F}(\mathbf{x},\mathbf{b})\right]$. Modelling error can be difficult to evaluate as it requires a model for **f** which includes all of the correct physics. If this is possible (which is rarely the case for atmospheric physics due to the complex nature of the processes in the atmosphere) and the physics can be modelled accurately, and **F** is simply a numerical approximation then evaluating model error is straightforward. The forward model error source is likely to be systematic.

2.5.4.4 Smoothing error

This error term arises when it is assumed that the retrieval is an estimate of the true state rather than an estimate of the state that has been smoothed by the averaging kernel. The true state will not be known in general (which is why the measurement is being made in the first place) thus the actual smoothing error cannot be estimated. Instead, the statistics of the error can be investigated from looking at the mean and covariance from an ensemble of

states. To estimate the smoothing error covariance, the covariance matrix of a real ensemble of states must be known.

2.5.5 Iterating and convergence

The optimal estimation retrieval approach finds the most probable solution consistent with both the measurements and the *a priori* knowledge. In the non-linear case, this requires the solving of a complex equation relating all of the measurements, *a priori* knowledge, the forward model parameters and other inputs to the retrieval.

The maximum *a posteriori* (MAP) approach can be used to solve non-linear problems. This method requires the minimisation of a cost function which, for Gaussian errors and using a Bayesian approach (defined in Rodgers, [2000]), is:

$$-2\ln P(\mathbf{x}\mid\mathbf{y}) = [\mathbf{y}-\mathbf{F}(\mathbf{x})]^T \mathbf{S}_y^{-1}[\mathbf{y}-\mathbf{F}(\mathbf{x})] + [\mathbf{x}-\mathbf{x}_a]^T \mathbf{S}_a^{-1}[\mathbf{x}-\mathbf{x}_a] + \text{constant} \qquad (2.56)$$

In equation 2.56, $\mathbf{y}$ is the measurement vector, $\mathbf{F}(\mathbf{x})$ is the forward model, $\mathbf{S}_a$ is the *a priori* error covariance, $\mathbf{S}_y$ is the measurement error covariance, $\mathbf{x}_a$ is the *a priori* state vector and $\hat{\mathbf{x}}$ is the estimated solution. Finding the zero gradient of the cost function, or in other words the minimum, yields:

$$\nabla_x\{-2\ln P(\mathbf{x}\mid\mathbf{y})\} = -[\nabla_x\mathbf{F}(\hat{\mathbf{x}})]^T \mathbf{S}_y^{-1}[\mathbf{y}-\mathbf{F}(\hat{\mathbf{x}})] + \mathbf{S}_a^{-1}(\hat{\mathbf{x}}-\mathbf{x}_a) = 0 \qquad (2.57)$$

As $\nabla_x\mathbf{F}(\mathbf{x}) = \mathbf{K}(\mathbf{x})$ the equation to be solved is:

$$-\mathbf{K}^T\mathbf{S}_y^{-1}[\mathbf{y}-\mathbf{F}(\hat{\mathbf{x}})] + \mathbf{S}_a^{-1}(\hat{\mathbf{x}}-\mathbf{x}_a) = 0 \qquad (2.58)$$

If the forward model is linear, i.e. $\mathbf{F}(\hat{\mathbf{x}}) = \mathbf{K}\hat{\mathbf{x}}$, then the solution for $\hat{\mathbf{x}}$ follows:

$$\hat{\mathbf{x}} = \mathbf{x}_a + \left(\mathbf{K}^T\mathbf{S}_y^{-1}\mathbf{K} + \mathbf{S}_a^{-1}\right)^{-1}\mathbf{K}^T\mathbf{S}_y^{-1}(\mathbf{y}-\mathbf{K}\mathbf{x}_a) \qquad (2.59)$$

with a covariance given by:

$$\hat{\mathbf{S}} = \left(\mathbf{K}^T\mathbf{S}_y^{-1}\mathbf{K} + \mathbf{S}_a^{-1}\right)^{-1} \tag{2.60}$$

and its averaging kernel matrix is defined as:

$$\mathbf{A} = \left(\mathbf{K}^T\mathbf{S}_y^{-1}\mathbf{K} + \mathbf{S}_a^{-1}\right)^{-1}\mathbf{K}^T\mathbf{S}_y^{-1}\mathbf{K} \tag{2.61}$$

Non-linear problems are best solved by some form of iteration technique, for example by linearising the problem and use a linear solution method optimal estimation. Another class of moderately nonlinear problems require other methods to find the solution efficiently but are sufficiently linear in the neighbourhood of the solution for linearization to be used in the error analysis. These problems require a regularisation factor in the iteration scheme; a common variation of Newtonian iteration and used in the retrieval schemes is the Levenburg-Marquardt iteration technique.

2.5.5.1 Newtonian iteration

If the problem is not too non-linear then Newtonian iteration can be used to find the best estimate of the state $\hat{x}$. Newton's method for finding the zero of a scalar function f(x) of one variable is:

$$\mathbf{x}_{i+1} = \mathbf{x}_i - \left(\frac{df(\mathbf{x}_i)}{d\mathbf{x}}\right)^{-1} f(\mathbf{x}_i) \tag{2.62}$$

The version for a vector-valued function of a vector, $\mathbf{g}(\mathbf{x})$, is:

$$\mathbf{x}_{i+1} = \mathbf{x}_i - \left(\nabla_x \mathbf{g}(\mathbf{x}_i)\right)^{-1}\mathbf{g}(\mathbf{x}_i) \tag{2.63}$$

where the inverse is a matrix inverse.

Applying $\mathbf{g}(\mathbf{x})$ to the maximum *a posteriori* problem,

$$\mathbf{g}(\mathbf{x}) = -\mathbf{K}^T\mathbf{S}_y^{-1}[\mathbf{y} - \mathbf{F}(\mathbf{x})] + \mathbf{S}_a^{-1}[\mathbf{x} - \mathbf{x}_a] \tag{2.64}$$

$$\therefore \nabla_x\mathbf{g} = -\nabla_x\mathbf{K}^T\mathbf{S}_y^{-1}[\mathbf{y} - \mathbf{F}(\mathbf{x})] + \mathbf{K}^T\mathbf{S}_y^{-1}\mathbf{K} + \mathbf{S}_a^{-1} \tag{2.65}$$

$\nabla_x \mathbf{K}^T$ is usually small compared to the other terms, so ignoring this term the iteration becomes:

$$\mathbf{x}_{i+1} = \mathbf{x}_i - \left(\mathbf{S}_a^{-1} + \mathbf{K}_i^T \mathbf{S}_y^{-1} \mathbf{K}_i\right)^{-1} \left(-\mathbf{K}_i^T \mathbf{S}_y^{-1} [\mathbf{y} - \mathbf{F}(\mathbf{x}_i)] + \mathbf{S}_a^{-1} [\mathbf{x}_i - \mathbf{x}_a]\right) \quad (2.66)$$

By expressing x_{i+1} as a departure from x_a rather than x_i equation 2.67 can be rearranged to form:

$$\mathbf{x}_{i+1} = \mathbf{x}_a + \left(\mathbf{S}_a^{-1} + \mathbf{K}_i^T \mathbf{S}_y^{-1} \mathbf{K}_i\right)^{-1} \left(\mathbf{K}_i^T \mathbf{S}_y^{-1} [\mathbf{y} - \mathbf{F}(\mathbf{x}_i)] + \mathbf{K}_i [\mathbf{x}_i - \mathbf{x}_a]\right) \quad (2.67)$$

It is usually chosen to start the iteration with $\mathbf{x}_0 = \mathbf{x}_a$.

2.5.5.2 Levenberg-Marquardt Iteration

This iteration technique is not dissimilar to Gauss-Newton iteration but with the addition of an extra constant term, γ, which aids convergence [Marquardt, 1963]:

$$\mathbf{x}_{i+1} = \mathbf{x}_i - \left(\mathbf{S}_a^{-1} + \mathbf{K}_i^T \mathbf{S}_y^{-1} \mathbf{K}_i + \gamma \mathbf{D}\right)^{-1} \left(-\mathbf{K}_i^T \mathbf{S}_y^{-1} [\mathbf{y} - \mathbf{F}(\mathbf{x}_i)] + \mathbf{S}_a^{-1} [\mathbf{x}_i - \mathbf{x}_a]\right) \quad (2.68)$$

where D is a necessary diagonal scaling matrix; the simplest choice is to set it equal to $\mathbf{S}_a^{-1}$.

The value of γ is initialized to a small value of one. If the value obtained from the iteration reduces the error, the new estimate, $\mathbf{x}_{i+1}$, is accepted and γ is divided by ten. If the error increases on $\mathbf{x}_{i+1}$, however, then γ is multiplied by ten and equation 2.68 is solved again until an increment is obtained that reduces the error,

There are many other methods that can be used for iterating towards a solution but they are mostly variations of the two approaches described in sections 3.6.1 and 3.6.2. In general the other schemes require some "tweaking" of a parameter at each iteration step which in turn determines the step size but can also determine the direction in which the solution moves. The MIPAS-E operational retrievals performed by the ESA use an iteration scheme based on the Levenberg-Marquardt approach [Ridolfi *et al.*, 2000].

2.5.5.3 Convergence of iteration techniques

The iterations in a Gauss-Newton or a Levenberg-Marquardt retrieval scheme are stopped once a suitable convergence criterion is reached. There are two common methods used to impart convergence criteria in the retrieval process.

a) $\mathbf{F}(\mathbf{x}_{i+1})$ compared with $\mathbf{F}(\mathbf{x}_i)$

For quadratic convergence, the difference $\mathbf{F}(\mathbf{x}_i)-\mathbf{F}(\mathbf{x}_{i+1})$ is a good estimate of the convergence error in $\mathbf{y}_i$ so it is a useful overestimate of the convergence error in $\mathbf{y}_{i+1}$.

b) $\mathbf{x}_{i+1}$ compared with $\mathbf{x}_i$

The difference $\mathbf{x}_i - \mathbf{x}_{i+1}$ is a good estimate of the convergence error in $\mathbf{x}_i$, so it is a useful overestimate of the error in $\mathbf{x}_{i+1}$. The MIPAS-E operational processor employs this technique and halts the iterations when the change in $\hat{x}$ is below some threshold [Ridolfi *et al.*, 2000].

The estimation of $\hat{\mathbf{x}}$ in optimal estimation represents the minimisation of the cost function, χ^2, a value dependent on the difference between measured, $\mathbf{y}$, and modelled radiances, $\mathbf{F}(\mathbf{x})$, and also the difference between $\hat{\mathbf{x}}$ and $\mathbf{x}_a$:

$$\chi^2 = (\mathbf{y}-\mathbf{K}\mathbf{x})^T \mathbf{S}_y^{-1}(\mathbf{y}-\mathbf{K}\mathbf{x}) + (\mathbf{x}-\mathbf{x}_a)^T \mathbf{S}_a^{-1}(\mathbf{x}-\mathbf{x}_a) \qquad (2.69)$$

The size of the cost function itself can also be a useful test in order to determine how well the solution fits to the measurements. An example of such a test is:

$$\chi^2 = (\hat{\mathbf{x}}_n - \hat{\mathbf{x}}_{n+1})^T \hat{\mathbf{S}}^{-1}(\hat{\mathbf{x}}_n - \hat{\mathbf{x}}_{n+1}) << n \qquad (2.70)$$

This means that the size of the step in state space is small compared to the retrieval error. To limit the computing time, it is also sensible to assume that converge has not been reached if the number of iterations exceeds a predetermined number.

Another issue that has to be addressed is the case where χ^2 is too large, meaning that the retrieval does not fit the measurements. Numerous explanations exist for this scenario. The measurements themselves could be poorly calibrated or the measurement errors could be underestimated. The forward model itself may have incorrect physics incorporated within it and may not represent the system well or even that the *a priori* may be inapt (i.e. it may be too tightly constrained). Conversely, if χ^2 is too small the measurement noise may be overestimated or the *a priori* could be too loosely set.

2.5.6 Retrieval Schemes

Two retrieval schemes were used in this study, developed specifically for the retrieval of atmospheric constituents from MIPAS-E measurements; the OPtimal Estimation Retrieval Algorithm (OPERA) and a fast-forward model scheme developed at the Juelich research institute in Germany by Hoffmann *et al.* [2004].

The OPERA scheme was constructed as part of this thesis project at the University of Leicester and used an optimal estimation approach [Rodgers, 2000] to retrieve useful gas concentration information from MIPAS-E spectral measurements. The OPERA performs a joint retrieval by calculating a mean spectral signature at each altitude in two distinct regions, one of which is sensitive to the target gas (e.g. HCFC-22) and the other to 'aerosol'. In effect, MIPAS-E data are treated as a radiometer rather than a spectrometer. This is potentially advantageous for some of the heavy halocarbons, where it is hard to distinguish individual line features. The advantage of performing a joint retrieval with aerosol is that the region chosen to measure aerosol is particularly sensitive to thin clouds, including cirrus, [Spang *et al.*, 2002] which are prevalent in the tropical upper troposphere. Optically thin clouds do not generally saturate gas emission features and measuring the extinction of thin clouds allows the concomitant benefit of obtaining accurate profile information at lower altitudes than would be otherwise possible with a single retrieval approach. Other important features of the OPERA scheme include:

- Option on *a priori* to use climatology [Remedios, 1999] or update the climatology with MIPAS-E level 2 offline or near real time products (including pressure, temperature or one of the six operational species)

- Possible to incorporate multiple microwindows containing spectral information for the target gas
- The signal from each microwindow (target gas and "aerosol" is averaged). In effect MIPAS-E instrument is treated as a multi-channel radiometer.
- Spectral microwindows can be up to 8 cm^{-1} wide.
- Incorporates the Oxford Reference Forward Model (RFM) to model limb radiance spectra and weighting functions.
- Incorporates HITRAN 2000 (MIPAS-E modified to remove negative values) version of line and cross-section data in the RFM.
- Assumes a pre-flight measured apodized ILS [Nett *et al.*, 2001].
- Trapezoidal 3 km instrument field of view assumption.
- Levenberg-Marquardt damping.
- A correlation length of 6 km is assumed.

Validation of the MIPAS-E target parameters used in the OPERA scheme (including version 4.61 pressure, temperature, and the gas concentrations of water vapour, ozone, nitric acid, methane, nitrous oxide and nitrogen dioxide data) was performed in 2004. The findings were presented at the second Atmospheric Chemistry Validation of ENVISAT (ACVE) workshop in 2004.

The second scheme was developed at the "Forschungszentrum" research centre in Juelich, Germany [Hoffmann *et al.*, 2004], and uses rapid radiative transfer calculations to retrieve primarily CFC-11 and CFC-12 from MIPAS-E observations. The optimal estimation approach employs rapid forward modelling based on a broad-band approach and the use of emissivity look-up tables (precomputed based on 'exact' line-by-line calculations) to compute the atmospheric radiative transfer (the BANDPAK model, described by Marshall *et al.*, [1994]), which although compromising the accuracy of the results to a small degree (discussed in section 2.5.4), dramatically reduces computational costs. The parameters for tabulation are pressure, temperature and gas concentration, chosen to expand over a range of atmospheric conditions. Spectral means for the Planck function are calculated for different temperatures. To derive trace gas volume mixing ratios from MIPAS-E observations, the optimal estimation-based scheme minimises the cost function using the Levenberg-Marquardt technique.

2.6 Summary

In this chapter, the theory behind the process of transmission of electromagnetic radiation through the atmosphere, and the influence of the atmosphere upon it (radiative transfer) is introduced. One method of measuring the electromagnetic radiation emission from the atmosphere by a spaceborne instrument (atmospheric limb sounding) is also described here. A forward model capable of accurately modelling limb emission spectra, the Oxford Reference Forward Model, is introduced, which was used as part of the retrieval process in Chapters 4, 5 and 6.

One method of inverting the spectral measurements from an infrared limb sounding instrument into meaningful atmospheric parameters is described in detail (optimal estimation). The retrieval scheme that was developed as part of this thesis project was also introduced here and the optimal estimation approach advantages (full error analysis given by the technique) and disadvantages (limb measurement problems are often underconstrained) are listed. Another retrieval scheme, against which results from the retrieval scheme developed for this thesis were compared (chapter 5), is also described here. Other methods of inverting spectral measurements available but are not used in this project and so are not described.

The theory relating to the spectroscopy of "heavy" molecule halocarbons and CFC-12 and HCFC-22 in particular is presented in this chapter. The principles of measuring halocarbons by the Fourier Transform Spectroscopy technique is also introduced, the technique used by the MIPAS-E onboard the European Space Agency ENVIronamental SATellite (ENVISAT), obtains spectral data. It is these spectral data which are inverted in this thesis to meaningful HCFC-22 and CFC-12 (and aerosol extinction) volume mixing ratios (and extinction) information.

Chapter 3

3 The MIPAS instrument on ENVISAT

3.1 The ENVISAT Mission

The European Space Agency (ESA) launched the ENVIronmental SATellite (ENVISAT) on March 1st 2002. ENVISAT is a polar-orbiting Earth observation satellite [Fischer and Oelhaf, 1996] which has provided and continues to provide measurements of the atmosphere, ocean, land and ice over a five year period. The payload of the satellite is ambitious and innovative but with the concomitant benefit of ensuring continuity of data measurements of the ESA ERS-1 and ERS-2 satellites important for further understanding, modelling and predicting environmental and climatic changes.

A total of nine instruments comprise the payload of ENVISAT, listed in Table 3.1 and schematically shown in Figure 3.1. The satellite also carries a laser retroreflector (LRR) that allows tracking of the satellite by ground based stations and is used to calibrate the radar altimeter 2 (RA-2) instrument onboard the satellite.

An orbiting satellite is subjected a many gravitational influences due to the Earth being an oblate spheroid and having an uneven mass distribution. The sun, moon and other planets also contribute a gravitational influence. The net result is to apply a very small torque to the orbit which manifests itself in an orbital precession with a period of 365 days for an inclination of 98.55 degrees and an orbital height of about 1000 km. This is a major natural advantage when observing the Earth from space. In such an orbit, the ENVISAT satellite crosses periapsis at about the same local time every orbit. In order to maintain exact synchronous timing, it is sometimes necessary to conduct propulsive manoeuvres to adjust the orbit.

The repeat cycle of the reference orbit is 35 days and for most sensors with a wide swath range, complete global coverage is achieved within one to three days. This 35-day repeat pattern has been well established by ERS-1 and ERS-2. The satellite crosses the equator

southwards at 10 am local solar time (MLST) at a 98.55 inclination. It has a payload mass of over 2000 kg, with a total mass of 8000 kg.

To make near real time data products available to the user within three hours the ENVISAT stores complete orbits of data for most instruments before downloading to the main ESA ground stations or via the ARTEMIS relay satellite.

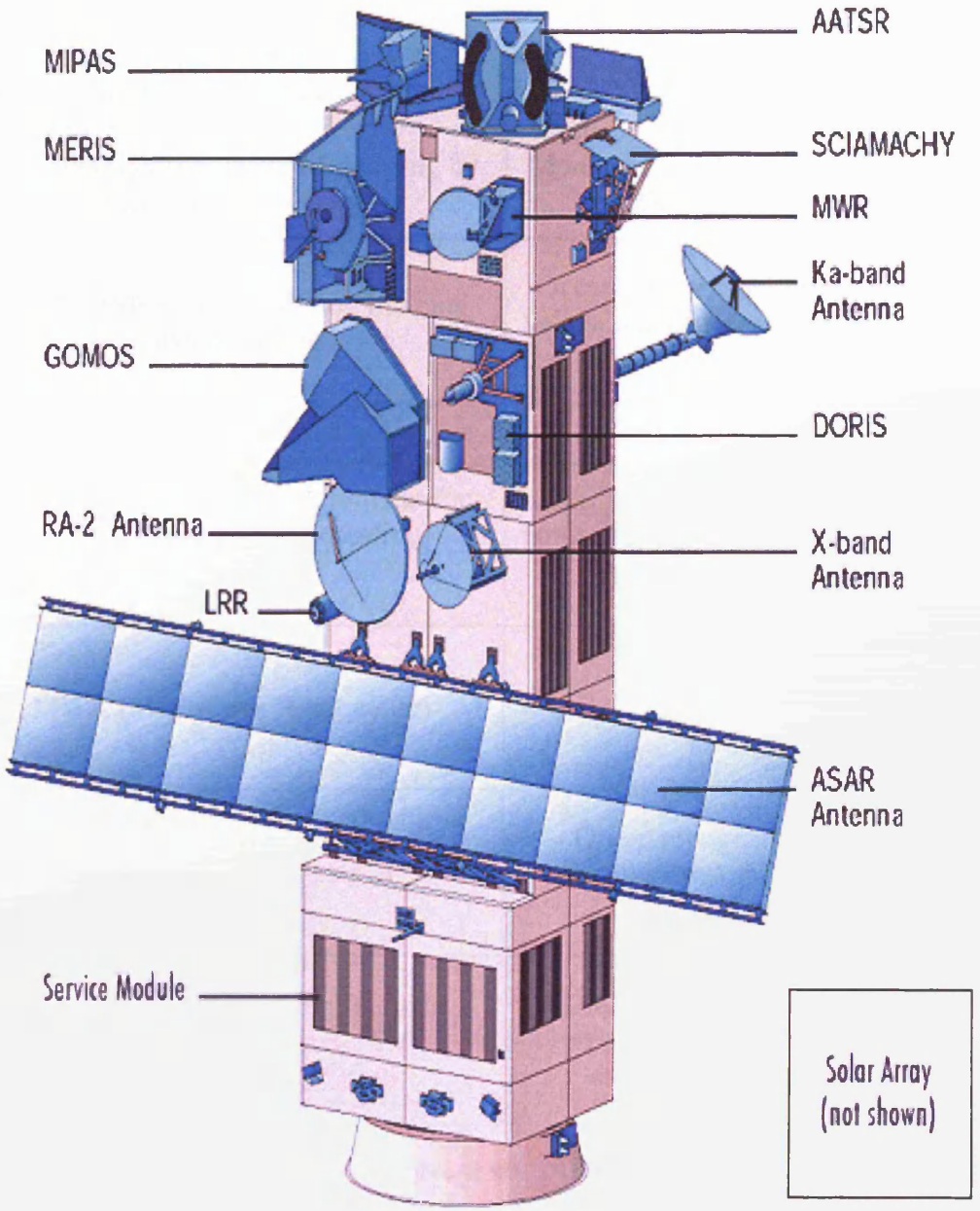

Figure 3.1 An artist's impression of the European Space Agency's (ESAs) ENVISAT satellite showing all nine of the scientific instrument onboard. [Image courtesy of the European Space Agency; website : http://envisat.esa.int/instruments].

Instrument	Application
AATSR (Advanced Along Track Scanning Radiometer)	Precise land and sea surface temperature, vegetation indices, aerosol, cloud parameters
ASAR (Advanced Synthetic Aperture Radar)	Ocean waves, sea ice extent and motion, land surface (deforestation, desertification)
DORIS (Doppler Orbitography and Radiopositioning Integrated by Satellite)	Precise satellite positioning
GOMOS (Global Ozone Monitoring by Occultation of Stars)	Monitoring and understanding of Ozone depletion in the stratosphere
MERIS (Medium Resolution Imaging Spectrometer)	Ocean colour monitoring (chlorophyll, yellow substance, suspended matter) and vegetation status
MIPAS (Michelson interferometer for Passive Atmospheric Sounding)	Ozone chemistry, monitoring of global distribution of major greenhouse gases, atmospheric dynamics, clouds (including polar stratospheric clouds)
MWR (Microwave Radiometer)	Total atmospheric water column measurement for correction of RA measurements
RA-2 (Radar Altimeter 2)	Ocean topography, marine geoid characteristics, wind speed and wave height)
SCIAMACHY (Scanning Imaging Absorption Spectrometer for Atmospheric Cartography)	Global distribution of trace gases, air pollution, aerosols, clouds and stratospheric ozone chemistry

Table 3.1 The nine scientific instruments onboard the ENVISAT satellite including the MIPAS. Further details on the other eight instruments can be found on the ESA website: http://envisat.esa.int.

3.2 Details of the MIPAS-E instrument

The Michelson Interferometer for Passive Atmospheric Sounding on ENVISAT (MIPAS-E), shown in Figure 3.2, has been designed to measure limb radiance emissions in the wavelength range 4.15 to 14.6 μm with an approximate height resolution of 3 km in the upper troposphere and the stratosphere. These spectroscopic measurements contain pressure and temperature information as well as the concentration of up to thirty trace gas species in the atmosphere including many of the halocarbon compounds such as CFC-12 and HCFC-22.

The primary MIPAS-E operational products, including pressure, temperature, water vapour (H_2O), ozone (O_3), methane (CH_4), nitrous oxide (N_2O), nitric acid (HNO_3) and nitrogen dioxide (NO_2), are contributing to improved understanding in stratospheric chemistry, atmospheric dynamics and upper tropospheric chemistry. These measurements are also invaluable for updating the global climatology of these gases. Information about the atmospheric distribution of aerosol particles, tropospheric cirrus clouds properties and the occurrence of polar stratospheric clouds (PSCs) can also be derived from MIPAS-E data.

Measurements are made for all seasons and, due to the use of infrared radiation as a measurement source, independently of illumination, i. e. during both day and night.

3.2.1 Fourier Transform Spectroscopy

The MIPAS-E is a rapid scanning Fourier Transform Spectrometer (FTS). Fourier transform spectrometers have a multiplex advantage for signal; that is, an FTS simultaneously measuring a signal over a range of frequencies, obtains a $t^{1/2}$ advantage in the time t required to obtain a given signal-to-noise ratio compared to that which would be necessary using dispersive methods (such as a grating spectrometer or filter radiometer). The FTS has a multiplex disadvantage for noise. However, the greater signal achieved by FTS techniques makes them desirable for remote sensing of trace gases from space where the number of measurements is to be maximised. Fourier transform spectrometers also usually can achieve a high spectral resolution in the infrared, are fairly easy to calibrate, and since they detect all the radiation all the time. A major advantage of using this

instrument is the simultaneous measurement of all mid-infrared wavenumbers or wavelengths.

The MIPAS-E is based on a variant of the classical Michelson Interferometer. The input telescope collects incoming infrared radiation (indicated in blue in Figure 3.2) from the atmosphere. The radiation is then collimated by the input collimator and directed to one of the input ports of the interferometer. Inside the interferometer, the radiation is split into two equal parts by the beamsplitter. In MIPAS-E, the beamsplitter is a semi-transparent mirror with optical coatings designed to reflect 50 % of the incoming infrared radiation and transmit the remaining fraction. Both the transmitted beam and the reflected (purple in Figure 3.2) are then reflected to two corner retro-reflectors which reflect the beams back to the beamsplitter where they are recombined. Once more the beamsplitter separates the recombined beam into two beams (green in Figure 3.2) and each beam is directed to an output port and collected by infrared detectors. The result is that the recombined beams give an interference pattern. The intensity reaching the detector will depend on the interference pattern, with the signal being a minimum when destructive interference of the beams occurs and maximum when constructive interference of the two beams occurs.

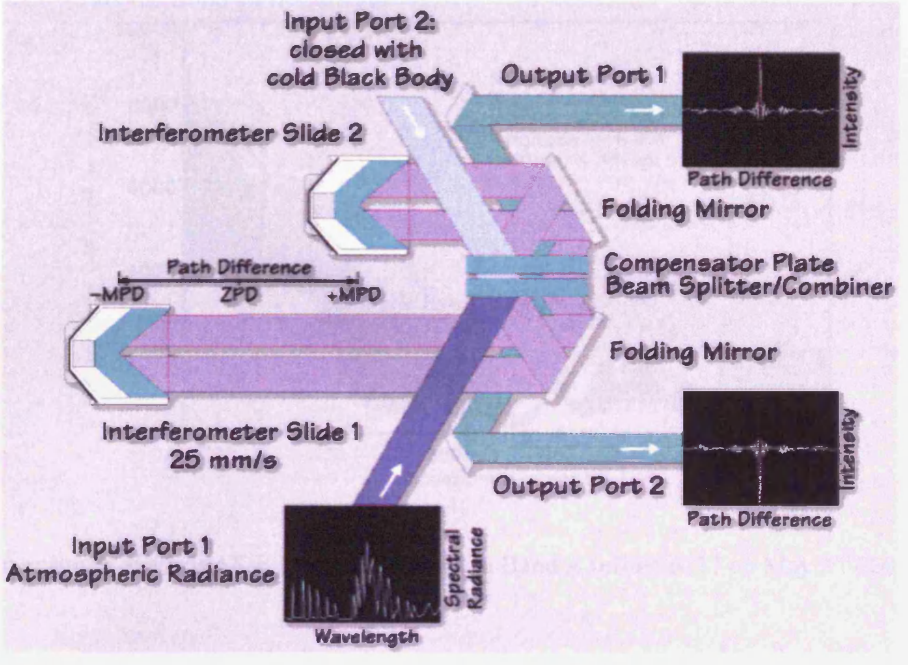

Figure 3.2 The MIPAS-E interferometer

Moving the corner reflectors with respect to one another, also varies the difference in the optical path and hence so, too, does the interference pattern. The detector will record a succession of signals of varying intensity as the interference varies between constructive

and destructive, known as an interferogram (Figure 3.3). The interference also depends on the wavelength and spectral intensity of the incoming radiation. By performing a Fourier transform calculation on an interferogram, a complete spectrum of measured spectral radiation can be reproduced from the measured signals. Figure 3.4 is an example of the spectrum from part of the Fourier transformed interferogram in MIPAS-E band A.

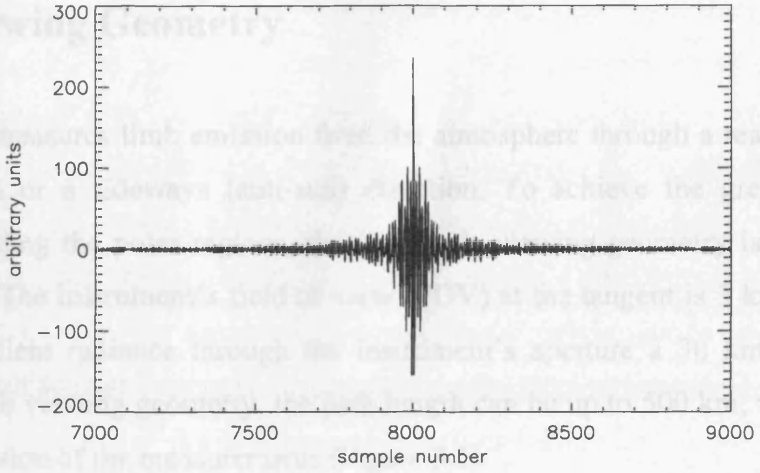

Figure 3.3 An example of part of a full MIPAS-E interferogram.

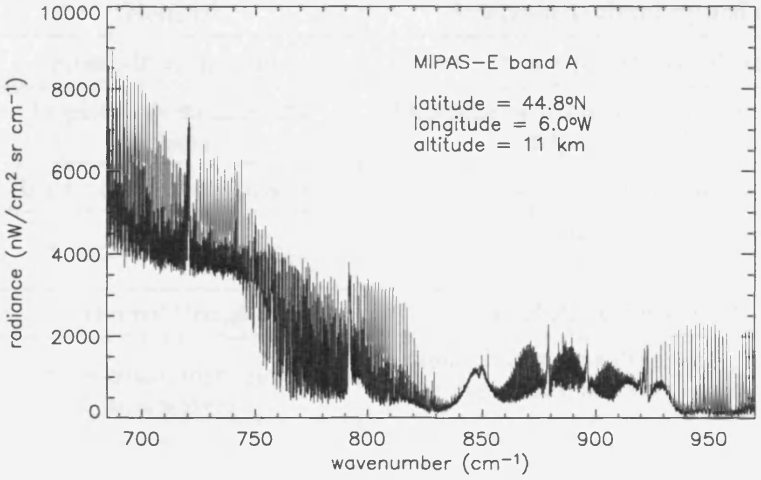

Figure 3.4 An example of a MIPAS-E level 1b spectrum in Band A (orbit 06117 on May 2nd 2003)

The spectrum of incoming radiation from the atmosphere contains detailed information about the chemical composition of the measured view and also the concentration of the constituents. It is possible to identify the presence of a molecule by checking whether a measured spectrum contains a spectral line of that given molecule. The intensity of the line is proportional to the concentration of a molecule and so the intensity of a line for an

identified gas gives concentration information for the gas itself (section 2.5). An added complication to this idea is that the pressure and temperature of an air parcel also determines the intensity and width of a line and must be taken into account when inverting spectra to retrieve concentrations. This is usually handled in the forward model (section 2.4.1).

3.2.2 Viewing Geometry

The MIPAS-E measures limb emission from the atmosphere through a rearwards (or anti-flight) direction or a sideways (anti-sun) direction. To achieve the greatest latitudinal coverage, including the polar regions, the rearwards viewing geometry is employed as a nominal mode. The instrument's field of view (FOV) at the tangent is 3 km vertically but to collect sufficient radiance through the instrument's aperture a 30 km wide swath is needed. For limb viewing geometry, the path length can be up to 500 km, which limits the horizontal precision of the measurements (Figure 3.5).

Observation mode	Observation description	Scientific objective
N/A	Nominal	Stratospheric chemistry and dynamics
S1	Polar winter chemistry	Polar chemistry and dynamics
S2	Tropospheric-stratospheric exchange	Exchange between troposphere and stratosphere, tropospheric chemistry
S3	Impact of Aircraft emissions	Study of major air traffic corridor
S4	Stratospheric dynamics	To identify and observe transport processes within the stratosphere
S5	Diurnal changes	Diurnal changes near the terminator
S6	Upper troposphere/ lower stratosphere	Study of important dynamical processes in the upper troposphere and lower stratosphere region of the atmosphere
UA1	Validation	Confirmation of predicted non-LTE effects on the retrieval of pressure, temperature and the six target species
UA2	Upper polar vortex dynamics	Stratosphere mesosphere exchange and dynamics
UA3	Radiative energy budget of the mesosphere and lower thermosphere	Hydrogen, nitrogen and carbon budgets in the upper atmosphere, mesospheric dynamics and non-LTE studies
UA4	Non-LTE studies of NO	Radiative cooling of the thermosphere

Table 3.2 The eleven observation modes of the MIPAS-E. The instrument operates for approximately 80 % of its operational time in nominal mode.

Each MIPAS-E sweep, i. e. a single interferogram, produces a high resolution spectrum in under 4 seconds, corresponding to about 25 km of the satellite's forward motion (plus 0.6 seconds taken to reverse the slide). For about 80% of its measuring time, MIPAS operates in the nominal observation mode with one MIPAS-E scan comprising seventeen tangent height sweeps (6 to 42 km at a step size of 3 km, 42 to 52 at a step size of 5 km and 52 to 68 at a step size of 8 km) and so one scan takes approximately 75 seconds to complete. For the remaining 20 % of the measurement time the MIPAS-E operates in "special event" mode as the instrument also has the capability of monitoring special atmospheric events, such as large intrusions of ash and sulphur dioxide into the stratosphere from volcanic eruptions or monitoring the stratospheric distribution of nitrous oxide to observe polar vortex splitting. Upper atmospheric observation modes are also possible to observe the effects of non-local thermodynamic equilibrium (non-LTE) in the atmosphere. The pointing for these two non-operational viewing modes can be performed between 5 and 160 km tangent height with varying step sizes of between 1 and 10 km. The eleven observation modes of the MIPAS-E are listed in Table 3.2.

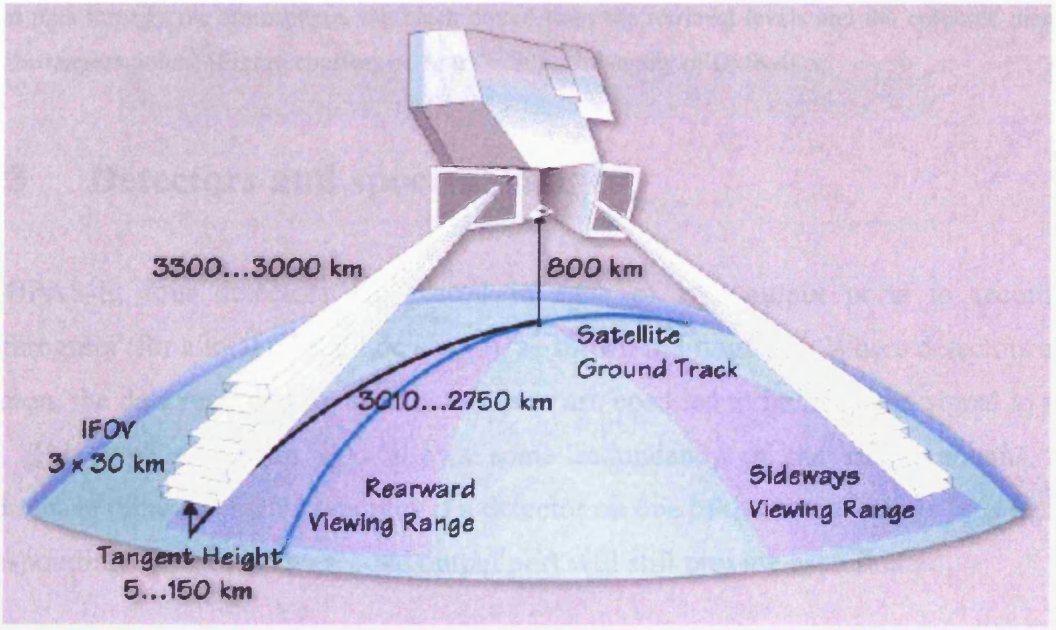

Figure 3.5 The MIPAS-E viewing geometry

The tangent path geometry for consecutive limb scans in the MIPAS-E nominal observing mode is shown in (Figure 3.6). Limb views from successive scans intersect at 10 km and the lowest altitude at which views from one limb view intersect the next measured profile is 20 km. This nominal mode undersamples the horizontal structure in the atmosphere,

particularly the lower atmosphere, and for gases with strong horizontal gradients, such as ozone, this leads to a smearing of the horizontal features in the retrieval.

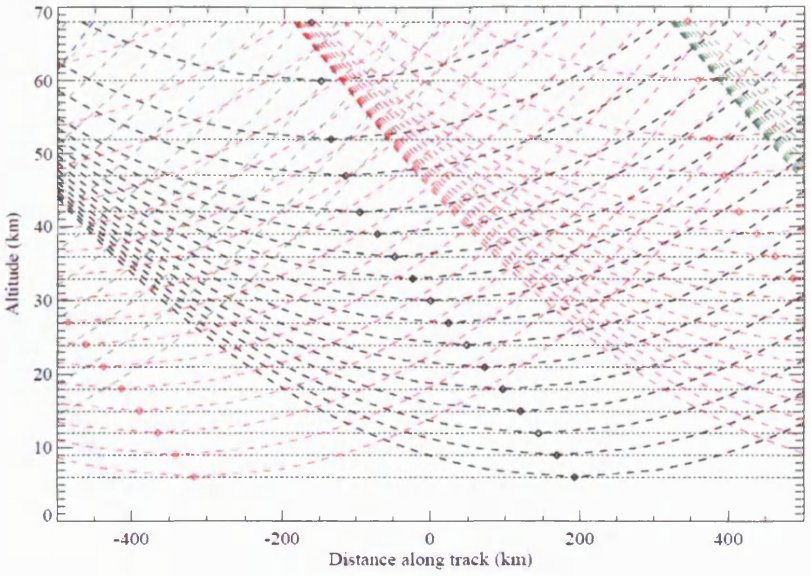

Figure 3.6 Tangent path geometry for MIPAS-E in nominal mode. The coloured dashed lines represent the tangent path through the atmosphere, the black dotted lines the retrieval levels and the coloured diamonds show the tangent points. [Figure courtesy of Anu Dudhia, University of Oxford].

3.2.3 Detectors and spectral ranges

In MIPAS-E, four detectors are placed in each of two output ports to record the interferogram (for a total of eight detectors), as shown in Figure 3.7. Where detectors are in common, the data recorded by each output port are coadded to increase the signal to noise ratio. This type of set-up also allows some redundancy of the measurements, very important in remote sensing, whereby if a detector on one of the output points fails then the corresponding detector in the second output port will still provide useful data.

The four detectors are a mixture of Mercury, Cadmium and Tellurium (HgCdTe) and each has been optimised for a particular spectral range. Together, the four detectors cover the spectral range 685-2410 cm^{-1} (41500-14600 nm). The four detectors are named A, B, C and D with detectors A, C and D of port 1 and 2 being identical, whereas detectors B are different for each port and are designated AB and B. The eight detectors are combined to cover the five spectral bands illustrated in Table 3.3.

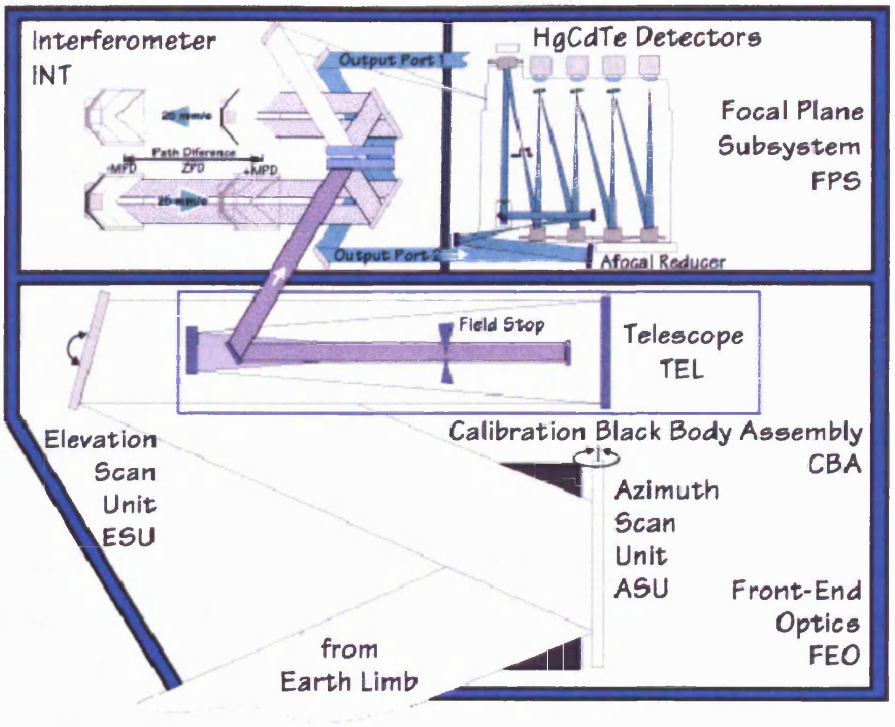

Figure 3.7 The MIPAS-E instrument.

Band	Detectors	Spectral range (cm^{-1})
A	A1 and A2	685-970
AB	B1	1020-1170
B	B2	1215-1500
C	C1 and C2	1570-1750
D	D1 and D2	1820-2410

Table 3.3 The five spectral bands measured by the MIPAS-E.

3.2.4 Sampling the interferograms

Movement of the corner reflectors allows the interference pattern to move over the detectors. The modulated output has to be sampled at numerous regular optical path difference intervals to obtain a useful interferogram (30 nm for the MIPAS). To do this, a laser beam transmitted in the same optical set-up triggers the sampling electronics at very precise intervals.

The interferogram of the monochromatic laser is a pure sine wave and is detected by a pure metrology and a fringe counter to determine the optical path difference by the phase of the sine wave. The fringe counter modulates a "clock signal" that is sent to the analogue to digital converter in the on-board signal processor electronics. The fringes trigger the sampling of the interferogram. The sampling frequency has to stay within a narrow range otherwise sampling jitters would result, which means that the instrument must have a very constant optical path difference speed (i.e. the speed of the retro-reflectors).

3.3 Radiometric calibration

Radiometric calibration is the process by which physical units are attributed to the raw spectrum as derived from the measured interferogram, using measurements of well-defined targets. To calibrate radiometrically the spectra generated by the MIPAS-E two separate measurements are made, the first from an internal calibration blackbody at a temperature of 224 K [Kleinert, 2004], the second from deep space (at a tangent altitude of 235 km) where the radiance emission is negligible (or can also be thought of as a cold blackbody source at 2.7 K).

Calibration measurements are performed after the instrument slides have been stopped in order to re-establish a phase reference and as a result this calibration sequence is the first operation in any nominal measurement sequence.

3.3.1 Offset measurement

Deep space measurements are used to determine the instrument offset value, the contribution that the instrument's self-emission contributes to the signal measured. To compute the offset calibration takes 16.15 seconds (including transition times) with six measurement sweeps made at a lower spectral resolution. The process is repeated every five scans [Mantovani, 2003].

Validation studies suggest that the offset in the deep space view is less than 6 nW/ (cm^2 sr cm^{-1}). The maximum difference between two consecutive offset measurements can change by up to 2 nW/(cm^2 sr cm^{-1}), [Kleinert, 2004].

3.3.2 Gain measurement

The internal blackbody is used to establish the instrument responsivity, or gain. Gain calibration requires 1200 measurements (600 deep space sweeps and 600 internal black body measurements) at a resolution ten times less than the nominal operating resolution of the MIPAS-E and then co-added at the ground station to reduce noise. The radiometric gain calculation takes around 18 minutes. During the early stages of the MIPAS-E mission these measurements were carried out on a daily basis but after the temporal behaviour had been established these measurements were reduced to once every two days by March 2004 [Mantovani, 2004].

3.3.3 Noise Equivalent Spectral Radiance

Successful retrieval of trace gas species from atmospheric measurements requires a large signal to noise ratio (SNR) so that results are not limited by random noise errors. The sensitivity of the MIPAS-E to noise is calculated in terms of noise equivalent spectral radiance (NESR). Pre-flight upper limit instrument noise requirements were defined for each of the 5 spectral bands, listed in Table 3.5.

MIPAS-E spectral band	Noise Equivalent Spectral Radiance requirements (nW/cm^2 sr cm^{-1})
A	50
AB	40
B	20
C	6
D	4.2

Table 3.4 MIPAS-E noise equivalent spectral radiance requirements

Estimates from in-flight MIPAS-E measurements from July 24th 2002 indicated that these requirements were met for most wavenumbers in all spectral bands as shown in Figure 3.8. The only regions where the requirements were breached in orbit 02081 were at wavenumbers below 720 cm^{-1} in band A and at wavenumbers above 2180 cm^{-1} in band D.

When the averaged NESR data for orbit 02081 are split into their four separate measurement components, Figure 3.9, there are subtle variations of NESR observed with height. The lowest NESR is calculated at heights above 68 km for all 5 spectral bands. The highest NESR levels are in measurements below 9 km although for most wavenumbers the calculated values are within pre-flight specifications.

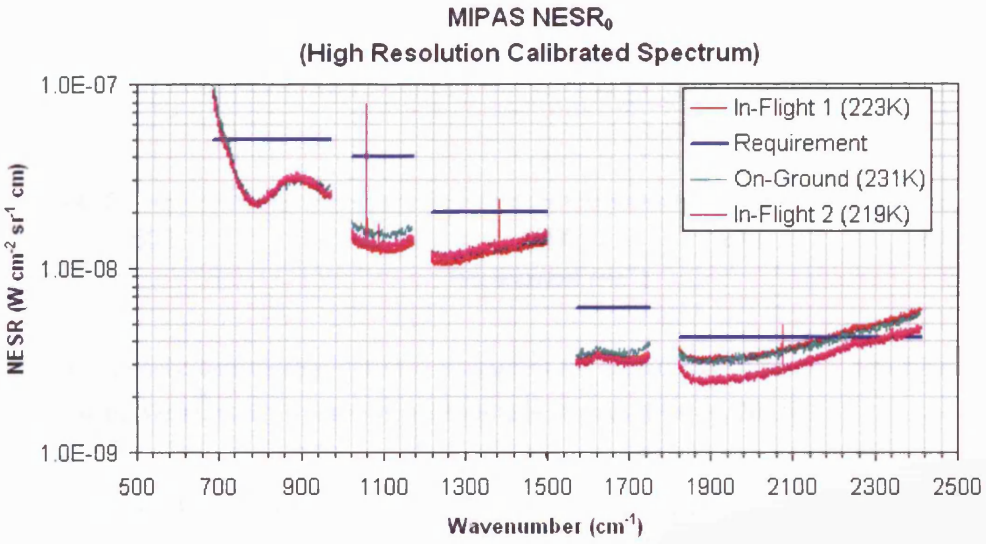

Figure 3.8 A noise equivalent spectral radiance assessment for orbit 02081 of MIPAS-E data from July 24th 2002 (source: [Perron, 2003])

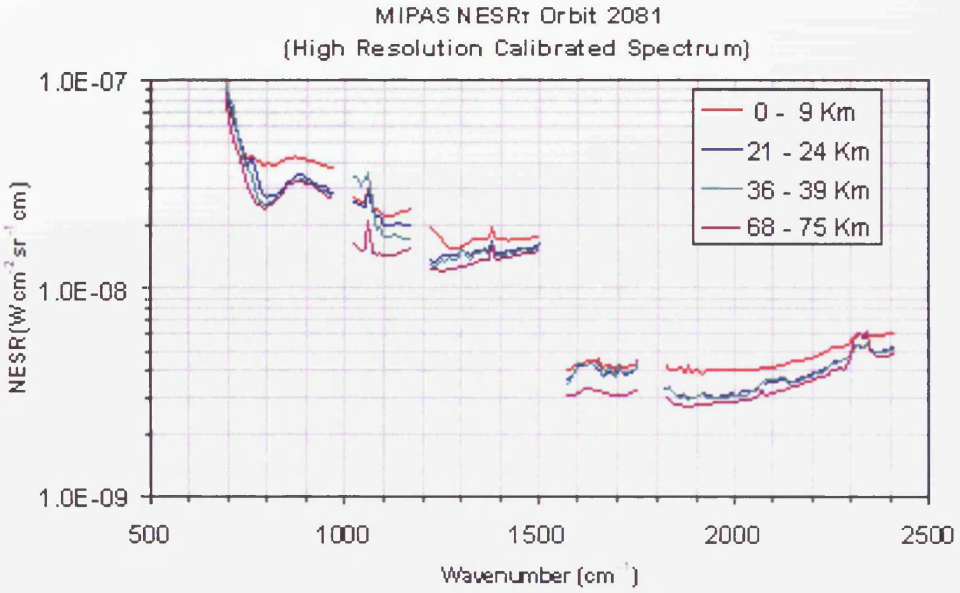

Figure 3.9 A noise equivalent spectral radiance assessment for orbit 02081 of MIPAS data from July 24th 2002, showing the variation of this quantity with altitude (source: [Perron, 2003])

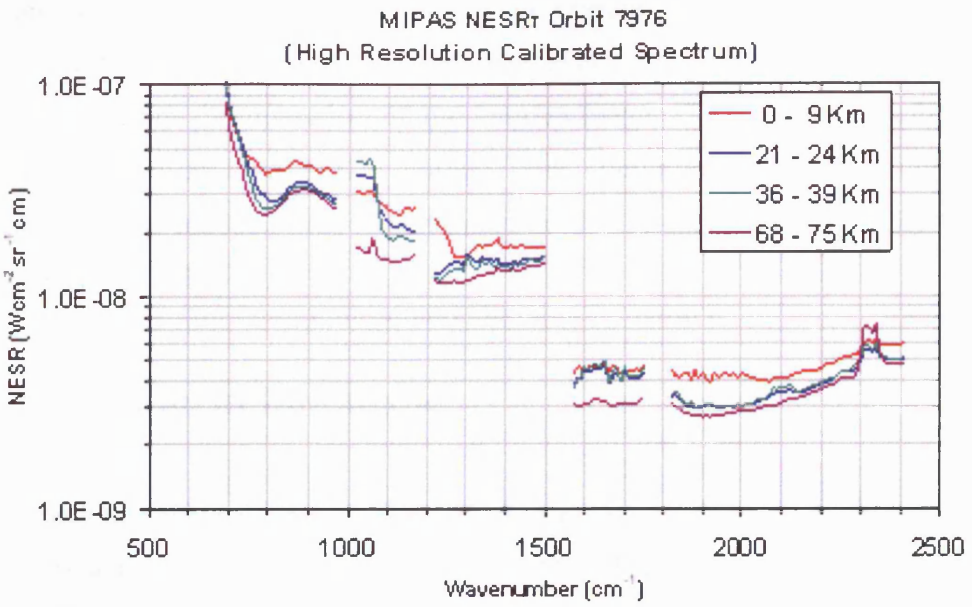

Figure 3.10 A noise equivalent spectral radiance assessment for orbit 07976 of MIPAS data from September 9th 2003, showing the variation of this quantity with altitude (source: [Perron, 2003]).

During the lifetime of the MIPAS-E on ENVISAT further routine estimates of NESR have been derived. By September 2003, no significant changes in NESR were observed compared to July 2002, Figure 3.10, with the MIPAS-E still predominantly operating within pre-flight requirements thus indicating that the data obtained have remained at a very high quality through the first one and a half years of operation.

3.4 Spectral calibration

Band	Target gas	Spectral interval (cm^{-1})	Number of coadditions	Used for Spectral calibration	Used for ILS Retrieval
A	CO_2	945.98 – 954.54	14	yes	yes
AB	O_3	1128.75 - 1151.73	3	yes	no
B	H_2O	1399.20-1429.94	1	yes	yes
C	H_2O	1616.71 - 1677.75	1	yes	no
D	H_2O	1866.38 - 1889.57	2	yes	yes

Table 3.5 Reference lines and spectral windows used for spectral calibration and ILS retrieval (source: envisat.esa.int)

Measurements by the MIPAS-E are affected by Doppler shifting caused by the relative movement of the satellite and the Earth and also from non-negligible shifts in the frequency scale from the operation of the interferometer. Calibration is performed with comparison of measured MIPAS-E spectra with synthesised spectra produced using accurate line-by-line models. This is performed in all five spectral bands using lines from the gases listed in Table 3.5.

3.4.1 Instrument line shape

The instrument line shape (ILS) is a polynomial function that defines the observed width of spectral lines and is dependent on the instrument's characteristics. In particular for the MIPAS-E a long maximum path difference (MPD) between the two retro-reflector mirrors inside the interferometer produces a narrow ILS. To retrieve ILS from MIPAS-E measurements requires the fitting of a synthesised spectrum with well-known spectral lines to the data.

The main contributor to the ILS is the maximum path difference between the two mirrors of the interferometers, the longer the MPD is, the thinner the ILS is. Other contributors to the ILS are the finite optical resolution of the instrument and misalignment of the optical components.

For the purpose of this thesis, the intrinsic instrument lineshape is apodized with a Norton-Beer strong function (Norton and Beer, [1976] with subsequent correction by Norton and Beer, [1977]) which minimises the sidelobes.

3.4.2 Pointing and line of sight

Accurate determination of both the pointing and line of sight (LOS) of limb sounding instruments is necessary to produce accurate profiles of atmospheric constituents.

The two pointing mirrors of MIPAS-E enable accurate measurements of tangent altitude to be made. The elevation mirror has an angular coverage of 3° that enables it to point between altitudes of 5 km and 250 km. This is important for deep space offset calibrations. The mirror determines the tangent altitude and then corrects it for the Earth geometry and the altitude the instrument is orbiting at. The azimuth mirror is used to determine the

latitude and longitude of the pointing area. The azimuth mirror is fixed while information about the altitude is obtained, the mirror then rotated for the next measurement. This feature allows MIPAS-E to obtain global coverage.

Line of sight calibration is required to determine pointing bias. The LOS calibration is performed by observing the motion of stars moving through the field of view. The time taken for the star to cross the field of view is compared to the expected time. This information is then used to derive the calibration. The pointing biases between the MIPAS-E observation and ENVISAT are used to correct pointing errors.

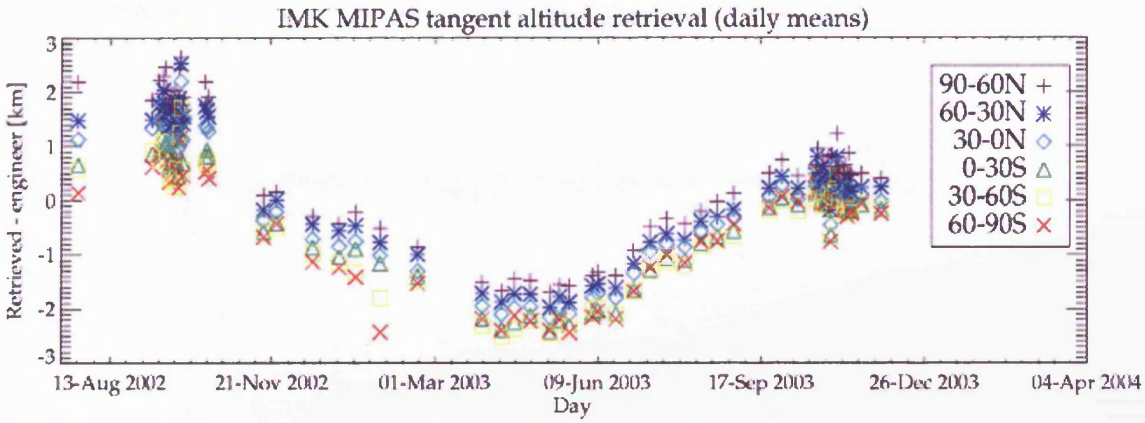

Figure 3.11 Calculated differences between the IMK retrieved altitudes and the MIPAS engineering altitudes, for the period August 2002 to December 2003 (source: M. Keifer, IMK, personal communication).

The accuracy specification for the pointing of MIPAS-E is 1.8 km. The tangent altitudes measured by the MIPAS-E are also included in the Level 1b and level 2 data. A validation study on the MIPAS-E pointing accuracy was performed by von Clarmann *et al.*, [2003]. They used an off-line data processor developed at the Institut für Meteorologie und Klimaforschung (IMK) to investigate the accuracy of the MIPAS-E retrieved altitudes. The results showed that the retrieved tangent altitude differed substantially from the MIPAS-E pointing information. In early MIPAS-E data, July 24th 2003, differences of up to 3 km were measured.

3.5 MIPAS-E data processing

The operational data processing chain for MIPAS-E has been defined in the following 4 stages and is shown schematically in Figure 3.12:

- Level 0 : Reformatted, time-ordered, satellite data, in computer compatible format
- Level 1a : Reconstructed interferograms
- Level 1b : Radiometrically and spectrally calibrated emission spectra
- Level 2 : Profiles of atmospheric pressure, temperature and constituents along the orbit track

The interferograms received by the ground segment are referred to as level 0 data. The data themselves, an example in Figure 3.3, have undergone a minimal amount of on board processing, details of which can be found in the MIPAS data products handbook [available from the ESA website, http://envisat.esa.int/dataproducts/mipas/CNTR.htm].

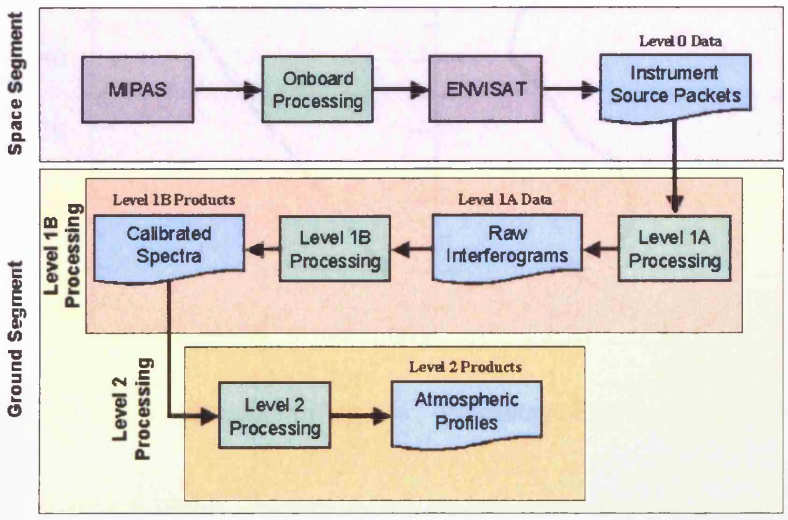

Figure 3.12 Data processing chain for MIPAS (source: envisat.esa.int/instruments/mipas/)

The ground based processing of MIPAS data can be sectioned into two parts, level 1b and level 2. The aim of level 1b processing is to convert all of the received interferograms into fully calibrated (both radiometrically and spectrally), validated, corrected and geolocated spectra of radiance (Figure 3.4). The corrections performed on the data include the gain, offset, Doppler shift and detector non-linearities mentioned previously in this section. The ILS and NESR are including in the level 1b data along with pointing and geolocation data.

Once those level 1b spectra have been formulated, the aim of the level 2 processing is to convert these spectra into vertical profiles of specific atmospheric molecules using state of the art inversion models. As the spectral line intensity is a function of pressure and temperature, as well as of concentrations of gases, the level 2 processor firstly retrieves

these two quantities using CO_2 lines. This is possible as CO_2 is a well-mixed gas in the atmosphere and its vertical concentration is well-known. The volume mixing ratios of six other greenhouse gases are then calculated using strong emission "microwindows" in the spectra that contain prominent information about the target gas with little information from interfering species. The ordering is for the retrieval of water vapour (H_2O), ozone (O_3), methane (CH_4), nitrous oxide (N_2O), nitrogen dioxide (NO_2) and nitric acid (HNO_3). This is partly dictated by the desirability of using retrieved water vapour and ozone for example in retrievals of the other gases further down the processing chain. An example of a vertical profile retrieval from simulated measurements can be found in Figure 3.13.

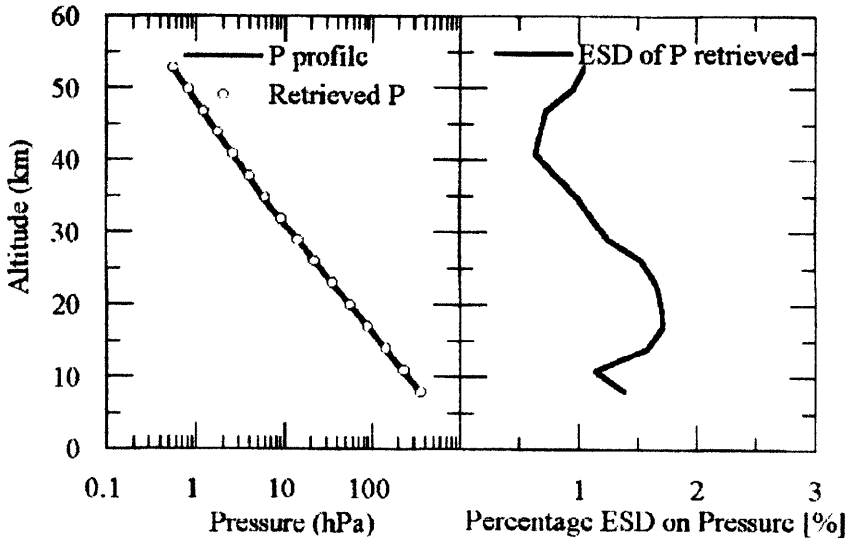

Figure 3.13 Simulated vertical profile of pressure (left) and estimated standard deviation (right) (source: MIPAS handbook)

3.6 Summary

This chapter gives a general overview of the European Space Agency's (ESAs) ENVIronmental SATellite (ENVISAT) mission and a description of all nine instruments onboard and the environmental parameters they measure. In particular the MIPAS-E instrument is described in greater detail as spectral measurements from this instrument were inverted as part of this thesis into meaningful volume mixing ratios of CFC-12 and HCFC-22. The MIPAS-E measurement principles, including the viewing geometry of the instrument and the spectral ranges covered by the detectors and the sampling of the interferograms themselves by the detectors is introduced.

The processes involved in the calibration of the MIPAS-E measurements (both radiometric and spectral calibration) is discussed with particular reference to the calculation of the offset, gain, noise equivalent spectral radiance and the instrument line shape. The calibration forms part of the data quality processing of MIPAS-E measurements. An overview of the MIPAS-E data processing chain from the raw level 0 interferograms to the level 2 volume mixing ratio, pressure and temperature data is given.

The following chapter explores the detection of halocarbons in MIPAS-E spectral data and the strength of the signal observed. It also presents the first retrieval results of HCFC-22 by the OPERA retrieval scheme developed for this thesis.

Chapter 4

4 Halocarbons in MIPAS-E data

In the previous chapter it was shown that the MIPAS-E instrument is capable of measuring high resolution spectra of the atmosphere. The purpose of this section is to show that the signatures of halocarbons can be detected and that retrieval schemes can be developed to determine the concentrations of HCFC-22 and CFC-12 in the atmosphere. Results from the OPERA retrieval scheme (outlined in section 2.5.6) will be shown for May 2nd 2003 and a full error analysis of these results is presented.

4.1 Detection of halocarbons in atmospheric spectra

All halocarbons are efficient greenhouse gases in the atmosphere and have specific thermal emission regions in the infrared which are compound dependent. Atmospheric conditions can be modelled well within a laboratory environment and using, for example, a Fourier transform spectrometer (FTS) the infrared cross-sections of any halocarbon can, in principle, be determined at any particular pressure or temperature. These measured infrared cross-sections are used for the determination of atmospheric concentrations of the species. Therefore the success of any infrared remote sensing experiment conducted in the atmosphere depends upon the availability of accurate, high resolution spectroscopic data.

4.1.1 Previous studies of halocarbon spectroscopy

To perform accurate retrievals of atmospheric constitution from remotely sensed measurements requires accurate spectroscopic data but also ideally an agreed, consistent molecular spectroscopic dataset used by the scientific community. The HIgh-resolution TRANsmission database (HITRAN) was first published in 1973 and has been recognized as the international standard for providing the necessary fundamental spectroscopic parameters for atmospheric radiance calculations used in the retrieval process. The results in this thesis that require cross-sectional data, use the year 2000 edition of the HITRAN database which has been modified for the MIPAS-E [Flaud *et al.*, 2003]. Sections 4.1.1.1

to 4.1.1.2 describe previous laboratory measurements to obtain cross-section for HCFC-22 and CFC-12, data which are included in HITRAN.

4.1.1.1 HCFC-22

The absorption cross-sections for HCFC-22 included in the HITRAN 2000 database are based primarily on the results of both Clerbaux *et al.* [1993] and by the Varanasi group. The database includes 29 HCFC-22 cross-sections from the 12.3 μm (Figure 4.1) emission band (765 to 855 cm^{-1}) at temperatures of 181 to 297 K, and pressures of 0 to 765 mb. HITRAN includes 31 HCFC-22 cross-sections from Varanasi for the 8.8 μm (Figure 4.2) emission band (1070 to 1195 cm^{-1}) at temperatures of 181 to 296 K and pressures of 22 to 761 mb. Three cross-sections from Clerbaux *et al.*, [1993] measured from a pure HCFC-22 sample, are included in the dataset for the same 8.8 μm emission band but for a slightly extended wavenumber range (1060 to 1210 cm^{-1}) at temperatures of 253 to 287 K. Three cross-sections are included in the dataset from the pure sample measurements of Clerbaux *et al.*, [1993] for the weak emission feature in the 7 μm band (1275 to 1380 cm^{-1}) at temperatures of 253 to 287 K. Temperature and total pressure were varied to represent atmospheric layers defined in the U.S. Standard Atmosphere table [U.S. Standard atmosphere, 1976]. The spectral resolution for all measurements was 0.03 cm^{-1}.

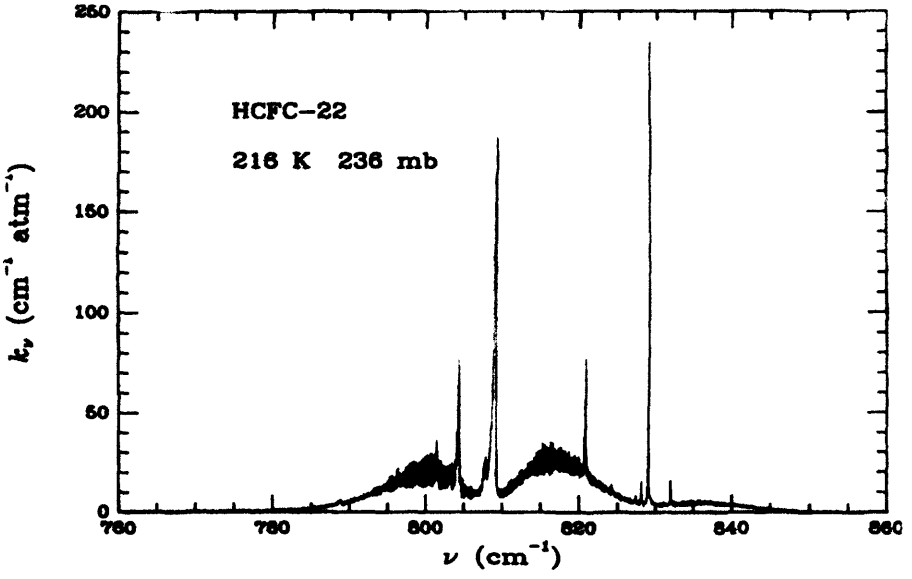

Figure 4.1 Spectral absorption coefficients in the 12.3 μm band of HCFC-22 at 216 K and 236 mb. The laboratory experimental conditions correspond to the 11 km level in the U. S. Standard Atmosphere. (Taken from Varanasi *et al.*, [1994]).

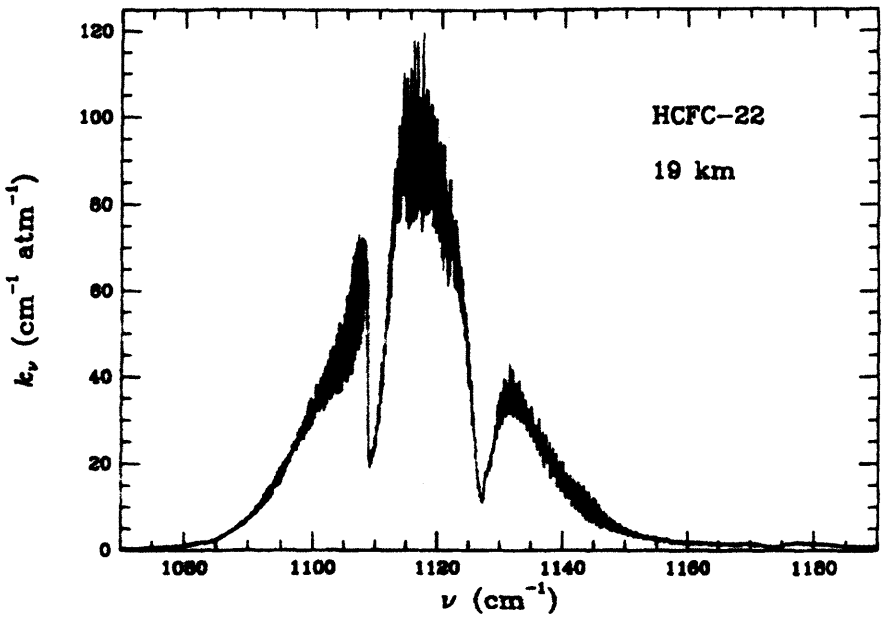

Figure 4.2 Spectral absorption coefficients in the 8.97 μm band of HCFC-22 at 216 K and 67 mb. The laboratory experimental conditions correspond to the 19 km level in the standard U.S Standard Atmosphere. (Taken from Varanasi *et al.*, [1994])

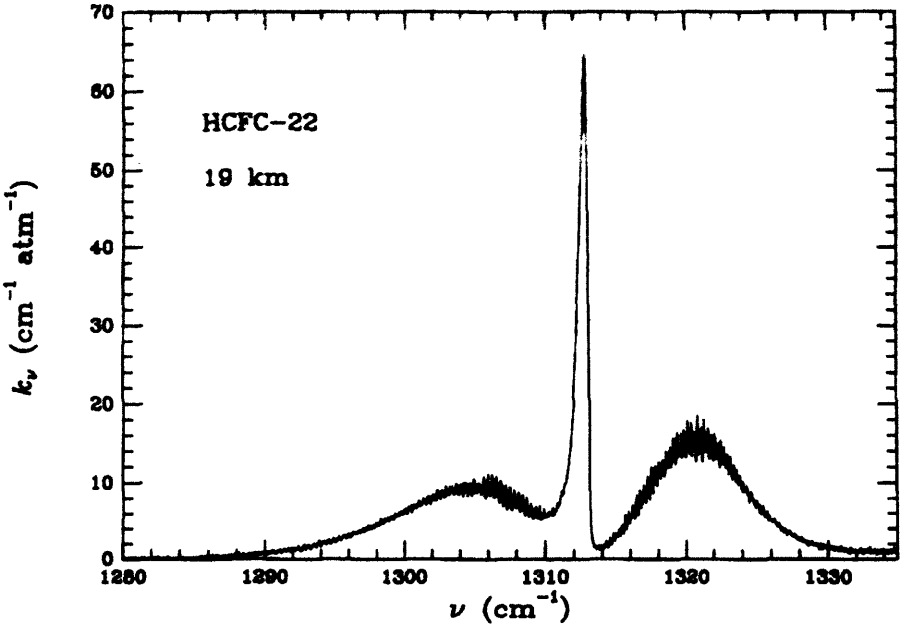

Figure 4.3 Spectral absorption coefficients of HCFC-22 in the 7.62 μm band. The experimental conditions 216 K and 67 mb correspond to the 19 km level in the U.S Standard Atmosphere (reproduced from Varanasi et al., [1994])

The integrated intensities (in units of 10^{-17} cm molecule^{-1}) measured by Varanasi *et al.*, [1994] of the 7.5 μm, 8.8 μm and 12.3 μm bands of HCFC-22 are 0.951, 6.885 and 2.282 respectively at 216 K with unfortunately no error estimates quoted. These estimates

compare very well with the results quoted by Clerbaux *et al.*, 1993, which are represented in Table 4.1. As for CFC-11 and CFC-12, integrated HCFC-22 cross-sections measured by Varanasi *et al.*, [1994] are systematically higher than previous estimates by McDaniel *et al.*, [1991] which were used in the HITRAN 1992 version. Differences range between 7 % for the 12.3 μm band and 15 % for the 8.8 μm band.

MOLECULE	INTEGRATION LIMITS, CM^{-1}	INTEGRATED CROSS-SECTIONS 287 K	270 K	253 K	UNCERTAINTIES
HCFC-22 ($CHClF_2$)	765 – 855	2.36	2.32	2.25	0.09
	1060 – 1210	6.83	6.73	6.64	0.17
	1275 – 1380	1.08	1.11	1.09	0.09

Table 4.1 Integrated cross-sections (cm $molecule^{-1}$ x 10^{-17}) for HCFC-22. (Adapted from Clerbaux *et al.*, [1993]).

4.1.1.2 CFC-12

The absorption cross-sections for CFC-12 included in the HITRAN 2000 database are based on the results of Varanasi and Nemtchinov, [1994]. They measured 104 CFC-12 cross-sections (104 in total) from the 9 μm (1050 to 1200 cm^{-1}) and 11 μm (850 to 950 cm^{-1}) emission bands using a high-resolution Fourier transform at temperatures of 190 to 296 K and pressures of 8 to 760 mb. Typical spectra are shown in Figure 4.4 and Figure 4.5. A spectral resolution of 0.03 cm^{-1} was considered to be adequate for obtaining the data at pressures exceeding 100 mb, while 0.01 cm^{-1} was used for lower pressures, since structure broadening observed in the CFC-12 bands broadens with pressure. The signal to noise ratio was typically 300:1 for the high resolution measurements.

Figure 4.6 shows the large change in the spectral absorption coefficients at the central, strong, Q-branches of the CFC-12 11 μm band at temperatures and pressures typical of three heights between the surface and a height typical of the lower stratosphere. Errors in the cross-section for any gas can propagate into large and potentially the most significant error source in the retrieval process. Figure 4.7 illustrates the variability that arises from measuring the CFC-12 cross-section at two distinct and very different resolutions. The previous CFC-12 spectroscopic measurements of Varanasi [1992a], performed at a resolution of 0.4 cm^{-1}, smear the two distinct 11 μm CFC-12 Q-branches into one spectral feature with an absorption coefficient which is approximately four times less intense. To

feature with an absorption coefficient which is approximately four times less intense. To fully exploit the capability of a high resolution instrument such as the MIPAS-E and to accurately model atmospheric radiative transfer with overlapping lines, cross-sections of resolutions 0.01 to 0.03 cm^{-1} are required.

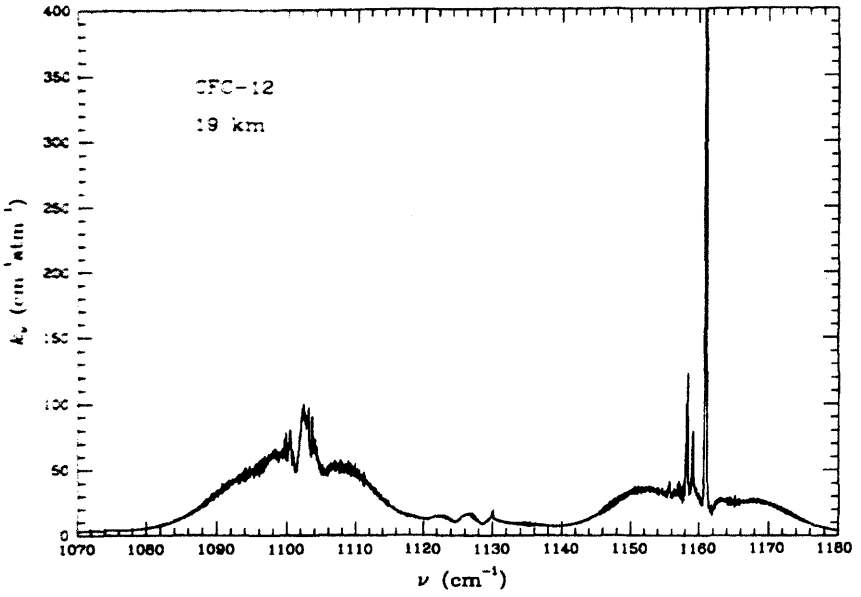

Figure 4.4 Spectral absorption coefficients of CFC-12 in the 9 μm bands. The experimental conditions 216 K and 67 mb correspond to the 19 km level in the U.S. Standard Atmosphere. (Taken from Varanasi and Nemtchinov, [1994]).

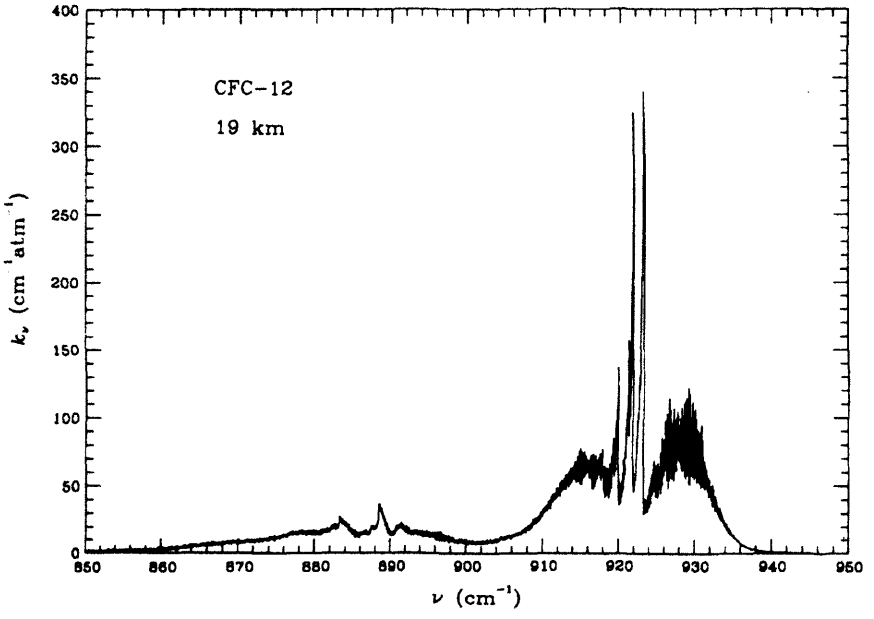

Figure 4.5 Spectral absorption coefficients of CFC-12 in the 11 μm bands. The experimental conditions 216 K and 67 mb correspond to the 19 km level in the U.S. Standard Atmosphere. (Taken from Varanasi and Nemtchinov, [1994]).

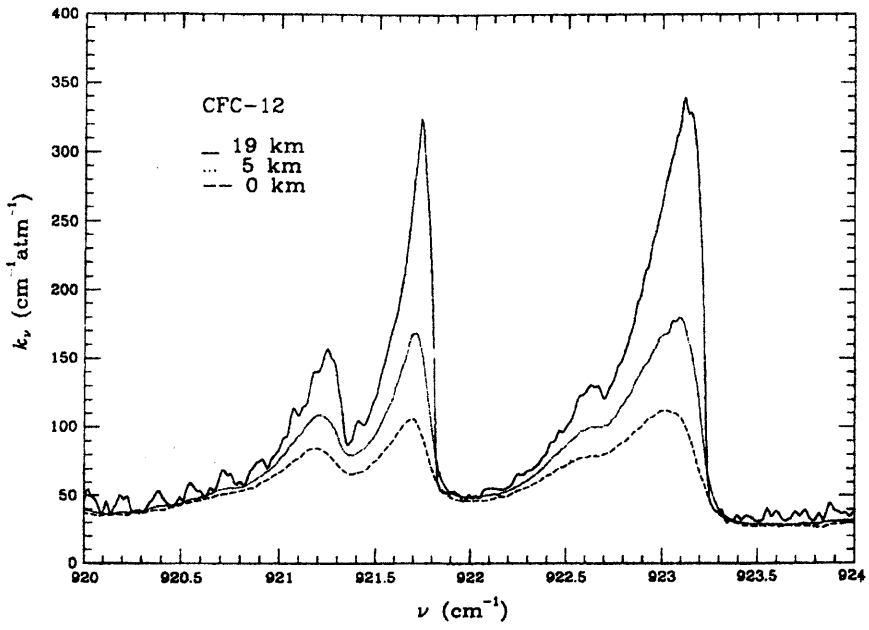

Figure 4.6 Spectral absorption coefficients in the central Q-branches of the 11 μm band of CFC-12. The laboratory conditions (temperature and pressure) were chosen as (294 K, 1013 mb), (253 K, 534 mb) and (216 K, 67 mb) in order to correspond to the surface, 5 km and 19 km levels, respectively of the U.S. Standard Atmosphere. (Taken from Varanasi and Nemtchinov, [1994]).

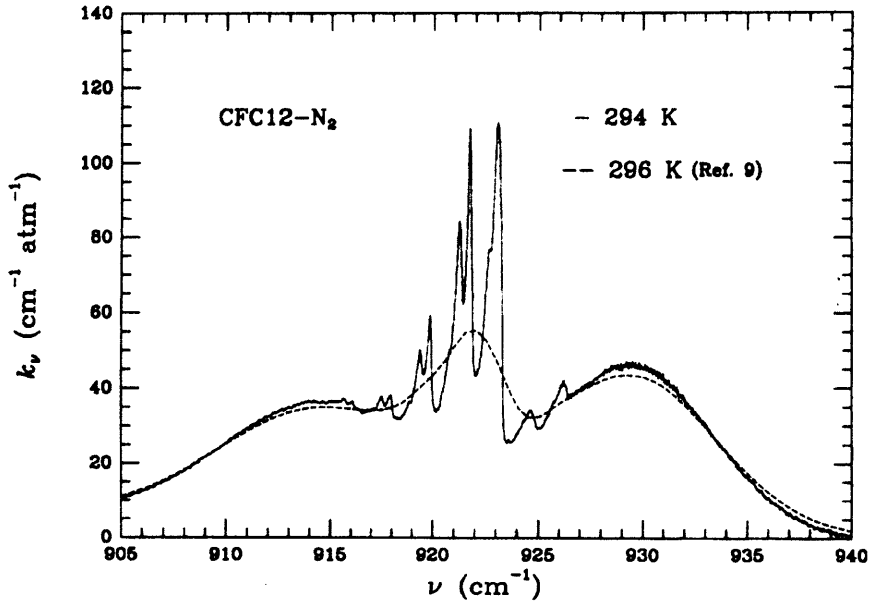

Figure 4.7 Comparison of the high resolution (0.01 cm^{-1}) absorption cross-section measurements of Varanasi and Nemtchinov, 1994 at 294 K and 84.9 mb and the low resolution (0.4 cm^{-1}) data measured by Varanasi, 1992 at 296 K and 92.4 mb (referred to on the plot key as 'Ref. 9'. (Taken from Varanasi and Nemtchinov, [1994])

The HITRAN 2000 measured integrated intensities (in units of 10^{-17} cm molecule^{-1}) of the 9 μm and 11 μm bands of CFC-12 are 7.595 ± 0.070 and 5.869 ± 0.068 respectively.

Clerbaux *et al.*, [1993], employed the same FTS technique and resolution as Varanasi and Nemtchinov and measure an integrated cross-section approximately 0.2 % lower in the 9 μm band and 0.2 % higher in the 11 μm band. Previous to this, results by McDaniel *et al.*, [1991], using the same set-up as Varanasi and Nemtchinov [1994] measured an integrated CFC-12 cross-section 6.5 % lower in the 9 μm band and 7.6 % lower in the 11 μm band compared to the results of Varanasi and Nemtchinov. Errors are assigned in the HITRAN spectroscopic database for CFC-12 (and HCFC-22)

4.1.2 Modelling target regions for the MIPAS-E instrument

Section 4.1.1 described previously identified absorption/emission regions for two major halocarbons (three for HCFC-22 and two for CFC-12). All these broadband spectral regions are measurable by the MIPAS-E but the computational analysis of a region as broad as the 11 μm CFC-12 band would be difficult or even impracticable for operational data analysis. The number of unknown parameters, such as interfering gases, also decreases by using a smaller "microwindow" region. The microwindow approach also excludes regions where the measured spectrum is not well reproduced by the forward model. An optimum microwindow contains prominent but usually nonsaturated transitions of the target species (for example HCFC-22 or CFC-12), leading to high absolute sensitivities of the measured spectral signal to the target parameter. CFC-12 was sufficiently strong to be identified in previously measured spectra from both ground-based and balloon measurements (including MIPAS-B) and also from spaceborne missions such as the ATMOS FTS flown 3 times onboard the ATLAS-3 platform [Gunson *et al.*, 1996].

The 829 cm^{-1} Q-branch feature of HCFC-22 has been identified unambiguously in IR balloon and ground measurements and also in ATMOS solar occultation spectral. Further investigation was required to investigate whether this feature was identifiable for the first time in thermal emission spectra from a spaceborne instrument. Previous spaceborne infrared satellite instruments to measure trace gases such as the CRISTA [Offermann *et al.*, 1999] measured at too low a spectral resolution (2 cm^{-1}) to identify the HCFC-22 $2\nu_2$ feature.

4.1.2.1 Microwindow selection

	Microwindow number	Start wavenumber (cm^{-1})	End wavenumber (cm^{-1})	Gases in the microwindow
1	F22_0091	827.925	830.925	H_2O, CO_2, O_3, NO_2, NH_3, HNO_3, ClO, OCS, HCN, C_2H_2, C_2H_6, COF_2, HCFC-22, $ClONO_2$, HNO_4
2	F22_0092	806.975	809.975	H_2O, CO_2, O_3, NO_2, NH_3, HNO_3, ClO, OCS, HCN, C_2H_2, C_2H_6, HCFC-22, CCl_4, $ClONO_2$, HNO_4
3	F22_0093	819.350	822.350	H_2O, CO_2, O_3, NO_2, NH_3, HNO_3, ClO, OCS, HCN, C_2H_2, C_2H_6, COF_2, HCFC-22, $ClONO_2$, HNO_4
4	F22_0094	1113.525	1116.500	H_2O, CO_2, O_3, N_2O, CH_4, SO_2, NH_3, HNO_3, CFC-11, CFC-12, HCFC-22
5	F22_0095	803.575	806.575	H_2O, CO_2, O_3, NO_2, NH_3, HNO_3, ClO, OCS, HCN, C_2H_2, C_2H_6, HCFC-22, CCl_4, $ClONO_2$, HNO_4
6	F22_0096	817.150	819.325	H_2O, CO_2, O_3, NO_2, NH_3, HNO_3, ClO, OCS, HCN, C_2H_2, C_2H_6, COF_2, HCFC-22, $ClONO_2$, HNO_4
7	F22_0097	1106.225	1107.500	H_2O, CO_2, O_3, N_2O, CH_4, SO_2, NH_3, HNO_3, CFC-11, CFC-12, HCFC-22
8	F22_0098	1110.250	1113.250	H_2O, CO_2, O_3, N_2O, CH_4, SO_2, NH_3, HNO_3, CFC-11, CFC-12, HCFC-22

Table 4.2 Oxford microwindow selection for HCFC-22 in order of expected information content from the MIPAS-E measurement.

One approach to microwindow selection is to simulate the propagation of random noise through the retrieval and select measurements that maximise the information content or degrees of freedom of the signal [Rodgers, 2000]. The approach developed at the University of Oxford by Dudhia *et al.*, [2002] selects microwindows by simulating a full profile retrieval, including the propagation of systematic error terms. The microwindows for H_2O, O_3, HNO_3, CH_4, N_2O and NO_2 selected by the Oxford MWMAKE algorithm are

used in the MIPAS-E near real time processor. For the halocarbons, equivalent runs were performed and resulted in the selection of eight microwindows for HCFC-22 (Table 4.2) and six suitable microwindows for CFC-12 (Table 4.3), [Dudhia, personal communication].

	MICROWINDOW NUMBER	START WAVENUMBER (CM^{-1})	END WAVENUMBER (CM^{-1})	GASES IN THE MICROWINDOW
1	F12_0101	921.400	924.400	H_2O, CO_2, NH_3, HNO_3, CFC-12, CFC-113
2	F12_0102	1159.700	1162.700	H_2O, O_3, N_2O, CH_4, CFC-12
3	F12_0103	918.375	921.375	H_2O, CO_2, NH_3, HNO_3, CFC-12, CFC-113
4	F12_0104	924.425	927.425	H_2O, CO_2, NH_3, HNO_3, CFC-12, CFC-113
5	F12_0105	929.125	932.125	H_2O, CO_2, O_3, NH_3, CFC-11, CFC-113
6	F12_0106	885.975	888.975	H_2O, CO_2, NH_3, HNO_3, CFC-12, CFC-113

Table 4.3 Oxford microwindow selection for CFC-12 in order of expected information content from the MIPAS-E measurement.

4.1.2.2 Identifying HCFC-22 microwindows for MIPAS-E

As discussed in section 2.4.1, the RFM is used in this study to simulate the radiances observed by the MIPAS-E. To investigate whether the version of the HITRAN database, HITRAN_MIPAS, used in this study effectively encapsulates the spectral features of the three halocarbons in the infrared and to test the model itself, limb radiance calculations were performed. For CFC-12, there are many instances in the literature [e.g. ATMOS and CRISTA] where this gas has been identified in spaceborne spectral measurements and retrievals performed with low retrieval errors. As CFC-12 has been identified in previous atmospheric IR measurements from space, this thesis does not attempt to replicate the identification of these gases. HCFC-22 has been previously identified in solar occultation measurements from space, including the ATMOS mission, but not in thermal emission measured from space. This section uses a modified version of the HCFC-22 microwindows provided by Dudhia and HCFC-22 cross-section information to identify candidate regions where the HCFC-22 emission signal is expected to dominate interfering gases such as water vapour or ozone.

To model the three emission regions of HCFC-22 the RFM was used. Profiles for all atmospheric trace gases emitting in the region were defined using the MIPAS standard atmosphere files of Remedios [1999]. Firstly, for each of the three regions, atmospheric limb emission spectra were calculated at a resolution of 0.025 cm^{-1} including HCFC-22 and known emitters in the regions. Secondly, emission spectra were calculated for each of the three regions including all these gases but now excluding HCFC-22. Differencing these two calculations left the radiance attributable to HCFC-22 in standard atmospheric conditions. Differencing of the spectra also amplifies the appearance of weak spectral features and reduces the influence of saturated lines which are less sensitive to the concentration of related trace species and where no information on a particular gas can be gained.

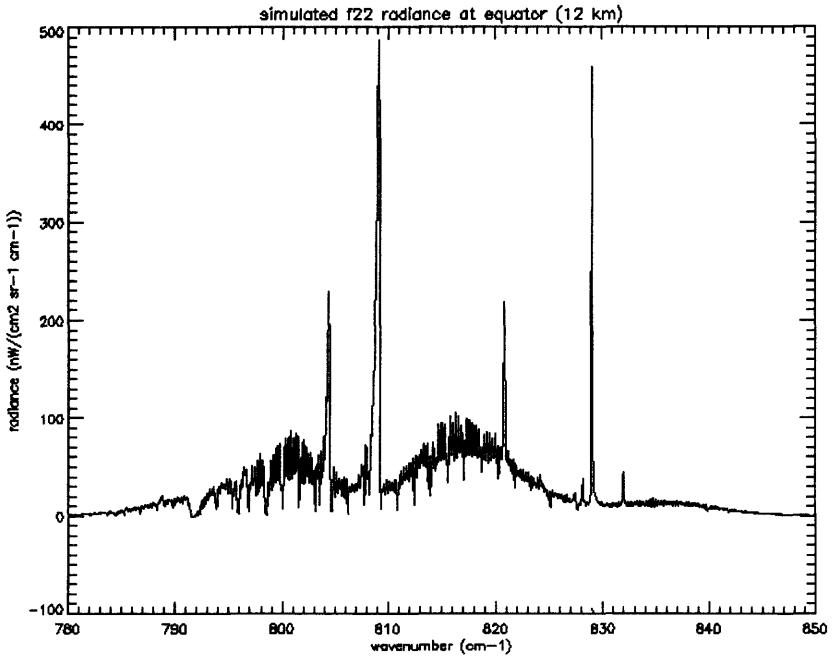

Figure 4.8 A difference plot of simulated line-by-line atmospheric limb emission spectrum for the 12.3 μm band of HCFC-22 (spectrum with all gases – spectrum including all gases apart from HCFC-22). This plot corresponds to 12 km in the tropics and the calculation incorporates HITRAN 2000 line and cross-sectional data and the standard atmosphere climatology used is that of Remedios [1999].

The differencing results presented in Figure 4.8 to Figure 4.10, were all calculated for an upper tropospheric limb scene in the tropics, at a tangent altitude of 12 km, with a pressure of 215 mb and a temperature of 222 K at that height. The difference spectrum from the simulated RFM radiances in Figure 4.8 clearly exhibits the two strong Q-branch features, presented in the cross-section results of Varanasi *et al.*, [1994] (centred at 809 cm^{-1} and 829 cm^{-1}), features which are not saturated in limb spectra calculated with average

conditions in the tropical upper troposphere (Figure 4.14 and Figure 4.15), and hence are potential regions that could be used to retrieve concentration information.

Performing the same emission calculation at standard atmospheric conditions at a tropical limb tangent height of 12 km within the HCFC-22 8.97 μm band, Figure 4.9, reproduces the same broad cross-sectional shape as observed in the spectral absorption coefficients of Varanasi *et al.*, [1994]. The lack of Q-branches is quite noticeable and also the effect of saturated lines, implying strong contaminant signals. Nonetheless, it would be possible, but less ideal, to retrieve in this region.

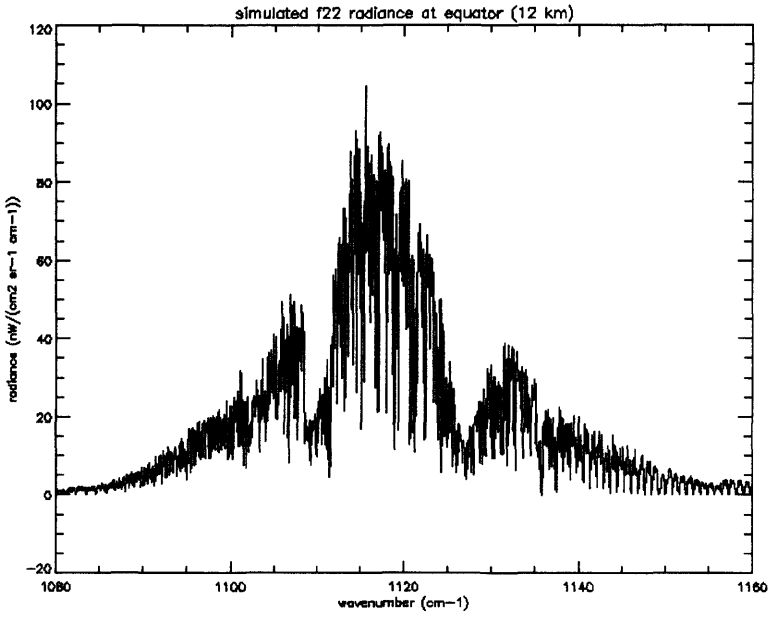

Figure 4.9 A difference plot of simulated line-by-line atmospheric limb emission spectrum for the 8.97 μm band of HCFC-22 (spectrum with all gases – spectrum including all gases apart from HCFC-22). This plot corresponds to 12 km in the tropics and the calculation incorporates HITRAN 2000 line and cross-sectional data and the standard atmosphere climatology used is that of Remedios, 1999.

The third region of the infrared spectrum where HCFC-22 has measured spectral absorption coefficients is centred at 7.62 μm. Performing the same limb emission calculation with the RFM as for the other two cases yielded results which showed no distinctive features compared with the laboratory measured HCFC-22 absorption coefficients in this region, Figure 4.10.

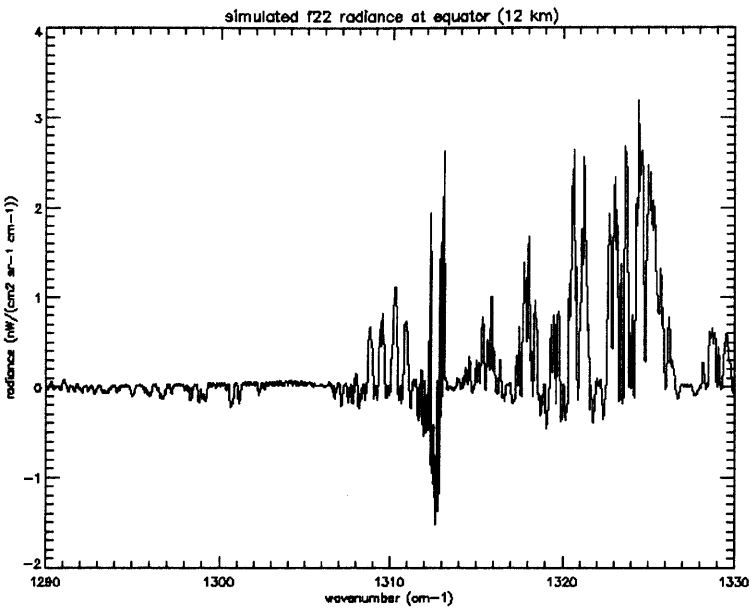

Figure 4.10 A difference plot of simulated line-by-line atmospheric limb emission spectrum for the 7.62 μm band of HCFC-22 (spectrum with all gases – spectrum including all gases apart from HCFC-22). This plot corresponds to 12 km in the tropics and the calculation incorporates HITRAN 2000 line and cross-sectional data and the standard atmosphere climatology used is that of Remedios [1999].

4.1.2.3 Confirmation Studies

The strongest spectral signatures of HCFC-22 were identified within the 775 to 855 cm^{-1} range. Atmospheric radiance spectra contain many other radiatively active gases and there can be a problem with overlapping lines of other species, at wavenumbers where the target gas has the strongest emission lines. The simulation tests in section 4.1.2.2 confirm that there are two strong spectral signatures of HCFC-22 in the HITRAN MIPAS database. However, masking by interfering gases could invalidate these candidate regions if the HCFC-22 signal were not stronger than an interfering gas. The following section identifies other emitters at the same wavenumbers as the strong Q-branches of HCFC-22.

Ideally, in identifying clear spectral features in simulated data and identifying the same features in measured radiance spectra requires at least one of the following:

a) observation of more than one spectral feature of the molecule (band or line).
b) observation of bands in more than one wavenumber region of the measurements.
c) identification of a unique spectral shape to a feature.

Factors a) and b) are not always possible but c) can work if the shape is well observed.

4.1.2.4 Identifying Spectral features of HCFC-22

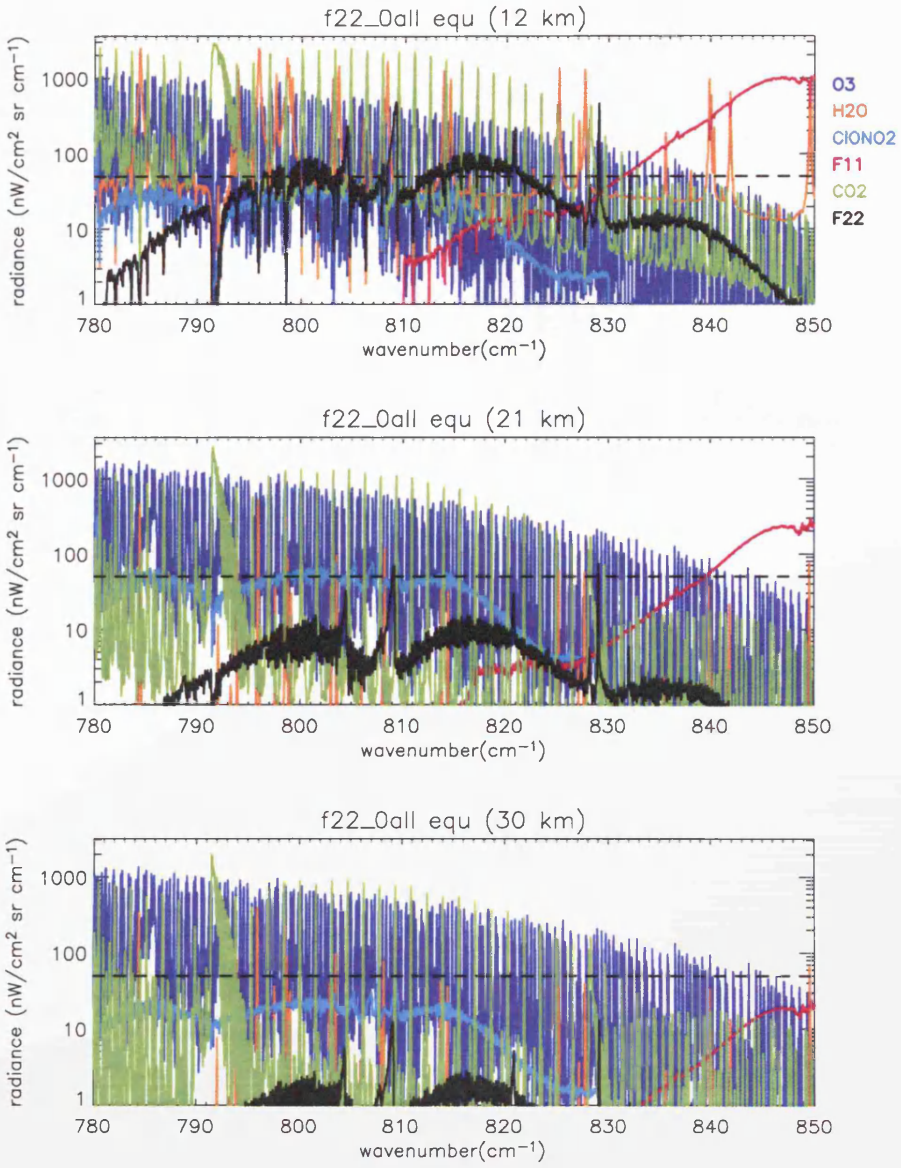

Figure 4.11 Plot of RFM modelled radiance contributions from the dominant radiatively active gas in the range 780 to 850 cm^{-1} in the tropics (30°N to 30°S). The black dotted line represents the expected noise equivalent spectral radiance (NESR) of the MIPAS which is based on pre-flight estimates of 50 $nW/(cm^2\ sr\ cm^{-1})$ for band A.

To identify each interfering gas over the whole region 780 to 850 cm^{-1} and to test the suitability of one of these peaks on which to perform retrievals, the radiance contribution for every emitting gas was calculated by the RFM. The same technique, as detailed in

section 4.1.2.2 to remove saturation effects, was used to calculate the radiance contribution of each gas.

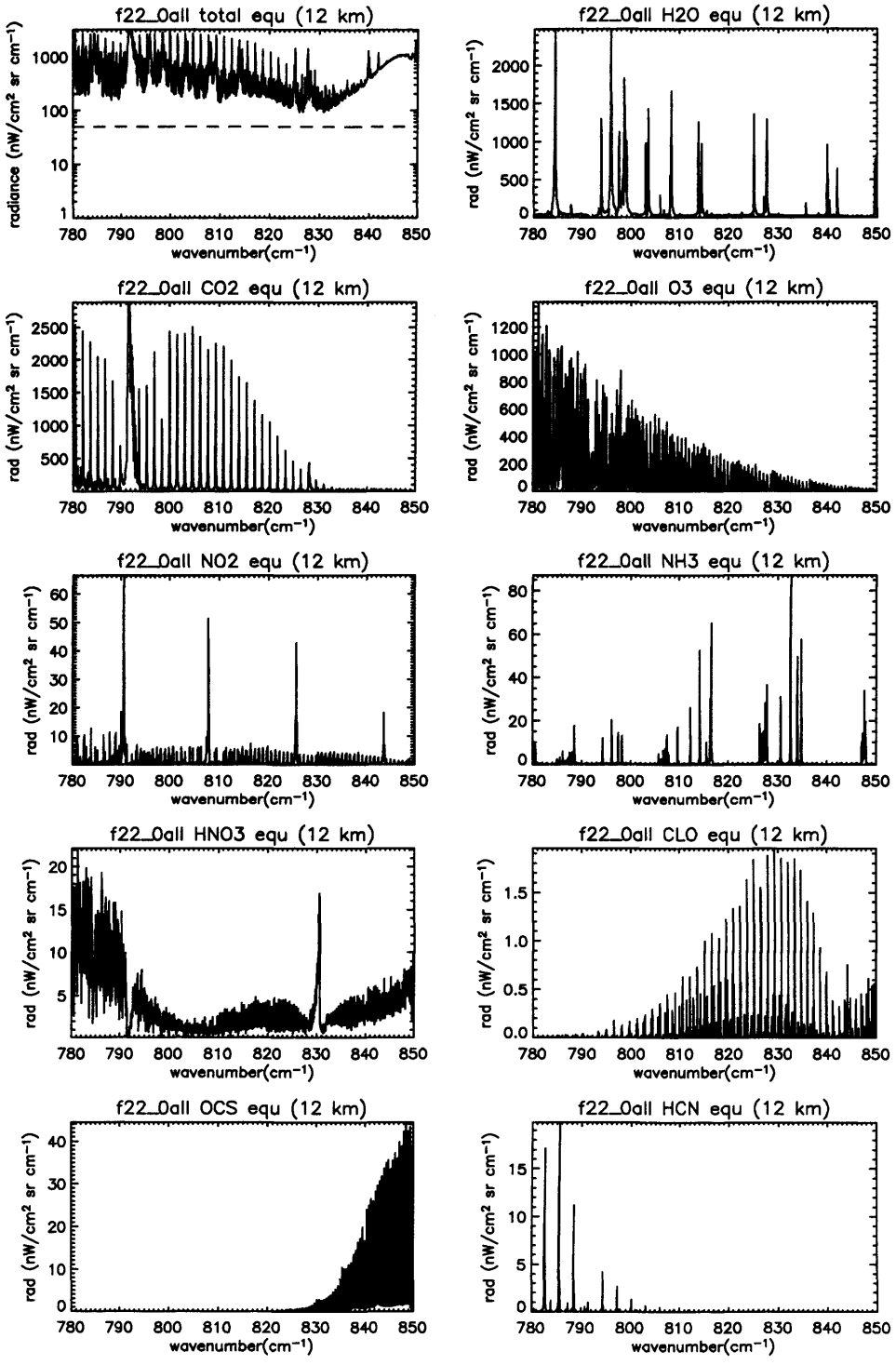

Figure 4.12 Plot of RFM modelled radiance contribution of each gas in the 780 to 850 cm^{-1} range in the tropics (30°N to 30°S). The black dotted line in the far top-left figure represents the expected noise equivalent spectral radiance (NESR) of the MIPAS which is based on pre-flight estimates of 50 $nW/(cm^2\ sr\ cm^{-1})$ for band A.

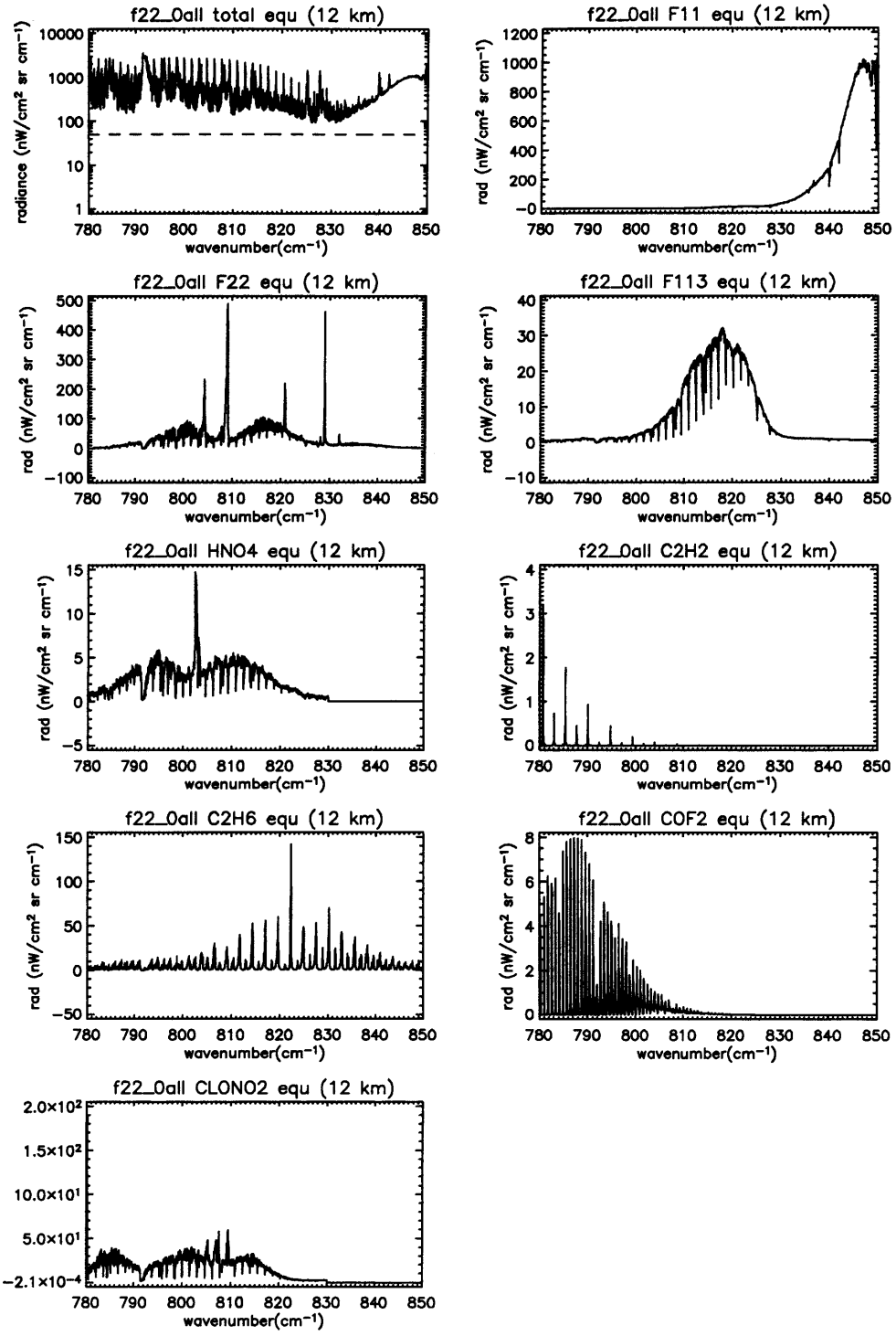

Figure 4.13 Plot of RFM modelled radiance contribution of each gas in the 780 to 850 cm^{-1} range in the tropics (30°N to 30°S).

Figure 4.11 shows the calculated emissions of each gas for the full 780 to 850 cm^{-1} range at tangent heights between 12 and 30 km in the tropics (30°S to 30°N). Calculations were performed at 3 km intervals between 6 and 30 km although only the results from 12, 21 and 30 km are shown. It is very clear that HCFC-22 is certainly not the only emitter over this wavenumber range, indeed it is apparent that it is only a minor contributor when

compared to H_2O and CO_2. This is understandable as the atmospheric concentration of HCFC-22 at 12 km is, on average, four orders of magnitude lower than H_2O, and emitted radiance is a function of atmospheric concentration.

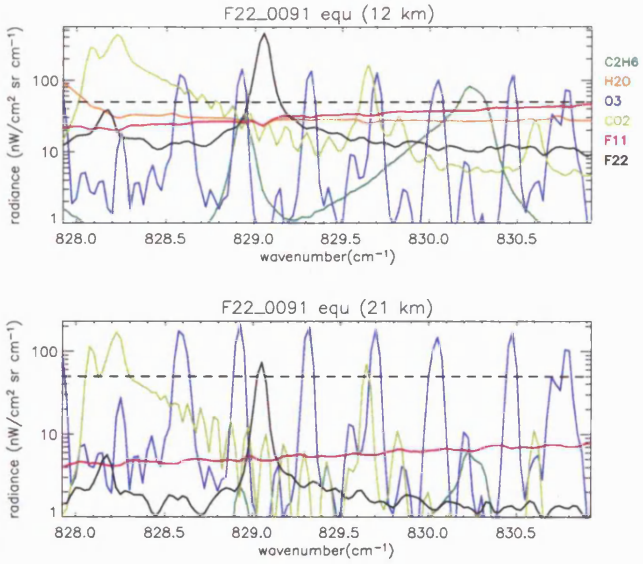

Figure 4.14 Plot of RFM modelled radiance contributions from the dominant radiatively active gas in the 828 to 831 cm^{-1} range in the tropics (30°N to 30°S). The black dotted line represents the expected noise equivalent spectral radiance (NESR) of the MIPAS which is based on pre-flight estimates of 50 $nW/(cm^2\ sr\ cm^{-1})$ for band A.

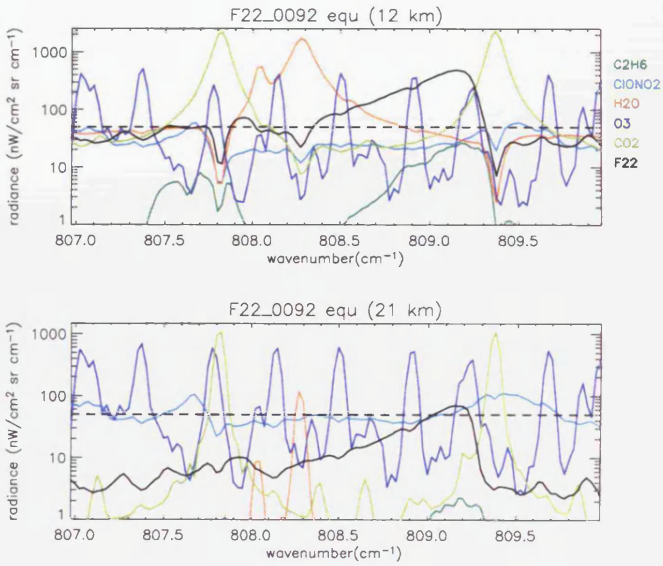

Figure 4.15 Plot of RFM modelled radiance contributions from the dominant radiatively active gas in the 807 to 810 cm^{-1} range in the tropics (30°N to 30°S). The black dotted line represents the expected noise equivalent spectral radiance (NESR) of the MIPAS which is based on pre-flight estimates of 50 $nW/(cm^2\ sr\ cm^{-1})$ for band A.

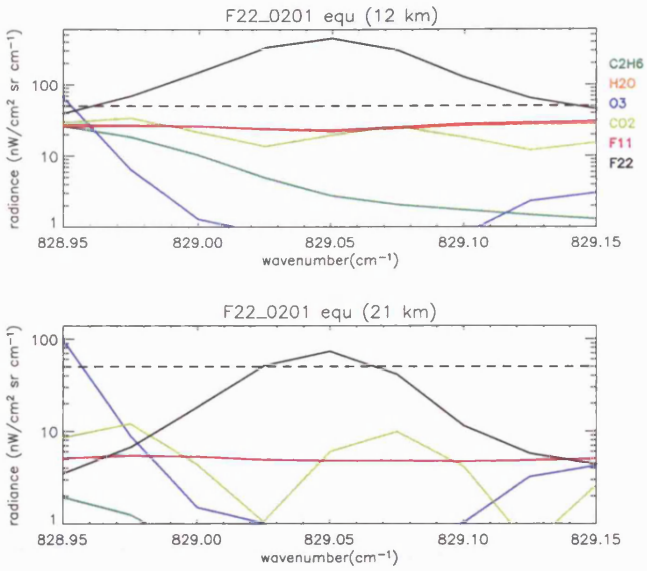

Figure 4.16 Plot of RFM modelled radiance contributions from the dominant radiatively active gas in the 828.95 to 829.15 cm^{-1} range in the tropics (30°N to 30°S). The black dotted line represents the expected noise equivalent spectral radiance (NESR) of the MIPAS which is based on pre-flight estimates of 50 $nW/(cm^2\ sr\ cm^{-1})$ for band A.

The contribution calculations in Figure 4.13 highlights the two strong HCFC-22 Q-branches at 809 and 829 cm^{-1} which, based on standard atmospheric profiles [Remedios, 1999], are calculated to be detectable above the MIPAS-E pre-flight noise estimate [Nett *et al.*, 2001] of 50 $nW/(cm^2\ sr\ cm^{-1})$ in the tropical UTLS (corresponding to heights of up to approximately 21 km). By 30 km the signal is below MIPAS-E noise level making detection impossible at current atmospheric levels. Other regions investigated were the mid-latitudes (30 to 65°S and 30 to 65°N) where the HCFC-22 signal was calculated to be higher than MIPAS-E noise at heights up to 18 km. In the polar summer (65 to 90 degrees, seasonal dependence) it is present at up to 21 km (c.f. tropics) and polar winter (65 to 90 degrees, seasonal dependence) up to 15 km.

Both the 809 cm^{-1} (labelled F22_0092 in Table 4.2) and 829 cm^{-1} (labelled F22_0091 in Table 4.2) regions appear suitable candidates for HCFC-22 microwindows in the UTLS but strong CO_2 and H_2O lines near 809 cm^{-1} could mask the HCFC-22 line. Ozone is also a strong absorber in this region and could mask the Q-branch at stratospheric levels. At 829 cm^{-1}, there are few strong absorbers although CO_2, H_2O and O_3 lines are all in this vicinity. Reducing the range and performing the same radiance contributions calculations as performed earlier in this section but for these two smaller microwindows, Figure 4.14 and Figure 4.15 show that both regions contain a strong HCFC-22 signal but with an

interference from other gases. For the region labelled as F22_0091 CFC-11 emission could also contribute to the signal measured at 829 cm^{-1} although at current levels the signal is below the MIPAS-E NESR level. The HCFC-22 Q-branch in the F22_0092 region is also not masked, with most interfering species below the NESR level. Only ozone and CO_2 lines are present and above the noise level, but the distribution of CO_2 in the atmosphere is well known and also ozone concentrations are retrieved from MIPAS-E in the operational processor in the UTLS and can therefore included in the forward model making this region also suitable for HCFC-22 retrievals. An alternative, not explored in this thesis, would be to jointly retrieve O_3 also.

Although both regions may be suitable for HCFC-22 retrievals, only the 829 cm^{-1} Q-branch region has no interfering gases above the NESR level at 12 and 21 km (Figure 4.14 and Figure 4.15). Reducing the spectral range further (Figure 4.16) shows that at 12 km, only signal directly contributing from HCFC-22 is observed within the 828.95 to 829.15 cm^{-1} range. By 21 km, the HCFC-22 signal in the tropics is still above the NESR level.

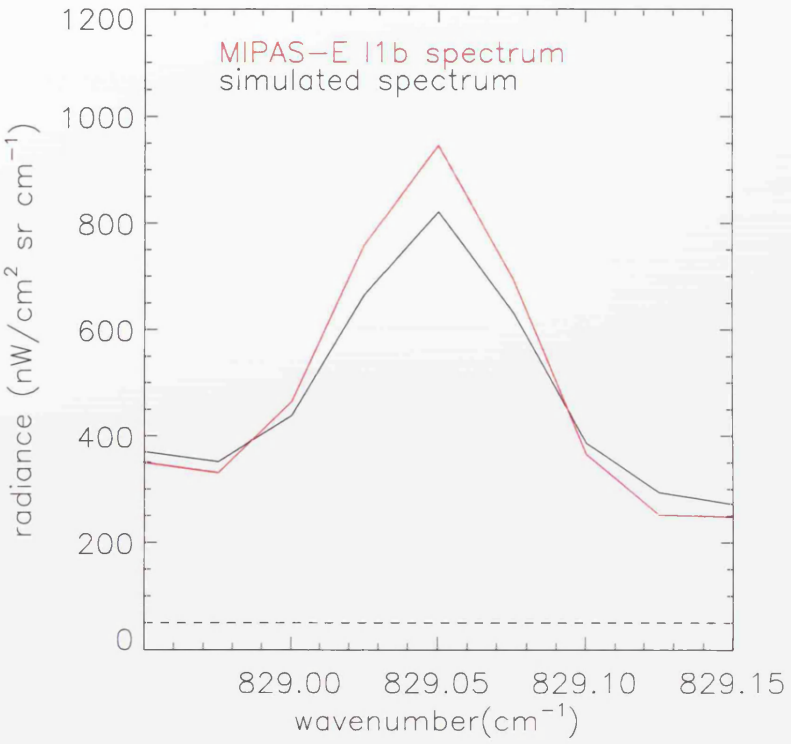

Figure 4.17. Plot of a measured MIPAS-E level 1b spectrum (red) at 11.4 km (1.0°S, 173.7°W) on May 2nd 2003 and a simulated spectrum by the RFM (black) at 12 km based on tropical climatology data [Remedios, 1999]. The black dashed line displays the MIPAS-E noise level.

From comparing a simulated spectrum for the tropics with a measured tropical MIPAS-E spectrum from May 2nd 2003, Figure 4.17, it can be seen that the 829.05 cm^{-1} HCFC-22 Q-branch is observed in this MIPAS-E data. The differences in the absolute radiances at 829.05 cm^{-1} (the HCFC-22 Q-branch feature) are likely due to an underestimation of the atmospheric concentration of HCFC-22 by the climatology; an underestimation of the total particle extinction; or a combination of both factors.

Using RFM simulations it has been possible to simply identify two spectral regions dominated by HCFC-22 emission between 12 and 21 km. Both regions could potentially be used for HCFC-22 retrievals but it has been decided that due to the domination of the 829 cm^{-1} feature in that particular wavenumber range and the fact that all interfering contributors are at or below the MIPAS-E NESR level the 828.95 to 829.15 cm^{-1} range is the one used. The following section investigates whether this feature is observed in one orbit of MIPAS spectral data on July 24th 2002, orbit 2081, by two methods. The following section, uses a correlation method between MIPAS data and simulated data to determine the existence of the feature in MIPAS-E data.

4.1.2.4.1 Correlation tests

The statistical comparison between two or more datasets can be highlighted or disproved by correlation analysis. Here, the similarities or disparities between simulated limb spectra and measured atmospheric limb spectra by the MIPAS are explored by correlation. If HCFC-22 is present in measured atmospheric spectra from MIPAS then it will exhibit the same lineshape as modelled in section 4.1.2.4, varying slightly with altitude due to pressure broadening effects lower in the atmosphere.

The correlation between two variables reflects the degree to which the variables are related. The most common measure of correlation is the Pearson Product Moment Correlation (called Pearson's correlation for short). When in a sample, it is designated by the letter "r" and is sometimes called "Pearson's r." Pearson's correlation reflects the magnitude of linear relationship between two variables and ranges from +1 to −1. A correlation of +1 means that there is a perfect positive linear relationship between variables.

The comparisons have been performed for three levels in the atmosphere: 12, 21 and 30 km. The RFM can simulate the effect a change in concentration of a gas a particular height has on the measured radiance itself. The Jacobian, as this quantity is commonly known as, (section 2.4.1.2), has been calculated for HCFC-22 between 828.950 and 829.150 cm^{-1} for each of the three heights. It is a quantity preferred here in the correlations, as modelling the radiance response to a change in the atmospheric concentration represents best the shape of the HCFC-22 line.

The measured MIPAS-E spectra all are tagged with an altitude; however there are errors in the altitude assignment in the level 1b data processing [von Clarmann *et al.*, 2003] and for this study the spectra used all correspond to the engineering altitude in the level 1b product, closest to the Jacobian height. For this experiment scan height 14, 11 and 8 were chosen which approximately correspond to 12 km, 21 km and 30 km respectively.

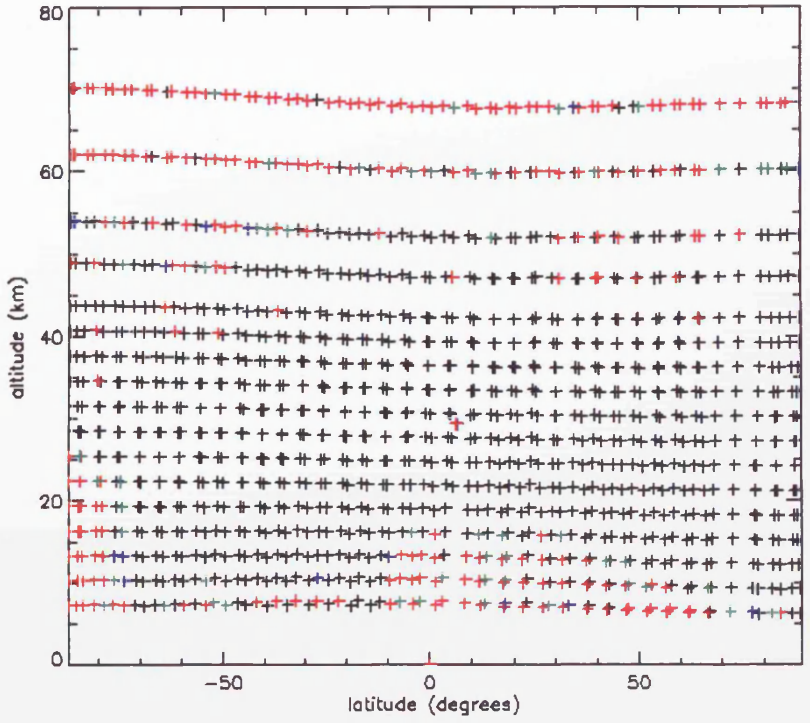

Figure 4.18 A cross-section of MIPAS-E measurement scans for orbit 02081 (July 24th 2002). The red crosses represent cloudy spectra with a CI ≤ 1.8, green represents data with 1.8 < CI ≤ 3 and blue indicates data 3 < CI ≤ 3.5. Black crosses indicate spectra with a CI > 3.5 (cloud-free).

A cloud filtering technique devised by Spang *et al.*, [2002] from CRyogenic Infrared Spectrometers and Telescopes for the Atmosphere (CRISTA) measurements, was employed to remove cloudy data from the correlation analysis. Clouds also contribute

considerable signals to limb spectra and, depending on where the cloud features occur, the extra signals may overlap a chosen microwindow and falsely enhance the signal and hence the estimated concentration of the gas. The microwindow region 828.95 to 829.15 cm^{-1} falls within "band A" of the MIPAS-E measurements. The filter technique introduced by Spang *et al.*, [2002] has three different cloud filters for bands A, B and D of the MIPAS-E. In this work, the cloud A filter has been applied to all MIPAS data before performing the correlation tests. Figure 4.18 shows cloudy and cloud-free data for orbit 02081 from July 24th 2002. Cloudy spectra are identified by either red (cloud index (CI) less than or equal to 1.8), green (CI greater than 1.8 and less than or equal to 3) or blue (CI greater than 3 but less than or equal to 3.5). Cloud-free data (CI > 3.5) are represented by black crosses. The cloud ratio test is only effective at altitudes below 45 km, and "cloudy" data above this height (as shown in Figure 4.18) is due to noise in the MIPAS-E spectral data.

Figure 4.19 shows all of the correlation coefficients between the 12 km HCFC-22 Jacobian and MIPAS spectral data globally for orbit 02081. The correlation coefficients, r, of all the cloud-free spectra (black) were all greater than 0.8. Many of the cloud-contaminated data with a cloud index of less than 1.8, show a low correlation between the HCFC-22 Jacobian and the measured data.

There are several instances in this one orbit where the Q-branch of HCFC-22 was not masked and therefore could still be used to retrieve concentration information. A cloud index between 1.8 and 4 indicates that the measured spectrum probably contains a "thin" cloud with a lower extinction or may also contain high water vapour content. However, from inspection of the correlations from orbit 02081 spectra with a threshold between 1.8 and 3.5 all have a correlation coefficient above 0.8 and so there is still potentially HCFC-22 spectral information in these data.

The same test was conducted on every interfering gas species in the microwindow interval 828.95 to 829.15 cm^{-1}. After HCFC-22, the joint highest correlation coefficients were found to be for H_2O and CFC-11. However, these correlation coefficients were below 0.4 at 12 km, well below a significance value for the small dataset of wavenumber points, giving a high degree of confidence that this wavenumber interval is dominated by HCFC-22 emission in the atmosphere above 12 km.

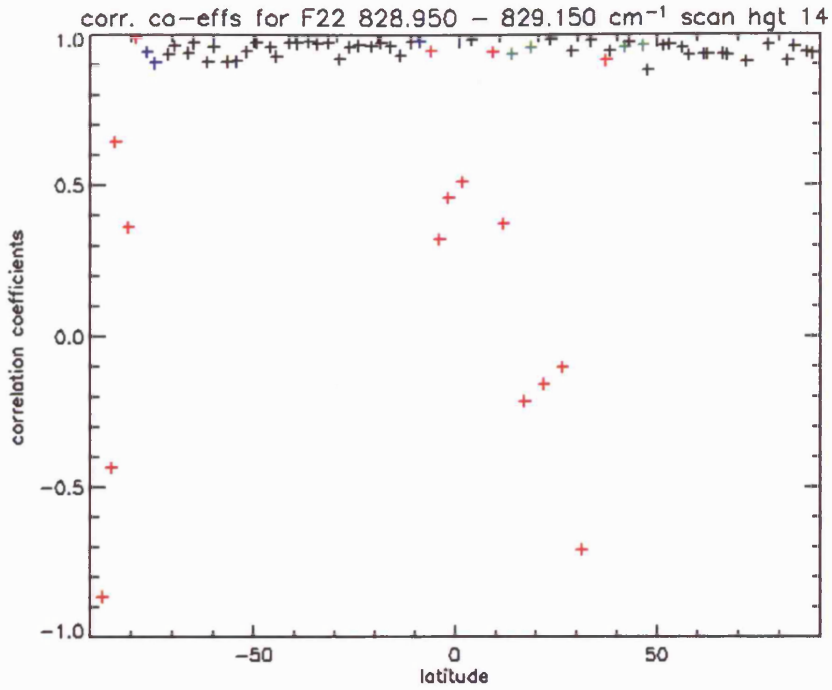

Figure 4.19 Correlation coefficients in the wavenumber range 828.95 to 829.15 cm^{-1} between MIPAS level 1b data, orbit 2081, at index height 14 and the 12 km HCFC-22 weighting function calculated by the RFM. Red crosses represent data with CI $\leq$ 1.8, green crosses indicate data with 1.8 < CI $\leq$ 3, and blue crosses 3 < CI $\leq$ 3.5. The black crosses represent cloud-free data (CI > 3.5).

At 21 km, Figure 4.20 shows a positive correlation in the HCFC-22 relationship in the Northern Hemisphere, with r above 0.4. However, only around a third of the entire data lie above r = 0.7. For some of the cloud-free data in the Southern Hemisphere, the correlation coefficients become very small and some are negative. This may be characteristic of the southern polar vortex as the data were taken from July 2002, a time when the vortex is strongest. Air descends into the vortex from higher altitudes and consequently brings down air with a lower concentration of HCFC-22. The geophysical behaviour with latitude is consistent with the expectation that the feature is due to HCFC-22.

At 30 km, correlation coefficients between the HCFC-22 Jacobian at 30 km and MIPAS spectral data at the same height yielded far more variable coefficients between -0.8 and 0.8 with the majority of coefficients between -0.2 and 0.2. This spread of r is far less desirable as it demonstrates that the MIPAS data is strongly influenced by noise at this height when measuring in this spectral domain and no information can be gleaned for HCFC-22 emissions, based on current atmospheric concentrations of the compound at 30 km.

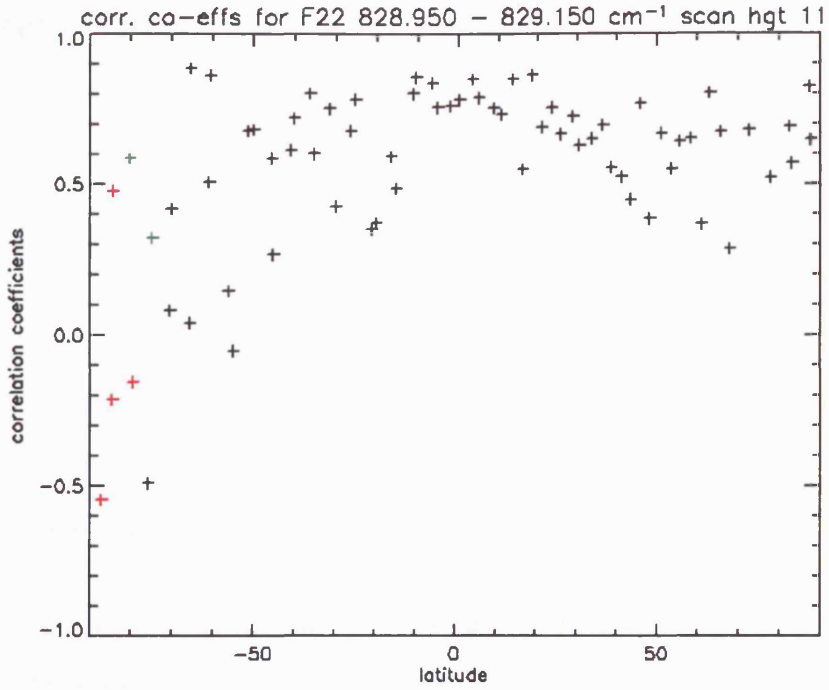

Figure 4.20 Correlation coefficients in the wavenumber range 828.95 to 829.15 cm^{-1} between MIPAS level 1b data, orbit 2081, at index height 11 and the 21 km HCFC-22 weighting function calculated by the RFM. Red crosses represent data with CI $\leq$ 1.8, green crosses indicate data with 1.8 < CI $\leq$ 3, and blue crosses 3 < CI $\leq$ 3.5. The black crosses represent cloud-free data (CI > 3.5).

Summarising, for these three tangent heights, the 12 km correlation coefficients between the MIPAS spectral data at these heights and the corresponding Jacobian calculation are all greater than 0.8 globally. For 21 km there are regions of reasonably high correlation, but also regions where there appears no relationship between the Jacobian and the measured spectra. This shows that the microwindow region 828.950 to 829.150 cm^{-1} can be used as a spectral region on which to perform a retrieval of HCFC-22 certainly at 12 km, and 21 km for scenarios where the HCFC-22 signal is much larger than the pre-flight MIPAS-E noise level. In the next section, a retrieval scheme to perform these tests is identified.

4.2 Retrieval tests

Having detected HCFC-22 in MIPAS-E spectra, the OPERA retrieval scheme could be applied to the MIPAS-E spectra to retrieve HCFC-22 as described in section 2.5.6. To investigate the potential accuracy of HCFC-22 retrievals from MIPAS-E spectra using OPERA, retrieval tests were firstly performed on synthesised spectra computed for representative atmospheric conditions. These results will be shown in this section.

4.2.1 Retrieval set-up

To represent average conditions to use in the retrieval tests it was decided to use reference atmospheres based on the version 3.1 climatology files of Remedios [1999]. For HCFC-22, it was known that the reference HCFC-22 climatology potentially underestimated the tropospheric concentration of HCFC-22 in 2003 (the time period for measurements used in this thesis from MIPAS-E) by up to 20 pptv. It was decided that the climatology still represented the best estimate of the HCFC-22 concentration available, although a 100 % uncertainty on these data were assumed in $\mathbf{S}_a$. HCFC-22 retrievals were performed between 9 and 30 km unless otherwise stated.

CFC-12 has been previously measured in the stratosphere from satellite measurements, such as ATMOS, with a precision of better than 5 %. Therefore, it would be expected that CFC-12 vmr information is retrievable from MIPAS-E data. To test the accuracy of the OPERA scheme and to later test the internal consistency of these data with HCFC-22, CFC-12 retrievals were also performed. In these simulation tests, the variability of the data compared to the climatology was estimated at 25 %. This is higher than the one sigma estimates in the climatology files for CFC-12 in the UTLS where variability is between 10 % in the polar regions and up to 20% in the tropics. However, as these estimates were made based on measurements made 5 years before this thesis the CFC-12 variability it was decided to loosen the *a priori* constraints. CFC-12 retrievals were performed between 9 and 30 km.

For aerosol extinction a very high 1000 % variability was assumed as little information on aerosol extinctions in the UTLS was known. In the presence of thin cirrus in the tropics, extinctions can be as high as 10^{-3} ext/km [Spang *et al.*, 2002], 1000 % times larger than the value in the aerosol "standard" atmosphere (based on HALOE measurements in August 2000 [Spang, personal communication]).

For much of the following analysis and throughout the rest of the thesis four regions were separated consistent with the regions in the reference atmospheres. These were the tropics (30°S to 30°N), mid-latitudes (30 to 65 degrees), polar summer (65 to 90 degrees, season dependent) and polar winter (65 to 90 degrees, season dependent).

The apodized instrument noise of the MIPAS-E was consistently below the 50 nW/(cm^2 sr cm^{-1}) requirement in spectral band A throughout the duration of the mission (up to 2004). Expected noise was introduced into the retrieval scheme via the measurement noise covariance matrix, S_ε and assumed to be 30 nW/(cm^2 sr cm^{-1}) for each spectral point, comparable to the measured NESR level for orbit 2081 between 800 and 950 cm^{-1} [Perron, 2002]. A 30 nW/(cm^2 sr cm^{-1}) random noise was also added to the synthesised spectra so that they accurately represented expected MIPAS-E measurements as closely as possible. Noise was introduced via the random number generator in the graphics program IDL.

4.2.2 Synthesised spectra

Spectra for HCFC-22 and CFC-12 were calculated in the UTLS at a very high spectral resolution of 0.0005 cm^{-1}, between 9 and 30 km (at 3 km intervals, c.f. MIPAS-E). These spectra were based on various atmospheric scenarios based on reported recent trends in the IPCC, and possible future trends depending on future releases of the two compounds. Results shown in section 4.2.2.1 were based upon tropical profile data [30°N to 30°S]. In section 4.2.2.2 results were global and shown for four regions; tropical [30°N to 30°S], mid-latitudes [30 to 65 degrees], and the summer and winter poles [65 to 90 degrees].

According to IPCC report of 2001, levels of CFC-12 in the atmosphere were increasing steadily at a rate of 4.4 pptv/yr in 1998 but by January 2004, concentrations of CFC-12 were almost stable, with only a 0.6 pptv/yr increase calculated from an average of global ground measurements (section 1.2). For HCFC-22, the IPCC report reported a linearly increasing trend of 5 pptv/yr in 1998, a slightly greater year on year increase than CFC-12. By early 2004, atmospheric HCFC-22 levels were still linearly increasing at 5.2 pptv/yr based on averaged surface measurements (section 1.2). The reference atmospheres were consistent with atmospheric conditions for many trace gases in late 1998 and early 1999. More recent updates were added for HCFC-22 and CFC-12 and values in these files were consistent with atmospheric concentrations in the year 2000 for HCFC-22 and CFC-12.

The following experiments all tested the feasibility of HCFC-22 and CFC-12 retrievals from MIPAS-E spectra using OPERA. All tests assumed "current" atmospheric profiles based on the reference atmospheres. It was noted that whereas for CFC-12 this was a good approximation as the tropospheric levels of the compound remained relatively stable until 2005, it may underestimate tropospheric HCFC-22 levels, based on estimates presented by

Rinsland *et al.*, [2005] by up to 20 pptv. Increasing HCFC-22 trends, and the ability of the OPERA scheme to reproduce them were, however, investigated in the sensitivity tests in section 4.2.2.2.

The gases included in the synthesised spectra were:

- HCFC-22 microwindow (828.95-829.15 cm^{-1}): HCFC-22, CFC-11, H_2O, CO_2, O_3, NO_2, HNO_3, $ClONO_2$, NH_3, ClO, OCS, C_2H_6 and aerosol
- CFC-12 microwindow (921.4-924.4 cm^{-1}): CFC-12, H_2O, CO_2, HNO_3, NH_3, CFC-113 and aerosol.
- total extinction microwindow (832.3-834.4 cm^{-1}): H_2O, CO_2, O_3, CFC-113, $ClONO_2$, HNO_3, CFC-11, HCFC-22, C_2H_6, NH_3 and aerosol.

Unless otherwise stated, these were the gases used in each experiment.

The computational expense of calculating limb radiance spectra for each iteration by the RFM was expected to be the limiting factor in the number of retrievals possible. One method of reducing computation costs in the RFM is to reduce the resolution of the fine mesh resolution used in the ILS convolution. The default resolution in the RFM is 0.0005 cm^{-1} and Section 4.2.2.1.1 investigates performing calculations at a coarser resolution noting how the time per iteration alters but also observing if there is a reduction in retrieval accuracy if the fine mesh resolution is reduced.

As a reference, the known climatology was on a height grid (Δz_{clim}) of 1 km for pressure, temperature and each gas contained within the file. The synthesised spectra shown in the following sections are spaced at the nominal MIPAS-E height grid (Δz_{MIPAS}) of 3 km, the equivalent of what MIPAS-E observes. The retrieved state vector (Δz_x) is also at a height spacing of 3 km. The effect of altering Δz_{clim} to 3 km, which is more realistic for MIPAS-E observations is investigated in section 4.2.2.1.2.

Reduction of the number of gases in each microwindow will reduce iteration time. Section 4.2.2.1.3 explores reduction in the number of gases in each window and both the effect on the iteration time but also the effect on the retrieval accuracy.

In the real atmosphere the likely state of the atmosphere is likely to vary from the climatology. Section 4.2.2.2 investigates the ability of the OPERA scheme to retrieve a perturbed atmospheric state. The original reference atmosphere *a priori* is used.

4.2.2.1 Retrievals based on reference atmospheres

It is a trivial problem to retrieve an HCFC-22 or CFC-12 profile from simulated 'measurements' which are calculated from a climatology that is identical to the *a priori* profile used in OPERA. These initial tests were conducted globally (in the four distinct regions described in section 4.2.1) when OPERA was in development and the retrieved profiles were found to be identical to the *a priori* profile. However, this problem becomes non-trivial when random measurement noise is added onto the same simulated measurements. The first aim of this section was to test the OPERA to examine that the scheme was able to reproduce almost identical HCFC-22 and CFC-12 profiles when measurement noise was introduced to simulated spectra. The noise values added to the spectra were generated by using the random number generator in IDL (a number between −1 and 1) and multiplying this by 50 nW/cm^2 sr cm^{-1} (the expected noise of MIPAS-E measurements in band A, section 3.3.3).

Due to the computationally expensive weighting function and radiative transfer calculations in the forward model it is useful to try and reduce computation time of each iterative step. This is crucial where computer resources are limited and the number of retrievals are to be maximised. This section also attempts to find an optimum retrieval set-up which maximises the accuracy of the retrieval but also with a short iteration period. Shorter iteration times can be achieved by either decreasing the spectral resolution of the forward model calculations or the number of atmospheric heights used. Sections 4.2.2.1.1 and 4.2.2.1.2 investigate this and the resultant change in accuracy of the retrieval.

4.2.2.1.1 Adjusting spectral resolution of the forward model calculations

To attempt to represent typical atmospheric spectra accurately at nominal MIPAS-E tangent between 9 and 30 km, synthesised spectra were produced by the RFM at the default fine mesh resolution of 0.0005 cm^{-1} and a height resolution, Δz_{clim}, of 1 km for each region. The section investigates the effect on both the iteration time and change in accuracy of the retrieved state vector by varying the fine mesh resolution used in the retrieval between the default 0.0005 cm^{-1} to 0.001 cm^{-1} and 0.01 cm^{-1}. It was found that results from using a fine mesh resolution in the RFM of 0.0005 cm^{-1} and 0.001 cm^{-1} were

almost identical. Therefore, only results from using a fine mesh resolution of 0.001 cm^{-1} and not 0.0005 cm^{-1} are shown.

4.2.2.1.1.1 HCFC-22 and total extinction

Comparison of the global results for HCFC-22 (Figure 4.21), shows that there was generally good agreement between the OPERA retrieved HCFC-22 and the known profile. Below 21 km, the agreement was better than 15 % in mid-latitude and polar winter data. It was also shown that results were more variable in the tropics and polar summer below 21 km. Differences in the polar summer were up to 20 % whilst at 21 km in the tropics the retrieved vmr was 35 % higher than the known value.

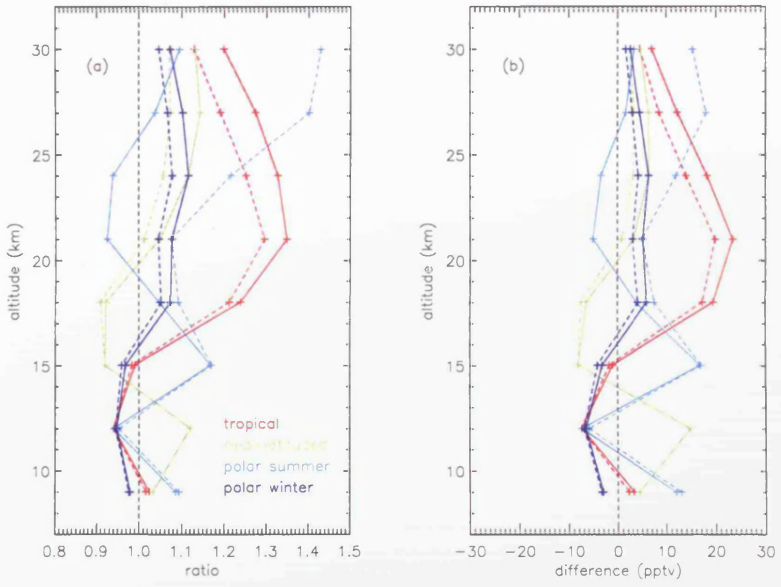

Figure 4.21 Ratio (a) and difference (b) plots of OPERA HCFC-22 retrievals from synthesised spectra and the known state. The experiment tested the effect of altering the fine mesh resolution in the forward modelling of limb spectra. Results from fine mesh resolutions of using 0.01 cm^{-1} (dashed lines) and 0.001 cm^{-1} (solid lines) are shown. Results were from four regions; tropical (30°S to 30°N), mid-latitudes (30 to 65 degrees), polar summer (65 to 90 degrees, season dependent) and polar winter (65 to 90 degrees, season dependent).

There were some systematic differences between the results at the 0.001 cm^{-1} and 0.01 cm^{-1} resolutions. These were most notable above 15 km in all regions. In the polar summer data in particular, the differences were highest at between 5 % at 18 km and 40 % at 30 km. In the other three regions the retrievals at 0.01 cm^{-1} resolution were lower than at 0.001 cm^{-1} by between 5 and 10 %.

A comparison of the time taken to compute one iterative step showed a large discrepancy between the three different scenarios (Table 4.4). Although more gases were included in the RFM for HCFC-22 than for the CFC-12 run, the smaller HCFC-22 microwindow meant that one iteration took between 25 and 150 seconds less for HCFC-22. The iteration time for the highest resolution (0.0005 cm^{-1}) retrievals were almost ten times greater than at the coarsest (0.01 cm^{-1}) resolution.

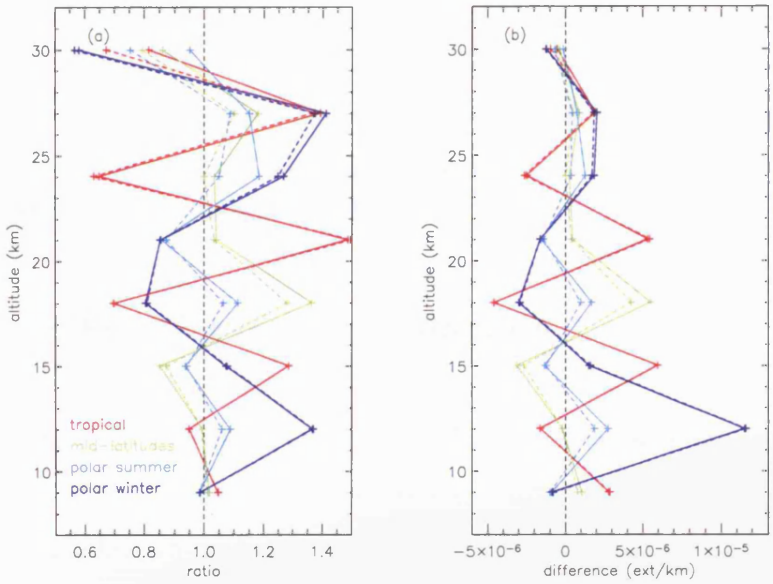

Figure 4.22 Ratio (a) and difference (b) plots of total extinction retrievals from synthesised spectra and the known state. The experiment tested the effect of altering the fine mesh resolution in the forward modelling of limb spectra. These data were from the joint retrieval with HCFC-22 shown in Figure 4.23. Results from fine mesh resolutions using 0.01 cm^{-1} (dashed lines) and 0.001 cm^{-1} (solid lines) were used. Results were from four regions; tropical (30°S to 30°N), mid-latitudes (30 to 65 degrees), polar summer (65 to 90 degrees, season dependent) and polar winter (65 to 90 degrees, season dependent).

TIME PER ITERATION (SECONDS)		
0.0005 cm^{-1} resolution (default)	0.001 cm^{-1} resolution	0.01 cm^{-1} resolution
1072	577	137

Table 4.4 A comparison of the time taken for one iteration of the OPERA retrieval scheme using three different resolutions of the fine mesh calculation. These estimations are only valid for CFC-12 retrievals using the 921.4 to 924.4 cm^{-1} spectral range and the aerosol microwindow (832.3 to 834.4 cm^{-1}).

It was also found that the number of iterations taken for OPERA to converge was independent of fine mesh resolution for all regions. The total time taken for convergence ranged between 2805 and 3740 seconds (47 minutes to 62 minutes) difference between the finest and coarsest resolutions. Considering this difference in time taken and also the lack

of any noticeable accuracy improvement between resolutions, to maximise the number of MIPAS-E retrievals the 0.01 cm^{-1} resolution should be used in the RFM.

REGION	ITERATIONS REQUIRED FOR CONVERGENCE		
	0.0005 cm^{-1} resolution (default)	0.001 cm^{-1} resolution	0.01 cm^{-1} resolution
TROPICAL	3	3	3
MID-LATITUDES	4	4	4
POLAR SUMMER	4	4	4
POLAR WINTER	4	4	4

Table 4.5 A comparison of the number of iterations required for the OPERA scheme to converge when using three different resolutions of the fine mesh calculation.

4.2.2.1.1.2 CFC-12 and total extinction

From comparing the retrieved state vector results for this experiment (Figure 4.23) with the known profile, it was discovered that at 24 km and below the retrieved CFC-12 data were in agreement with the known profile to within 3 %. This was independent of the resolution used in the fine mesh calculation within the RFM. Above 24 km there was more variability with the data, particularly within the polar summer data (Figure 4.23a) with an overestimate of up to 25 %. In absolute terms the difference was up to 12 pptv. Above 24 km in the tropics and mid-latitudes the retrieved result was high biased by up to 7 % using the coarsest 0.01 cm^{-1} resolution.

The jointly retrieved aerosol data displayed much higher variability when compared to the known profile than the CFC-12 data did, but this was expected as the *a priori* covariance was forty times higher for the aerosol data. The best agreement was in the polar summer at less than 2 % at every height in the 0.0005 and 0.001 cm^{-1} fine mesh resolutions. Even results at the coarse resolution were in agreement to better than 17 %.

A comparison of the time taken to compute one iterative step shows large discrepancy between the three different scenarios (Table 4.6). The iteration time for the retrievals performed using a resolution of 0.0005 cm^{-1} was over ten times greater than the time for a 0.01 cm^{-1} iteration. Although the number of iterations for convergence was generally higher for the coarsest resolution, the total time taken at the 0.01 cm^{-1} resolution was lower than at 0.0005 cm^{-1} by between 1600 and 630 seconds.

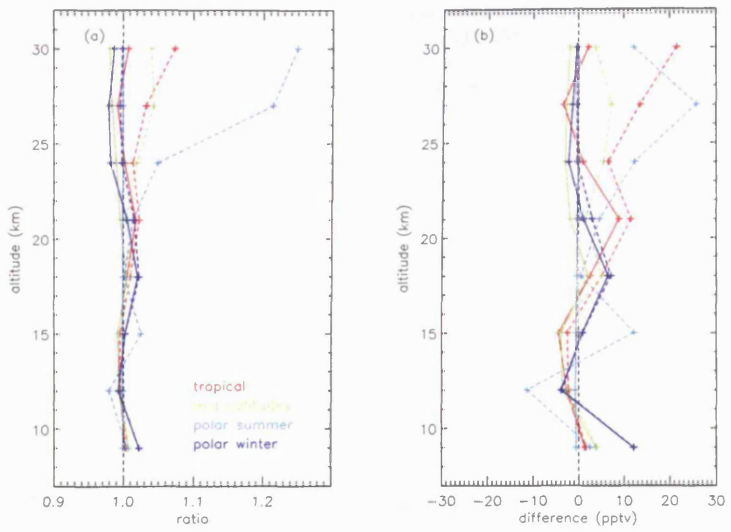

Figure 4.23 Ratio (a) and difference (b) plots OPERA CFC-12 retrievals from synthesised spectra with the known state. This experiment tested the effect of altering the fine mesh resolution in the forward modelling of limb spectra. Results from retrievals performed using a fine mesh resolution in the RFM of 0.01 cm^{-1} (dashed lines) and 0.001 cm^{-1} (solid lines). The results were from four regions; tropical (30°S to 30°N), mid-latitudes (30 to 65 degrees), polar summer (65 to 90 degrees, season dependent) and polar winter (65 to 90 degrees, season dependent).

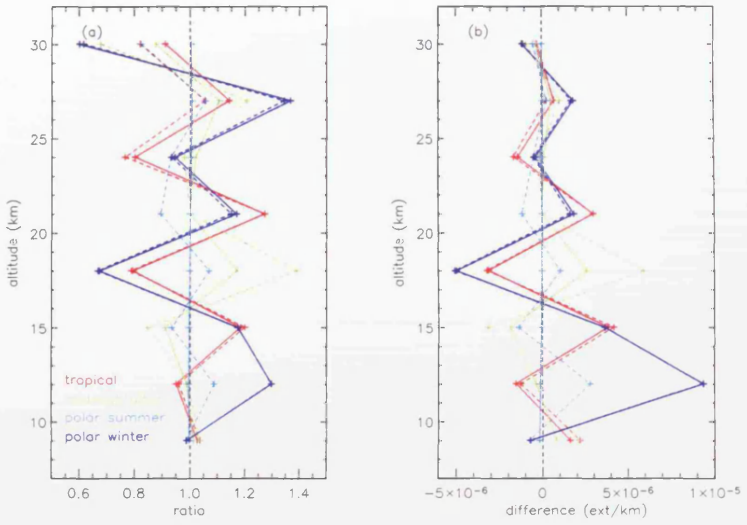

Figure 4.24 Ratio (a) and difference (b) plots of OPERA extinction retrievals from synthesised spectra and the known state. The experiment tested the effect of altering the fine mesh resolution in the forward modelling of limb spectra. These data were from the joint retrieval with CFC-12 shown in Figure 4.23. Results from retrievals performed using a fine mesh resolution in the RFM of 0.01 cm^{-1} (dashed lines) and 0.001 cm^{-1} (solid lines). The results were from four regions; tropical (30°S to 30°N), mid-latitudes (30 to 65 degrees), polar summer (65 to 90 degrees, season dependent) and polar winter (65 to 90 degrees, season dependent).

TIME PER ITERATION (SECONDS)		
0.0005 cm^{-1} resolution (default)	0.001 cm^{-1} resolution	0.01 cm^{-1} resolution
1122	590	110

Table 4.6 A comparison of the time taken for one iteration of the OPERA retrieval scheme using three different resolutions for the fine mesh calculation in the RFM. These estimations are only valid for CFC-12 retrievals using the 921.4 to 924.4 cm^{-1} spectral range and the aerosol 832.3 to 834.4 cm^{-1} regions.

As the results between the 0.0005 and 0.001 cm^{-1} fine mesh resolution were generally equal to the nearest whole number OPERA retrievals converged within the same number of iterations for both cases. The difference in the total time taken for convergence ranged between approximately 1050 seconds in the tropics and mid-latitudes to over 3000 seconds in the polar summer. Although the results at a fine mesh resolution of 0.001 cm^{-1} were slightly more accurate the time saved by using a coarser resolution were considerable and the differences between CFC-12 results were less than 5 % below 24 km.

REGION	ITERATIONS REQUIRED FOR CONVERGENCE		
	0.0005 cm^{-1} resolution (default)	0.001 cm^{-1} resolution	0.01 cm^{-1} resolution
TROPICAL	2	2	6
MID-LATITUDES	2	2	4
POLAR SUMMER	6	6	4
POLAR WINTER	4	4	4

Table 4.7 A comparison of the number of iterations required for the OPERA scheme to converge when using three different resolutions.

4.2.2.1.2 Adjusting the height grid of the forward model calculations

Iteration time can also be reduced by defining fewer heights at which the radiative transfer is calculated, by adjusting Δz_{clim}. This section investigates loss of accuracy and/or shape in the retrieval by reducing to a 3 km height grid and using a fine mesh resolution of both 0.001 and 0.01 cm^{-1}. It was shown in the previous section that there was no advantage for the HCFC-22 OPERA retrievals by using a fine 0.001 cm^{-1} fine mesh resolution compared to 0.01 cm^{-1}. It was still decided, however, for the purposes of synthesised retrievals to

compare results at these two resolutions as for other scenarios there may be an effect on the state vector of different resolution.

4.2.2.1.2.1 HCFC-22 and total extinction data

It will be shown in section 4.2.3 that OPERA is expected to only gain information for HCFC-22 from the MIPAS-E measurements at up to four levels, only in very favourable conditions. The mean number of levels with information was three. It was decided therefore to reduce the retrieval range. To accommodate for possible errors at the uppermost retrieval height due to discontinuities between the state vector and the climatology in the RFM, it was decided to retrieve from five levels between 9 and 21 km. This reduction to modelling MIPAS-E spectra at only five altitudes instead of the previous eight would be expected to also reduce iteration time. This section analyses this and also effects on retrieval accuracy.

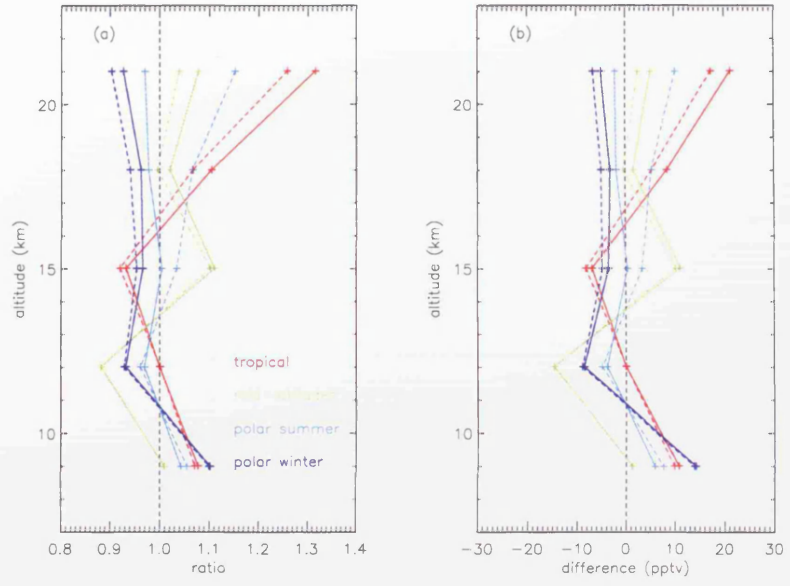

Figure 4.25 Ratio (a) and difference (b) plots of OPERA HCFC-22 retrievals from synthesised spectra and the known state. The experiment tested the effect of altering the height grid of Δz_{clim} in the forward modelling of limb spectra. Results from using a fine mesh resolution of 0.01 cm^{-1} (dashed lines) or 0.001 cm^{-1} (solid lines). The results were from four regions; tropical (30°S to 30°N), mid-latitudes (30 to 65 degrees), polar summer (65 to 90 degrees, season dependent) and polar winter (65 to 90 degrees, season dependent).

At the reduced altitude range, the tropical data were shown to exhibit (Figure 4.25a) similar characteristic to the full 9 to 30 km data in section 4.2.2.1.1.1. Data between 9 and 15 km were in agreement to the known data by better than 10 %. At 18 and 21 km, the

OPERA data were between 10 and 35 % higher but the values were comparable as for the 9 to 30 km data.

The mid-latitude results show better than 15 % agreement with the known data (Figure 4.25a). The ratio of the 9-21 km mid-latitude data was anti-correlated with the mid-latitude results in section 4.2.2.1.1.1. It was shown that individual mid-latitude MIPAS-E retrievals will probably oscillate.

Both poles show very good agreement between the retrieved and known states between 9 and 21 km. The differences were less than 10 %. In the polar summer (Figure 4.25a) it was noted that the agreement over the reduced height range was better than was shown between 9 and 30 km. The retrieved polar winter data were lower than the known state between 12 and 21 km. At 9 km, however, the retrieved result was 10 % higher than the known value. As a consequence, it may be seen in later data that the 9 km polar winter retrievals may be higher in the mean by up to 20 pptv.

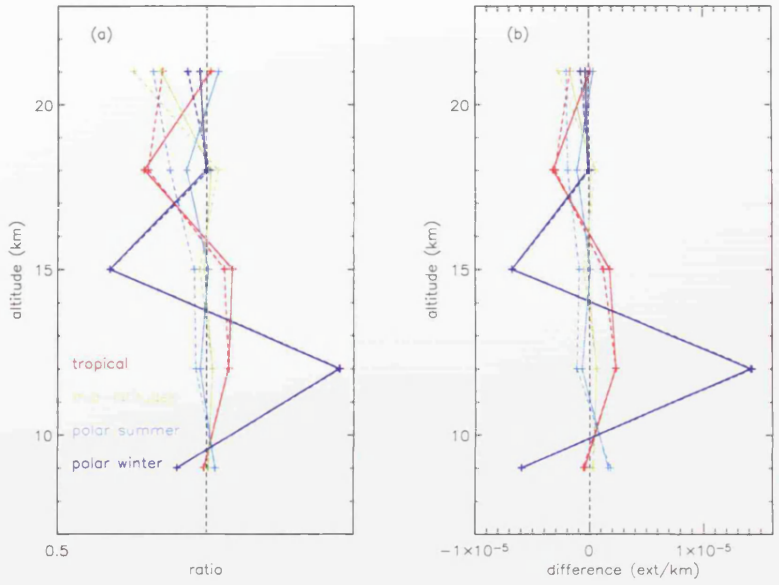

Figure 4.26 Ratio (a) and difference (b) plots of OPERA total extinction retrievals from synthesised spectra and the known state. The experiment tested the effect of altering the height grid of Δz_{clim} in the forward modelling of limb spectra. These data were from the joint retrieval with HCFC-22 shown in Figure 4.25. Results from using fine mesh resolution of 0.01 cm^{-1} (dashed lines) or 0.001 cm^{-1} (solid lines). The results were from four regions; tropical (30°S to 30°N), mid-latitudes (30 to 65 degrees), polar summer (65 to 90 degrees, season dependent) and polar winter (65 to 90 degrees, season dependent).

The retrieved total extinction data for each region, apart from the polar winter, showed agreement with the known data by better than 25 %. The polar winter data oscillated wildly

between 9 and 15 km with differences to the known of up to 45 %. Although these results show that "realistic" extinction can be measured from MIPAS-E, the polar winter data should perhaps be treated with more caution. The data should perhaps be used to look at extreme events rather than to produce an extinction "mean" profile. The potential to do this from other regions was shown to be more promising here.

4.2.2.1.2.2 CFC-12 and total extinction

The OPERA CFC-12 results were globally less than 3 % different to the "known" profile for both the 0.001 cm^{-1} and the 0.01 cm^{-1} resolution results between 9 and 24 km. The tropical results did show, however, that the 18 km retrieved data may be up to 7 % too high. Sharp gradients of temperature occur at the tropical tropopause (18 km in the CFC-12 reference atmosphere). Radiance is a function of both temperature and concentration and the coarse 3 km height resolution was insufficient in the simulations to model the "real" atmosphere at 18 km based on the tropical climatology.

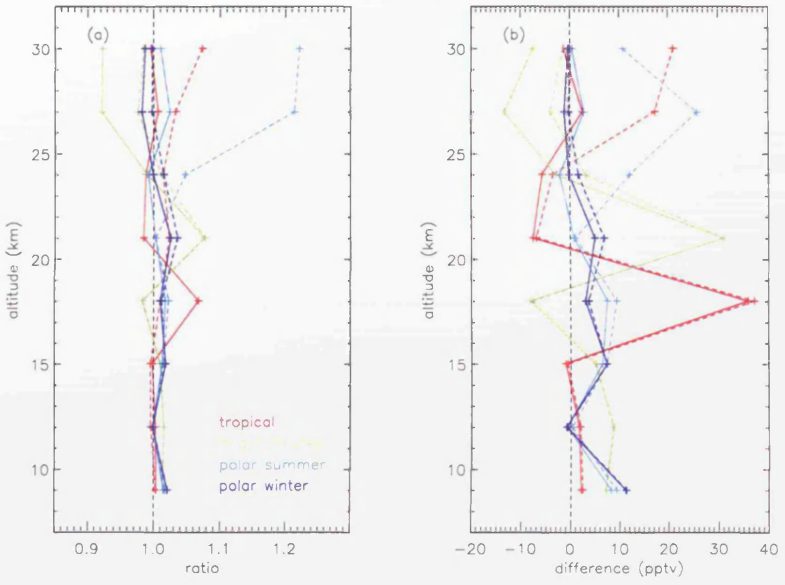

Figure 4.27. Ratio (a) and difference (b) plots of OPERA CFC-12 retrievals from synthesised spectra and the known state. The experiment tested the effect of altering the height grid of Δz_{clim} in the forward modelling of limb spectra. Results from using fine mesh resolutions in the RFM of 0.01 cm^{-1} (dashed lines) or 0.001 cm^{-1} (solid lines). The results were from four regions; tropical (30°S to 30°N), mid-latitudes (30 to 65 degrees), polar summer (65 to 90 degrees, season dependent) and polar winter (65 to 90 degrees, season dependent).

It was found in the aerosol results that the best agreement between the retrieved and known aerosol profiles was in the tropics, mid-latitudes and polar summer between 9 and 21 km, at better than 20 %. Results from the polar winter, however, were no better than 40 % at both 12 and 15 km. Although the reason for the poorer polar winter extinction result was unclear, it was shown that the polar winter CFC-12 (Figure 4.27a) was not affected as this data showed some of the best agreement with the expected data.

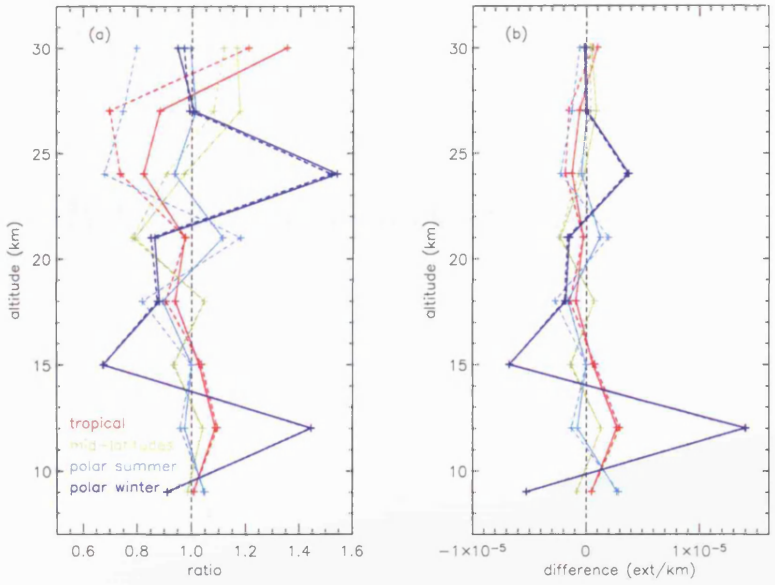

Figure 4.28. Ratio (a) and difference (b) plots of total extinction retrievals from synthesised spectra and the known state. The experiment tested the effect of altering the height grid of Δz_{clim} in the forward modelling of limb spectra. These data were from the joint retrieval with CFC-12 shown in Figure 4.28. Retrievals were performed using a fine mesh resolution in the RFM of 0.01 cm^{-1} (dashed lines) or 0.001 cm^{-1} (solid lines). The results were from four regions; tropical (30°S to 30°N), mid-latitudes (30 to 65 degrees), polar summer (65 to 90 degrees, season dependent) and polar winter (65 to 90 degrees, season dependent).

4.2.2.1.3 Reducing the number of gases in the target gas and total extinction microwindows

The synthesised spectra used for the previous experiments in this chapter have all used spectra calculated using all known emitters in each microwindow. This section investigates whether retrievals from the same synthesised spectra but reducing the number of gases in OPERA has a strong influence on the accuracy of the results. If the gas contributed less than 5 % to the total signal it was removed.

In this section, the gases included in OPERA are:

- HCFC-22: HCFC-22, CO_2, H_2O, O_3, CFC-11, C_2H_6, HNO_3, $ClONO_2$ and aerosol (reduced from thirteen to nine, now excluding NH_3, ClO, OCS and NO_2)
- CFC-12: CFC-12, H_2O, CO_2, O_3, HNO_3 and aerosol (reduced from seven to six, now excluding NH_3)
- Aerosol/extinction: H_2O, CO_2, O_3, HNO_3, C_2H_6, CFC-11, HCFC-22, $ClONO_2$ and aerosol (reduced from eleven to nine, excluding NH_3 and CFC-113)

All other parameters were as in 4.2.2.1.2.

4.2.2.1.3.1 HCFC-22 and total extinction

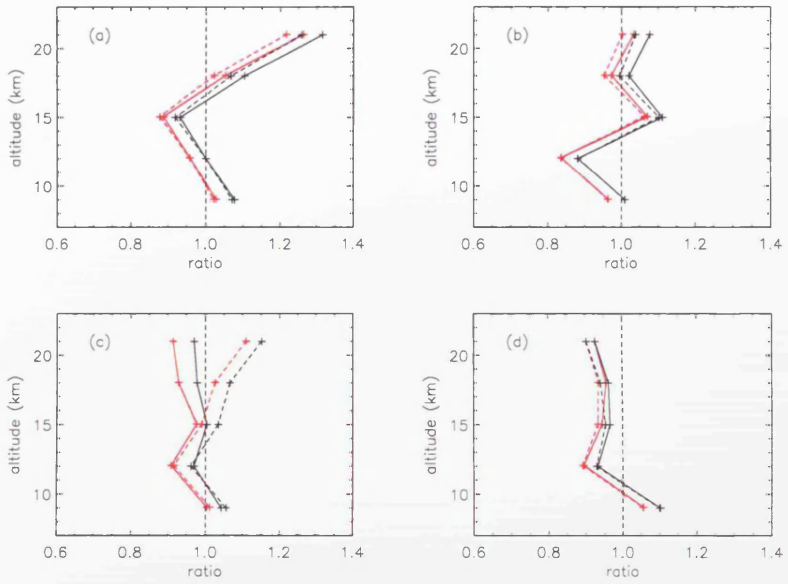

Figure 4.29 Ratio plot of OPERA HCFC-22 retrievals from synthesised spectra and the known state. For this experiment OPERA used a reduced number of gases in the RFM for each iteration, removing the negligible emitters. Retrievals were performed using a fine mesh resolution in the RFM of 0.01 cm^{-1} (red dashed lines) or 0.001 cm^{-1} (red solid lines) The results were from four regions; (a) 30°S to 30°N, (b) 30 to 65 degrees, (c) 65 to 90 degrees; in polar summer and (d) 65 to 90 degrees; in polar winter. Results from using a reduced height grid, but with all emitters included (Figure 4.25), are shown for comparison - fine mesh resolution 0.01 cm^{-1} (black dashed lines) and 0.001 cm^{-1} (black solid lines).

The effect of reducing the number of gases in both the HCFC-22 and aerosol microwindows was shown to have a minimal effect on the retrieved HCFC-22. The difference between the results in section 4.2.2.1.2.1 and the same criteria but reducing the number of gases presented in this section, were mainly less than 5 %. These results show

that the number of gases in the HCFC-22 retrieval can be reduced without a strong effect on the accuracy of the HCFC-12 result. The iteration time is also reduced further.

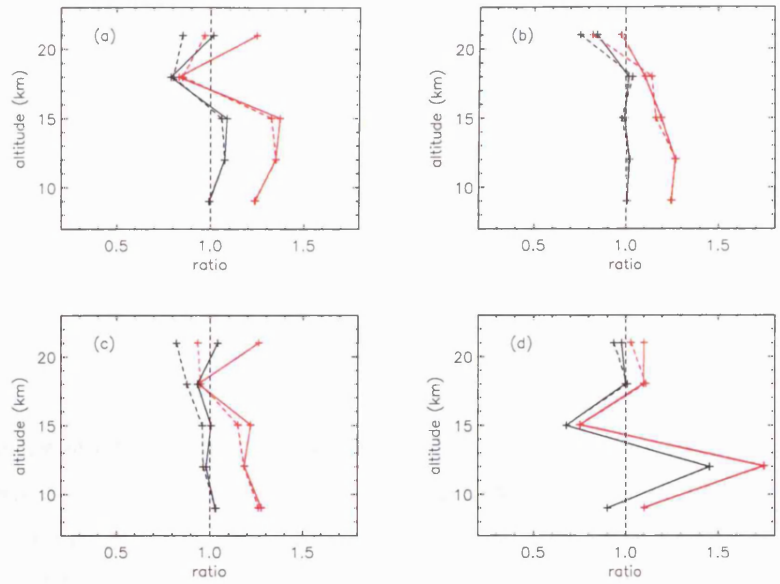

Figure 4.30 Ratio plot of OPERA retrieved total extinctions from synthesised spectra and the known state. For this experiment OPERA used a reduced number of gases in the RFM for each iteration, removing the negligible emitters. This data were retrieved with the HCFC-22 data in Figure 4.29. Retrievals were performed using a fine mesh resolution in the RFM of 0.01 cm^{-1} (red dashed lines) or 0.001 cm^{-1} (red solid lines) The results were from four regions; (a) (30°S to 30°N), (b) 30 to 65 degrees, (c) 65 to 90 degrees; in polar summer and (d) 65 to 90 degrees; in polar winter. The results from using a reduced height grid, but with all emitters included (Figure 4.26), are shown for comparison - fine mesh resolution of 0.01 cm^{-1} (black dashed lines) and 0.001 cm^{-1} (black solid lines)..

4.2.2.1.3.2 CFC-12 and total extinction

It was shown that the effect of reducing the number of gases in both the CFC-12 and aerosol microwindows was minimal on the CFC-12 data. The difference between the results in section 4.2.2.1.2.2 and the same criteria but reducing the number of gases, was less than 3 %. This gives confidence that the number of gases in the CFC-12 retrieval can be reduced without a major effect on the accuracy of the CFC-12 result.

For the total extinction data, there was more variability between results in section 4.2.2.1.2.2 and those presented here. In particular, for all regions, the 9 to 15 km extinctions were up to 20 % higher than those measured in 4.2.2.1.2.2. Above 21 km, the differences were less than 15 %.

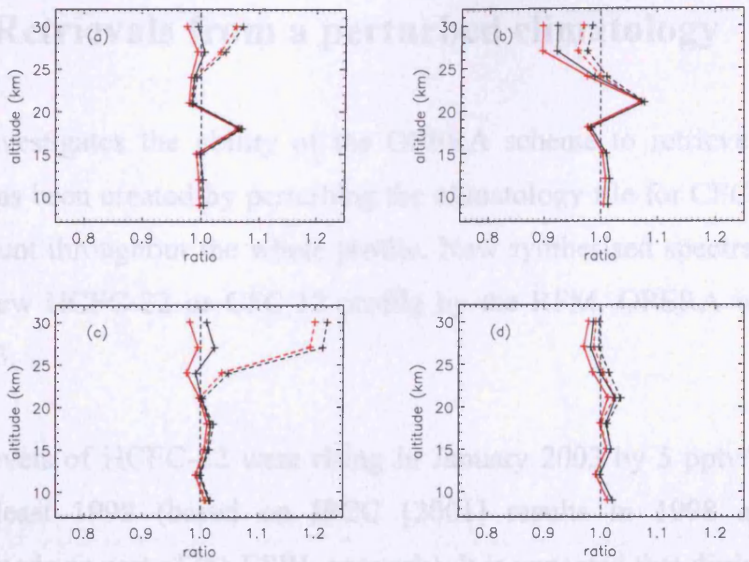

Figure 4.31 Ratio plot of OPERA CFC-12 retrievals from synthesised spectra and the known state. For this experiment OPERA used a reduced number of gases in the RFM for each iteration, removing the negligible emitters. Retrievals were performed using a fine mesh resolution in the RFM of 0.01 cm^{-1} (red dashed lines) or 0.001 cm^{-1} (red solid lines) The results were from four regions; (a) 30°S to 30°N, (b) 30 to 65 degrees, (c) 65 to 90 degrees; in polar summer and (d) 65 to 90 degrees in polar winter. The results from using a reduced height grid, but with all emitters included (Figure 4.26), are shown for comparison - fine mesh resolution of 0.01 cm^{-1} (black dashed lines) and 0.001 cm^{-1} (black solid lines).

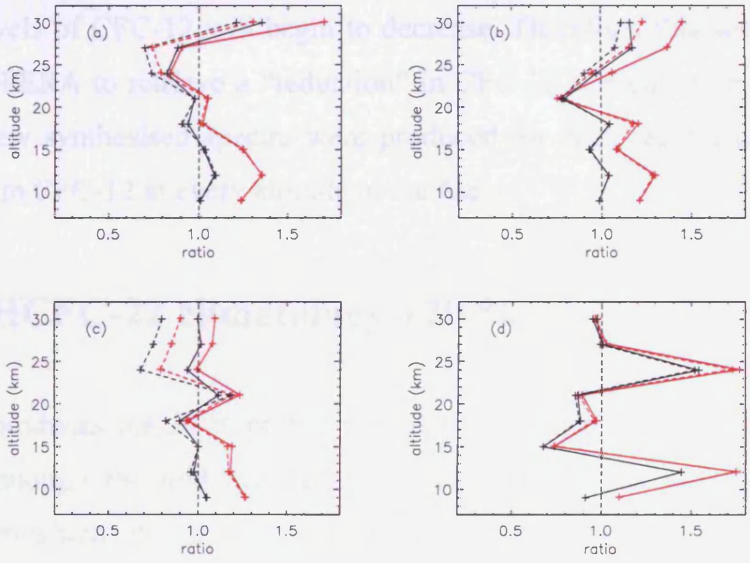

Figure 4.32. Ratio plot of OPERA total extinction retrievals from synthesised spectra and the known state. For this experiment OPERA used a reduced number of gases in the RFM for each iteration, removing the negligible emitters. Retrievals were performed using a fine mesh resolution in the RFM of 0.01 cm^{-1} (red dashed lines) or 0.001 cm^{-1} (red solid lines) The results were from four regions; (a) 30°S to 30°N, (b) 30 to 65 degrees, (c) 65 to 90 degrees; in polar summer and (d) 65 to 90 degrees in polar winter. The results from using a reduced height grid, but with all emitters included (Figure 4.26), are shown for comparison - fine mesh resolution of 0.01 cm^{-1} (black dashed lines) and 0.001 cm^{-1} (black solid lines)

4.2.2.2 Retrievals from a perturbed climatology

This section investigates the ability of the OPERA scheme to retrieve an atmospheric profile which has been created by perturbing the climatology file for CFC-12 or HCFC-22 by a fixed amount throughout the whole profile. New synthesised spectra were produced, based on the new HCFC-22 or CFC-12 profile by the RFM. OPERA was set-up as for section 4.2.2.1.3.

Tropospheric levels of HCFC-22 were rising in January 2003 by 5 pptv/yr and had done this since at least 1998 (based on IPCC [2001] results in 1998 and tropospheric measurements made as part of the ESRL network). It is expected that during the lifetime of the MIPAS-E mission that the atmospheric concentration of HCFC-22 would continue to rise. Therefore synthesised spectra were produced to investigate the accuracy of OPERA HCFC-22 compared to an atmospheric change in the gas.

For CFC-12, recent ground measurements made by the ESRL ground network [Montkza, 1993] showed that tropospheric levels of the compound were growing by only 0.6 pptv/yr in January 2003. During the lifetime of the MIPAS-E measurements it is expected that tropospheric levels of CFC-12 will begin to decrease. Therefore, this section investigates the ability of OPERA to retrieve a "reduction" in CFC-12 concentration compared to the climatology. New synthesised spectra were produced for each region, calculated from a 10 % reduction in CFC-12 at every altitude in the file.

4.2.2.2.1 HCFC-22 climatology +20 %

The scheme reproduces the 20 % profile perturbation particularly well in the tropics and polar winter although the mid-latitude and polar summer data also show some good agreement. Throughout the tropical and polar winter data, OPERA reproduced the perturbation to better than 15 % throughout between 9 and 21 km. Mid-latitude data were also within 15 % throughout the same range, but the profile oscillated somewhat.

These results show that in most cases OPERA could effectively measure a 20 % HCFC-22 perturbation, and produce results to better than 15 % in most instances, and in many cases better than 5 %.

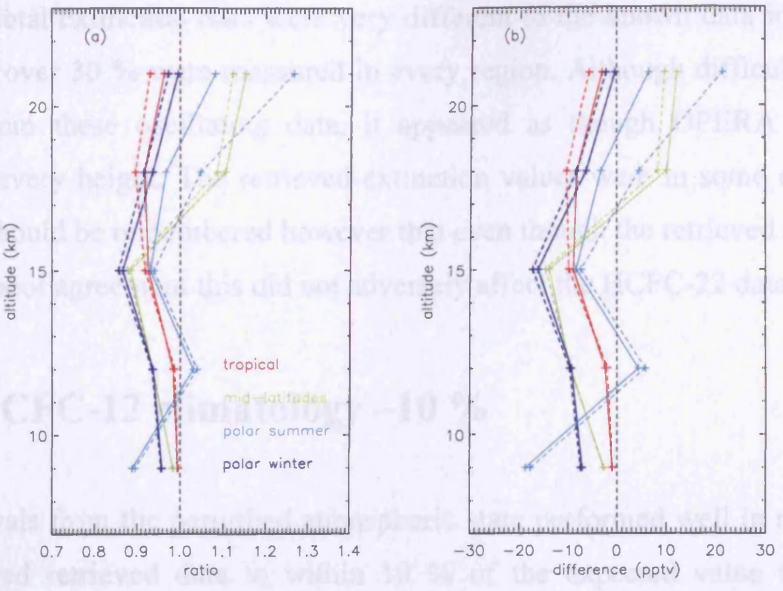

Figure 4.33. Ratio (a) and difference (b) plots of OPERA HCFC-22 data from synthesised spectra with the known state. The experiment investigated the accuracy of OPERA data to an increase of 20 % in HCFC-22. Retrievals were performed using a fine mesh resolution of 0.01 cm^{-1} (dashed lines) or 0.001 cm^{-1} (solid lines) The results are from four regions; tropical (30°S to 30°N), mid-latitudes (30 to 65 degrees), polar summer (65 to 90 degrees, season dependent) and polar winter (65 to 90 degrees, season dependent).

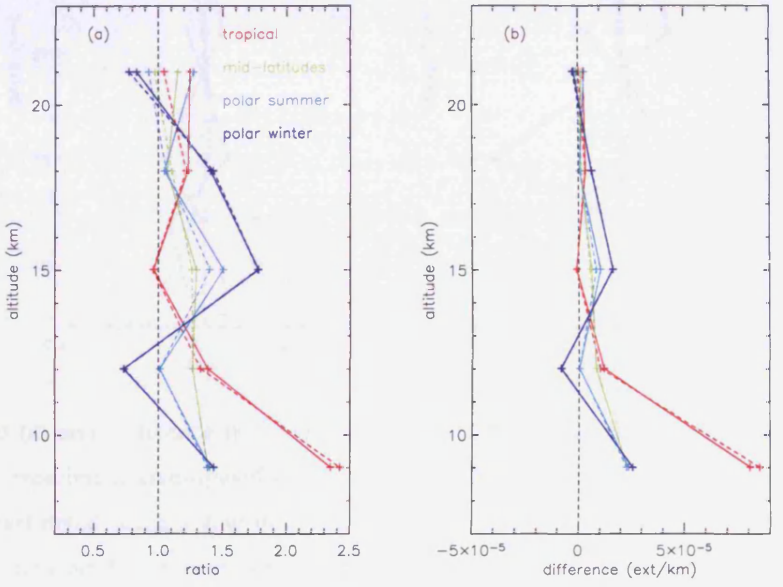

Figure 4.34. Ratio (a) and difference (b) plots of OPERA total extinction data from synthesised spectra with the known state. The experiment investigated the accuracy of OPERA data to an increase of 20 % in HCFC-22. Retrievals were performed using a fine mesh resolution of 0.01 cm^{-1} (dashed lines) or 0.001 cm^{-1} (solid lines). The results are from four regions; (a) tropical (30°S to 30°N), (b) mid-latitudes (30 to 65 degrees), (c) polar summer (65 to 90 degrees, season dependent) and (d) polar winter (65 to 90 degrees, season dependent).

The retrieved total extinction data were very different to the known data in every region. Differences of over 30 % were measured in every region. Although difficult to draw firm conclusions from these oscillating data, it appeared as though OPERA overestimated extinction for every height. The retrieved extinction values were in some cases no better than 50 %. It should be remembered however that even though the retrieved extinction data showed some poor agreement this did not adversely affect the HCFC-22 data.

4.2.2.2.2 CFC-12 climatology –10 %

CFC-12 retrievals from the perturbed atmospheric state performed well in most instances. All data showed retrieved data to within 10 % of the expected value throughout the profiles.

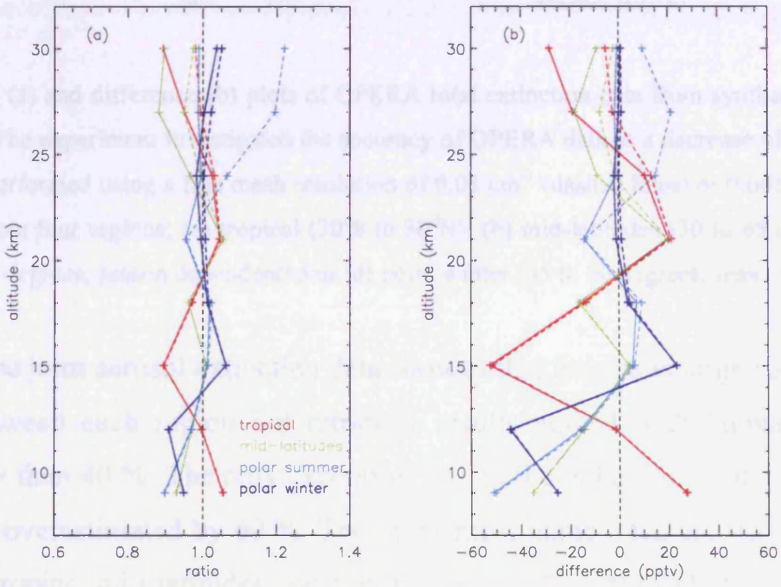

Figure 4.35. Ratio (a) and difference (b) plots of OPERA CFC-12 data from synthesised spectra with the known state. The experiment investigated the accuracy of OPERA data to a decrease of 10 % in CFC-12. Retrievals were performed using a fine mesh resolution of 0.01 cm^{-1} (dashed lines) or 0.001 cm^{-1} (solid lines). The results are from four regions; (a) tropical (30°S to 30°N), (b) mid-latitudes (30 to 65 degrees), (c) polar summer (65 to 90 degrees, season dependent) and (d) polar winter (65 to 90 degrees, season dependent).

Potential biases in the 9 km data were highlighted. The mid-latitude and polar data overestimated the known CFC-12 perturbation, resulting in retrieved CFC-12 data at 9 km lower than the known value by up to 10 %. The results at this level are commented on

because the MIPAS-E results at this height could provide trend information for CFC-12 in the troposphere.

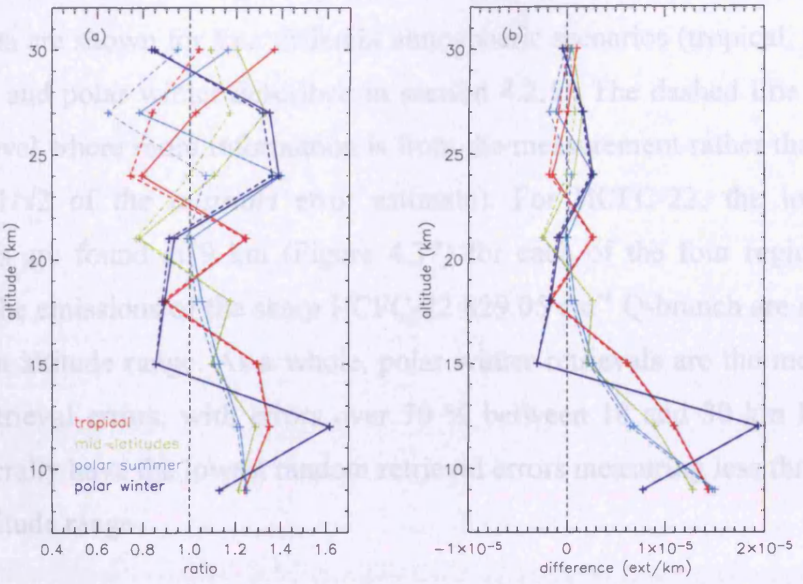

Figure 4.36 Ratio (a) and difference (b) plots of OPERA total extinction data from synthesised spectra with the known state. The experiment investigated the accuracy of OPERA data to a decrease of 10 % in CFC-12. Retrievals were performed using a fine mesh resolution of 0.01 cm^{-1} (dashed lines) or 0.001 cm^{-1} (solid lines) The results are from four regions; (a) tropical (30°S to 30°N), (b) mid-latitudes (30 to 65 degrees), (c) polar summer (65 to 90 degrees, season dependent) and (d) polar winter (65 to 90 degrees, season dependent).

Results from the joint aerosol extinction data showed that there was large variability within the results between each region but retrieved results agreed with known extinction to generally better than 40 %. The only exception was in the polar winter at 12 km where the extinction was overestimated by 60 %. The other most notable feature was between 9 and 15 km in the tropics, mid-latitudes and summer pole. The retrieved extinction data were always high compared to the known value, by up to 35 %.

4.2.3 Retrieved random errors

Retrieved random errors are calculated by the equation:

$$\mathbf{S}_x = \left(\mathbf{S}_a^{-1} + \mathbf{K}^T\mathbf{S}_y^{-1}\mathbf{K}\right)^{-1} \tag{4.1}$$

where $\mathbf{S}_x$ is the retrieval error covariance, $\mathbf{S}_a$ is the *a priori* covariance matrix, $\mathbf{S}_y$ is the measurement covariance matrix and $\mathbf{K}$ is the weighting function matrix. Figure 4.37 shows the square root of the diagonal elements of the retrieval error covariance matrix for HCFC-22. Data are shown for four different atmospheric scenarios (tropical, mid-latitudes, polar summer and polar winter described in section 4.2.1). The dashed line on the figure represents a level where more information is from the measurement rather than the a priori information ($1/\sqrt{2}$ of the *a priori* error estimate). For HCFC-22, the lowest random retrieval errors are found at 9 km (Figure 4.37) for each of the four regions (less than 25 %) where the emissions of the sharp HCFC-22 829.05 cm^{-1} Q-branch are strongest over the 9 to 30 km altitude range. As a whole, polar winter retrievals are the most dominated by random retrieval errors, with errors over 70 % between 18 and 30 km Polar summer retrievals generally have the lowest random retrieval errors measuring less than 40 % in the 9 to 15 km altitude range.

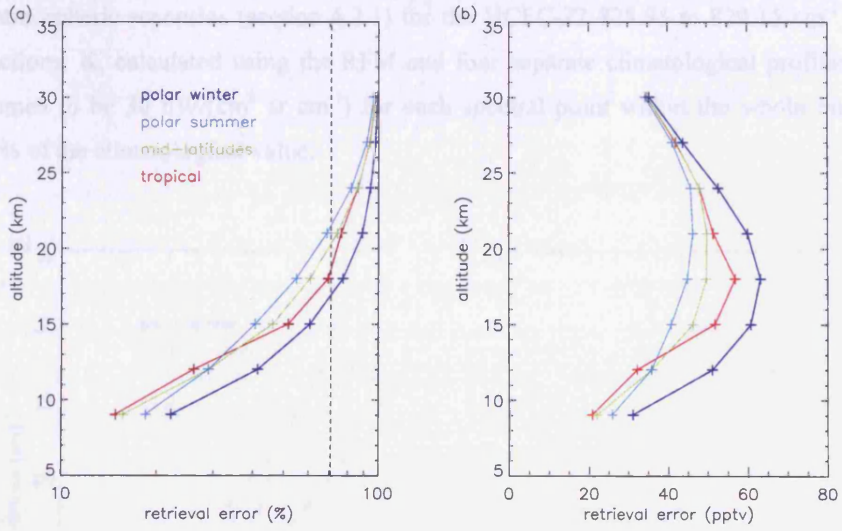

Figure 4.37 Retrieval random errors for the HCFC-22 828.95 to 829.15 cm^{-1} microwindow, over the 9 to 30 km altitude range plotted as (a) percentage errors and (b) absolute errors. The dashed black line in (a) represents where more information is gained from the measurement than the *a priori* information.

Both the degrees of freedom for signal and the information content are low for HCFC-22. Retrievals in the polar summer have the highest dfs with 4.02 quantities measured, followed by the mid-latitudes (3.73), the tropics (3.56) and finally by the polar winter (2.81). The information content is also highest in the polar summer retrievals with $2^{4.1}$ atmospheric states being distinguishable. This is followed by the mid-latitudes with 3.94 bits and the tropics with 3.86 bits. The polar winter is not a favourable region from

which to obtain useful profile information for HCFC-22 as only $2^{2.81} \approx 7$ different atmospheric states can be distinguished.

	POLAR WINTER		POLAR SUMMER		MID-LATITUDES		TROPICS	
Height	**d_s**	**H**	**d_s**	**H**	**d_s**	**H**	**d_s**	**H**
30	0.01	0.01	0.05	0.03	0.03	0.02	0.03	0.02
27	0.03	0.02	0.12	0.06	0.08	0.04	0.09	0.05
24	0.08	0.04	0.26	0.15	0.20	0.11	0.20	0.11
21	0.16	0.09	0.43	0.28	0.36	0.22	0.33	0.20
18	0.32	0.19	0.60	0.46	0.53	0.38	0.42	0.27
15	0.53	0.38	0.76	0.71	0.70	0.60	0.64	0.51
12	0.75	0.69	0.87	1.00	0.86	1.00	0.89	1.09
9	0.92	1.24	0.94	1.41	0.96	1.56	0.96	1.61
Total	**2.81**	**2.66**	**4.02**	**4.10**	**3.73**	**3.94**	**3.56**	**3.86**

Table 4.8 Calculated degrees of freedom for signal (d_s) and information content (H), measured in bits, for four separate atmospheric scenarios (section 4.2.1) for the HCFC-22 828.95 to 829.15 cm^{-1} microwindow. Weighting functions, **K**, calculated using the RFM and four separate climatological profiles, one for each region. $\mathbf{S}_y$ assumed to be 30 $nW/(cm^2\ sr\ cm^{-1})$ for each spectral point within the whole microwindow. $\mathbf{S}_a$ assumed at 25 % of the climatological value.

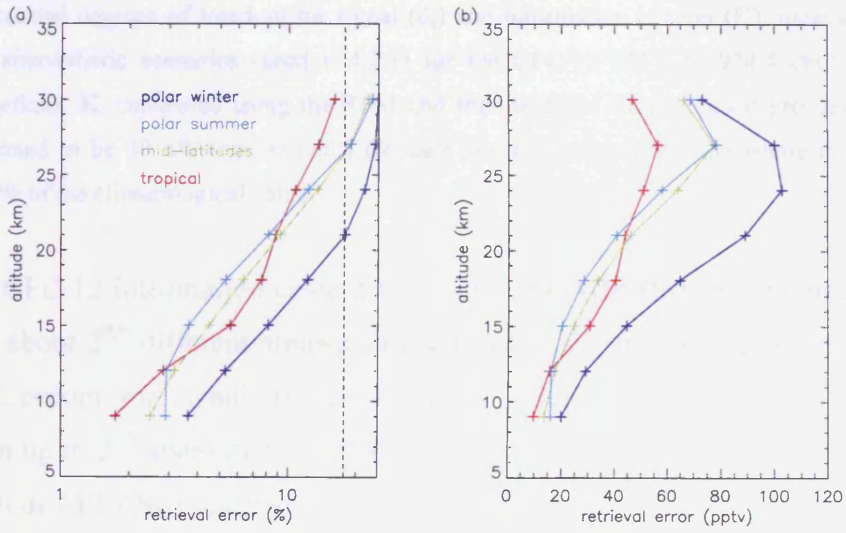

Figure 4.38 Retrieval random errors for the CFC-12 921.4 to 924.4 cm^{-1} microwindow, over the 9 to 30 km altitude range plotted as (a) percentage errors and (b) absolute errors. The dashed black line in (a) represents where more information is gained from the measurement than the *a priori* information.

The lowest CFC-12 random retrieval errors are found at 9 km for each of the four regions (less than 4 %), where the broadband emissions of CFC-12 are strongest over the 9 to

30 km altitude range. Tropical retrievals are least dominated by random retrieval errors with significant information coming from the measurements over the whole height range. Polar winter retrievals are the most dominated by random retrieval errors, with errors up to 25 % by 27 km, and more information coming from the measurements rather than the *a priori* at heights above 21 km. Both polar summer and mid-latitude retrievals are calculated to have similar retrieval random error profiles, with an error less than 25%/√2 between 9 and 24 km.

	POLAR WINTER		POLAR SUMMER		MID-LATITUDES		TROPICS	
Height	d_s	**H**	d_s	**H**	d_s	**H**	d_s	**H**
30	0.01	0.003	0.11	0.06	0.17	0.09	0.56	0.41
27	0.06	0.03	0.40	0.25	0.41	0.26	0.67	0.56
24	0.22	0.12	0.73	0.66	0.68	0.57	0.79	0.78
21	0.46	0.31	0.88	1.05	0.85	0.93	0.86	0.98
18	0.73	0.66	0.95	1.46	0.92	1.29	0.89	1.12
15	0.88	1.05	0.97	1.83	0.96	1.63	0.94	1.42
12	0.95	1.47	0.98	2.05	0.98	1.97	0.98	2.08
9	0.97	1.84	0.98	2.06	0.99	2.21	0.99	2.56
Total	**4.28**	**5.48**	**6.00**	**9.42**	**5.96**	**8.95**	**6.70**	**9.90**

Table 4.9 Calculated degrees of freedom for signal (d_s) and information content (H), measured in bits, for four separate atmospheric scenarios (section 4.2.1) for the CFC-12 921.4 to 924.4 cm^{-1} microwindow. Weighting functions, **K**, calculated using the RFM and four separate climatological profiles, one for each region. $\mathbf{S}_y$ assumed to be 30 $nW/(cm^2\ sr\ cm^{-1})$ for each spectral point within the whole microwindow. $\mathbf{S}_a$ assumed at 10 % of the climatological value.

The highest CFC-12 information content (H) within the MIPAS-E measurements is in the tropics with about $2^{9.9}$ different atmospheric states that can be distinguished. As with the degrees of freedom for signal, the lowest information content is in the polar winter scenario with up to $2^{5.5}$ states distinguishable. The information content from polar summer and mid-latitude MIPAS-E scans are 9.4 and 9.0 respectively.

From the degrees of freedom for signal (dfs) shown in Table 4.9 it is seen that although the polar winter region is the most dominated by random retrieval errors in the stratosphere, CFC-12 profile information can still be gained from the up to 4.3 height levels. In the tropics the dfs indicates 6.7 quantities can be distinguished and measured quantities for the polar summer and mid-latitude scenarios are 6.

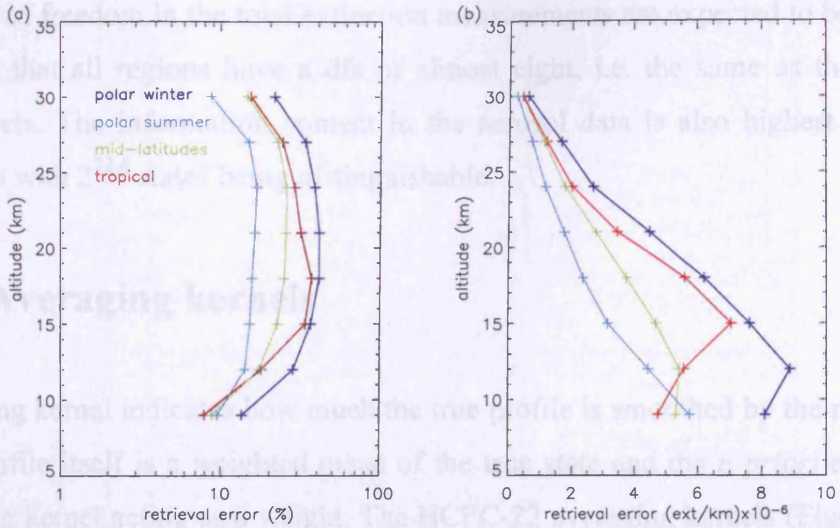

Figure 4.39. Retrieval random errors for the total extinction 832.3 to 834.4 cm^{-1} microwindow, over the 9 to 30 km altitude range plotted as (a) percentage errors and (b) absolute errors.

	POLAR WINTER		POLAR SUMMER		MID-LATITUDES		TROPICS	
Height	**d_s**	**H**	**d_s**	**H**	**d_s**	**H**	**d_s**	**H**
30	0.99	2.42	1.00	3.17	1.00	2.67	0.99	2.61
27	0.98	2.01	1.00	2.65	0.99	2.27	0.99	2.19
24	0.98	1.86	0.99	2.54	0.99	2.16	0.98	2.08
21	0.97	1.77	0.99	2.62	0.99	2.20	0.98	2.02
18	0.97	1.78	1.00	2.68	0.99	2.26	0.98	1.91
15	0.98	1.91	1.00	2.73	0.99	2.37	0.98	2.00
12	0.99	2.15	1.00	2.80	0.99	2.61	0.99	2.59
9	1.00	2.84	1.00	3.17	1.00	3.24	1.00	3.36
Total	**7.85**	**16.73**	**7.97**	**22.37**	**7.93**	**19.79**	**7.90**	**18.76**

Table 4.10. Calculated degrees of freedom for signal (d_s) and information content (H), measured in bits, for four separate atmospheric scenarios (section 4.2.1) for the total extinction 832.3–834.4 cm^{-1} microwindow. Weighting functions, **K**, calculated using the RFM and four separate climatological profiles, one for each region. $\mathbf{S}_y$ assumed to be 30 $nW/(cm^2\ sr\ cm^{-1})$ for each spectral point within the whole microwindow. $\mathbf{S}_a$ assumed at 1000 % of the climatological value.

For total extinction the random retrieval errors are generally lowest in the polar summer and are never greater than 18 % on a single measurement. The polar winter errors are generally the highest at up to 50 %. Of course the aerosol extinction can vary by up to two orders of magnitude if there is contamination of the instrument LOS with thin cloud for example. It should be remembered that the random error will decrease on a single measurement if the extinction increases.

The degrees of freedom in the total extinction measurements are expected to be high. It has been shown that all regions have a dfs of almost eight, i.e. the same as the number of retrieval levels. The information content in the aerosol data is also highest in the polar summer data with $2^{22.4}$ states being distinguishable.

4.2.4 Averaging kernels

The averaging kernel indicates how much the true profile is smoothed by the retrieval. The retrieved profile itself is a weighted mean of the true state and the *a priori* estimate with the averaging kernel acting as a weight. The HCFC-22 averaging kernels (Figure 4.40) are strongly peaked in the upper troposphere and lowermost stratosphere. For the tropics, mid-latitudes and polar summer the area of the averaging kernels are close to unity for 4 heights, although the 18 km averaging kernels are very broad implying a resolution of no better than 5 or 6 km at this height. The polar winter has sharply peaked averaging kernels at 9 and 12 km. By 15 km, the polar winter averaging kernel broadens to a resolution of no better than 6 km and above 18 km the retrieved HCFC-22 concentrations are heavily biased towards the *a priori* as the averaging kernel peaks are close to zero. As expected, the best results are found for polar summer.

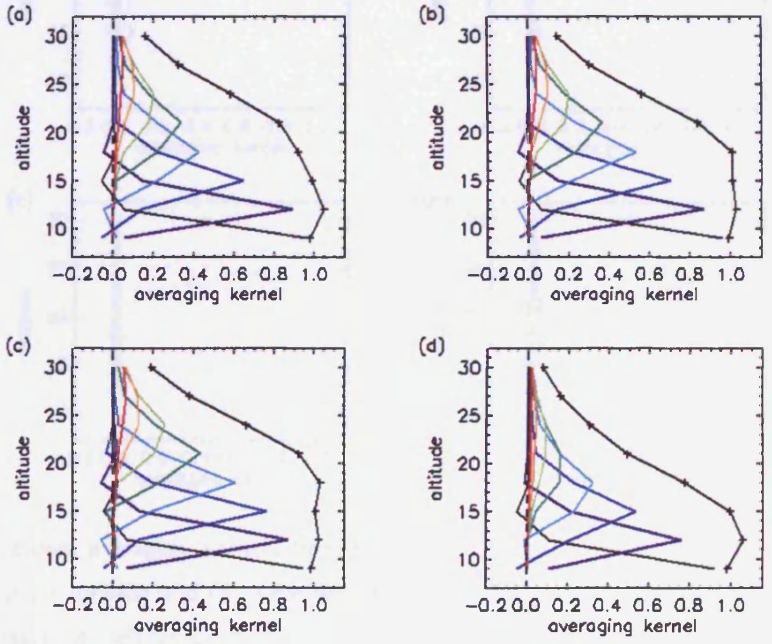

Figure 4.40 The HCFC-22 averaging kernels from the HCFC-22 microwindow for: (a) the tropics, (b) the mid-latitudes, (c) polar summer and (d) polar winter. The black line represents the sum of the rows of the averaging kernel matrix at each tangent height.

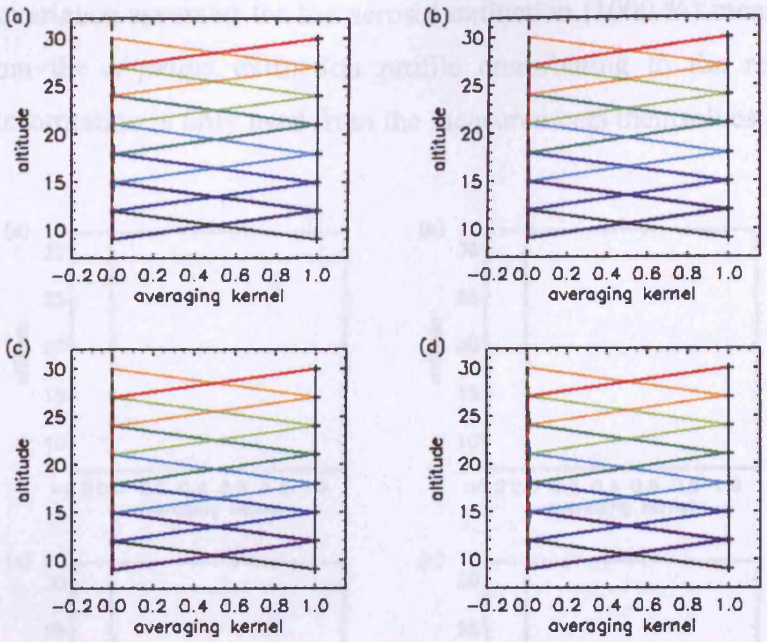

Figure 4.41 Averaging kernels for the aerosol microwindow : (a) tropical, (b) mid-latitudes, (c) polar summer and (d) polar winter. The black line displays the sum of each row of the averaging kernel matrix at every tangent height.

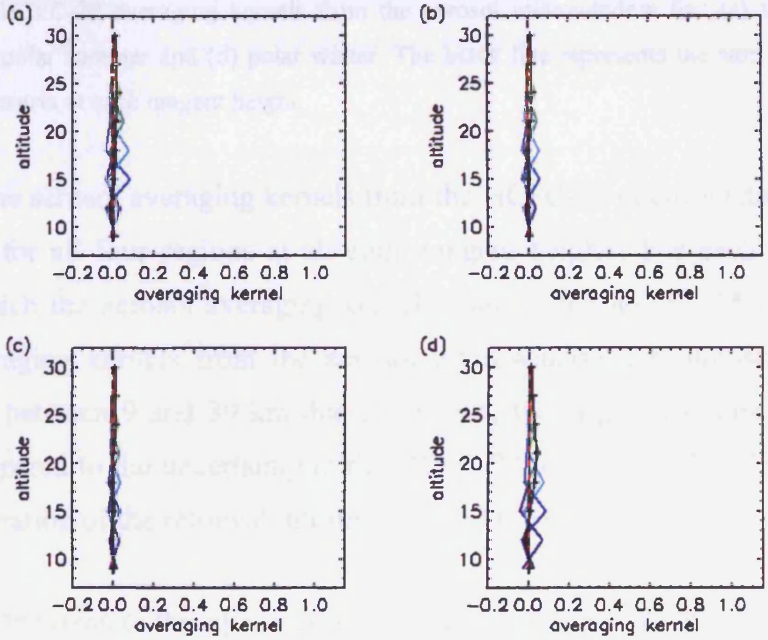

Figure 4.42 The aerosol averaging kernels from the HCFC-22 microwindow for: (a) the tropics, (b) the mid-latitudes, (c) polar summer and (d) polar winter. The black line represents the sum of the rows of the averaging kernel matrix at each tangent height.

The aerosol averaging kernels are sharply peaked, each with a value of approximately one (Figure 4.41) for all four regions at all eight tangent heights. The reason for this is that the

high *a priori* covariance assumed for the aerosol extinction (1000 %) means there is little information from the *a priori* extinction profile contributing to the retrieved aerosol extinction and information is only used from the measurements themselves.

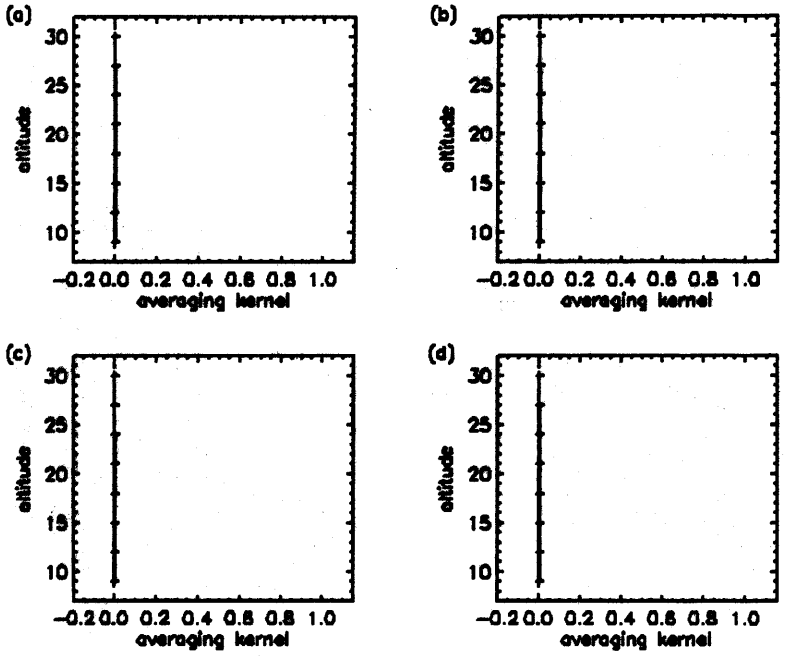

Figure 4.43 The HCFC-22 averaging kernels from the aerosol microwindow for: (a) the tropics, (b) the mid-latitudes, (c) polar summer and (d) polar winter. The black line represents the sum of the rows of the averaging kernel matrix at each tangent height.

The peaks of the aerosol averaging kernels from the HCFC-22 microwindow (Figure 4.42) are below 0.1 for all four regions at all eight tangent heights. For each region the only heights for which the aerosol averaging kernel is above 0.5 are 12, 15 and 18 km. The HCFC-22 averaging kernels from the aerosol microwindow are almost zero for every tangent height between 9 and 30 km due to, in part, the large uncertainty in the aerosol extinction compared to the uncertainty in the HCFC-22 *a priori* profile. Therefore there is very good separation of the retrieval information for HCFC-22 and aerosol.

In Figure 4.44, the rows of the square averaging kernel matrix A are plotted for CFC-12 for each of the four regions. The area of the averaging kernel (indicated by the solid black towards the right of each plot in) is approximately equal to one where the retrieval is accurate. The tropical CFC-12 averaging kernels have an area close to one throughout the whole of the UTLS region. Both the polar summer and mid-latitude cases have sharply peaked averaging kernels between 9 and 24 km. Polar winter averaging kernels are sharp in the upper troposphere and lowermost stratosphere in the polar winter scenario, but

become very broad at heights above 18 km implying a vertical resolution in the retrieval of greater than 3 km above these tangent height.

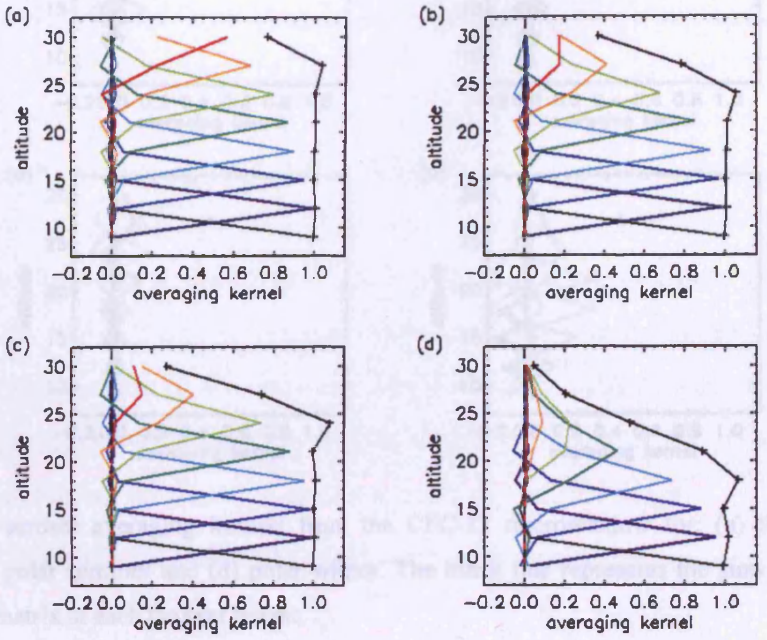

Figure 4.44 Averaging kernels for the CFC-12 microwindow : (a) tropical, (b) mid-latitudes, (c) polar summer and (d) polar winter. The black line displays the sum of each row of the averaging kernel matrix at every tangent height.

The aerosol microwindow used in the CFC-22 joint retrieval is identical to the aerosol microwindow used in the HCFC-22 joint retrieval assuming the same *a priori* extinction profile and the matching 1000 % uncertainty in the extinction. As such the averaging kernels are identical to those shown in Figure 4.41 and are not reproduced here.

The peaks of the aerosol averaging kernels from the CFC-12 microwindow are largest in the polar winter (Figure 4.45d) between 15 and 21 km implying that the retrieval is most sensitive to the aerosol extinction in this region between these heights. Although not as strongly peaked, the tropical averaging kernels (maximum value of 0.25 at 24 and 27 km) are sharp and above 0.2 between 18 and 30 km. The lowest influence of aerosol on the CFC-12 retrievals is in the polar summer scenario (Figure 4.45c) with the peaks of the averaging kernels less than 0.2 between 9 and 30 km.

The CFC-12 averaging kernels from the aerosol microwindow are zero for every height because CFC-12 is not an emitter in the 832.3 to 834.4 cm^{-1} range. Therefore, results are not shown.

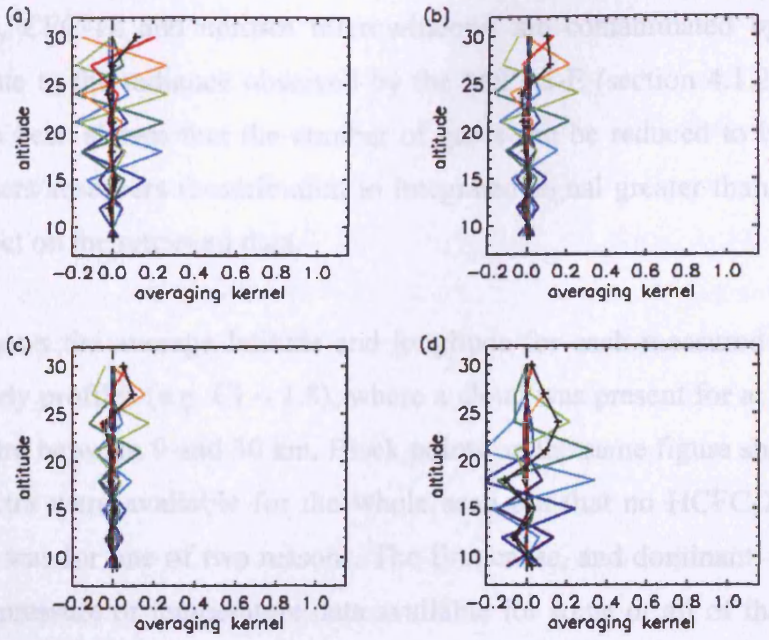

Figure 4.45 The aerosol averaging kernels from the CFC-12 microwindow for: (a) the tropics, (b) the mid-latitudes, (c) polar summer and (d) polar winter. The black line represents the sum of the rows of the averaging kernel matrix at each tangent height.

4.2.5 Retrievals from MIPAS-E spectral data

Retrievals of constituent profiles from MIPAS-E data are performed here using the OPERA retrieval scheme. Reference will be made to "profile retrievals" but it should be remembered that the MIPAS-E only uses one scan mirror which is repositioned for each measurement. As the satellite itself moves along its orbit between each measurement, the profile will become skewed.

The MIPAS-E has provided regular limb measurements of the atmosphere since September 2002. However, problems with decontamination of ice formation on some of the sensors, a malfunction with one of the slide mirrors and general problems with data availability have meant that data coverage has not been continuous since that time. However, for the purposes of this initial study to test the feasibility of halocarbon retrievals a single day (May 2nd 2003) was identified. The large number of operationally retrieved level 2 [Carli *et al.*, 2004] pressure, temperature and water vapour data (version 4.61) from this day made it ideal. May 2nd 2003 was also chosen because the day had a fairly low number of optically thick clouds (cloud index less than 1.8) which mask spectral features.

The HCFC-22, CFC-12 and aerosol microwindows are contaminated by several gases which contribute to the radiance observed by the MIPAS-E (section 4.1.2). From section 4.2.2.1.3 it has been shown that the number of gases can be reduced to include only the strongest emitters/absorbers (contribution to integrated signal greater than 5 %) with less than a 3 % effect on the retrieved data.

Figure 4.46 shows the average latitude and longitude for each measured scan. Red data highlights cloudy profiles (e.g. CI < 1.8), where a cloud was present for at least one of the measured spectra between 9 and 30 km. Black points on the same figure show scans where MIPAS-E spectra were available for the whole scan but that no HCFC-22/CFC-12 data retrieved. This was for one of two reasons. The first cause, and dominant, reason was that there were no pressure or temperature data available for some or all of the heights in the scan. The second reason was that the retrieval itself did not converge.

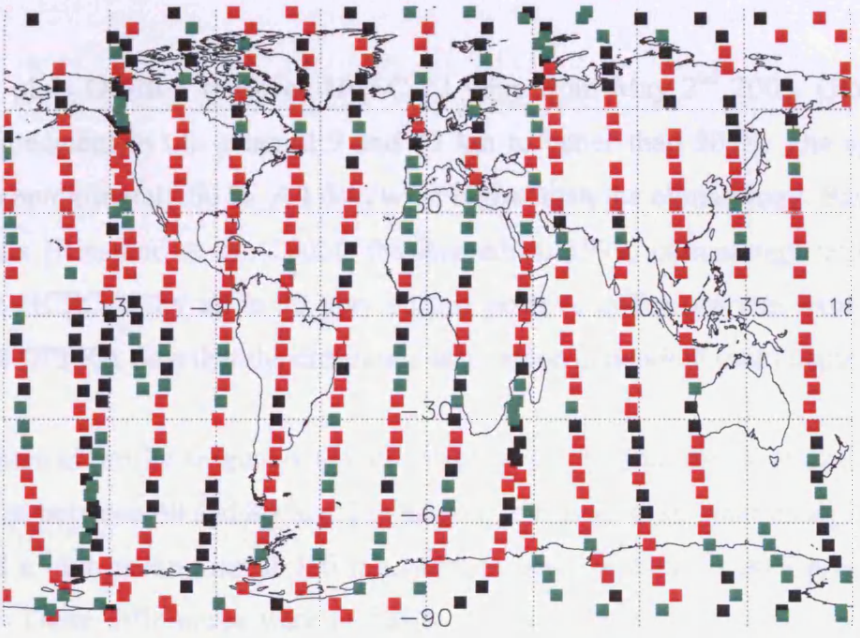

Figure 4.46 The available offline level 2 data available for May 2nd 2003 (orbits 06115 to 06122). The data are plotted for the mean latitude and longitude for the scan. Red squares indicate scans which contain cloudy spectra for at least one height between 9 and 30 km [CI < 1.8]. Black squares represent non-cloudy data but the retrieval scheme did not converge for this scan or there were incomplete pressure or temperature data hence no retrieval was performed. Green squares represent scans where there were complete pressure and temperature data and the retrieval converged.

The radiance measured by the MIPAS-E is a function of pressure and temperature and the retrieved concentrations are highly sensitive to inaccuracies (section 4.2.6) in these two

parameters. If data for these were incomplete then no retrieval was performed from the scan. Water vapour inaccuracies account for up to a 2 % error in the retrieval (section 4.2.6) in the tropical UTLS for HCFC-22. It was also decided than scans including incomplete water vapour data should also be excluded. To increase the number of retrievals from the dataset where data were incomplete for minor contributors over the height range of interest interpolated data were used. For ozone or, in the case of CFC-12, nitric acid, the "gaps" were filled by interpolating between the climatology onto the measurement height levels that had level 2 data missing. The calculated errors introduced into the retrieval due to ozone and nitric acid inaccuracies are low in the lowermost stratosphere (< 1 %) and only become important at pressures below 30 mb (4.2.6). Below 30 mb (approximately 30 mb) the information content within the MIPAS-E measurements for CFC-12 and HCFC-22 are low in any case.

4.2.5.1 HCFC-22 retrievals

Figure 4.47 plots OPERA retrieved HCFC-22 vmrs from May 2nd 2003. Globally, there was good agreement in the mean at 9 and 12 km to better than 30 %. The agreement at 15 km was approximately 60 %. All data were higher than the climatology. Based on 2003 measurements [Rinsland *et al.*, 2005], the Remedios, 1999, climatology underestimated tropospheric HCFC-22 by up to 20 pptv so this positive difference was expected. It was shown in the OPERA data that the difference was region dependent (see chapter 6).

The mean tropical profile (Figure 4.47a and Table 4.11) showed the most difference to the climatology at between 40 and 80 % (52 to 68 pptv). The polar summer data (Figure 4.47c) also showed a high mean vmr at 350 mb, with a mean of over 53 pptv greater than the climatology. These differences were probably not due to OPERA itself. It was shown in section 4.2.2.2.1 that OPERA was likely to indeed underestimate a change rather than overestimate as was found here for the polar summer and the tropics. The mean profile of the Southern polar results varies positively by between 30 and 45 % compared to the climatology.

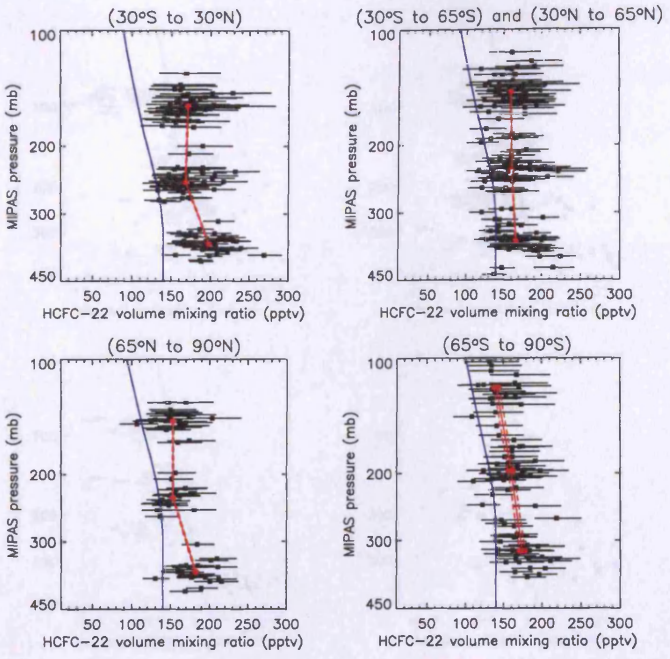

Figure 4.47 Retrieved HCFC-22 data from MIPAS-E level 1b data measured on May 2nd 2003. Black squares represent the HCFC-22 data, and on each square is overplotted the corresponding random retrieval error. The solid blue line represents the HCFC-22 climatology of Remedios, 1999. The solid red line is a mean of the HCFC-22 data plotted at a mean pressure for each measured level. The dashed red line represents the standard error on the mean.

TROPICAL			MID-LATITUDES		
Mean pressure (mb)	Mean (pptv)	Standard deviation (pptv)	Mean pressure (mb)	Mean (pptv)	Standard deviation (pptv)
157	171	22	145	160	22
248	169	24	233	161	24
359	198	25	356	167	26
POLAR SUMMER			POLAR WINTER		
Mean pressure (mb)	Mean (pptv)	Standard deviation (pptv)	Mean pressure (mb)	Mean (pptv)	Standard deviation (pptv)
145	153	20	119.4	142	20
230	153	15	197.4	160	21
360	182	22	319.0	175	21

Table 4.11 statistics from the OPERA HCFC-22 retrievals from May 2nd 2003 for each of the four latitude regions described in section 4.2.1.

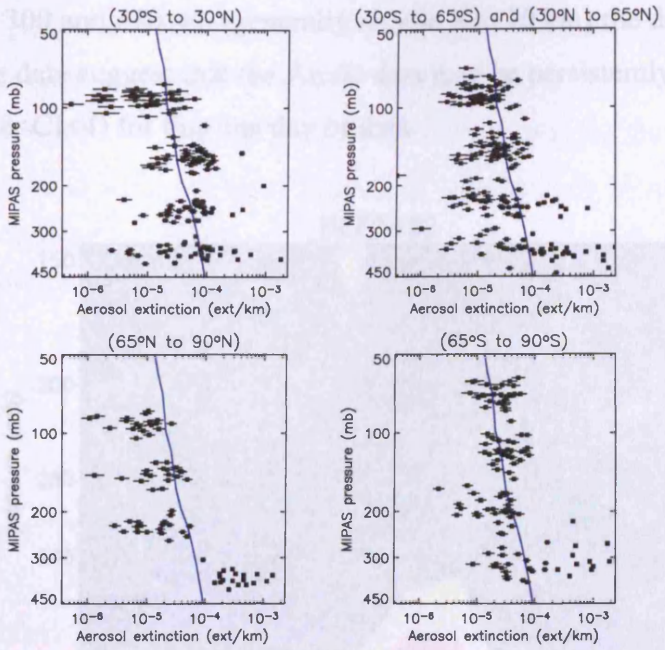

Figure 4.48 OPERA retrieved total extinction data from MIPAS-E level 1b data measured on May 2nd 2003. Black squares represent the aerosol data, and on each square is overplotted the corresponding random retrieval error. The solid black line represents the *a priori* aerosol profile.

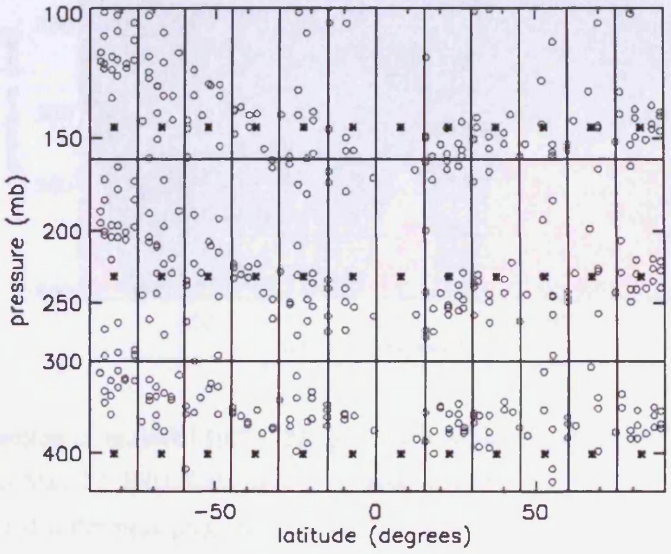

Figure 4.49 The pressure-latitude grid used to produce retrieved gas and aerosol cross-section plots. Data from each grid box are averaged (HCFC-22 data points for May 2nd 2003 are plotted as circles) and plotted at a fixed pressure level at the central latitude of each grid box (400, 230 or 145 mb), shown by black asterisks.

Retrieved total extinction is plotted at three levels for all four regions in Figure 4.48. There is variability within the data for all four regions generally up to the 1000 % assumed *a priori* variability, with some additional outliers. For the Northern polar retrievals at

pressures between 300 and 450 mb (generally around 8 to 10 km) the data all lay above the climatology. These data suggest that the Arctic data may be persistently "contaminated" by thin cloud (with 1.8<CI<4) for this one day of data.

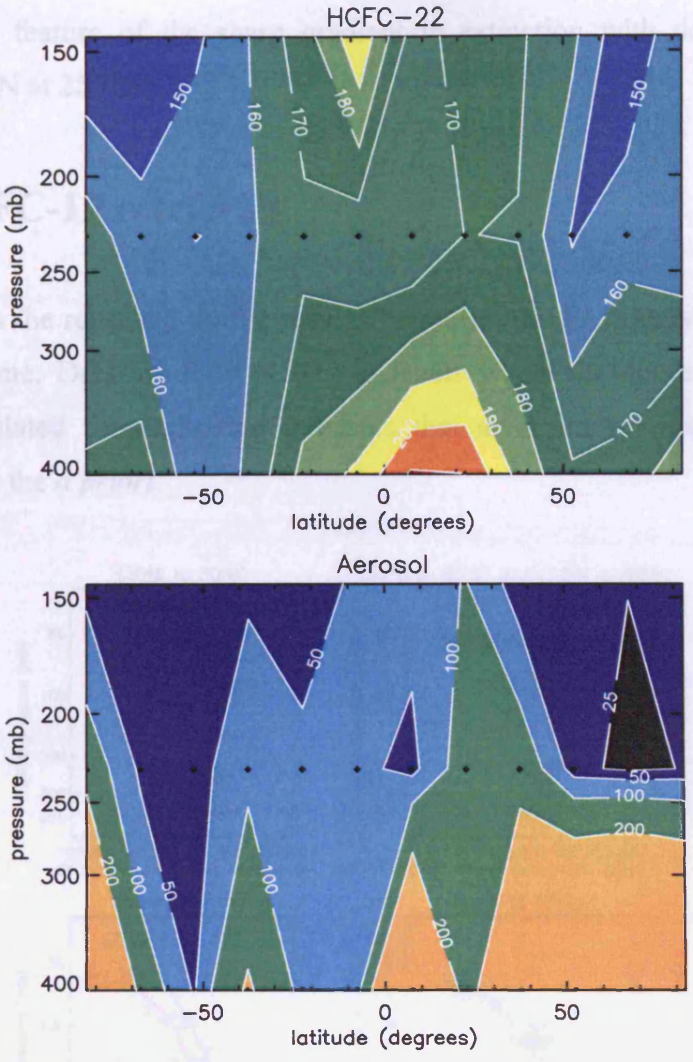

Figure 4.50 A cross-section of retrieved HCFC-22 (pptv) and Aerosol (ext/km x10^{-6}) data from MIPAS-E measurements made on May 2nd 2003. Data have been gridded within 60 bins. All data within one bin has been averaged and plotted at the mean pressure and latitude of the bin, represented by black diamonds.

The cross-section data of both HCFC-22 and aerosol from May 2nd 2003 were gridded onto 3 pressure levels (shown in Figure 4.49) at 400, 230 and 145 mb and 12 latitude bins each 15 degrees in width, the first centred on 82.5°S and increasing in the 15 degree increments up to 82.5°N. The centre of each bin is plotted on Figure 4.49. The highest HCFC-22 values were in the tropical UTLS for this day between 20°S and 30°N. Data between 0 to 15°N on Figure 4.50 should be treated with caution however as only one profile comprises the cross-section plot in that range (Figure 4.49). A secondary HCFC-22 maximum was

observed in the tropics between 150 to 200 mb which may be a real feature in the data but definite conclusions cannot be reached with so few data in that region. The total extinction cross-section in the UTLS is expectedly very similar to that for the CFC-12 results in 4.2.5.2. Total extinctions were generally highest in the Northern Hemisphere UTLS with the most striking feature of the sharp gradient in extinction with decreasing pressure between 50 to 90°N at 250 mb.

4.2.5.2 CFC-12 retrievals

Figure 4.51 shows the retrieved profile results from orbit 06117 from May 2nd 2003 using the OPERA scheme. Data are only plotted at levels where the degrees of freedom for signal (dfs) calculated for each scan indicates that more information arises from the measurement than the *a priori*.

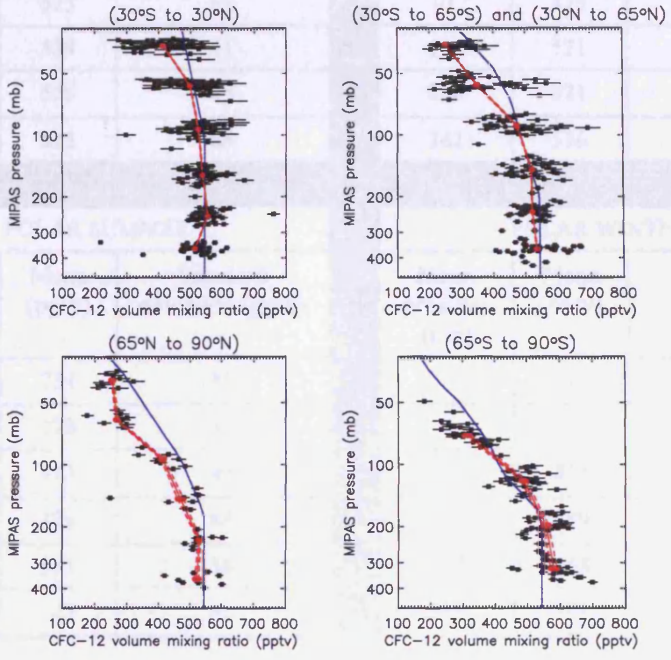

Figure 4.51. OPERA retrieved CFC-12 data (black squares) from MIPAS-E level 1b data measured on May 2nd 2003. The solid black line represents the CFC-12 climatology of Remedios, 1999. The solid red line is a mean of the CFC-12 data plotted at a mean pressure for each measured level. The standard error on the mean is also plotted, represented by the dashed red line.

The mean profile of the tropical results (Figure 4.51a) showed excellent agreement with the climatology. It was shown that at every pressure level, the OPERA CFC-12 data were lower than the climatology. The difference was small and comparisons of both data were

better than 15 %. In particular the mean results between 300 and 50 mb (12 to 21 km) were less than 3 % different.

The mean mid-latitude OPERA profile also lay below the climatology, although general agreement in profile shape was again very good. All OPERA data lay within 11 % of the climatology with agreement better than 6 % at pressures above 100 mb. The lower OPERA CFC-12 compared to the climatology could suggest that the profile within the CFC-12 climatology is incorrect.

TROPICAL			MID-LATITUDES		
Mean pressure (mb)	Mean (pptv)	Standard deviation (pptv)	Mean pressure (mb)	Mean (pptv)	Standard deviation (pptv)
37	413	76	36	251	53
57	498	69	57	348	91
93	525	61	91	475	78
157	539	41	148	521	57
249	556	45	238	521	41
360	515	64	362	536	66
POLAR SUMMER			POLAR WINTER		
Mean pressure (mb)	Mean (pptv)	Standard deviation (pptv)	Mean pressure (mb)	Mean (pptv)	Standard deviation (pptv)
39	254	35	/	/	/
61	270	41	/	/	/
94	413	49	72	315	50
148	470	88	120	489	45
233	531	36	199	558	41
361	523	61	321	581	52

Table 4.12 Statistics from the OPERA CFC-12 retrievals from May 2nd 2003 for each of the four latitude regions described in section 4.2.1.

Few Northern Hemisphere polar CFC-12 retrievals converged when compared to the other three regions. Reasons for this are not clear and only ten profiles comprise the plot making it difficult to draw any conclusion on the results. One reason could be the known HNO_3 bias in some the MIPAS-E version 4.61 data of up to 10 % [Oelhaf, 2004]. Although not important at lower altitudes, above 21 km HNO_3 becomes a significant emitter in the

CFC-12 microwindow. The systematic bias due to HNO_3 in the retrieval is investigated in section 4.2.6.2

The mean profile results from the southern pole vary by up to 17 % compared to the climatology. Unlike the other regions which show a decrease in CFC-12 compared to the climatology at all altitudes, at pressures above 200 mb the southern polar results show a positive difference compared by the climatology of up to 6 %.

The OPERA scheme also retrieved total extinction in the UTLS. Retrieved extinction is plotted at up to seven levels for all four regions in Figure 4.52. There was variability within the data for all four regions up to 1000 % from the climatology, the assumed *a priori* variability, with some additional outliers. For the retrievals at pressures between 300 and 500 mb (generally around 8 to 10 km) many data lay above the climatology and also exceeded 10^{-3} km^{-1}. In the northern polar region in particular there are data above the climatology value with no data below. This could indicate thin cloud contamination of the spectra (1.8<cloud index<4) which the OPERA scheme is able to retrieve and quantify.

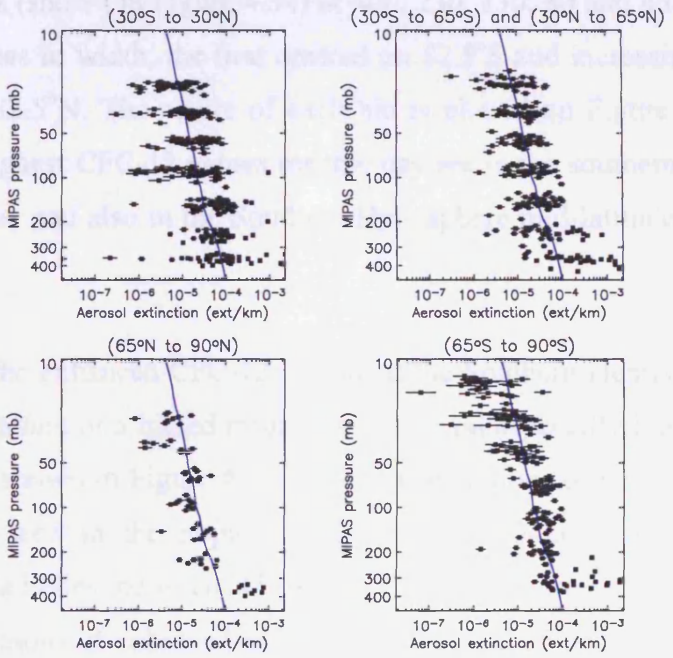

Figure 4.52 Retrieved total extinction data (black squares) from MIPAS-E level 1b data measured on May 2nd 2003. On each data point is over plotted the corresponding random retrieval error. The solid blue line represents the extinction "climatology".

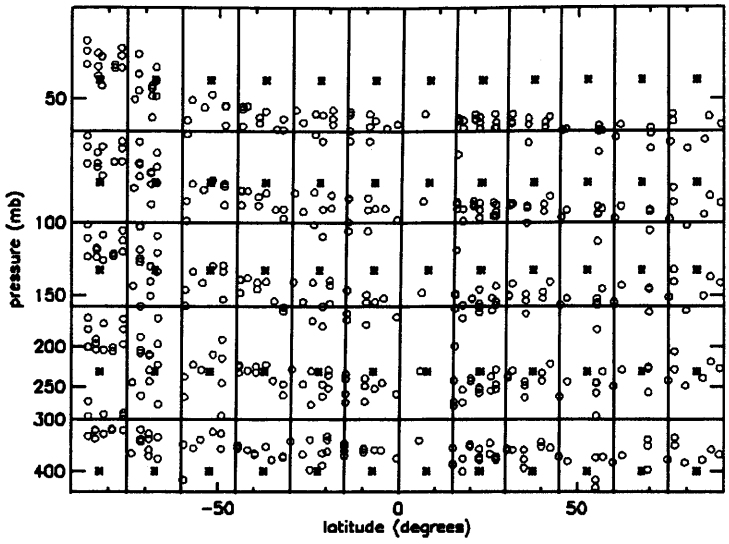

Figure 4.53 The pressure-latitude grid used to produce retrieved gas and aerosol cross-section plots. Data from each grid box are averaged (CFC-12 data points for May 2nd 2003 are plotted as circles) and plotted at a fixed pressure level at the central latitude of each grid box (400, 230, 130, 80 or 45 mb), shown by black asterisks.

The cross-section data of both CFC-12 and aerosol from May 2nd 2003 were gridded onto five pressure levels (shown in Figure 4.54) at 400, 230, 130, 80 and 45 mb and 12 latitude bins each 15 degrees in width, the first centred on 82.5°S and increasing in the 15 degree increments up to 82.5°N. The centre of each bin is plotted on Figure 4.53. As shown in Figure 4.51, the highest CFC-12 values for this day are in the southern pole UTLS region south of 60 degrees, and also in the Southern Hemisphere mid-latitude UTLS between 30 and 40 degrees.

It is unlikely that the enhanced CFC-12 feature at the Southern Hemisphere pole was real and could be an artefact of a biased mean due to several especially high CFC-12 values at the Southern Pole shown in Figure 4.51. Low concentrations of CFC-12 compared to the climatology were seen in the tropical UTLS between 0 and 30°N and the Northern Hemisphere mid-latitudes between 45 and 60°N. These areas show some degree of correlation with regions of enhanced aerosol. Aerosol extinctions are generally highest in the Northern Hemisphere UTLS with the most striking feature of the sharp gradient in extinction with decreasing pressure between 50 to 90°N at 250 mb.

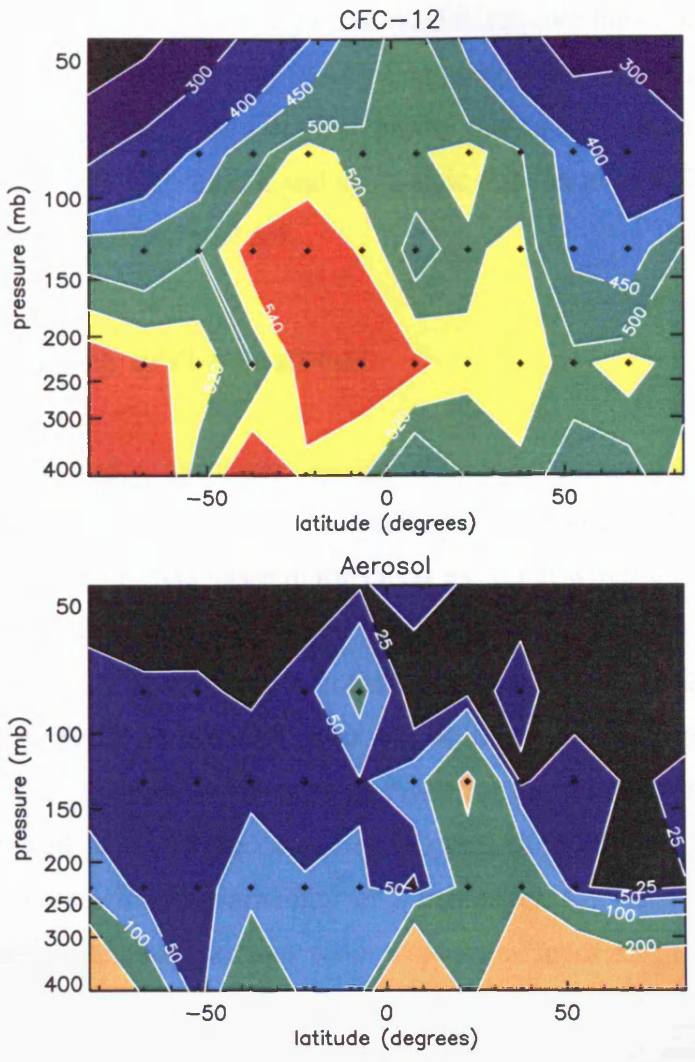

Figure 4.54 A cross-section of retrieved CFC-12 (pptv) and Aerosol (ext/km x10^{-6}) data from MIPAS-E measurements made on May 2nd 2003. Data have been gridded within 60 bins. All data within one bin has been averaged and plotted at the mean pressure and latitude of the bin, represented by black diamonds.

4.2.6 Error Analysis

Any measurement of the atmosphere is subject to errors within the measurement. Whether these errors are constant between consecutive measurements or vary randomly determines if the error is classed as systematic or random. The total error on a MIPAS-E measurement is the sum of these two terms. The distinction can be somewhat arbitrary for some terms (such as the accuracy of the climatology profiles and their variability over time) and an error source random on one scale could be systematic on another. Retrieval noise errors are wholly random, uncorrelated in time or along the orbit path. Model parameter errors, for example inaccuracies in the interfering gas concentrations within a microwindow, may be

truly systematic, if, for example, the algorithm used to retrieve the concentrations had the incorrect line strength data within it. Or the concentration of the interfering gases may vary more randomly about a mean climatological profile due to local mixing processes. The technique to calculate both the random and systematic error sources follows from Rodgers [2000], and the theory described in 2.5.4.

4.2.6.1 Random error sources

Two main sources of random error are considered, random retrieval errors (described in section 4.2.3), and model parameter error, the error propagating into the retrieval from the incorrect estimate of contaminant gases in the target gas microwindow. The forward model parameter error can be highly variable between adjacent measurements due to atmospheric variability of temperature, pressure or a contaminant gas. If their changeability can be quantified then an upper limit error estimate can be produced for each parameter, **b**. A detailed analysis of the random component of this error due to pressure and temperature was performed as well as all of the contaminant gases in the three halocarbon retrieval microwindows. Estimates for the variability of a parameter, $\mathbf{S_b}$, were based on a "mean" variability for pressure, temperature and water vapour, as reported in the MIPAS-E near real time level 2 data files for this day, for four latitude regions, section 4.2.1. Means were constructed only from profiles where the data were complete between 6 and 30 km. For the other interfering species $\mathbf{S_b}$ was based on estimates from the MIPAS standard atmosphere files reported by Remedios [1999].

4.2.6.1.1 HCFC-22

HCFC-22 model parameter errors (Figure 4.55 to Figure 4.58) are dominated by inaccuracies in the MIPAS level 2 data. The temperature and pressure errors are comparable at most levels and do not exceed 8 % and are generally less than 3 %. The errors are highest at the highest pressure and generally decrease with decreasing pressure (due mainly to decreasing information content in the measurements). The error contribution of each interfering gas within the HCFC-22 microwindow does not exceed 1 % and is generally less than 0.5 % and is therefore contributing a small error term to each retrieval performed.

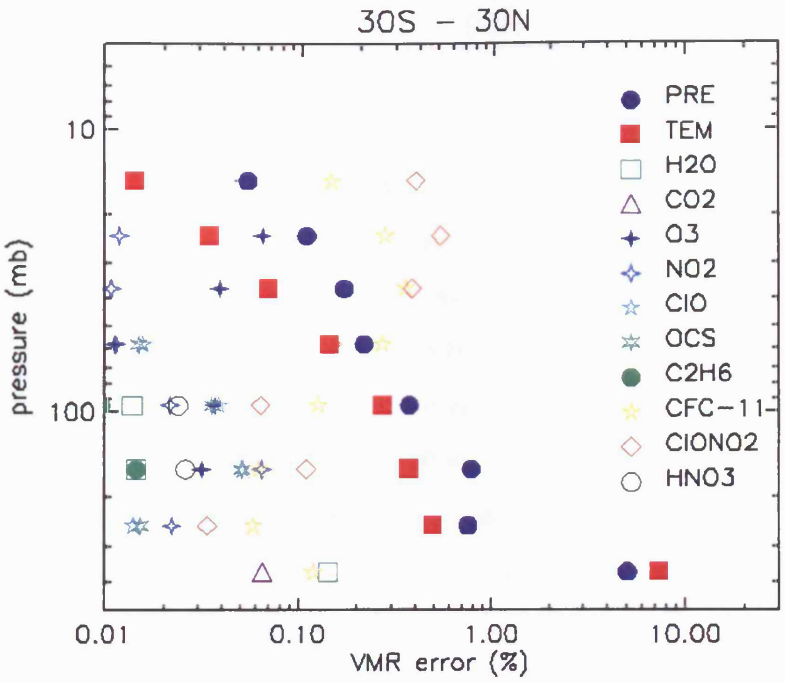

Figure 4.55 Tropical (30°S to 30°N) HCFC-22 random model parameter errors calculated incorporating reprocessed MIPAS level 2 data on May 2nd 2003 for estimates of pressure, temperature, water vapour (H_2O), nitric acid (HNO_3) and ozone (O_3) covariance. The covariances of the other gases used estimates from the tropical climatology of Remedios [1999].

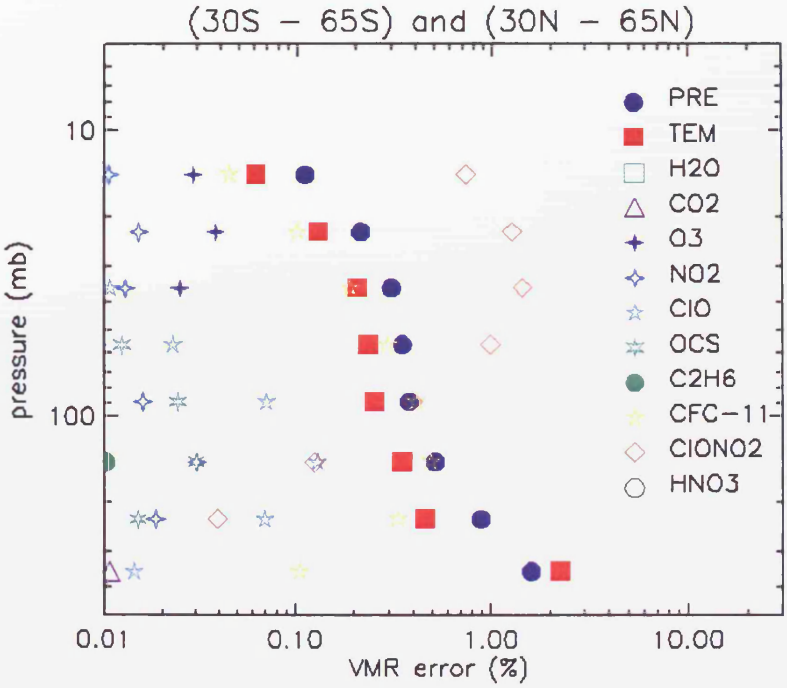

Figure 4.56 Mid-latitude (30 to 65 degrees) HCFC-22 random model parameter errors calculated incorporating reprocessed MIPAS level 2 data on May 2nd 2003 for estimates of pressure, temperature, water vapour (H_2O), nitric acid (HNO_3) and ozone (O_3) covariance. The covariances of the other gases used estimates from the mid-latitude day climatology of Remedios [1999].

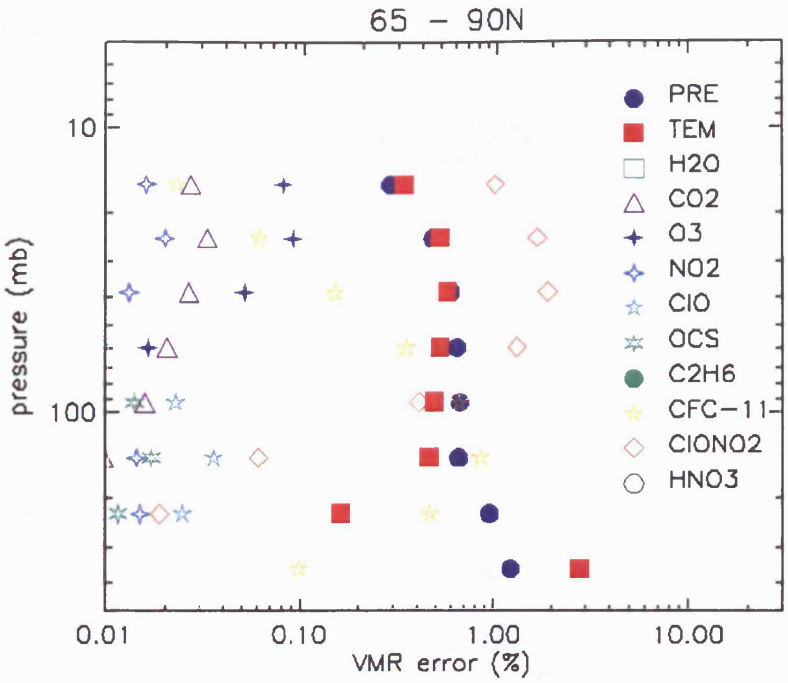

Figure 4.57 Northern Hemisphere polar (65 to 90°N) HCFC-22 random model parameter errors calculated incorporating reprocessed MIPAS level 2 data on May 2nd 2003 for estimates of pressure, temperature, water vapour (H_2O), nitric acid (HNO_3) and ozone (O_3) covariance. The covariances of the other gases used estimates from the polar summer climatology of Remedios [1999].

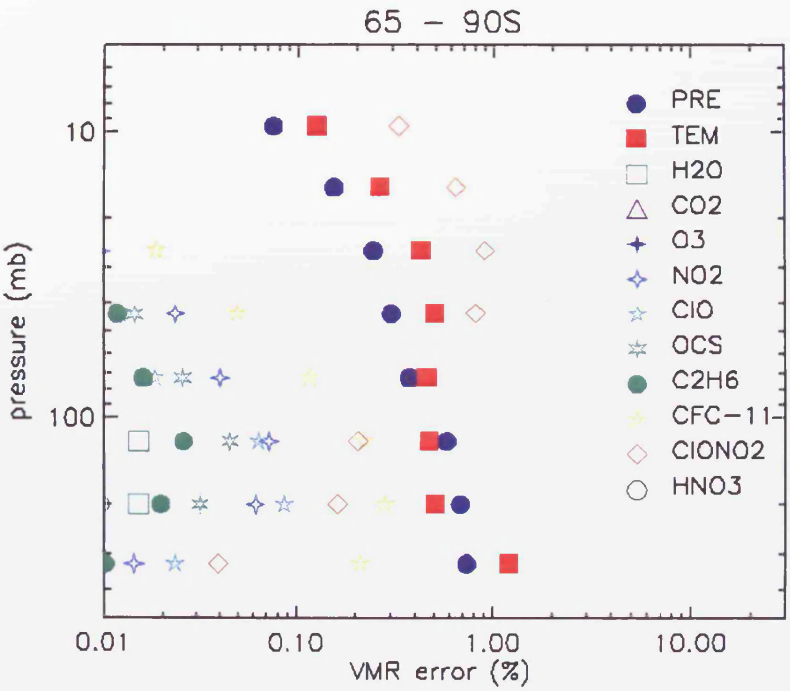

Figure 4.58 Southern Hemisphere polar (65 to 90°S) HCFC-22 random model parameter errors calculated incorporating reprocessed MIPAS level 2 data on May 2nd 2003 for estimates of pressure, temperature, water vapour (H_2O), nitric acid (HNO_3) and ozone (O_3) covariance. The covariances of the other gases used estimates from the polar winter climatology of Remedios [1999].

4.2.6.1.2 CFC-12

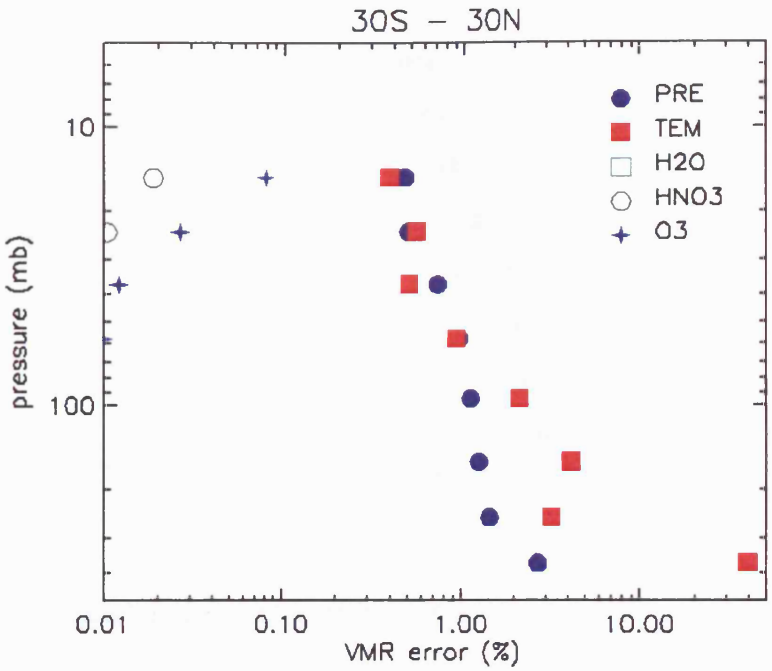

Figure 4.59 Tropical (30°S to 30°N) CFC-12 random model parameter errors calculated incorporating reprocessed MIPAS level 2 data on May 2nd 2003 for estimates of pressure, temperature, water vapour (H_2O), nitric acid (HNO_3) and ozone (O_3) covariance.

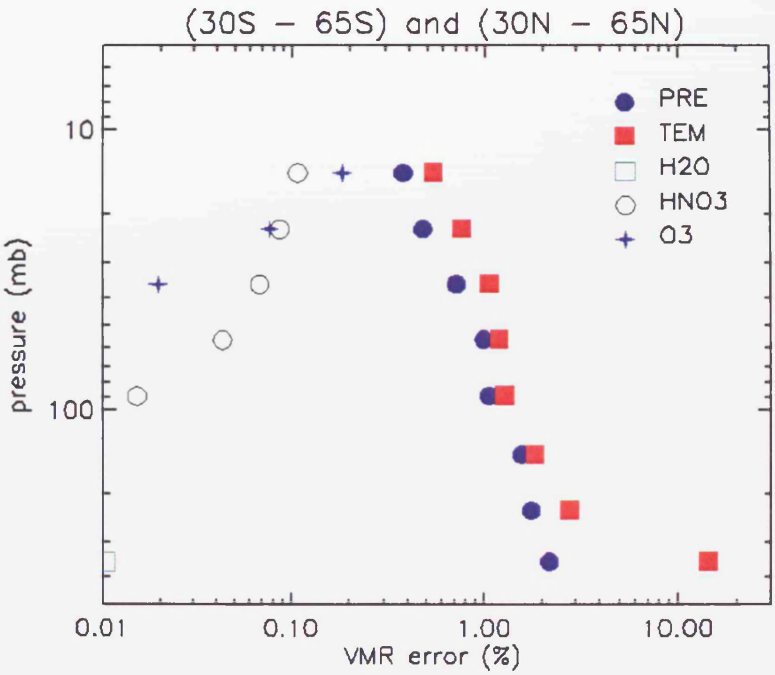

Figure 4.60 Mid-latitude (30 to 65 degrees) CFC-12 random model parameter errors calculated incorporating reprocessed MIPAS level 2 data on May 2nd 2003 for estimates of pressure, temperature, water vapour (H_2O), nitric acid (HNO_3) and ozone (O_3) covariance.

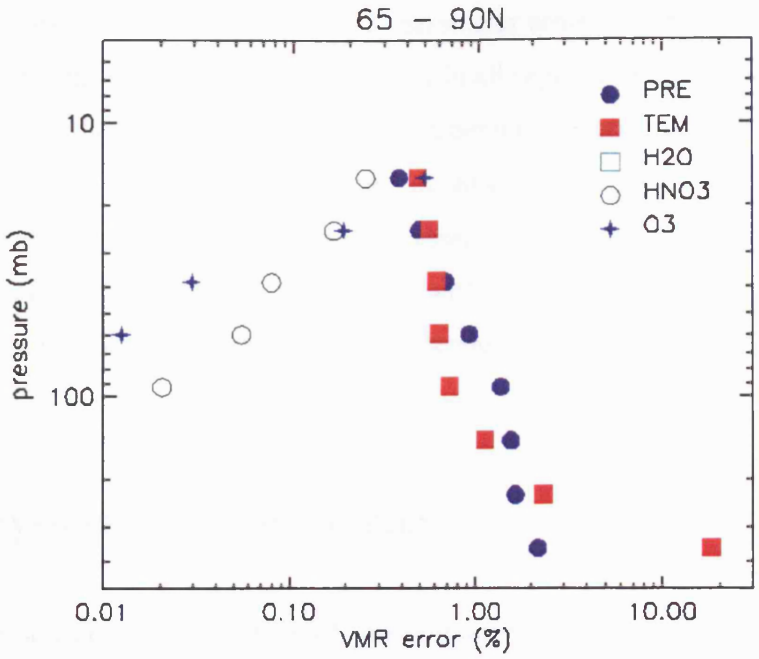

Figure 4.61 Northern Hemisphere polar (65 to 90°N) CFC-12 random model parameter errors calculated incorporating reprocessed MIPAS level 2 data on May 2nd 2003 for estimates of pressure, temperature, water vapour (H_2O), nitric acid (HNO_3) and ozone (O_3) covariance.

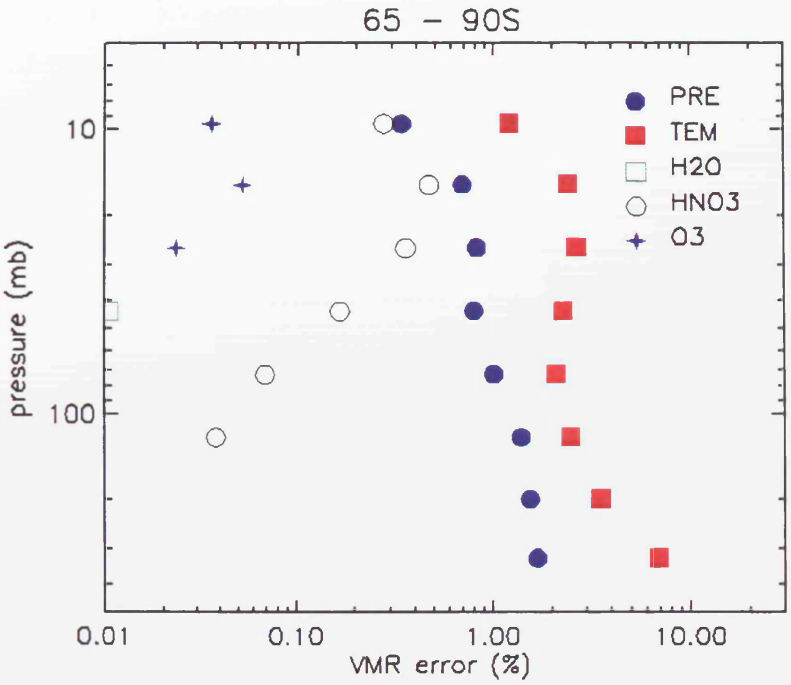

Figure 4.62 Southern Hemisphere polar (65 to 90°S) CFC-12 random model parameter errors calculated incorporating reprocessed MIPAS level 2 data on May 2nd 2003 for estimates of pressure, temperature, water vapour (H_2O), nitric acid (HNO_3) and ozone (O_3) covariance.

For CFC-12, high estimates of random model parameter error (Figure 4.59 to Figure 4.62) arise from pressure and temperature uncertainties in all regions, with temperature errors in turn generally higher than the pressure errors. Temperature errors are highest at the highest pressure (corresponding approximately to 9 km altitude) ranging from 7 to 39 % and generally decrease with decreasing pressure. Pressure errors are lower than 3 % for all regions. Nitric acid and ozone errors increase with decreasing pressure but both gases contribute less than 1 % each to the total model parameter error - a result independent of latitude.

4.2.6.2 Systematic error sources

Systematic error sources for the MIPAS-E measurements include model parameter, gain, offset and spectroscopic uncertainties. The random component of model parameter error was evaluated in the previous section (4.2.6.1). The systematic components of model parameter error establish an upper limit to the error that would propagate into the retrieval if the interfering parameter were underestimated or overestimated throughout the whole retrieval range. This could arise chiefly due to incorrect spectroscopic line data used in the prior retrieval of the interfering gases or if tropospheric concentrations of one of the interfering gases were increasing rapidly and the gas had a decadal or longer lifetime in the stratosphere and the measurements or modelled data to comprise the climatology were several years old, the effect may introduce errors into the target gas retrieval.

The estimated error in the MIPAS-E pressure, temperature and interfering gases were based on:

- Temperature – 1 K, based on the findings of Dethof [2004].
- Pressure – assumed 2 % from analysis of a limited number of level 2 data.
- Water vapour – 20 % based on the findings of Lahoz *et al.*, [2004] who reported a low tropical water vapour bias of 20 % in version 4.61 MIPAS-E data. This estimate may also be affected by larger short-term variability of tropical water vapour content. A validation study of MIPAS-E H_2O with other measurements by Weber [2004], found that POAM measured 40 % higher than MIPAS-E at 15 km.
- Ozone - 10 % although from validation studies this varied between 5 and 25 % [Kerridge *et al.*, 2004]
- Nitric acid – 10 % from the results of Oelhaf *et al*, [2004].

Another important systematic error source is uncertainties in the radiometric gain of the MIPAS-E instrument during its operational lifetime. The gain error calculates the effect an assumed ± 2 % error in measured radiance (based on the findings of Kleinert, [2004]) has on the retrieved halocarbon concentrations. Another instrumental error source is the offset error which represents inaccuracies in measuring the instruments self-emission. For MIPAS-E the offset is measured be less than 2 nW/(cm2 sr cm-1) [Spang *et al.*, 2005]. Spectroscopic errors represent inaccuracies in the HITRAN cross-section data used [Flaud *et al.*, 2003] and the propagating effect on the retrieval. For CFC-12 the spectroscopic error on the integrated cross-section was calculated at 1.2 % [Varanasi *et al.*, 1994] and for HCFC-22 3.5 % [Clerbaux *et al.* 1993].

4.2.6.2.1 HCFC-22

Tropical HCFC-22 retrievals (Figure 4.63) are dominated by spectroscopic error at all pressures, ranging from 2 % to 8% apart from at 130 mb where CFC-11 errors are expected to dominate (3 %). Temperature and pressure errors are generally above 1 % and less than 3 %. Gain error is over 1 % and less than 5 %, peaking at 350 mb. At 350 mb water vapour errors are 4 % and of a similar magnitude to the CFC-11 error, which itself is between 2 and 4 % for all heights. Below 50 mb, chlorine nitrate ($ClONO_2$) and ozone errors are greater than 1 %. From section 5.2.2.1 the $ClONO_2$ and O_3 errors are small compared to the random retrieval error. Offset error is less than 0.2 %. The total rms error for the four sources is less than 12 % for the whole profile and is no greater than 5 % between 70 and 200 mb.

Mid-latitude HCFC-22 retrievals (Figure 4.64) are also dominated by spectroscopic error at pressures below 200 mb and by gain error above. Spectroscopic error is between 2 and 11 %, and gain error between 1 and 5 %. Pressure and temperature uncertainties are generally between 1 and 2 %. For the gas model parameter errors CFC-11 is dominant and contributes between 2 % and 3 % to error budget at pressures above 70 mb. Nitric acid errors are greater than 1 % at pressures below 50 mb and peak at 3 %. Ozone errors are greater than 1 % at pressures below 20 mb and peak at 3 % at 10 mb (approximately 30 km). Offset errors are lower than 0.2 %. The total rms error is between 5 and 13 % peaking at pressures below 50 mb.

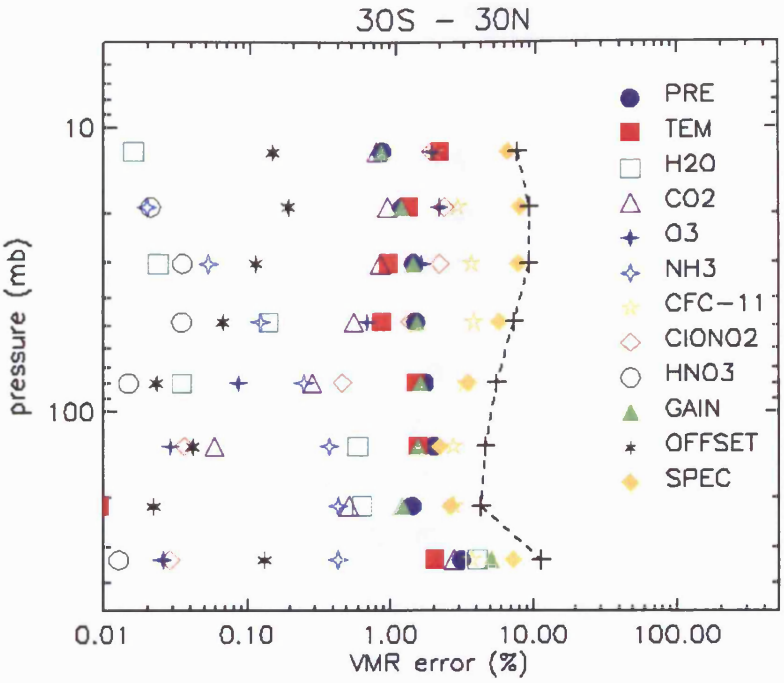

Figure 4.63 Calculated systematic errors for HCFC-22 retrievals in the tropics [30°S to 30°N]. The dashed line represents the rms of all the systematic error sources at each pressure level.

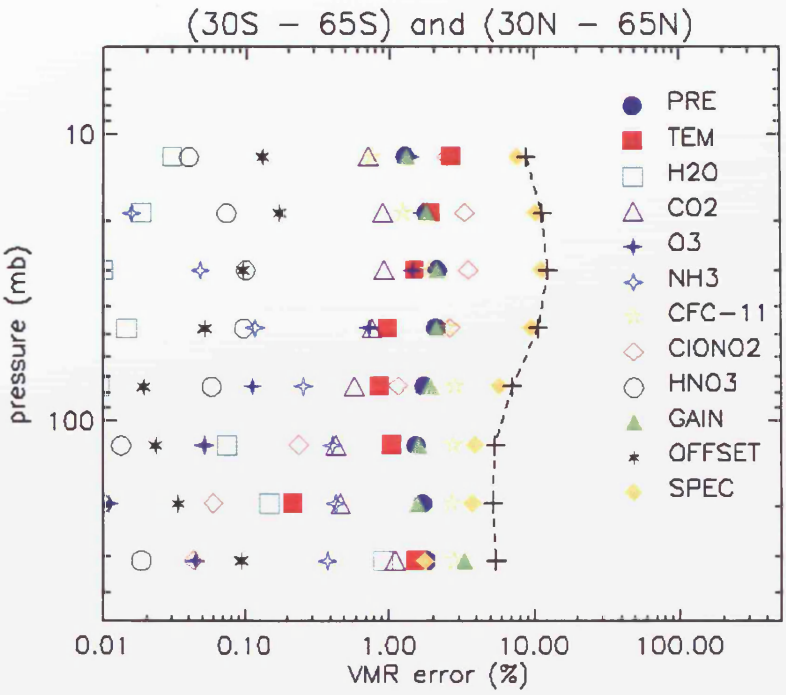

Figure 4.64 Calculated systematic errors for HCFC-22 retrievals in the mid - latitudes [30°S to 65°S and 30°N to 65°N]. The dashed line represents the rms of all the systematic error sources at each pressure level.

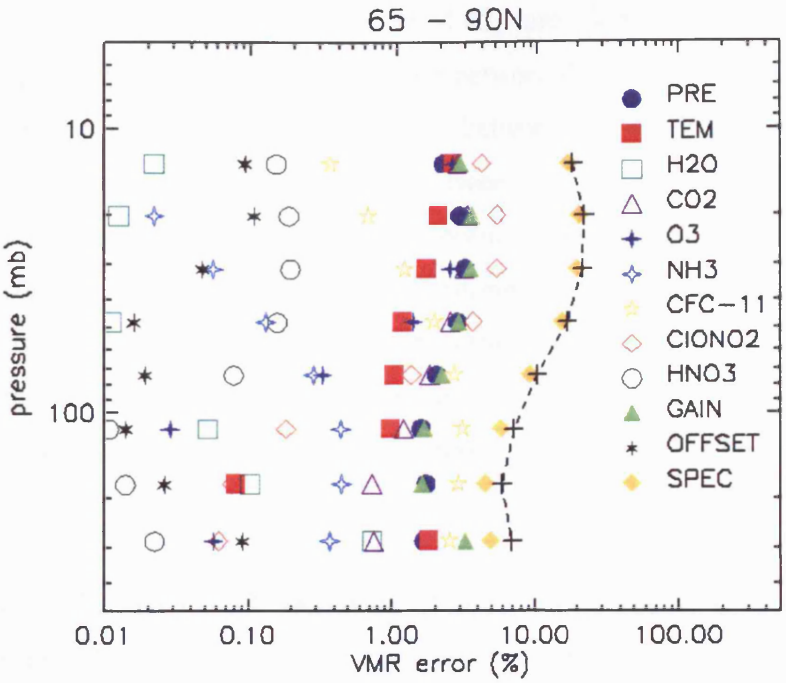

Figure 4.65 Calculated systematic errors for HCFC-22 retrievals at the summer pole [65 to 90 degrees in the summer hemisphere]. The dashed line represents the rms of all the systematic error sources at each pressure level.

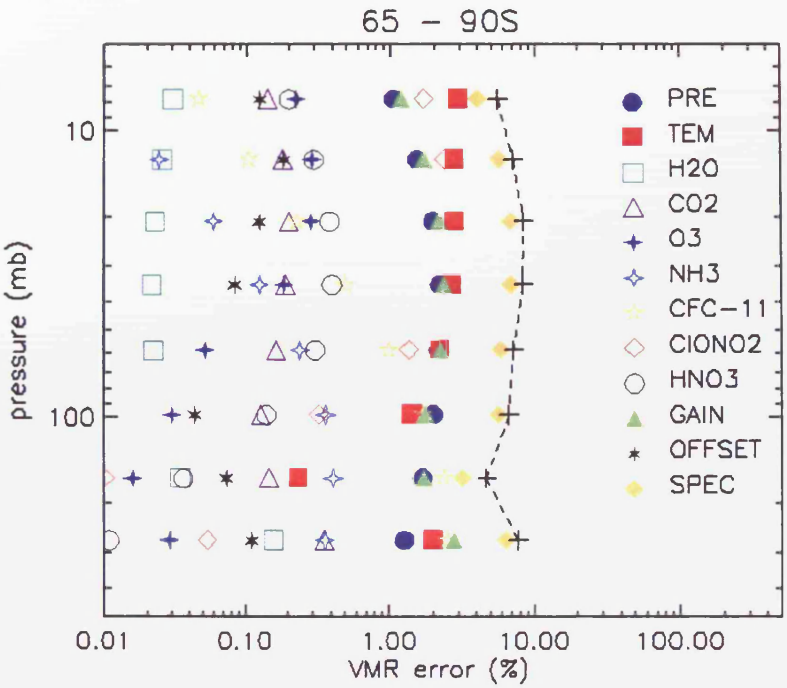

Figure 4.66 Calculated systematic errors for HCFC-22 retrievals at the winter pole [65 to 90 degrees in the winter hemisphere]. The dashed line represents the rms of all the systematic error sources at each pressure level.

Northern polar HCFC-22 retrievals (Figure 4.65) are dominated by spectroscopic uncertainties propagating into the scheme and are between 4 and 20 %. At pressures above 50 mb, the error is less than 10 %. Gain errors are between 2 and 4 %, peaking at 300 mb. Pressure and temperature errors are generally between 1 and 3 %. Gas model parameter errors are dominated by CFC-11, this error contributing a maximum of between 2 and 3 % to the budget between 70 and 300 mb. Chlorine nitrate and ozone uncertainties contribute more than 1 % below 50 mb but again, random retrieval errors dominate here with little information from the MIPAS-E measurements for HCFC-22. Offset errors amount to less than 0.1 % of the budget. The total rms error is less than 10 % and is largest at pressures below 20 mb.

In the Southern polar HCFC-22 retrievals (Figure 4.66) spectroscopic error again dominates and ranges between 2 and 6 %. Gain error is between 1 and 3 %, pressure and temperature errors are of a similar magnitude. Errors because of CFC-11 inaccuracies peak above 100 mb between 1 and 3 %. For other contaminants in the microwindow only $ClONO_2$ errors are greater than 1 %, these only occur at pressures less than 60 mb. Offset error is insignificant at less than 0.2 %. The total rms systematic error is between 4 and 7 %, generally lower than the other three regions, but random errors are shown to dominate this region.

4.2.6.2.2 CFC-12

Tropical CFC-12 retrievals (Figure 4.67) are dominated by uncertainties in the gain at pressures above 30 mb, uncertainties between 1 % at 30 mb and 9 % at 350. Temperature, pressure and spectroscopic errors each contribute over 1 % to the error budget at pressure above 30 mb with pressure errors contributing approximately 2 % at each pressure level. Temperature and spectroscopic errors are more variable and peak at 5 % each at 350 mb. Model parameter errors and offset errors each contribute less than 1 %. Root mean square (rms) results show that the total systematic error for the four sources is less than 12 % for the whole profile and generally less than 5 % at pressure below 350 mb.

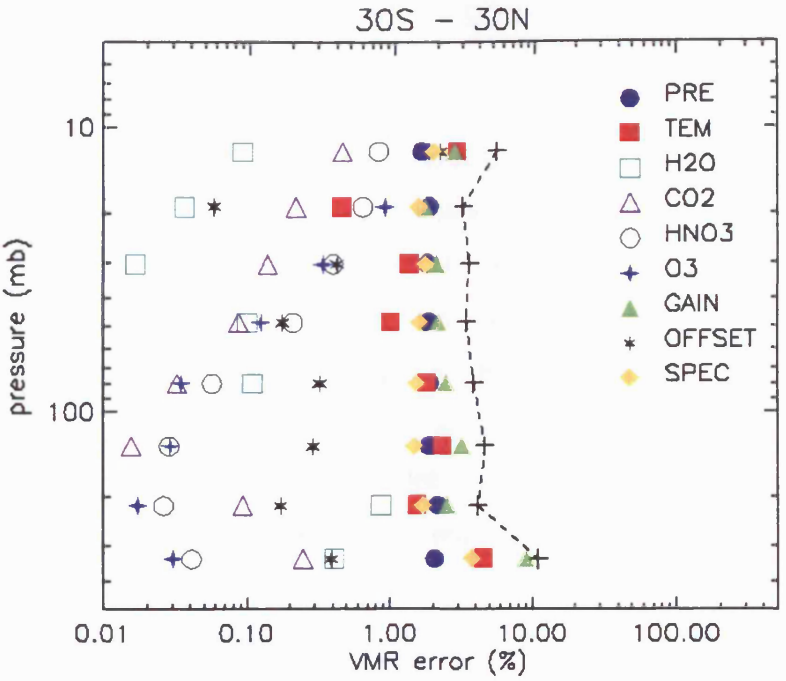

Figure 4.67 Calculated systematic errors for CFC-12 retrievals in the tropics [30°S to 30°N]. The dashed line represents the rms of all the systematic error sources at each pressure level.

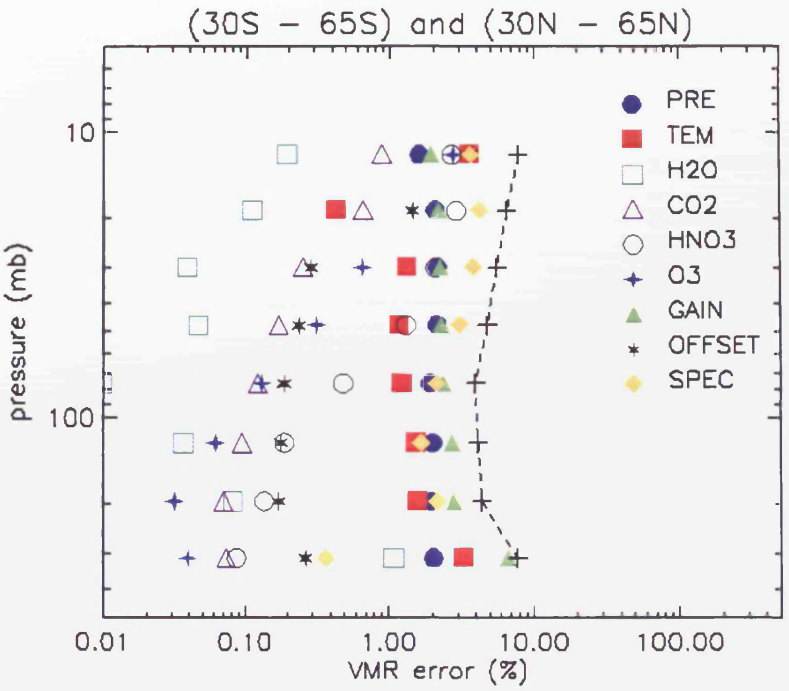

Figure 4.68 Calculated systematic errors for CFC-12 retrievals in the mid-latitudes [30°S to 65°S and 30°N to 65°N]. The dashed line represents the rms of all the systematic error sources at each pressure level.

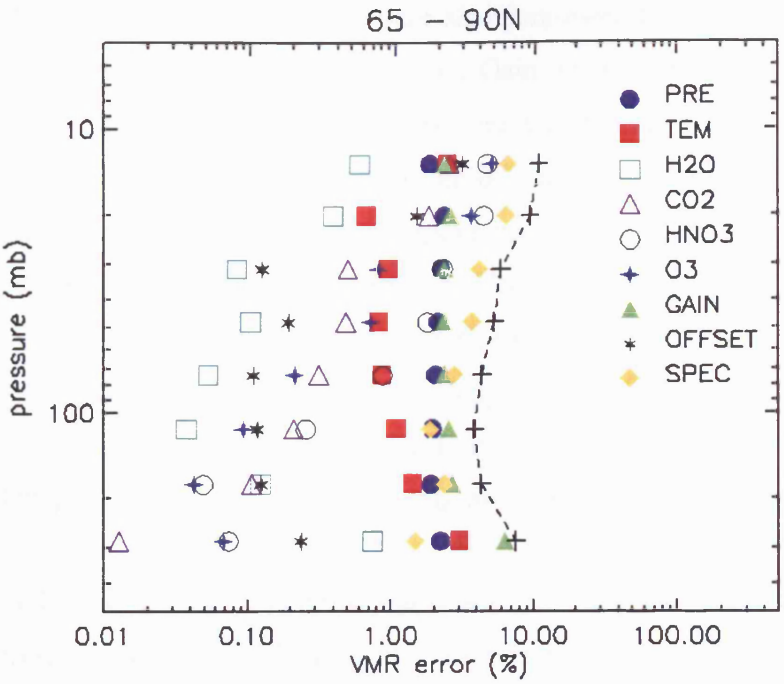

Figure 4.69 Calculated systematic errors for CFC-12 retrievals at the summer pole [65 to 90 degrees in the summer hemisphere]. The dashed line represents the rms of all the systematic error sources at each pressure level.

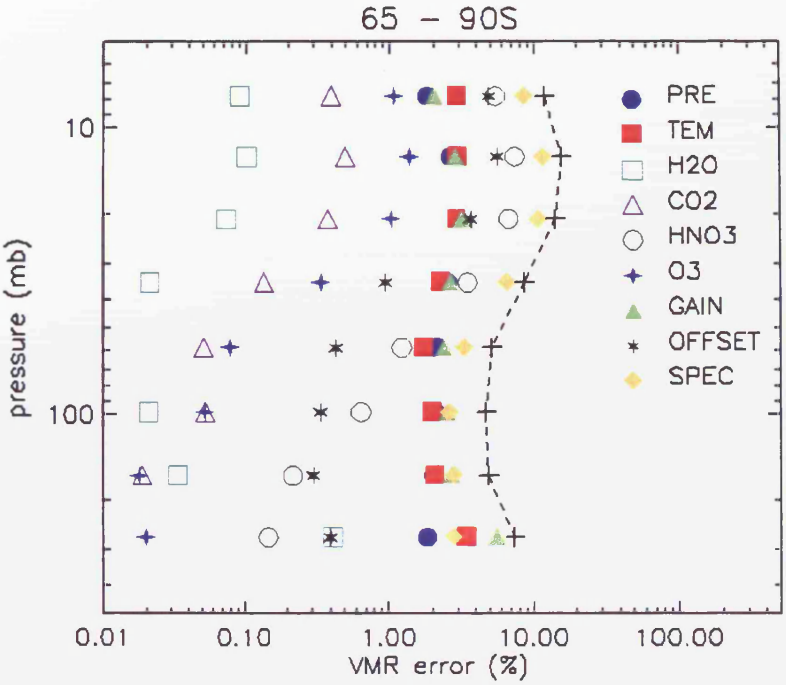

Figure 4.70 Calculated systematic errors for CFC-12 retrievals at the winter pole [65 to 90 degrees in the winter hemisphere]. The dashed line represents the rms of all the systematic error sources at each pressure level.

Mid-latitude CFC-12 retrievals (Figure 4.68) are also dominated by gain error at pressures above 70 mb and by spectroscopic errors below. Gain errors are between 2 and 7 %, spectroscopic errors between 0.5 and 4 %. Pressure and temperature uncertainties are similar for each level and each contribute between 0.5 and 4 % to the total error budget. For the gas model parameter errors water vapour contributes 1 % to error budget at pressure above 350 mb but below 1 % at pressures below this. Nitric acid errors are greater than 1 % at pressures below 50 mb and peak at 3 %. Ozone errors are greater than 1 % at pressures below 20 mb and peak at 3 % at 10 mb (approximately 30 km). Offset errors are greater than 1 % at pressures below 20 mb and do not exceed 3 %. The total rms error is between 4 and 8 % peaking at pressures above 350 mb where gain error is largest.

Northern polar CFC-12 retrievals (Figure 4.69) are generally dominated by gain and spectroscopic errors but with a significant contribution from both temperature and pressure uncertainties at higher pressures and ozone, nitric acid and offset errors at lower pressures. Gain errors again dominate at pressures above 100 mb ranging between 2 % at 100 mb and 7 % by 300 mb. Below 100 mb spectroscopic errors are largest at between 2 and 7 %. Water vapour error contribution is less than 1 % for the 10 to 400 mb range. Below 50 mb uncertainties in nitric acid measurements contribute an error greater than 1 %, ozone and carbon dioxide error is greater than 1 % at pressures below 20 mb. The total rms error is less than 10 % and is largest at pressures below 20 mb.

Southern polar CFC-12 retrievals (Figure 4.70) are mostly dominated by spectroscopic errors although gain error dominates at 300 mb. Spectroscopic error ranges between 2 % at 100 mb and 10 % below 20 mb. Pressure and temperature errors contribute between 2 and 4 % each for every level of the retrieval. Gain error has a similar error profile to temperature and the error never exceeds 6 %. Model parameter errors are dominated by nitric acid, with this error source above 1 % below 60 mb and peaking at 7 % at 15 mb. Offset error is between 1 and 6 % between 5 and 35 mb. The total rms error budget is between 4 and 17 %.

4.2.6.3 Total Error

This section shows the total error calculation on a single retrieval for HCFC-22 and CFC-12. Both total random errors (including retrieval and model parameter) and

systematic errors (including model parameter, spectroscopic and instrument gain and offset) were evaluated and a total error on each measurement calculated.

Table 4.13 shows the total random error on a single measurement. For HCFC-22 the lowest random errors were at 9 km in mid-latitudes (16 %) and increasing globally up to 100 % by 30 km. Single profile HCFC-22 data were dominated by random retrieval error throughout the whole profile.

For CFC-12, the lowest random errors were at 12 km (globally) at approximately 4 % on a single measurement. The error increased with altitude, reaching 25 % at the winter pole at 30 km. The highest random error was in the tropics at 9 km (40 %) which was due to MIPAS-E temperature and water vapour uncertainties.

GAS	REGION	TOTAL RANDOM ERROR (%)							
		9 km	12 km	15 km	18 km	21 km	24 km	27 km	30 km
HCFC-22	T	17.3	26.1	51.8	69.4	76.3	85.9	93.7	97.6
	M	15.9	29.0	46.2	60.7	74.0	85.8	94.0	97.8
	PS	18.7	28.9	40.7	54.8	68.6	81.8	91.7	96.5
	PW	22.2	41.4	60.6	77.1	88.7	94.2	97.8	99.3
CFC-12	T	39.8	4.5	7.1	8.0	8.9	10.8	13.6	15.9
	M	14.7	4.5	5.1	6.5	9.3	13.6	18.7	22.5
	PS	18.5	4.1	4.1	5.5	8.2	12.3	18.9	23.5
	PW	8.0	6.5	8.6	12.4	17.9	21.9	24.3	25.0

Table 4.13. Total random error for each CFC-12 and HCFC-22 data point retrieved from MIPAS-E data using OPERA. (Abbreviations: T = tropics [30°S to 30°N], M = mid-latitudes [30 to 65 degrees], PS = polar summer [65 to 90 degrees - summer Hemisphere], PW = polar winter [65 to 90 degrees - winter Hemisphere]

Systematic errors were less variable than the random component. For HCFC-22, the error ranged from a low 4 % in the tropics at 12 km, up to 22 % at 27 km at the summer pole. For heights where most information comes from the measurement, the systematic error was less than 11 %.

The lowest systematic component for CFC-12 was in the tropics at 3 % between 21 and 27 km. The highest error was actually found lower down in the atmosphere at 9 km in the tropics. The accuracy of tropical CFC-12 data at 9 km suffered from uncertainties in MIPAS-E temperature, but instrument gain and spectroscopic uncertainties were also important.

GAS	REGION	TOTAL SYSTEMATIC ERROR (%)							
		9 km	12 km	15 km	18 km	21 km	24 km	27 km	30 km
HCFC-22	T	11.4	4.3	4.5	5.5	7.3	9.2	9.2	7.5
	M	8.1	5.1	5.5	7.0	10.4	12.2	11.2	8.6
	PS	6.9	5.9	7.1	10.3	16.9	21.6	22.2	18.4
	PW	7.6	4.5	6.4	6.9	8.1	8.2	7.0	5.4
CFC-12	T	11.1	4.1	4.5	3.8	3.3	3.5	3.0	5.1
	M	7.7	4.2	4.0	3.8	4.6	5.4	6.0	7.2
	PS	7.5	4.3	3.8	4.3	5.2	5.7	8.6	9.5
	PW	7.3	4.8	4.5	4.9	8.3	13.8	15.3	11.7

Table 4.14. Total systematic error for CFC-12 and HCFC-22 retrieved from MIPAS-E data using OPERA. (Abbreviations: T = tropics [30°S to 30°N], M = mid-latitudes [30 to 65 degrees], PS = polar summer [65 to 90 degrees - summer Hemisphere], PW = polar winter [65 to 90 degrees - winter Hemisphere]

GAS	REGION	TOTAL ERROR (%)							
		9 km	12 km	15 km	18 km	21 km	24 km	27 km	30 km
HCFC-22	T	20.8	26.5	52.0	69.6	76.6	86.4	94.2	97.9
	M	16.8	29.5	46.5	61.1	74.7	86.6	94.7	98.2
	PS	19.9	29.5	41.3	55.8	70.6	84.6	94.3	98.2
	PW	23.5	41.6	60.9	77.4	89.1	94.6	98.0	99.4
CFC-12	T	41.3	6.1	8.4	8.8	9.5	11.3	13.9	16.7
	M	16.5	6.2	6.4	7.6	10.4	14.6	19.7	23.7
	PS	20.0	5.9	5.6	7.0	9.7	13.5	20.8	25.3
	PW	10.8	8.1	9.7	13.3	19.8	25.9	28.7	27.6

Table 4.15. Total error (both random and systematic components) for CFC-12 and HCFC-22 retrieved from MIPAS-E data using OPERA. (Abbreviations: T = tropics [30°S to 30°N], M = mid-latitudes [30 to 65 degrees], PS = polar summer [65 to 90 degrees - summer Hemisphere], PW = polar winter [65 to 90 degrees - winter Hemisphere].

The total error for a single HCFC-22 measurement was dominated by random error and to obtain useful information from the single profiles, many data had to be averaged. The error increased for all regions with height but was less than 25 % for 9 km data and increasing with altitude. By 21 km, errors were globally no better than 70 %.

For CFC-12, the total error on a single measurement varied between 6 and 14 % in the tropics between 12 and 27 km. Tropical 9 km data had an associated error of 41 % due to large temperature, gain and spectroscopic uncertainties. In mid-latitudes and the summer

pole, the total error was better than 10 % between 12 and 21 km giving very good accuracy for single profile retrievals. At 9 km both the mid-latitude and polar data had an error of 17 % and 20 % respectively. Polar winter retrievals below 18 km had a total error of less than 14 %.

4.3 Summary

This chapter has attempted to identify HCFC-22 in MIPAS-E spectra. Using RFM simulations it has been possible to simply identify two spectral regions dominated by HCFC-22 emission between 12 and 21 km. Both regions could potentially be used for HCFC-22 retrievals but it has been decided that due to the domination of the 829 cm^{-1} feature in that particular wavenumber range and the fact that all interfering contributors are at or below the MIPAS-E NESR level the 828.95 to 829.15 cm^{-1} range is the one to be used.

Random retrieval errors have been calculated for HCFC-22, CFC-12 and aerosol. This error source is lowest for both HCFC-22 and CFC-12 at 9 km globally (less than 25% and 4 % respectively). The error increases with altitude for both gases. The same is not true for total extinction. The climatology aerosol profile is almost constant with height above 21 km. With warmer stratospheric temperatures, the signal will increase with altitude, lowering the error.

Retrieval tests on synthesised spectra were performed to both maximise the accuracy of the results from the scheme and also minimise iteration time. It was found that by reducing the number of gases and reducing the resolution of the fine mesh calculations (section 4.2.2.1.3), it was still possible to retrieve perturbed HCFC-22 and CFC-12 profiles to an accuracy of better than 10 %. The retrieved total extinction however was affected by reducing the resolution and number of gases. Although the retrieved extinction compared to the known profile was generally better than 40 %, the differences in some data exceeded 50 %. It was decided that MIPAS-E retrievals, for both optimum accuracy and low iteration time, to perform retrievals from MIPAS-E data using a fine mesh resolution in the model of 0.01 cm^{-1}. The gases that should be included for the HCFC-22 window are HCFC-22, CFC-11, H_2O, CO_2, O_3, HNO_3, $ClONO_2$, C_2H_6 and aerosol. For the CFC-12 window it was decided to include CFC-12, H_2O, CO_2, HNO_3, CFC-113 and aerosol. The

aerosol microwindow should include H_2O, CO_2, O_3, HNO_3, C_2H_6, CFC-11, HCFC-22, $ClONO_2$ and aerosol.

To test the scheme on measured MIPAS-E data, retrievals of both HCFC-22 and CFC-12 were performed from data on May 2nd 2003. A positive difference was found in the mean profile of the data compared to the climatology of up to 40 pptv. This is investigated further in chapter 6. The CFC-12 data were very similar to the climatology exhibiting the same profile shape. The best agreement was between the tropical results at better than 15 %. Between 50 and 300 mb agreement was better than 3 %.

A full error analysis on the expected accuracy of the trace gas retrieval was also carried out in this chapter. This included both the random and systematic components on an individual retrieval. The HCFC-22 total error was dominated by the random error, due mainly to the random retrieval component. The lowest errors were at 9 km at less than 24 %. For CFC-12, the lowest errors were at 12 km globally at less than 9 % and below 24 km the CFC-12 total errors were less than 25 %. The only exception to this was in the tropics at 9 km where the total error was over 40 %. The reason for this was the propagation of temperature uncertainties in the MIPAS-E operational product into OPERA.

Averaging data will reduce the random retrieval noise by a factor of the square root of the number of measurements. Therefore when analysing data from a whole week, random error is greatly reduced and is not significant.

Systematic errors for HCFC-22 are less than 12 % below 18 km. At the poles the systematic errors are comparable between 9 and 15 km to within 2 %. There are differences between 9 km and 15 km in the mid-latitudes of 3 % increasing up to 7 % in the tropics.

For CFC-12, the systematic errors show little change with altitude. In particular the tropical systematic error is between 3 and 5 % between 12 and 30 km. The mid-latitude data only vary between 4 and 7 % over the same altitude range. Polar summer errors are between 4 and 6 % at 12 to 24 km. Polar winter errors exhibit the most variability with altitude although between 12 and 18 km the error varies by less than 1 %. At 9 km, the systematic error is higher than that at 12 km by between 2 % in the polar winter and 7 % in the tropics.

Chapter 5

5 Validation of halocarbon retrievals

5.1 Introduction

Data derived from satellite measurements requires both good calibration of the satellite sensors and also wherever possible validation of the geophysical parameter being derived. Calibration of the MIPAS-E instrument is performed routinely and is outlined in sections 3.3 and 3.4.

Validation of data is a measure of the quality of derived products from the sensor (for MIPAS-E this is routinely the pressure, temperature and gas volume mixing ratio (vmr) data derived from the fully-calibrated level 1b spectra) as measured by independent means. This can be done by direct profile comparisons with other independent measurements of the same scene (section 5.4), by indirect assessments of expected mixing ratios or by verification with results retrieved from the same spectral measurements but performed by an independent scheme (section 5.2).

Indirect assessments for validation can be performed by taking advantage of knowledge of surface measurements, which for well-mixed gases such as the halocarbons will also yield information of their concentration in the upper troposphere. In the lower stratosphere, the quality of the OPERA retrieved halocarbon data can be examined by taking advantage of expected correlation relations with other long-lived species such as nitrous oxide or methane (for example [Plumb, 1996] or [Chang *et al.*, 1996]). The benefit of using surface measurements and correlations with other well-mixed species is that the trend of these compounds can also be examined over time.

Unfortunately, not as much correlative HCFC-22 data were available as would be desirable. The HCFC-22 comparisons in this chapter relied on direct comparisons with ACE satellite data. Other sources were less direct and included surface measurements and inferred values from ATMOS data.

5.2 Comparison with retrievals using a rapid radiative transfer approach

ICG-1, the scientific research institute in Juelich, has developed its own retrieval scheme (described in section 2.5.6) to retrieve concentrations of halocarbons in the atmosphere, primarily CFC-11 and CFC-12, from MIPAS-E data. To test the quality of (CFC-12) OPERA retrievals, a verification of the consistency between results from the Juelich and the OPERA joint retrieval schemes is presented. Unfortunately, HCFC-22 comparisons could not be undertaken because of the problems with the Juelich scheme for this molecule.

Twelve scans were chosen from MIPAS-E near real time (NRT) level 1b (version 4.57) data from orbit 06117 on May 2nd 2003 for comparison. These comprised of three profiles from each of the four latitude bands used to investigate the accuracy of the OPERA retrievals from synthesised spectra in section 4.2.2.1. This choice gave a good global sample of data to compare.

The two schemes both employ an optimal estimation approach. The main difference is the rapid forward modelling based on a broad-band approach and the use of emissivity look-up tables (precomputed based on 'exact' line-by-line calculations) by the Juelich scheme to compute the atmospheric radiative transfer. This is compared to the line-by-line radiance calculations performed by the OPERA scheme at each iteration. The parameters for tabulation by the Juelich approach are pressure, temperature and gas concentration, chosen to expand over the range of expected atmospheric conditions. The total CFC-12 error from the Juelich data was calculated to be between 7 and 10 % in the upper troposphere and lower stratosphere (Hoffmann *et al.*, 2004), compared to between 6 and 20 % in the OPERA estimation.

Both OPERA and the Juelich scheme reject spectra where the measured spectrum from the adjacent tangent height below is cloudy (CI < 1.8). However, the Juelich scheme rejects the height above whereas OPERA rejects only the cloudy height. This is important for some of the later retrievals. The test conditions were:

- CFC-12 microwindow (921.4 to 924.4 cm^{-1})
    - Gases included: CFC-12, H_2O, CO_2, HNO_3, NH_3, CFC-113 and aerosol.

- total extinction microwindow (832.3 to 834.4 cm^{-1})
    - Gases included: H_2O, CO_2, O_3, CFC-113, CFC-12, HNO_3, CFC-11, HCFC-22, C_2H_6, NH_3 and aerosol.
- CFC-12 *a priori* profile is the same in each scheme.
- Reference atmospheres from the version 3.1 files of Remedios [1999].
    - Profile information for CFC-113 from Dudhia, personal communication.
    - Profiles for pressure and temperature were superseded by MIPAS-E near real time (version 4.57) pressure and temperature data.
- CFC-12 *a priori* covariance of 25 % for OPERA. The *a priori* for Juelich was based on the one sigma values in the reference atmosphere.
- OPERA *a priori* aerosol profile based on a profile constructed from HALOE averages [Spang, personal communication], whereas the Juelich aerosol profile had a constant aerosol *a priori* extinction profile of 10^{-6} ext/km.
    - OPERA and Juelich scheme assumes a 1000 % aerosol *a priori* covariance.
- The MIPAS-E measurement noise ($\mathbf{S_y}$) of 30 nW/(cm^2 sr cm^{-1}) in both codes.
- 3 km 5-point field of view (described in section 2.4.1.1.3)
- Apodized instrument line shape (AILS) applied to the modelled spectra, as provided by the European Space Agency [Nett *et al.*, 2000].
- Cross-section and line data were taken from the HITRAN 2000 database.

5.2.1 Tropical [30°S to 30°N]

The three cloud-free tropical scans chosen were numbers 20 (6.8°N, 9.9°W, time scan identity (TID)-105187515), 22 (3.8°S, 9.9°W, TID-105187687) and 24 (13.9°S, 9.9°W, TID-105187849). Each of these scans had complete MIPAS-E level 2 NRT pressure and temperature data between 12 and 30 km inclusive.

All three tropical profiles displayed similar profile shapes (Figure 5.1a) between the OPERA and Juelich CFC-12 retrievals with the oscillations correlating closely. In particular, both schemes identified an anomalously high CFC-12 feature in scan number 24

at 230 mb (approximately 12 km) which could be due to inaccurate NRT pressure or temperature data at that height.

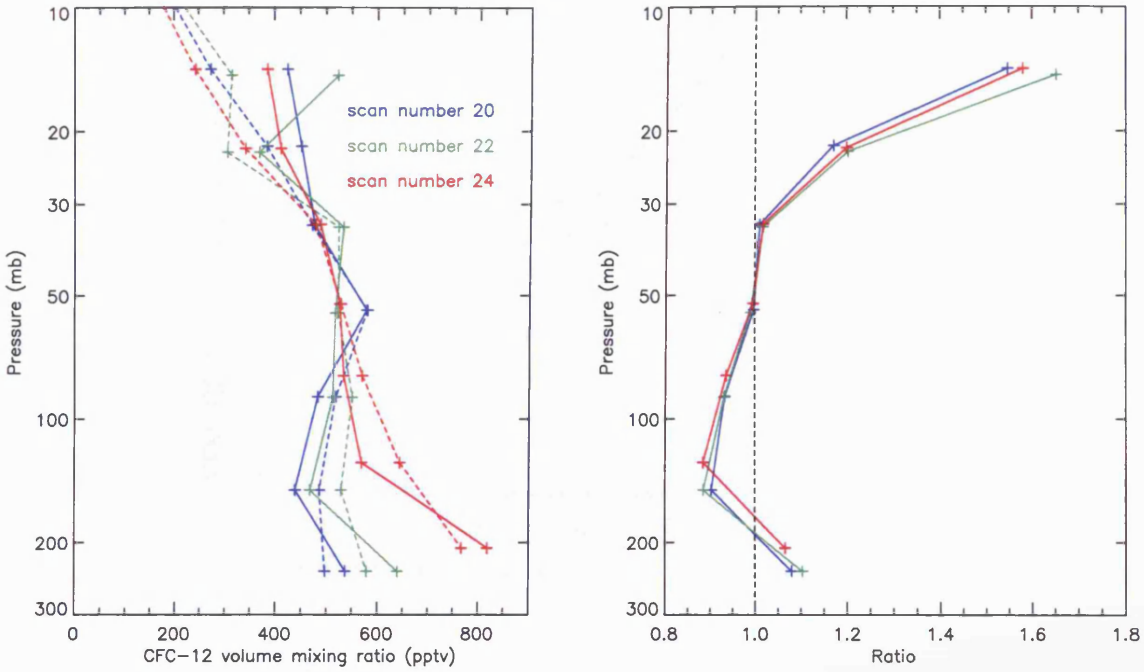

Figure 5.1 (a) retrieved CFC-12 data from OPERA (solid lines) and Juelich (dashed lines) schemes in the tropics. Data are from scan numbers 20 (6.8°N, 9.9°W, time scan identity (TID)-105187515 - blue), 22 (3.8°S, 9.9°W, TID-105187687 – green) and 24 (13.9°S, 9.9°W, TID-105187849 - red) from orbit 06117 on May 2nd 2003. (b) ratio plot of OPERA:Juelich results.

Overall, the profiles agreed to within 10 % between 12 and 24 km (30 to 250 mb). Above 24 km (below 30 mb), the OPERA results were up to 70 % higher than those from the Juelich scheme. The correlation between the two sets (Figure 5.2) of results was quite compact but was not conclusive. It appeared that where the Juelich scheme retrieved a CFC-12 concentration of below 400 pptv, there was a tendency for the OPERA concentration to be on average 100 pptv higher. Above 400 pptv, there was no systematic difference between the two datasets. It is not understood why there was such a difference between the data above 24 km although the differences in aerosol extinction results presented in section 5.2.5 may explain some of the differences.

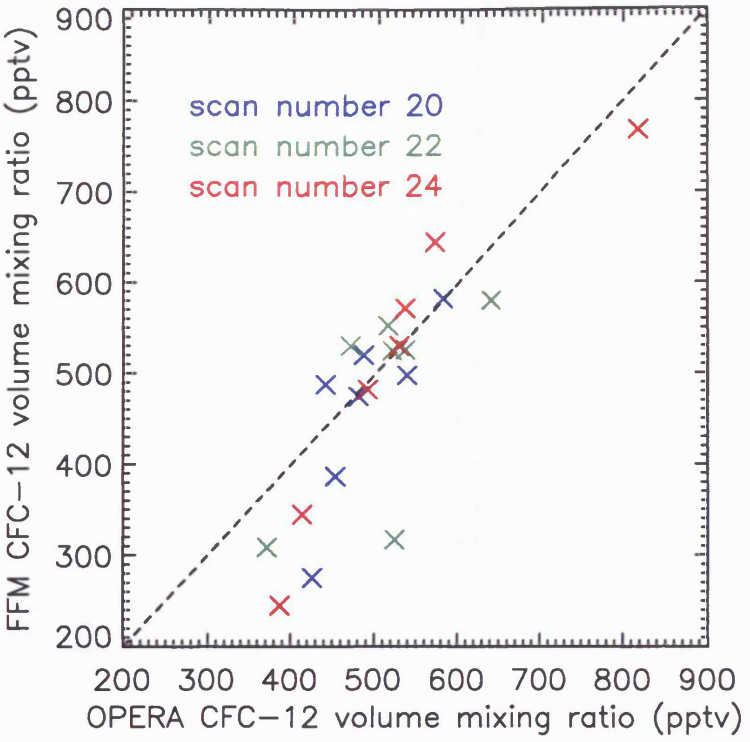

Figure 5.2 Correlation plot of Juelich CFC-12 data from their fast forward model (FFM) scheme against the OPERA CFC-12 data, orbit 06117 (May 2nd 2003), scan numbers 20, 22 and 24, in the tropics.

5.2.2 Mid-latitudes [30 to 65°S and 30 to 65°N]

The three mid-latitude scans incorporated both Northern Hemisphere and Southern Hemisphere data. The scans chosen from orbit 06117 were numbers 11 (51.5°N, 4°S, TID-105186766), 31 (47.9°S, 16.1°W, TID-105188426) and 33 (58.3°S, 17.3°W, TID-105188599).

The 9 km sweep of scan number 32 had a CI of 1.47 implying that an optically thick cloud was within the 9 km field of view. Although the 12 km sweep had a much higher CI of 5.8, suggesting no cloud contamination in the field of view of the 12 km measurement, the Juelich scheme rejected the entire scan, hence the lack of CFC-12 data at this point.

All three retrieved profiles showed excellent agreement in the profile shape between both schemes (Figure 5.3). The differences between the OPERA and Juelich results were less than 10 % between 12 and 18 km (approximately 250 to 50 mb), up to 21 km for scans 11 (Northern Hemisphere) and 31 (Southern Hemisphere). Below 50 mb, differences between the OPERA and Juelich data were above 10 %.

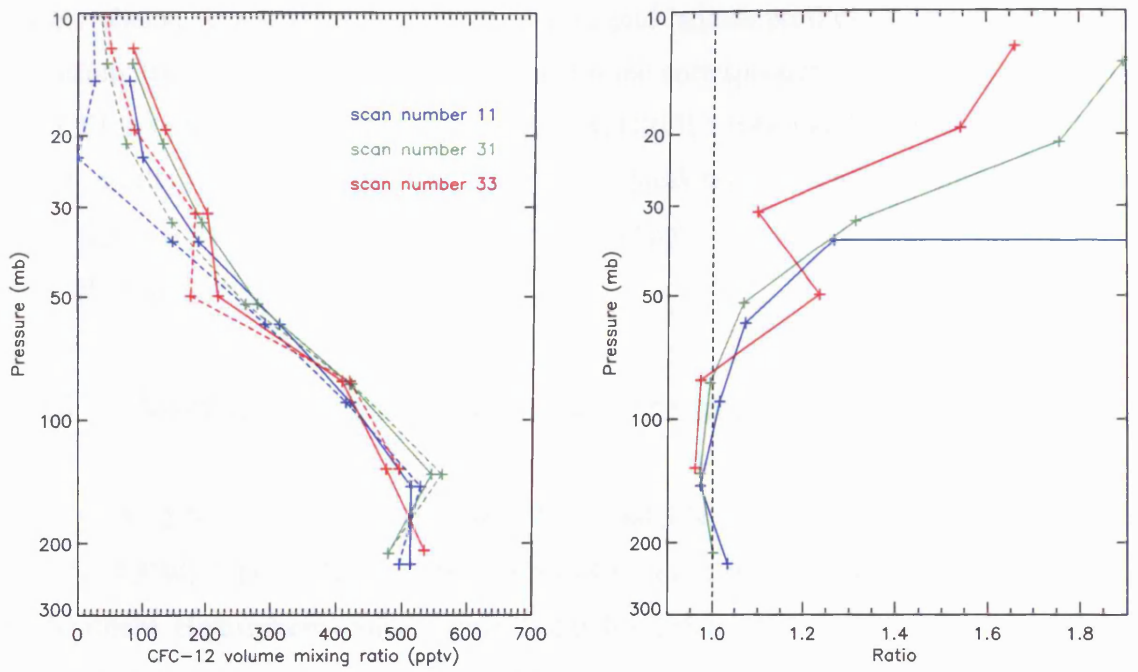

Figure 5.3 (a) retrieved CFC-12 data from OPERA (solid lines) and Juelich (dashed lines) schemes in the mid-latitudes. Data are from scan numbers 11 (51.5°N, 4°S, time scan identity (TID)-105186766 - blue), 31 (47.9°S, 16.1°W, TID-105188426 - green) and 33 (58.3°S, 17.3°W, TID-105188599 - red) from orbit 06117 on May 2nd 2003. (b) ratio plot of OPERA and Juelich results

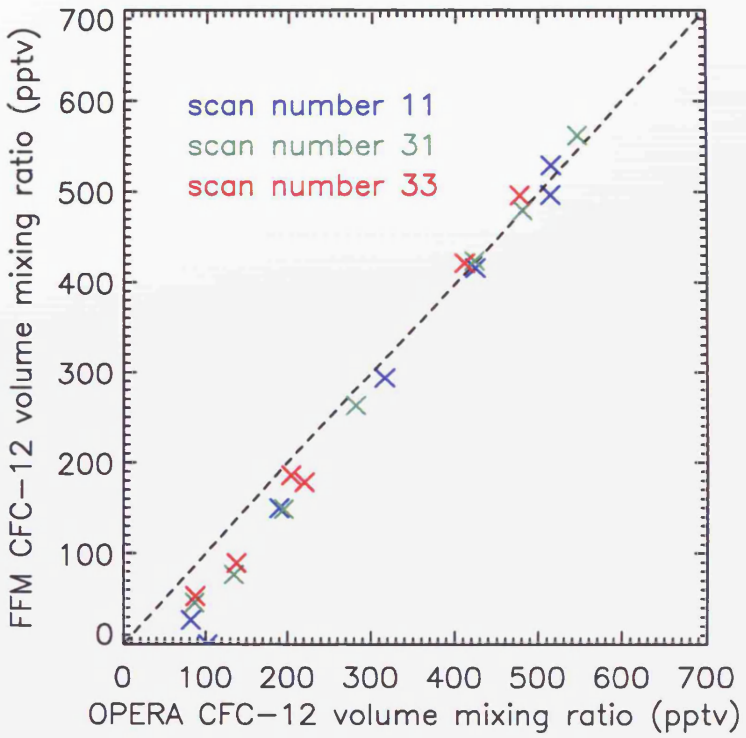

Figure 5.4 Correlation plot of Juelich CFC-12 data from their fast forward model (FFM) scheme against the OPERA CFC-12 data, orbit 06117 (May 2nd 2003), scan numbers 11, 31 and 33, in the mid-latitudes.

The correlation between the results for the three mid-latitude profiles was tight (Figure 5.4) and results lay to within 50 pptv of the one-to-one correspondence line. However, where the OPERA CFC-12 vmrs were below 350 pptv, OPERA was high biased compared to the Juelich results (compare Figure 5.3b and the tropical results). The maximum difference was 60 pptv, but the mean difference was below 40 pptv over the whole altitude range. The shape of the ratio plot is similar for both.

5.2.3 Northern Hemisphere polar region [65 to 90°N]

Scans 3 (89.2°N, 87.9°E, TID-105186107), 5 (80.5°N, 0.7°W, TID-105186269) and 7 (70.5°N, 1.3°W, TID-105186442) from ENVISAT orbit 06117 were chosen to represent the Northern Hemisphere polar region (latitudes greater than 65°N). It is noted that, although very early in the Northern Hemisphere summer season, the polar summer climatology was used in both schemes as it was the most representative *a priori* CFC-12 profile available.

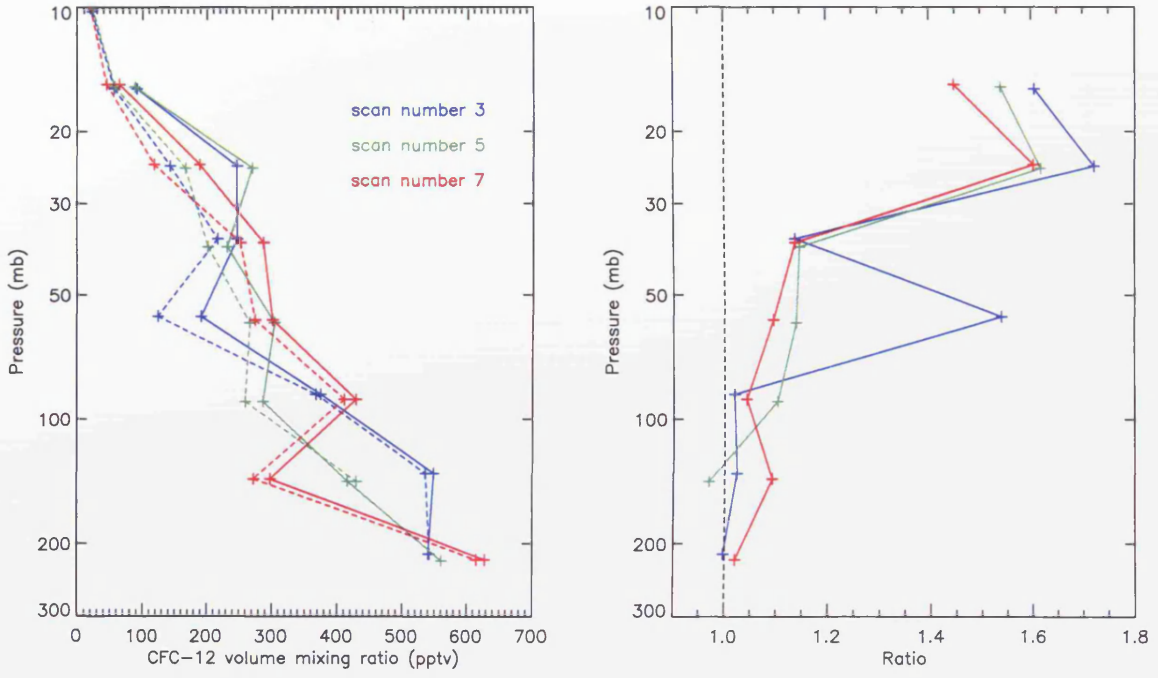

Figure 5.5 (a) retrieved CFC-12 data from OPERA (solid lines) and Juelich (dashed lines) schemes in the Northern Hemisphere. Data are from scan numbers 3 (89.2°N, 87.9°E, time scan identity (TID)-105186107 - blue), 5 (80.5°N, 0.7°W, TID-105186269 - green) and 7 (70.5°N, 1.3°W, TID-105186442 – red) from orbit 06117 on May 2nd 2003. (b) ratio plot of OPERA and Juelich results.

As for the tropics and mid-latitudes, there was an overall good agreement between the oscillations in the profiles with OPERA results slightly higher compared to Juelich (Figure 5.5). The differences increase with height (decreasing pressure) from below 10 % at pressures above 80 mb, up to 70 % below 30 mb (Figure 5.5b).

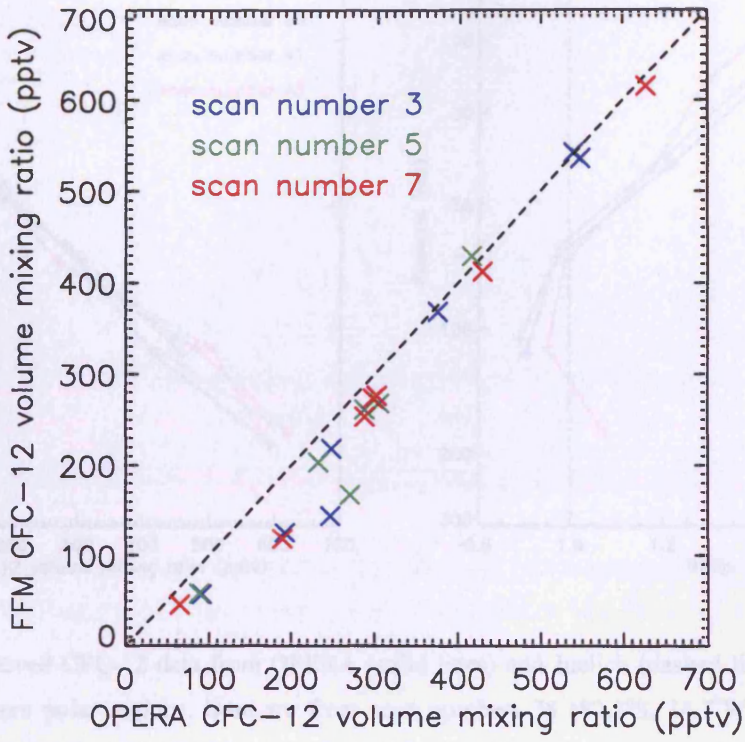

Figure 5.6 Correlation plot of Juelich CFC-12 data from their fast forward model (FFM) scheme against the OPERA CFC-12 data, orbit 06117 (May 2nd 2003), scan numbers 3, 5 and 7, in the Northern Hemisphere polar region.

The Northern Polar correlation plot (Figure 5.6) shows a fairly compact relationship between the OPERA and Juelich results with comparison of the mean to within 30 pptv. For Juelich results below 300 pptv, there was a mean systematic high bias compared to OPERA vmrs of 40 pptv.

5.2.4 Southern Hemisphere polar region [65 to 90°S]

Scan numbers 38 (82.3°S, 34.7°W, TID-105189014), 41 (82.5°S, 175.0°W, TID-105189257) and 43 (72.6°S, 174°E, TID-105189429) were chosen for comparison to represent the Southern Hemisphere polar region (latitudes greater than 65°S). The polar winter climatology was used as the *a priori* estimate for CFC-12 (and in the forward

modelling for the interfering gases). As for the other regions, NRT (version 4.57) level 2 MIPAS-E data were used to ascertain pressure and temperature information.

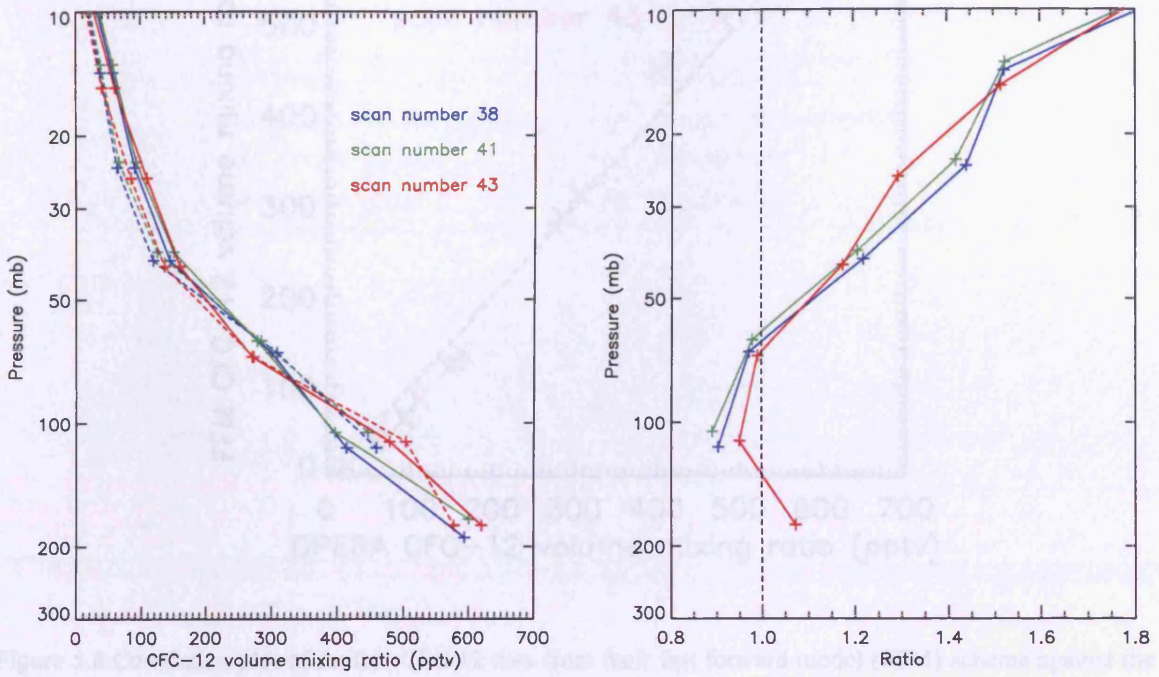

Figure 5.7 (a) retrieved CFC-12 data from OPERA (solid lines) and Juelich (dashed lines) schemes in the Southern Hemisphere polar regions. Data are from scan numbers 38 (82.3°S, 34.7°W, time scan identity (TID)-105189014 - blue), 41 (82.5°S, 175.0°W, TID-105189257 - green) and 43 (72.6°S, 174°E, TID-105189429 – red) from orbit 06117 on May 2nd 2003. (b) ratio plot of OPERA and Juelich results.

The Southern polar profiles were the least oscillatory (Figure 5.7) of all regions. There was good agreement to within 20 % between 40 and 200 mb. Above 50 mb, the OPERA results were up to 10 % lower than those from the Juelich scheme. Conversely, at pressures below 50 mb, OPERA results were generally higher than the Juelich vmrs by between 20 and 80 %. The only data at 12 km (190 mb) was from scan 43 and the results agreed to 7 %.

The correlation plot (Figure 5.8) of results from both schemes was very compact. The mean agreement was better than 20 pptv (less than 5 %). As for the three other regions, OPERA CFC-12 vmrs were higher than Juelich results at pressures below 50 mb (and where Juelich CFC-12 is below 150 pptv). OPERA data were higher by an average of 20 pptv.

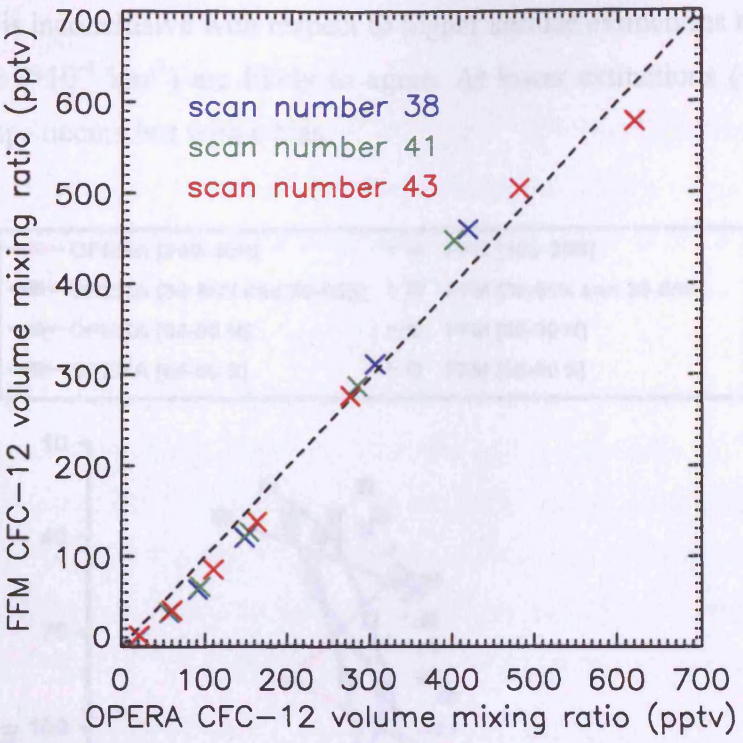

Figure 5.8 Correlation plot of Juelich CFC-12 data from their fast forward model (FFM) scheme against the OPERA CFC-12 data, orbit 06117 (May 2nd 2003), scan numbers 38, 41 and 43, in the Southern Hemisphere polar regions.

5.2.5 Total extinction

Both the Juelich and OPERA schemes jointly retrieve total extinction and the target gas, with the main aim of increasing the accuracy of the target gas retrieval. It also provides important information of the total extinction of the UTLS. Extinction means were constructed and intercompared for OPERA and Juelich data from orbit 06117 for each of the four regions (described in section 5.2) by averaging the three aerosol profiles from scans 20, 22 and 24 for the tropics, scans 11, 31 and 33 for mid-latitudes, scans 3, 5 and 7 for the Arctic and scans 38, 41 and 43 for Antarctica.

The mean total extinction profile results (Figure 5.9) show very good agreement at extinctions greater than 10^{-4} km^{-1} which tended to occur at 9 and 12 km. At lower altitudes, the extinctions were similar but there was a large systematic bias of a factor of three between OPERA and the Juelich scheme.

The comparison is inconclusive with respect to higher altitude extinctions but suggests that the two schemes (>10^{-4} km^{-1}) are likely to agree. At lower extinctions (<10^{-4} km^{-1}), the same relative shape occurs but with a bias.

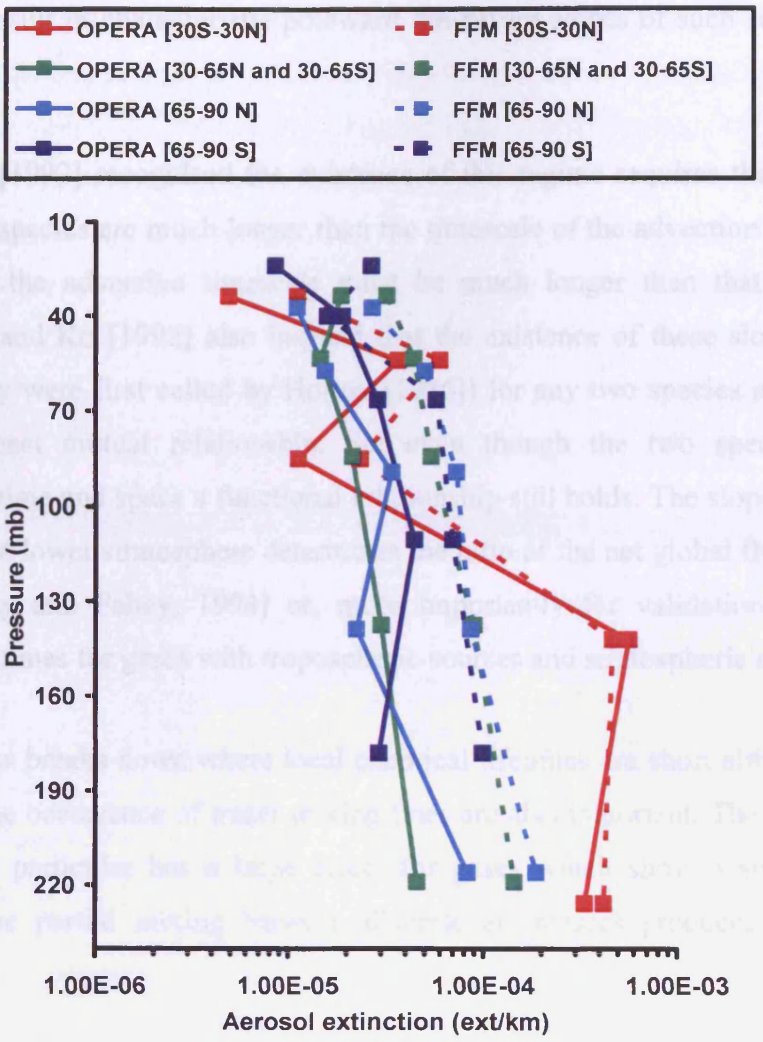

Figure 5.9 Mean aerosol profiles for both OPERA (solid lines) and Juelich fast forward model (FFM) scheme (dashed lines) from MIPAS-E level 1b near real time data (version 4.57) for orbit 06117 on May 2nd 2003. The 30°S-30°N profiles average retrievals from scans 20, 22 and 23, the mean 30-65 degree latitude profiles from scans 11, 31 and 33, the northern polar (65-90°N) mean profiles from scans 3, 5 and 7 and the southern polar (65-90°S) mean profiles from scans 38, 41 and 43.

5.3 Tracer-tracer correlations

Jones and Pyle [1984] first noted the similar meridional distributions of several long-lived atmospheric gases, such as methane (CH_4) and nitrous oxide (N_2O), in infrared measurements of the stratosphere and mesosphere from the Stratospheric and Mesospheric

Sounder (SAMS) instrument. Since that discovery it has been recognized that shapes of isopleths of long-lived stratospheric constituents such as CH_4 and N_2O (and also the halocarbons) are determined by meridional transport. They are a balance between the sloping residual mean circulation and the slope flattening effects of isentropic mixing processes and result in characteristic poleward downward slopes of such surfaces relative to isentropes.

Plumb and Ko [1992] recognised the existence of this regime requires that the chemical lifetimes of the species are much longer than the timescale of the advection by the residual circulation and the advective timescale must be much longer than that for isentropic mixing. Plumb and Ko [1992] also implied that the existence of these slope equilibrium surfaces (as they were first called by Holton [1986]) for any two species means that they exhibit a compact mutual relationship. So, even though the two species may vary substantially in time and space a functional relationship still holds. The slope of the species correlation in the lower stratosphere determines the ratio of the net global fluxes of the two species [Murphy and Fahey, 1994] or, more importantly for validation purposes, the atmospheric lifetimes for gases with tropospheric sources and stratospheric sinks.

The compactness breaks down where local chemical lifetimes are short although diffusion of tracers and the occurrence of tracer mixing lines are also important. The effect of tracer mixing lines in particular has a large effect for gases which show a smoothly curved relationship. The partial mixing between discrete air masses produces an anomalous mixing line.

The tracer-tracer correlation technique is used here to compare OPERA retrieved CFC-12 and HCFC-22 with operationally retrieved [Carli *et al.*, 2002] level 2 MIPAS-E N_2O data. These data are compared to previous stratospheric and upper tropospheric measurements of halocarbons and N_2O from the ATMOS in the early 1990s [Gunson *et al.*, 1996] and also with measurements of halocarbons from the current ACE mission of the Canadian Space Agency.

5.3.1 MIPAS-E N_2O data

Nitrous oxide (N_2O) was chosen as a suitable reference for comparing measurements of CFC-12 and HCFC-22 due to its long atmospheric lifetime (approximately 120 years,

[IPCC, 2001]). One positive aspect is that these MIPAS-E version 4.61 N_2O data have been validated. The findings of Camy-Peyret *et al.* [2004] suggest that MIPAS-E measured N_2O to within a 10 % level of precision. Their analysis suggested however a positive bias of up to 100 ppbv in MIPAS-E results in the UTLS (at pressures above 100 mb) compared to MIPAS-STR measurements. Their work also found it difficult to compare MIPAS-E with the balloon measurements in the lower part of the profile due to oscillations generated in the MIPAS-E system. MIPAS-E N_2O level 2 data points (version 4.61) were plotted between 9 and 21 km (approximately 400 to 50 mb) for May 2nd 2003 in Figure 5.10 along with a mean value at each height, plotted at a mean pressure level. The version 3.1 reference atmosphere of N_2O and associated one sigma limits derived by Remedios [1999] was also plotted for comparison.

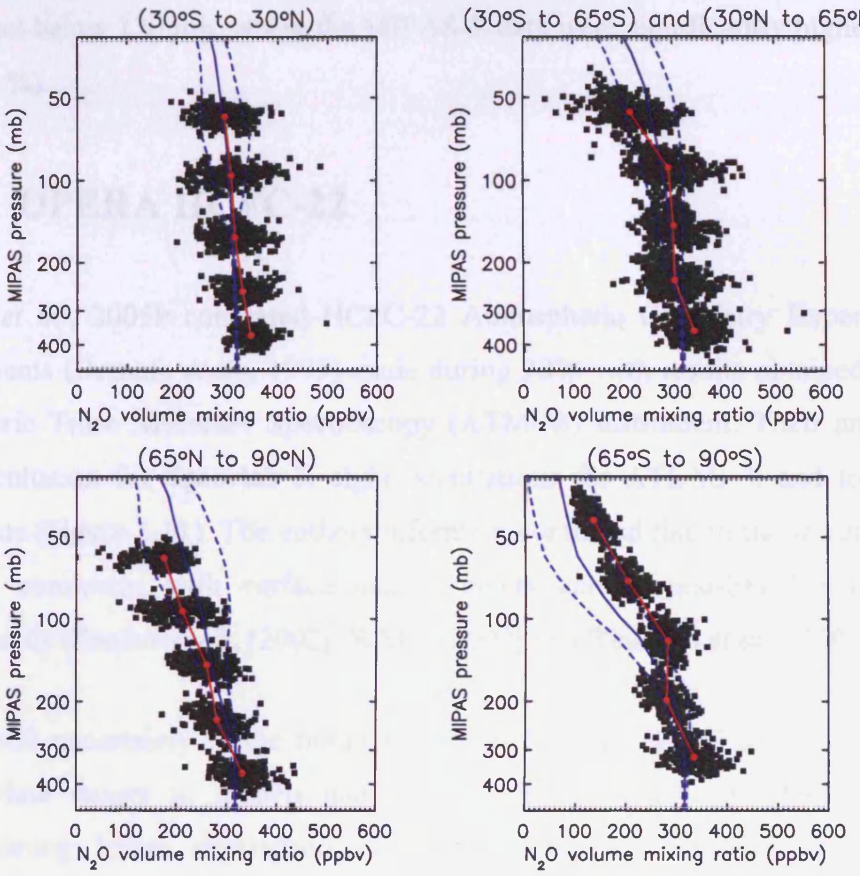

Figure 5.10 Version 4.61 MIPAS-E level 2 N_2O data (May 1st to 7th 2003) separated into four latitude regions. The black squares represent the MIPAS-E data themselves, the red circles joined by a solid line is the mean N_2O concentration at each measurement level (plotted at the mean pressure) and the dashed red line is the one sigma value of the data about the mean. The solid blue line is the N_2O climatology value of Remedios, 1999 (version 3.1 N_2O data plotted here consistent with 2001 concentrations) and the dashed blue lines are the one sigma limits on the climatology as reported in the files.

There is generally a close agreement between the MIPAS-E N_2O data (version 4.61) from the first week of May 2003 with the reference atmosphere. These data were derived from measurements from the Cryogenic Limb Array Etalon Spectrometer (CLAES) instrument [Roche *et al.*, 1993] and smoothed to remove possible effects of Mount Pinatubo aerosols on the data. There is particularly good agreement between the two data in the tropics where differences were less than 10 %, (largest around the 400 mb level). In the mid-latitudes, there was agreement between the mean MIPAS-E N_2O profile and the climatology to within 8 % between 90 and 400 mb although at approximately 50 mb, the mean MIPAS-E N_2O was lower compared to the climatology by 19 %. Between 65°N and 90°N, there was good agreement to within 7 % at pressures above 140 mb, but below this the MIPAS-E was lower by up to 20 %. Towards the Antarctic (65 to 90°S) the climatology and the mean MIPAS-E N_2O profiles have different profile shapes, particularly so in the lower stratosphere below 120 mb, where the MIPAS-E data were significantly higher (at between 25 and 70 %).

5.3.2 OPERA HCFC-22

Rinsland *et al.*, 2005b compared HCFC-22 Atmospheric Chemistry Experiment (ACE) measurements (Bernath *et al.*, 1995) made during 2004 with results obtained by using the Atmospheric Trace Molecule Spectroscopy (ATMOS) instrument. Their analysis used a single occultation for Spacelab 3, eight occultations for ATLAS 3, and forty-five ACE occultations (Figure 5.11). The authors inferred a continued rise in the lower stratospheric HCFC-22 consistent with surface measurements and ground-based solar absorption measurements (Zander *et al.*, [2002]; WMO [2002] and Rinsland *et al.*, [2005b]).

There is still uncertainty in the future long-term trend of HCFC-22 resulting from both large lifetime ranges in models and future industrial emission rates (WMO, 2002). The increasing lower stratospheric trend presented by Rinsland *et al.*, 2005b of 3.92 ± 2.08 pptv/yr which is the same within error as the tropospheric trend estimated from global ESRL measurements in section 1.2 of 5.2 pptv/yr. There was a positive gradient of the correlation plot for both the SL3 and ATLAS 3 measurements but there was no obvious relationship between HCFC-22 and N_2O vmrs according to the ACE results.

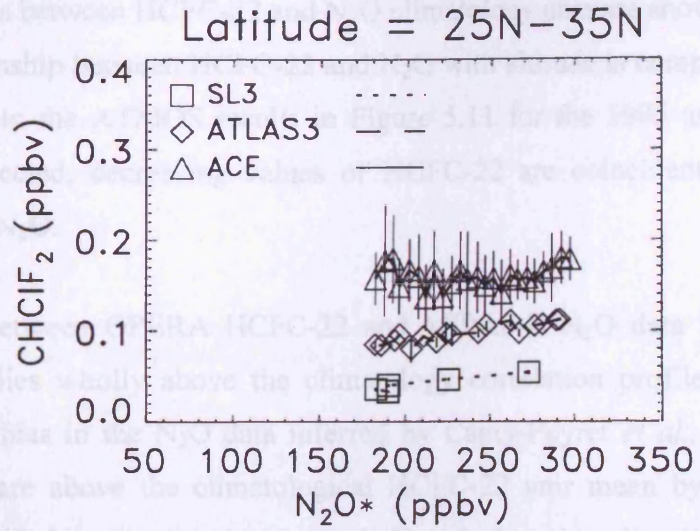

Figure 5.11 ATMOS 1985 (open triangles), ATMOS, 1994 (ATLAS 3), and ACE 2004 lower stratospheric HCFC-22 ($CHClF_2$) volume mixing ratios vs. N_2O. Open squares, open diamonds and open triangles display averages in overlapping 5 ppbv N_2O intervals with vertical lines indicating corresponding standard deviations. (Reproduced from [Rinsland *et al.*, 2005b])

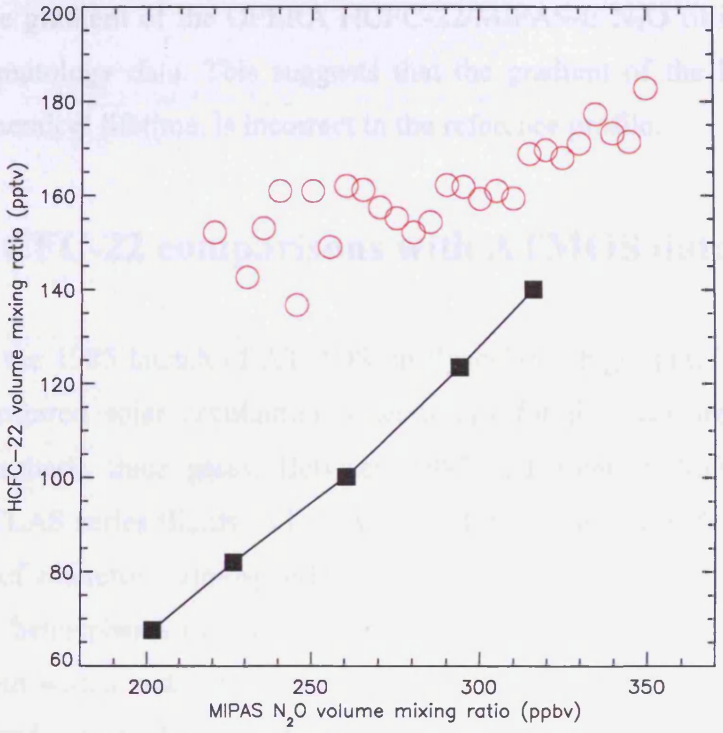

Figure 5.12 A correlation plot of globally averaged HCFC-22 and N_2O volume mixing ratios from both the version 3.1 climatology files of Remedios, 1999 plotted at 3 km intervals between 9 and 30 km, black squares. Also displayed is the global correlation plot (incorporates all data for May 2nd 2003) between OPERA retrieved HCFC-22 data and the corresponding version 4.61 MIPAS-E N_2O data (red circles). OPERA HCFC-22 data have been binned into 5 ppbv N_2O intervals and averaged.

Global correlations between HCFC-22 and N_2O climatology data are shown in Figure 5.12. The global relationship between HCFC-22 and N_2O with altitude is compact. These results were comparable to the ATMOS results in Figure 5.11 for the 1985 and 1994 ATMOS missions. As expected, decreasing values of HCFC-22 are coincident with decreasing concentrations of N_2O.

The correlation between OPERA HCFC-22 and MIPAS-E N_2O data is also plotted in Figure 5.12 and lies wholly above the climatology correlation profile. As well as the 30 ppbv positive bias in the N_2O data inferred by Camy-Peyret *et al.*, [2004] the mean HCFC-22 data were above the climatological HCFC-22 vmr mean by between 30 and 60 pptv (20 to 40 %). It was, however, believed that the climatology could have underestimated tropospheric HCFC-22 in 2003 by up to 20 pptv (discussed in section 4.2.2.1).

From the limited 348 point HCFC-22 dataset gridded and plotted here, it can be seen that there is an increase in OPERA retrieved MIPAS-E HCFC-22 vmrs coincident with an N_2O vmr increase. The gradient of the OPERA HCFC-22/MIPAS-E N_2O fit is shallower than the fit to the climatology data. This suggests that the gradient of the HCFC-22 profile effectively, the chemical lifetime, is incorrect in the reference profile.

5.3.2.1 HCFC-22 comparisons with ATMOS data

The results from the 1985 launch of ATMOS on Spacelab 3 highlighted the potential for high-resolution infrared solar occultation observations for the measurement of vertical profiles of atmospheric trace gases. Between 1992 and 1994 ATMOS was deployed onboard three ATLAS series flights (AT-1, AT-2 and AT-3) and provided observations of vertical profiles of numerous atmospheric constituents throughout the tropics and mid-latitudes, in both hemispheres over two seasons. During the AT-2 flight ATMOS made measurements both within and outside the Arctic polar vortex and during AT-3 ATMOS measured inside and outside the Antarctic vortex. The three flights in conjunction provide a near global coverage of measurements (Figure 5.13).

A positive correlation was found globally between operational MIPAS-E measurements of N_2O and OPERA retrieved HCFC-22 vmrs in Figure 5.12. The same HCFC-22 data are plotted in Figure 5.14 with a linear fit derived from OPERA HCFC-22 data that had been

binned into N_2O intervals of 5 ppbv (derived by the same technique as for CFC-12 described in section 5.3.3.1). Then, a one degree polynomial was calculated for the binned data using the poly_fit function in IDL. The OPERA coefficients for the HCFC-22/N_2O fit were; $a_0 = 91.483$, $a_1 = 0.268$. The associated one sigma (σ) uncertainty estimate for a_0 was 12.498 and for a_1 was 0.043.

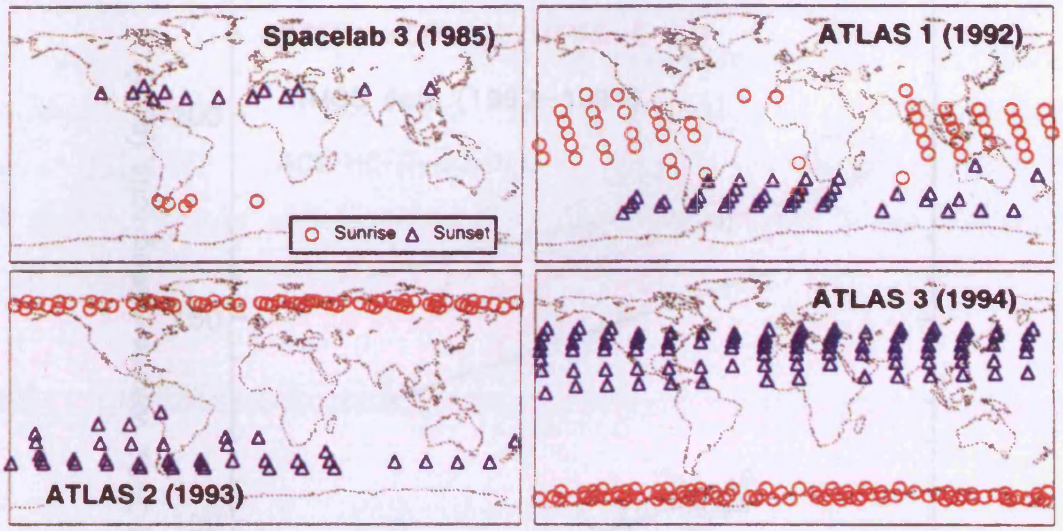

Figure 5.13 Sunrise (circles) and sunset (triangles) occultations observed by ATMOS on Space shuttle for (a) Spacelab 3, 29 April to May 7, 1985; (b) ATLAS-1, 24 March to 3 April 1992; (c) ATLAS-2, 8 to 16 April 1993; and (d) ATLAS-3, 3 to 14 Nov 1994. (Figure reproduced from [Gunson *et al.*, 1996]).

The ATMOS HCFC-22 data from all three ATLAS flights (version 2) were also binned into 5 ppbv N_2O increments to obtain averages. These data were plotted as blue triangles in Figure 5.14 with a linear fit also added (solid blue line), calculated as for the MIPAS-E data. The coefficients for the ATMOS HCFC-22/N_2O fit were $a_0 = 23.551$ ($\sigma = 8.288$) and $a_1 = 0.274$ ($\sigma = 0.032$). An estimate of the "best-fit" for 25 to 35°N ACE HCFC-22 data from 2004 is also plotted in Figure 5.14 with $a_0 = 120$ ($\sigma = 0.001$) and $a_1 = 0.200$ ($\sigma = 5.606 \times 10^{-6}$). Assuming that HCFC-22 was well mixed throughout the upper troposphere, the ACE data can be directly compared to the OPERA and ATMOS data.

Although the differences between the ATMOS and MIPAS-E HCFC-22 vmrs are large (between 10 to 15 %), the gradient in both sets of data are similar. Accounting for a lower stratospheric age of air of two years [Andrews *et al.*, 2001] and applying the growth rate derived from ESRL surface data, the increase of HCFC-22 in the troposphere between 1991 and 2001 was 52 pptv. As noted for CFC-12 correlations, the tropospheric N_2O vmr

growth rate has been linear since 1977 at 0.75 ppbv/yr [Rinsland *et al.*, 2005b]. These observed trends in both HCFC-22 and N_2O measurements were applied to the ATMOS data (black line). This gave an estimate of measurements "expected" from the MIPAS-E in 2003.

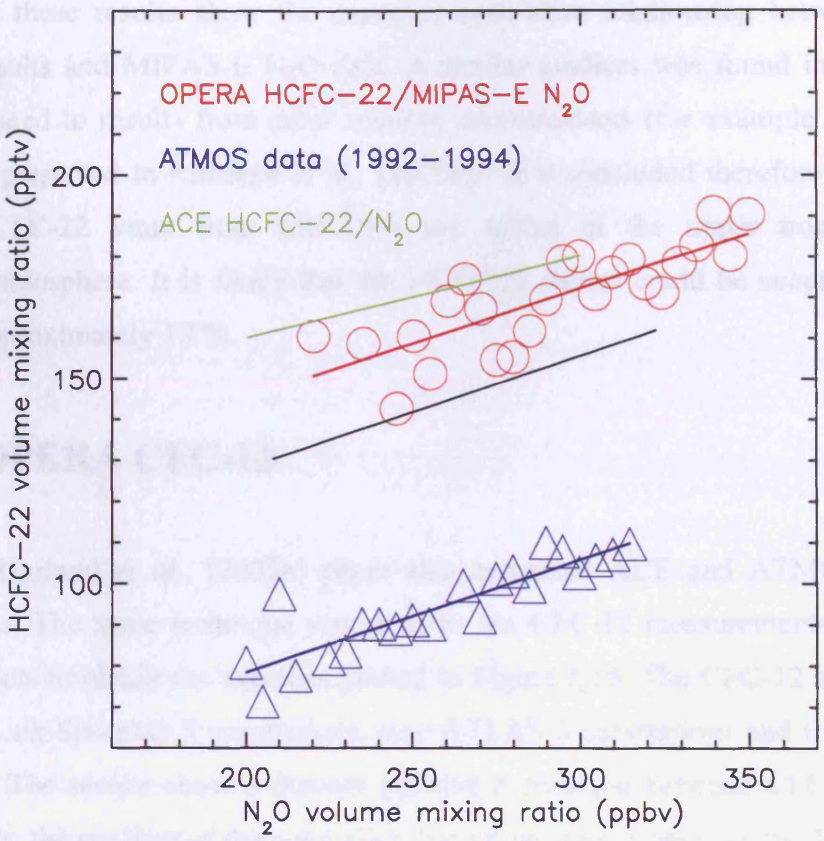

Figure 5.14 Global ATMOS 1992 – 1994 (blue open triangles) and MIPAS-E (red open circles) upper tropospheric and lower stratospheric HCFC-22 volume mixing ratios vs. N_2O. Open triangles and open squares display averages in 5 ppbv N_2O intervals. ATMOS data are only plotted where N_2O vmrs exceed 200 ppbv. The solid lines represent fits to the ATMOS (blue) and MIPAS-E (red) data. The solid black line shows a prediction of stratospheric HCFC-22 and N_2O levels based on the ATMOS data and global average trends derived from surface CMDL station data. An estimated "best-fit" line to the 25 to 35 N ACE data reported in Rinsland *et al.*, 2004 is overplotted in lime green for comparison. ACE data are only plotted between N_2O vmrs between 200 and 300 ppbv.

For this one day of MIPAS-E data (2nd May 2003), OPERA HCFC-22 results are larger than the predicted HCFC-22 vmrs in the lowermost stratosphere by between 10 and 20 pptv (approximately 10 to 15 %). Results from an estimated fit to ACE data presented in the Rinsland *et al.* [2005b] paper were also compared to MIPAS-E and ATMOS. The ACE results from 2004 were on average between 10 and 15 pptv greater than those from OPERA retrievals in 2003. The ACE results were also consistent with an increasing

atmospheric HCFC-22 concentration of approximately 7 pptv/yr since the 1994 ATMOS measurements, larger than the 5.2 pptv/yr derived from surface measurements. The OPERA results fall between the two sets of values indicating that the UTLS trend is of the order 5 to 7 pptv/yr.

In summary, these results show the expected correlative relationship between OPERA HCFC-22 results and MIPAS-E N_2O data. A similar gradient was found in the OPERA results compared to results from other satellite measurements (for example ATMOS and ACE results presented in Rinsland *et al.*, [2005b]). It is concluded therefore that OPERA retrieved HCFC-22 vmrs from MIPAS-E are robust in the upper troposphere and lowermost stratosphere. It is likely that the HCFC-22 values could be accurate to within 15 pptv or approximately 10 %.

5.3.3 OPERA CFC-12

The recent Rinsland *et al.*, [2005b] paper also compared ACE and ATMOS measured CFC-12 vmrs. The same technique was used to bin CFC-12 measurements into 5 ppbv N_2O increments to obtain the averages plotted in Figure 5.15. The CFC-12 averages were derived from six Spacelab 3 occultations, nine ATLAS 3 occultations and forty-five ACE occultations. The results show a distinct positive correlation between CFC-12 and N_2O measurements, the gradient of the correlation becoming steeper between the 1985 Spacelab 3 (SL3) measurements and those from the 1994 ATLAS-3 flight. There is very little difference between the 1994 ATMOS measurements and those made from ACE in 2004.

However, although Rinsland *et al.*, [2005b] conclude the significant slowing rate between 1985 and 2004 was consistent with other measurements (such as [Zander *et al.*, 2002]) the inferred trends showed a decrease in CFC-12 between 1994 and 2004. This contradicts results of the IPCC reports in 1995 and 2001, which reported increasing CFC-12 trends of 7 pptv/yr (1992 tropospheric trend) and 4.4 pptv/yr (1998 tropospheric trend) respectively. Although ESRL surface measurements in early 2004 suggested that the tropospheric levels of CFC-12 were almost stable, age of air considerations suggest that CFC-12 levels in the atmosphere (and particularly the stratosphere) should have increased by at least 30 pptv between 1994 and 2004.

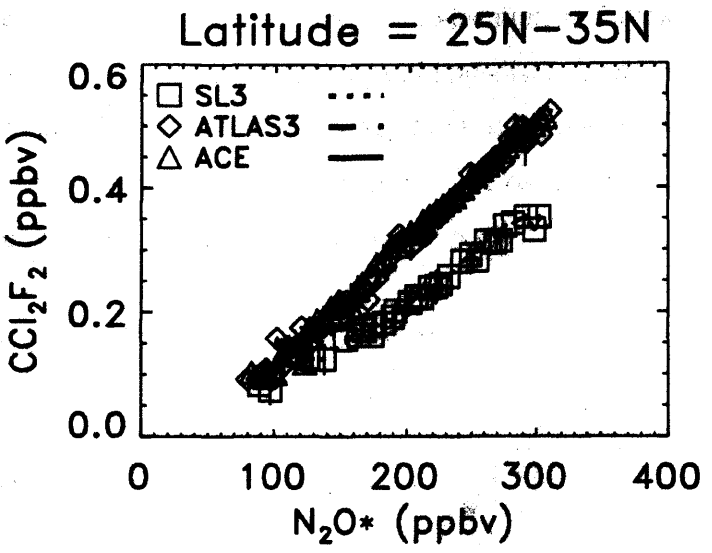

Figure 5.15 ATMOS 1985 (open triangles), ATMOS, 1994 (ATLAS 3), and ACE 2004 lower stratospheric CFC-12 (CCl_2F_2) volume mixing ratios vs. N_2O^*. N_2O^* is the adjusted N_2O accounting for the N_2O trend in the lower stratosphere as a function of time, assumed as a growth rate of 0.75 ppbv/yr . The trend was based on CMDL N_2O measurements since 1977. Open squares, open diamonds and open triangles display averages in overlapping 5 ppbv N_2O intervals with vertical lines indicating corresponding standard deviations. (Reproduced from Rinsland *et al.*, 2005)

Global correlations between both the CFC-12 and N_2O climatology data are shown in Figure 5.16, using the version 3.1 reference atmosphere files of Remedios, 1999 (section 2.4.1.1.1). The data were expected to be representative of atmospheric levels of both CFC-12 and N_2O in 2000. Climatology data were averaged from the four standard conditions, each representing a particular zonal region, at 3 km intervals between 9 and 30 km and one global climatology profile for both N_2O and CFC-12 produced.

At N_2O vmrs of below 300 ppbv (Figure 5.16), the global relationship between CFC-12 and N_2O with altitude was very tight, with decreasing values of CFC-12 seen also in decreasing concentrations of N_2O. Based on the regional results, a quasi-linear relationship between N_2O and CFC-12, where N_2O was below 300 ppbv, holds for all latitude bands (Figure 5.16).

Overplotted in Figure 5.16 are the global linear correlations (all converged data shown in Figure 4.51 for May 2nd 2003 were included) between OPERA retrieved CFC-12 and reprocessed version 4.61 MIPAS-E N_2O data for orbits 06115 to 06122 inclusive. The N_2O data were "binned" into fifty-one 5 ppbv intervals between 100 and 350 ppbv. The N_2O concentrations in each bin were matched to the corresponding OPERA retrieved CFC-12

measurements, averaged, and the mean CFC-12 concentration for each bin plotted against the centre of the N_2O bin. Due to the positive, and unrealistic, bias found in some N_2O data above 100 mb [Camy-Peyret *et al.*, 2004], N_2O data above 320 ppbv (the mean tropospheric value in 2004) + 10 %, i.e. 350 ppbv, were removed from the correlation plot; the 10 % factor accounts for the random error in the N_2O.

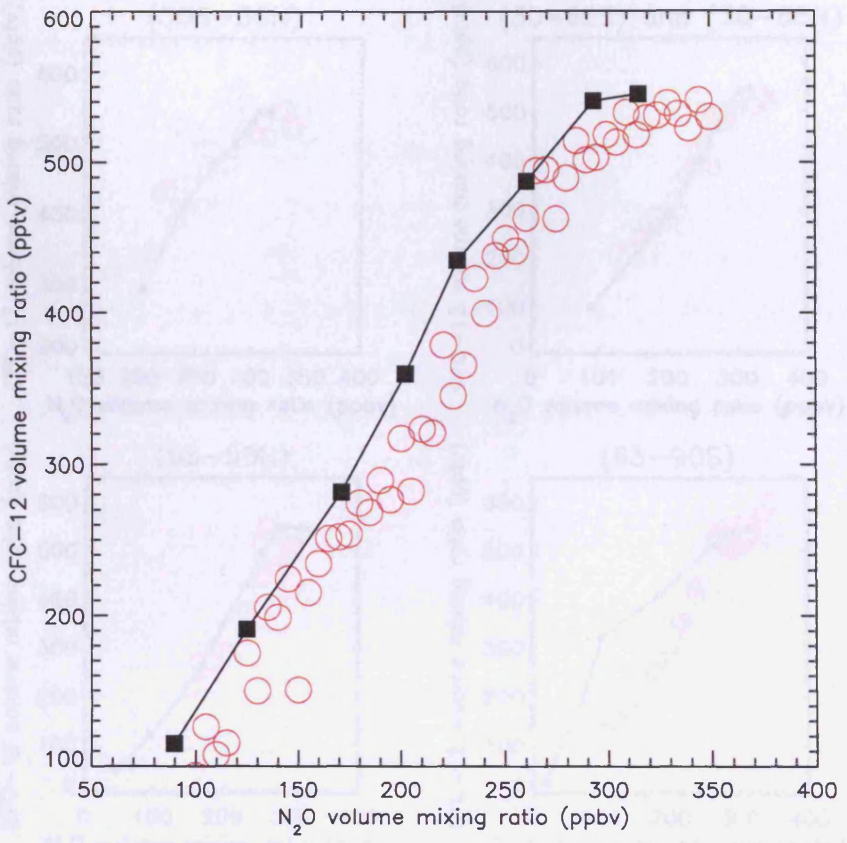

Figure 5.16 A plot of globally averaged CFC-12 and N_2O volume mixing ratios. The black squares represent a mean global profile from the version 3.1 climatology files of Remedios, 1999, averaged from the four latitude regions described in chapter 3 to produce a mean profile and plotted at 3 km intervals between 9 and 30 km. The global correlation plot (incorporates all data for May 2nd 2003) between OPERA retrieved CFC-12 data is also shown and the corresponding version 4.61 MIPAS-E N2O data. Open red circles display averages of CFC-12 data in 5 ppbv N_2O intervals.

The compact global correlation for these 546 data points shows there was a positive relationship in the retrieved data as expected between CFC-12 and N_2O in the upper troposphere and lower stratosphere and lay close to the climatological correlation profile but with a small shift of the profile to the right of the climatology. In Figure 5.16, it should be remembered that tropospheric N_2O concentrations have risen linearly since 1977 at 0.75 ppbv/yr. Based on this linear trend, the tropospheric concentration of N_2O was expected to be 320 ppbv, 3 ppbv higher than the climatology, but the increase does not

explain the offset of up to 20 ppbv in N_2O observed. Based on ESRL surface measurements, tropospheric CFC-12 levels were approximately constant between 2000 and 2003 although stratospheric values may have continued to rise in that time. The offset observed in Figure 5.16 may likely be explained by a bias in the version 4.61 MIPAS-E data for N_2O or retrieved CFC-12.

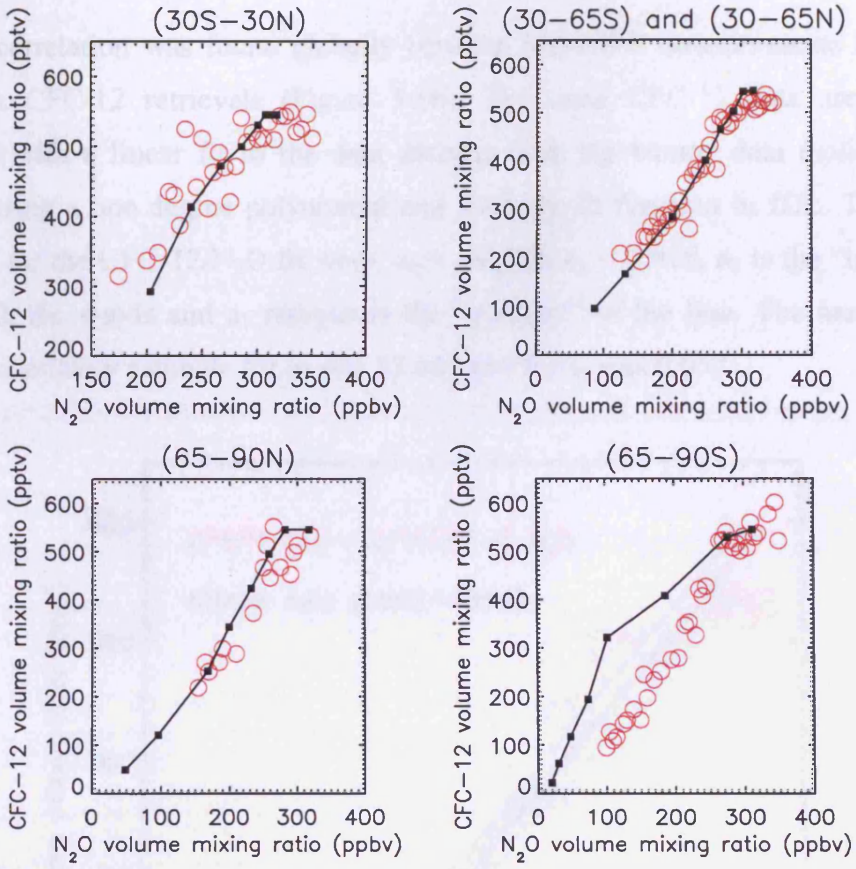

Figure 5.17 CFC-12 and N_2O volume mixing ratios from the version 3.1 climatology files of Remedios, 1999 at each MIPAS-E plotted at 3 km intervals between 9 and 30 km.

When analysed zonally, Figure 5.17, the CFC-12/N_2O correlations also showed close agreement between the measured and climatological data. The closest agreements were in mid-latitudes and the largest differences towards the Antarctic, but also with some variability about the climatology profile in the tropics. Assuming the small tropospheric N_2O increase of 3 ppbv since the climatology was produced tropical CFC-12 data were generally low compared to the climatology below 21 km. Above 24 km, the results lay above the climatology and may reflect the increasing stratospheric burden due to trends of CFC-12.

The most interesting feature was apparent in the southern polar data (65 to 90°S) where there was a positive difference between the retrieved data and the climatology of up to 50 ppbv along the N_2O axis.

5.3.3.1 CFC-12 comparisons with ATMOS data

A positive correlation was found globally between MIPAS-E measurements of N_2O and the OPERA CFC-12 retrievals (Figure 5.16). The same CFC-12 data are plotted in Figure 5.18 with a linear fit to the data derived from the binned data (solid red line), calculated using a one degree polynomial and the poly_fit function in IDL. The OPERA coefficients for the CFC-12/N_2O fit were; $a_0 = -76.426$, $a_1 = 1.916$, a_0 is the "intercept" of the line with the y-axis and a_1 represents the "gradient" of the line. The associated one sigma (σ) uncertainty estimate for a_0 was 13.647 and for a_1 was 0.057.

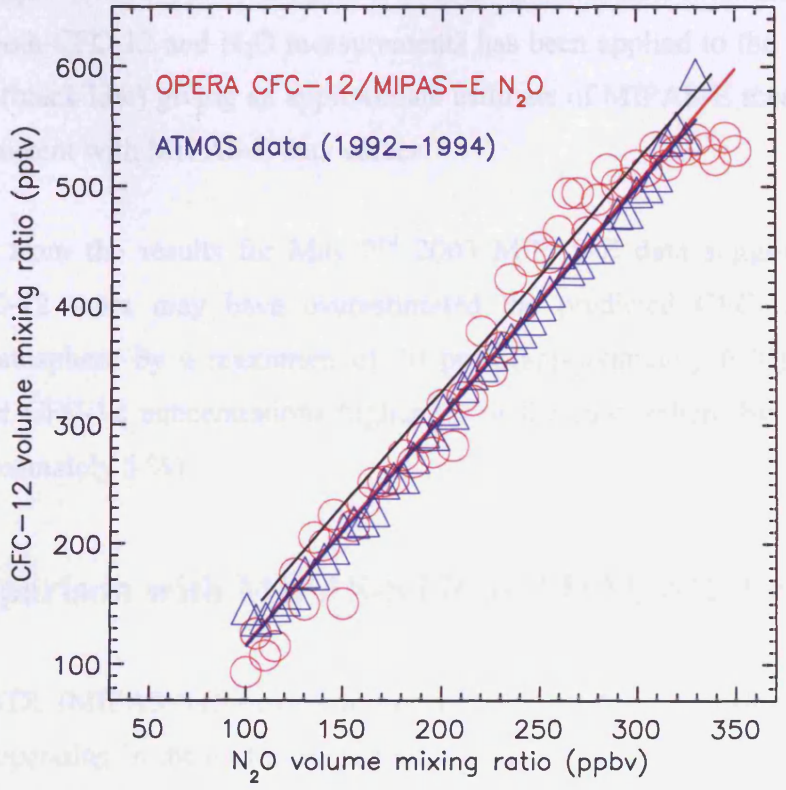

Figure 5.18 ATMOS 1992 – 1994 (blue open triangles) and MIPAS-E (red open circles) upper tropospheric and lower stratospheric CFC-12 volume mixing ratios vs. N_2O. Open triangles and open squares display averages in 5 ppbv N_2O intervals. The solid lines represent fits to the ATMOS (blue) and MIPAS-E (red) data. ATMOS data are only plotted where N_2O vmrs exceed 100 ppbv. The solid black line shows a prediction of stratospheric CFC-12 and N_2O levels based on the ATMOS data and global average trends derived from surface ESRL station data.

The ATMOS CFC-12 data from all three ATLAS flights (version 2) were binned into 5 ppbv N_2O increments to obtain averages. These data were plotted as blue triangles in Figure 5.18 with a linear fit also added (solid blue line), calculated as for the MIPAS-E data. The coefficients for the ATMOS CFC-12/N_2O fit were a_0 = -76.463 (σ = 5.038) and a_1 = 1.916 (σ = 0.022).

For CFC-12 vmrs below 350 pptv, the results between MIPAS-E and ATMOS were similar. Above CFC-12 vmrs of 350 pptv, the MIPAS-E results showed an increase of up to 50 pptv (10 %) in some of the UTLS data compared to the ATMOS CFC-12 vmrs.

Since the ATMOS measurements were made between 1992 and 1994, tropospheric levels of CFC-12 have increased variably by between 7 pptv/yr in 1992 [IPCC, 1995] and below 1 pptv/yr in 2003 (ESRL data). Accounting for a lower stratospheric age of air of two years [Andrews *et al.*, 2001] the growth rate of CFC-12 in the troposphere between 1991 and 2001 was 38 pptv (based wholly on global average ground measurements from ESRL). The trend in both CFC-12 and N_2O measurements has been applied to the linear fit to the ATMOS data (black line) giving an approximate estimate of MIPAS-E measurements that should be consistent with MIPAS-E data values.

The evidence from the results for May 2nd 2003 MIPAS-E data suggest that OPERA retrieved CFC-12 vmrs may have overestimated the predicted CFC-12 vmrs in the lowermost stratosphere by a maximum of 30 pptv (approximately 6 %). OPERA data underestimated CFC-12 concentrations higher up in the stratosphere by a maximum of 20 pptv (approximately 5 %).

5.4 Comparison with MIPAS-STR and HAGAR data

The MIPAS-STR (MIPAS-STRatospheric aircraft) is a Fourier Transform spectrometer (Figure 5.19) operating in the mid-infrared [Blom *et al.*, 2003], and works along the same principles as the MIPAS-E (section 3.2). The main difference with the MIPAS-STR is that the instrument is flown onboard the Geophysica aircraft (Figure 5.20), rather than a satellite, up to a height of 21 km. Limb views can be obtained below this height at a 2 km vertical resolution and a reduced height resolution above. The results give a 2-D distribution of the trace gases along the flight track in an altitude range covering the

lowermost stratosphere and the upper troposphere. The first version of the MIPAS-STR flew during the Antarctic campaign APE-GAIA in 1999 [Carli *et al.*, 2000].

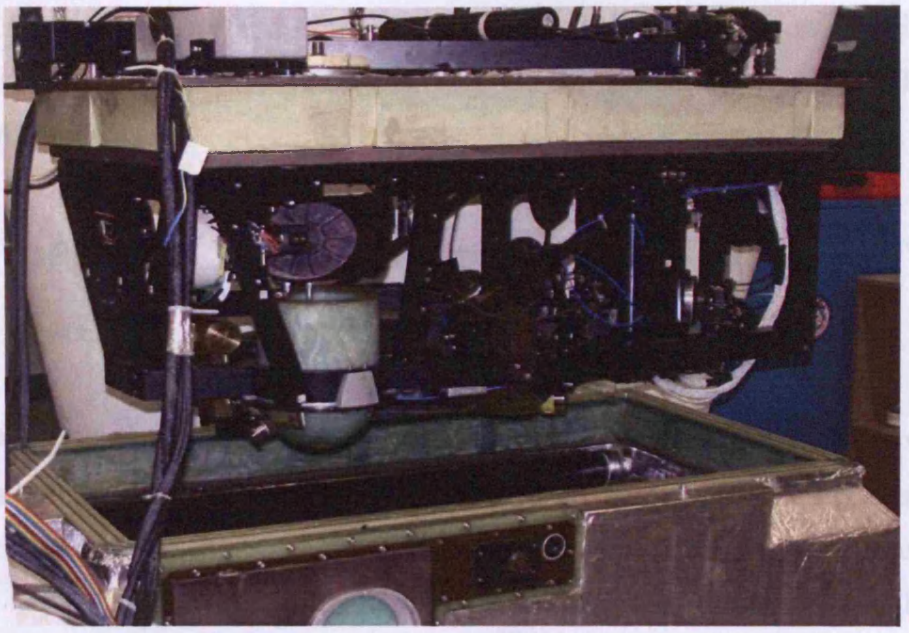

Figure 5.19 The MIPAS-STR instrument showing the sensor above the cooling optics. (Image courtesy of the IMK MIPAS-STR team website: http://www-imk.fzk.de/asf/mipas-str/).

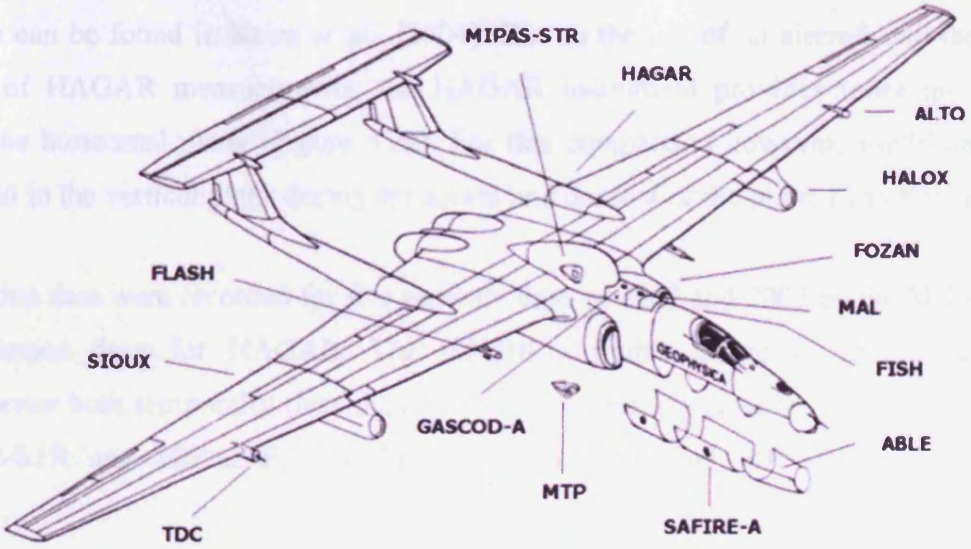

Figure 5.20 A sketch of the M55 Geophysica and the locations of its instrumental payload, including the MIPAS-STR and HAGAR. The aircraft was developed by Myasishchev Design Bureau and built by Smolensky aircraft plant to order of the USSR Government as a high-altitude reconnaissance aircraft. The aircraft's first flight was on the 16th of August 1988 and the M55 aircraft is the only subsonic aircraft in Russia and Europe performing long endurance flight at altitudes up to 21 km. (Image courtesy of the IMK MIPAS-STR team. Website: http://www-imk.fzk.de/asf/mipas-str/).

The High Altitude Gas AnalyseR (HAGAR), [Riediger *et al.*, 2000] records airborne in-situ measurements of trace gases, including CFC-12, using gas chromatography (GC-ECD) at a time resolution of 90 seconds. The nominal precision for CFC-12 is 0.3 % [Baehr, 2004]. In February and March 2003, the HAGAR was flown on board the M55 Geophysica aircraft to provide measurements for the validation of MIPAS-E level 2 version 4.61 products.

5.4.1 OPERA CFC-12 comparisons with MIPAS-STR and HAGAR

The MIPAS-STR and HAGAR instruments were flown as part of MIPAS-E validation campaigns during 2002 and 2003. MIPAS-STR measurements were made at fixed heights between 6 km and the flight altitude, with a spacing of 1.25 km at a resolution of 0.035 cm^{-1}. One complete measurement sequence took 160 seconds at a horizontal resolution of 30 km. Due to the 0.44 degrees field of view of the instrument at FWHM the lower altitudes were over sampled by a factor 2-3. For the halocarbons, measurements were made in channel 1 (770 to 970 cm^{-1}) at similar wavelengths to MIPAS-E. Information for the level 1 data processing and the data retrieval scheme using the IMK KOPRA scheme can be found in Keim *et al.*, [2004]. Due to the use of an aircraft and the in-situ nature of HAGAR measurements, the HAGAR instrument provides more information along the horizontal plane (Figure 5.22). For this comparison however, useful data were recorded in the vertical plane during the ascent and descent of the plane from Kiruna.

Validation data were recorded for five separate days in 2002 and 2003 by the MIPAS-STR and thirteen days for HAGAR. The validation flights aimed to provide excellent coincidence both temporally (less than 1 hour) and spatially (less than 200 km) between MIPAS-STR and MIPAS-E. Coincidence for HAGAR and MIPAS-E was less than 500 km.

For the comparison performed here, data from the 28th February 2003 (Figure 5.21) and 12th March (Figure 5.27) were used. Figure 5.21 and Figure 5.27 also show the flight tracks together with tangent points of MIPAS-STR and MIPAS-E. The plots are colour coded according to tangent heights (dark blue for 6 km, red for 20 km). The pressure levels at which HAGAR took in-situ measurements are shown in Figure 5.22 and Figure 5.28.

5.4.2 February 28th 2003

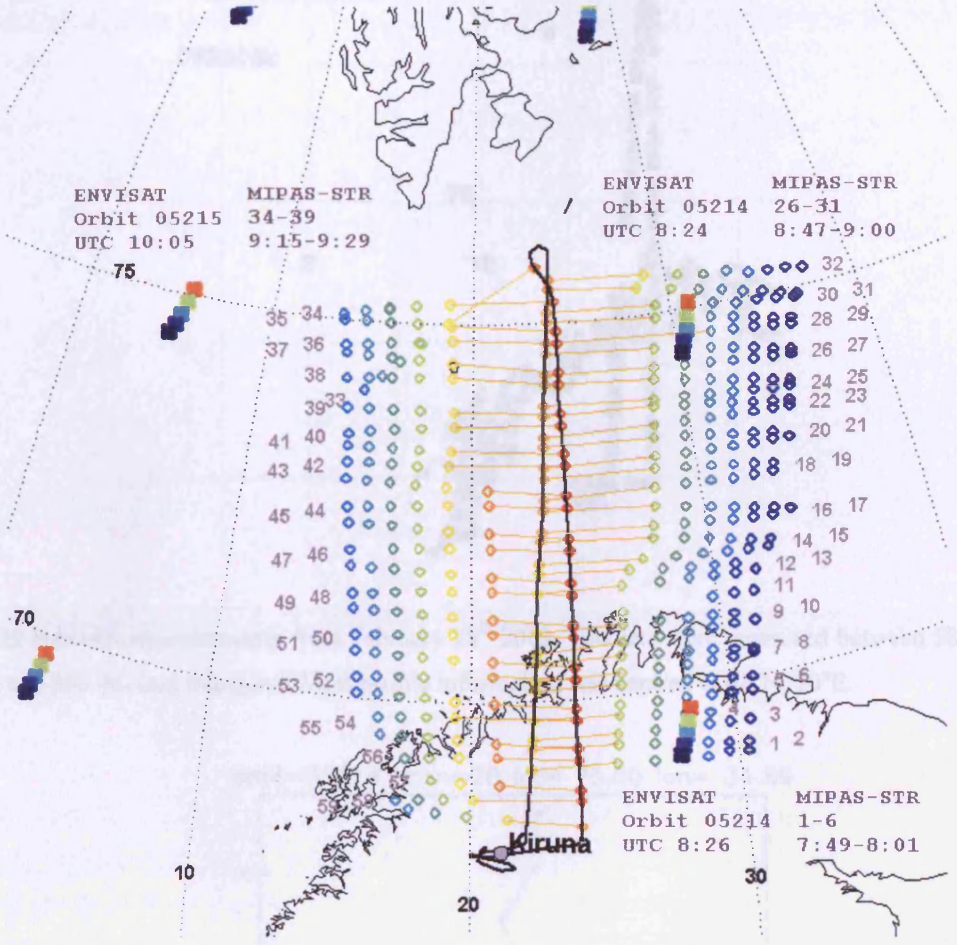

Figure 5.21 The flight track of the Geophysica aircraft (solid black line) and the corresponding MIPAS-STR measurements from this flight (open circles) on February 28th 2003. The data points are plotted at 1.5 km intervals from 6 km (red) to approximately 20 km (dark blue). The MIPAS-E scan information data (orbits 05214 and 05215) are also plotted at heights between approximately 9 (orange) and 21 km (dark blue) at the nominal MIPAS-E spacing of 3 km. The plot is courtesy of Corneli Keim (IMK) and adapted to include time identities for ENVISAT and MIPAS-STR measurements.

From the 28th February 2003 data, two MIPAS-E scans were coincident with the MIPAS-STR measurements (numbers 28 and 29 of orbit 05214, time identities of 99735903 and 99735995 respectively).

Using the cloud filtering technique discussed in section 4.1.2.4.1 with a cloud index (CI) threshold of 1.8, shows that scan #28 was cloud free throughout the upper troposphere and the whole of the stratosphere (Figure 5.23). Scan #29 was cloudy at 6 km but cloud-free above this height (Figure 5.24) although at 9 km (320 mb), a thin cloud or aerosol layer was present (CI=2.2).

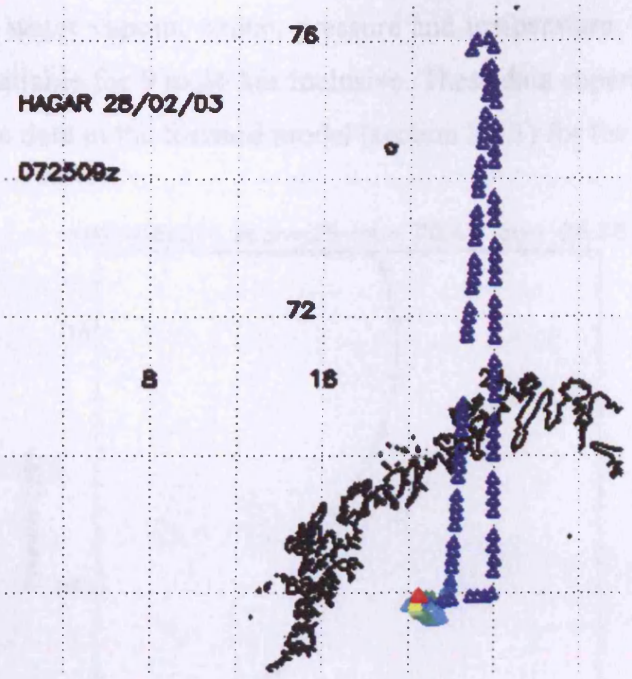

Figure 5.22 HAGAR measurements from February 28th 2003. The data were measured between 58 mb (blue triangles) and 850 mb (red triangles). Most profile information was centred at 68°N, 20°E.

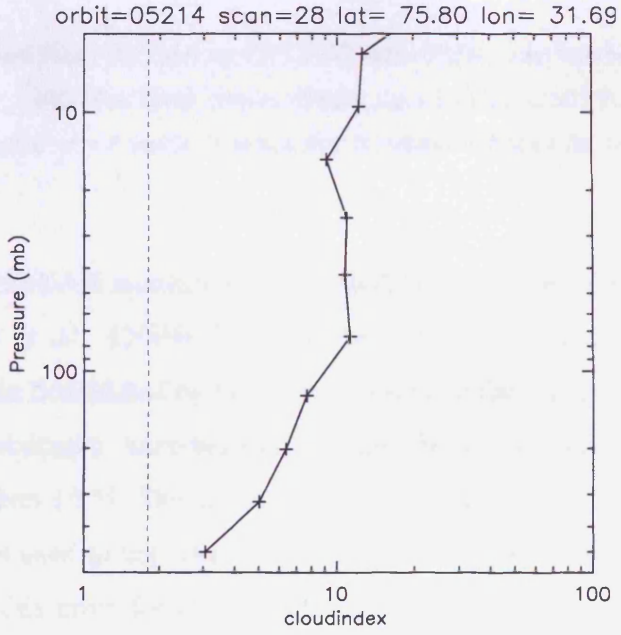

Figure 5.23 MIPAS-E Cloud index (CI) plot for ENVISAT orbit 05214, scan number 28, using the technique described by Spang *et al.*, 2002. The black crosses display the CI value at MIPAS-E tangent heights. The dashed line shows a CI value of 1.8 and a CI below this threshold indicates the sweep is contaminated by optically thick cloud.

Consolidated version 4.61 level 1b spectra were available for both scans between 6 and 68 km. For scan #28 consolidated level 2 data (version 4.61) were available between 6 to

68 km inclusive for water vapour, ozone, pressure and temperature. MIPAS-E nitric acid level 2 data were available for 9 to 36 km inclusive. These data superseded the version 3.1 reference atmosphere data in the forward model (section 2.4.1) for the relevant retrieval.

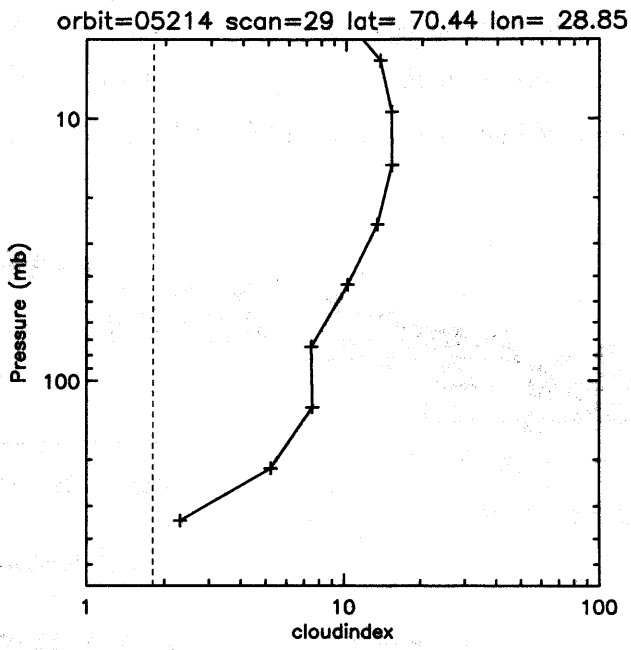

Figure 5.24 MIPAS-E Cloud index (CI) plot for ENVISAT orbit 05214, scan number 29 using the technique described by Spang *et al.*, 2002. The black crosses display the CI value at MIPAS-E tangent heights. The dashed line shows a CI value of 1.8 and a CI below this threshold indicates the sweep is contaminated by cloud.

The accuracy of the HAGAR measurements is better than 2 % for CFC-12 (assumed from the results of Gulde *et al.*, [2004] for HAGAR CFC-11 accuracy). The MIPAS-STR CFC-12 retrievals were dominated by two error sources in the retrieval [Keim *et al.*, 2004]. Errors to due spectroscopic uncertainties in the HITRAN data were significant but estimated to be less than 10 %. The second was the propagation of errors from incorrectly retrieved temperatures used in the scheme to obtain trace gases. Keim *et al.*, [2004] do not provide estimates of this error for CFC-12 explicitly but from figure 6 of their paper the total error for the MIPAS-STR data were estimated as not greater than 15 % so the increased uncertainty in the CFC-12 data due to temperature errors does not exceed 10 %.

The temporal difference between these measurements was low as MIPAS-E spectral measurements were made only 23 to 46 minutes before the six MIPAS-STR measurements considered here in the validation (scans 26 to 31).

Figure 5.25 compares OPERA retrieved CFC-12 for scan #28 of orbit 05214, six coincident MIPAS-STR CFC-12 profiles and in-situ HAGAR measurements. For the MIPAS-STR CFC-12, a mean profile (green triangles) was plotted alongside the data from the six scans that comprise this profile. Error limits of 15 % (estimated from Keim *et al.*, 2004) were included on the mean data points. The OPERA data include the total error estimate error bars for the root mean square of all error sources described in sections 4.2.6.1 and 4.2.6.2. The HAGAR data included error bars which were smaller than 5 pptv.

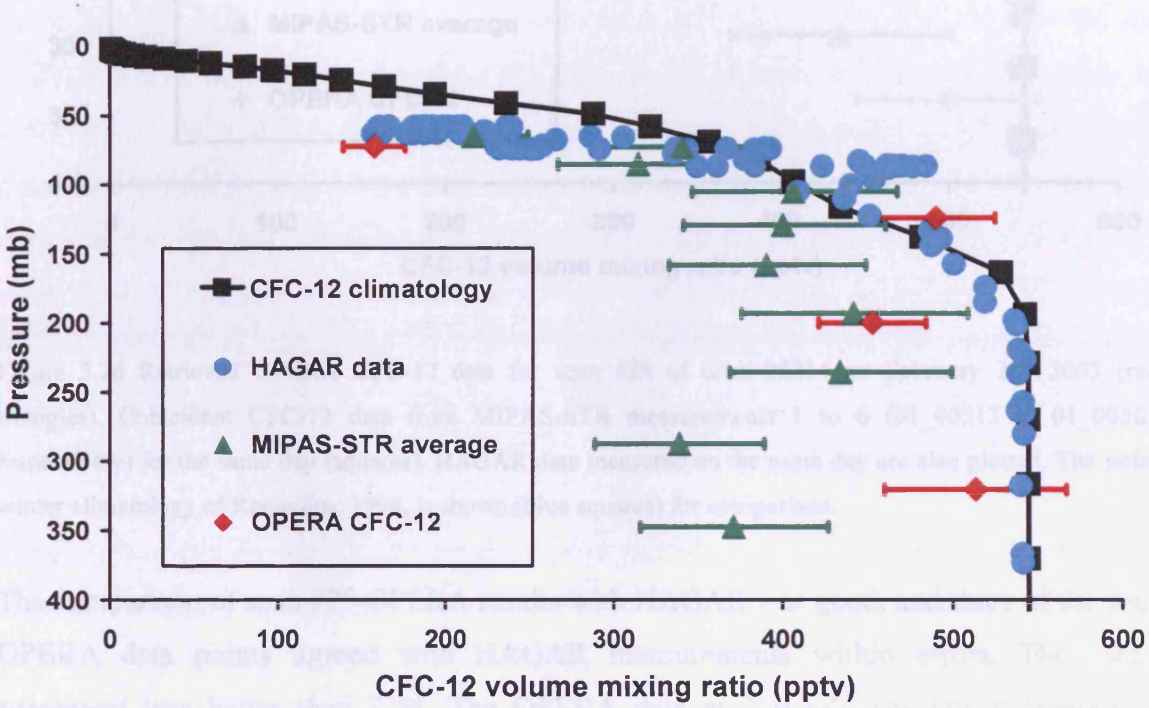

Figure 5.25 Retrieved OPERA CFC-12 data for scan #28 of orbit 05214 on February 28th 2003 (red triangles). Also plotted is the coincident CFC-12 data from MIPAS-STR measurements 26-31 (01_00890 – 01_00962 respectively) for the same day (squares). The polar winter climatology of Remedios, 1999, is also shown (blue squares) for comparison.

For scan #28, the agreement between HAGAR and OPERA at 320 mb and 120 mb is excellent at better than 25 pptv (5 %). Differences are up to 20 % at other heights. The agreement between MIPAS-STR and OPERA is very good within error limits between the 120 mb and 200 mb OPERA data with the MIPAS-STR data. At 320 mb, however, OPERA is much higher than MIPAS-STR by 150 pptv. These results suggest a problem with the MIPAS-STR data at that pressure level and not with OPERA data, due to the retrieval showing excellent agreement with the *in situ* measurement by HAGAR.

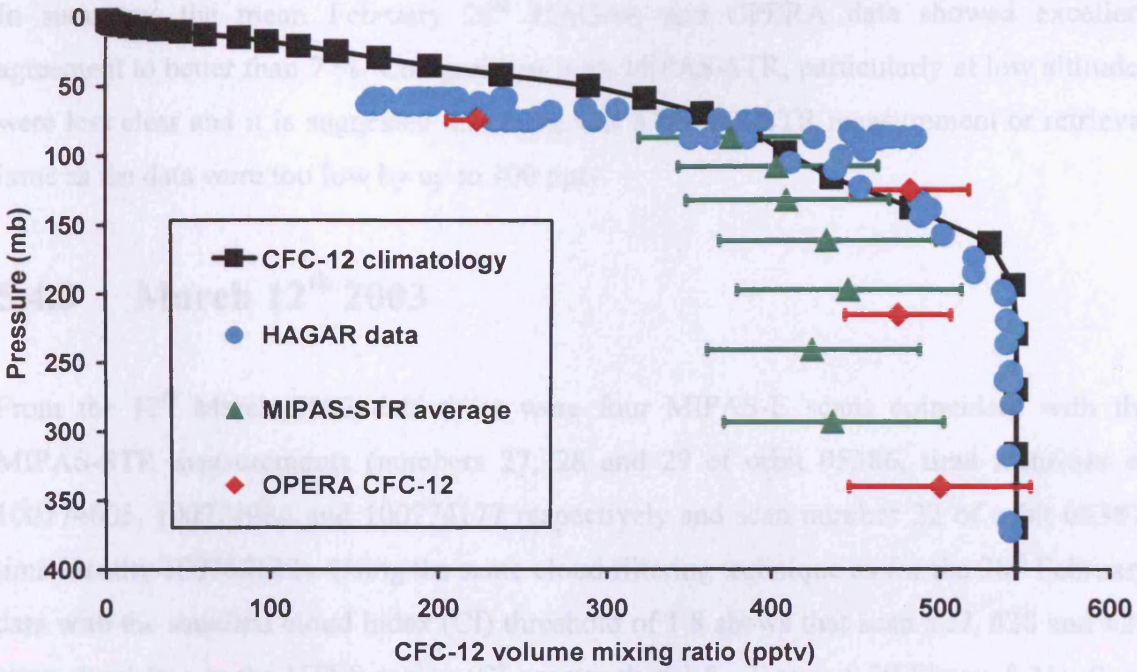

Figure 5.26 Retrieved OPERA CFC-12 data for scan #29 of orbit 05214 on February 28th 2003 (red triangles). Coincident CFC-12 data from MIPAS-STR measurements 1 to 6 (01_00513 to 01_00582 respectively) for the same day (squares). HAGAR data measured on the same day are also plotted. The polar winter climatology of Remedios, 1999, is shown (blue squares) for comparison.

The comparison of scan #29 OPERA results with HAGAR was good, and three of the four OPERA data points agreed with HAGAR measurements within errors. The mean agreement was better than 7 %. The OPERA data at 220 mb was low compared to HAGAR by approximately 60 pptv. It was not clear why this should have been the case.

For scan #29 of orbit 05214, OPERA CFC-12 results are comparable, within error, with MIPAS-STR data between 120 to 350 mb (Figure 5.26). It was noted that the OPERA retrieval at 320 mb had a cloud index value of 2.2 (Figure 5.24), only 0.4 above the optically thick cloud limit. The joint retrieval of total extinction for the scan showed an enhanced value of extinction compared to the climatology at 350 mb of 1.4×10^{-5} km^{-1} to 7.4×10^{-5} km^{-1}. This is evidence for OPERA producing reasonable retrieval data for CFC-12 even in the presence of thin cloud, at least within errors.

There was observed a low bias of up to 110 pptv between the mean MIPAS-STR profile and the HAGAR data.

In summary, the mean February 28th HAGAR and OPERA data showed excellent agreement to better than 7 %. Comparisons with MIPAS-STR, particularly at low altitudes were less clear and it is suggested that there was a MIPAS-STR measurement or retrieval issue as the data were too low by up to 100 pptv.

5.4.3 March 12th 2003

From the 12th March 2003 data there were four MIPAS-E scans coincident with the MIPAS-STR measurements (numbers 27, 28 and 29 of orbit 05386, time identities of 100774005, 100774086 and 100774177 respectively and scan number 22 of orbit 05387, time identity 100780122). Using the same cloud filtering technique as for the 28th February data with the standard cloud index (CI) threshold of 1.8 shows that scan #27, #28 and #29 were cloud free in the UTLS region (CI greater than 1.8 - Figure 5.29-Figure 5.31). Scan #22 of orbit 05387 was cloudy at 9 km and so was excluded from the validation study. Coincident data from HAGAR were also available for this day. The flight track is shown in Figure 5.28.

Consolidated version 4.61 level 1b spectra were available for all three orbit 05386 scans at all nominal tangent heights between 6 and 68 km. For scan #27 consolidated level 2 data (version 4.61) were available for water vapour, ozone, pressure and temperature between 9 and 68 km inclusive and nitric acid between 9 and 39 km inclusive. Both scans #28 and #29 had consolidated version 4.61 level 2 data available for water vapour, ozone, pressure and temperature between 6 and 68 km inclusive and nitric acid between 9 and 36 km inclusive and at 42 km.

Figure 5.32 compares OPERA retrieved CFC-12 for scan #27 of orbit 05386, six coincident MIPAS-STR CFC-12 profiles and coincident HAGAR CFC-12 measurements. The temporal difference between the measurements was again low as MIPAS-STR spectral measurements (scans 42 to 47) were made only 45 to 59 minutes before the six MIPAS-E measurements. For the MIPAS-STR CFC-12, a mean profile (green triangles) is plotted alongside the data from the six scans that comprise this profile, with the associated 15 % error limits to the data estimated from Keim *et al.*, [2004]. The OPERA retrieved data also include the total error estimate error bars for the root mean square of all error sources described in sections 4.2.6.1 and 4.2.6.2.

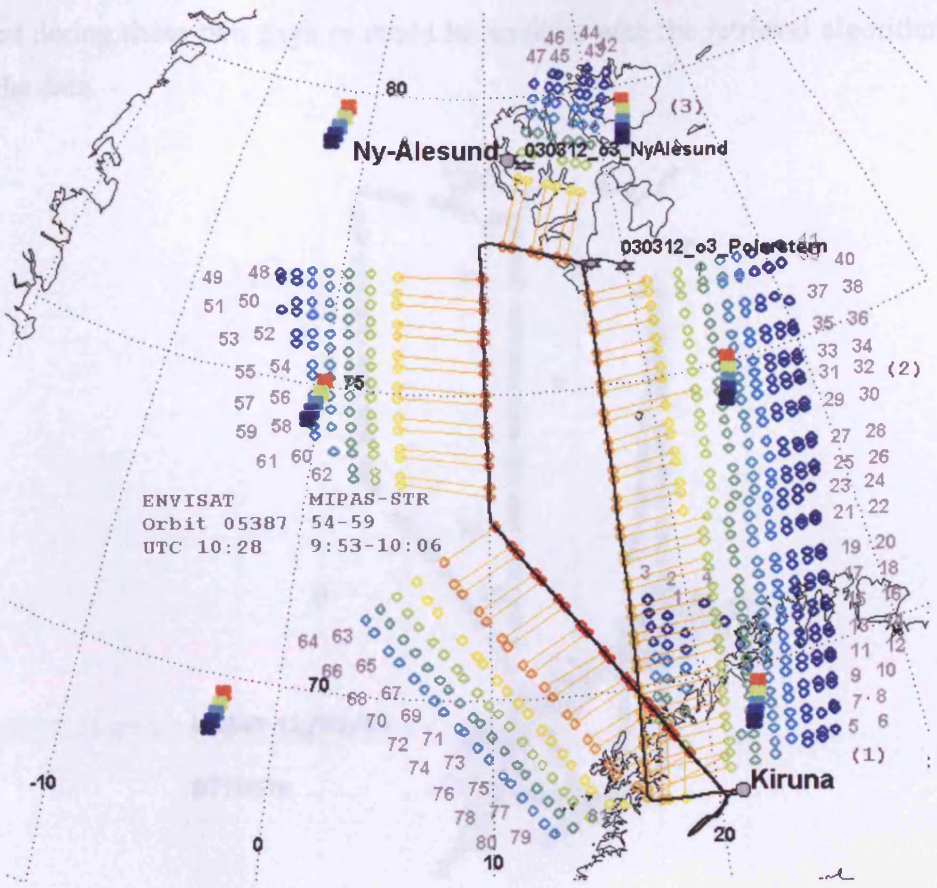

Figure 5.27 The flight track of the Geophysica aircraft (solid black line) and the corresponding MIPAS-STR measurements from this flight (open circles) on March 12th 2003. The data points are plotted at 1.5 km intervals from 6 km (red) to approximately 20 km (dark blue). The MIPAS-E scan information data (orbits 05386 and 05387) are also plotted at heights between approximately 9 (orange) and 21 km (dark blue) at the nominal MIPAS-E spacing of 3 km. (1) ENVISAT Orbit 05386, UTC 8:49; MIPAS-STR 6-11, UTC 9:16–9:30. (2) ENVISAT Orbit 05386, UTC 8:47; MIPAS-STR 31-36, UTC 8:45–8:58. (3) ENVISAT Orbit 05386, UTC 8:46; MIPAS-STR 42-47, UTC 7:47-8:01. Plot courtesy of Corneli Keim (IMK) and adapted to include time identity tags (1-3) for ENVISAT and MIPAS-STR measurements.

Results from March 12th (Figure 5.32, Figure 5.33 and Figure 5.34) showed very good mean agreement with HAGAR data on average to better than 30 pptv (6 %). Both data represented also show similarities in profile shape. The agreement between OPERA and MIPAS-STR was again poor for reasons mentioned earlier.

For the mean of the March 2003 data, MIPAS-STR data between 130 and 350 mb are consistently lower than both OPERA retrieved data and HAGAR data. Differences are up to 120 pptv (greater than 20 %) and largest at higher pressures. The reason for this persistent feature was not clear although it may suggest a problem with the MIPAS-STR

instrument during these two days or could be an issue with the retrieval algorithm used to retrieve the data.

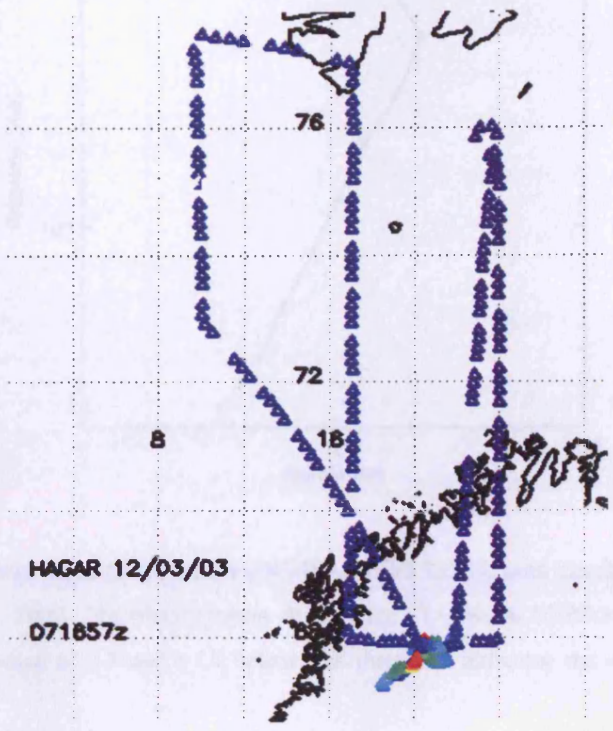

Figure 5.28. HAGAR measurements from March 12th 2003. The data were measured between 58 mb (blue triangles) and 800 mb (red triangles). Most profile information was centred at 68°N, 20°E.

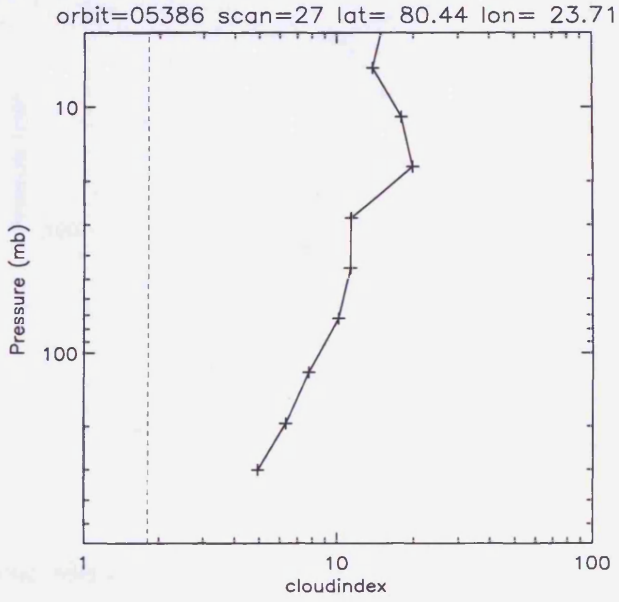

Figure 5.29 MIPAS-E Cloud index (CI) plot for ENVISAT orbit 05386, scan number 27 using the technique described by Spang *et al.*, 2002. The black crosses display the CI value at MIPAS-E tangent pressures. The dashed line shows a CI value of 1.8 and a CI below this threshold indicates the sweep is contaminated by cloud.

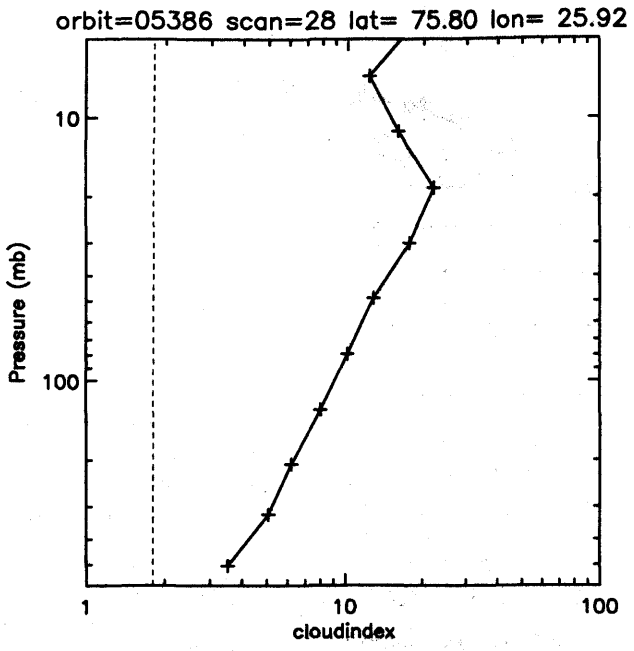

Figure 5.30 MIPAS-E Cloud index (CI) plot for ENVISAT orbit 05386, scan number 28 using the technique described by Spang *et al.*, 2002. The black crosses display the CI value at MIPAS-E tangent pressures. The dashed line shows a CI value of 1.8 and a CI below this threshold indicates the sweep is contaminated by cloud.

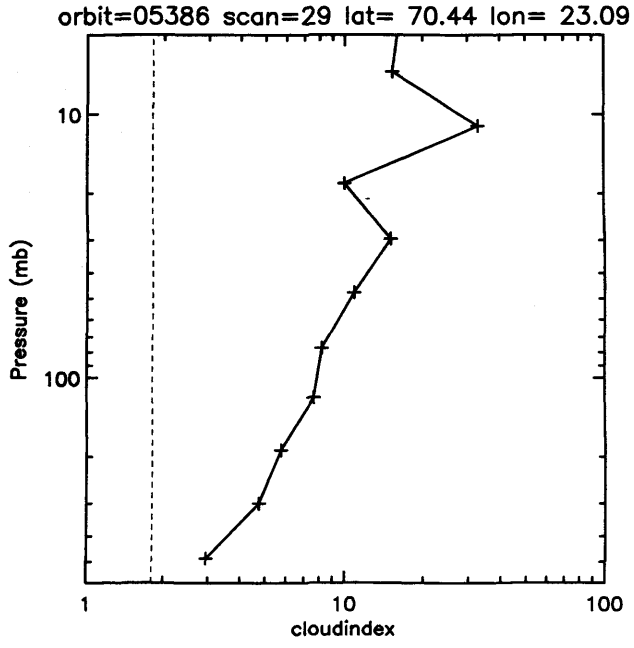

Figure 5.31 MIPAS-E Cloud index (CI) plot for ENVISAT orbit 05386, scan number 29 using the technique described by Spang *et al.*, 2002. The black crosses display the CI value at MIPAS-E tangent pressures. The dashed line shows a CI value of 1.8 and a CI below this threshold indicates the sweep is contaminated by cloud.

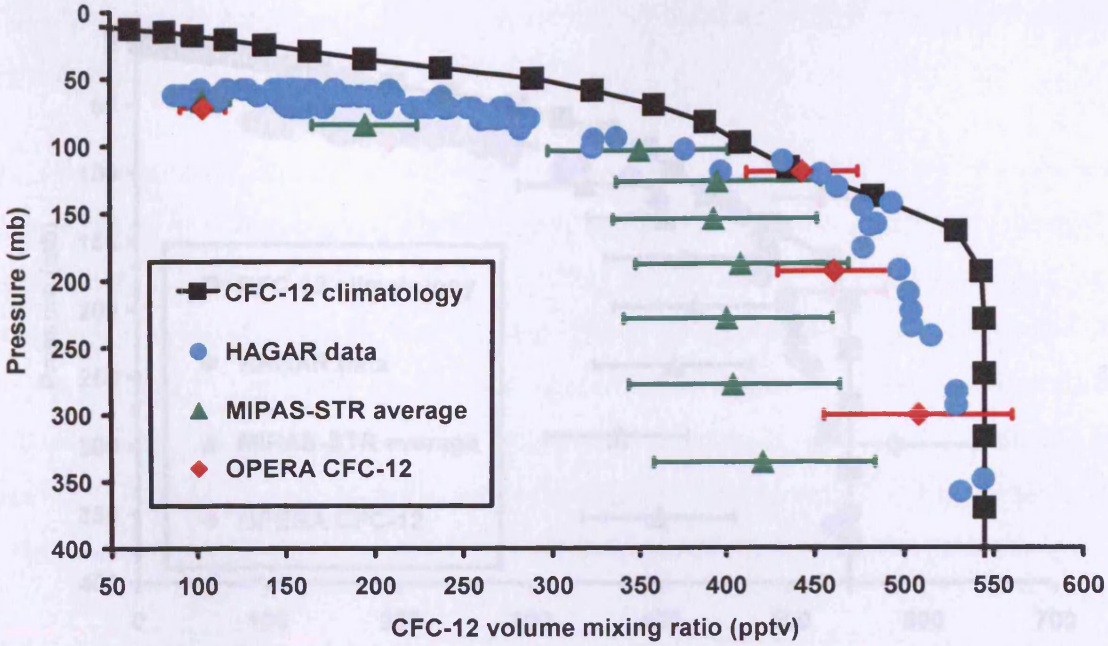

Figure 5.32 Retrieved OPERA CFC-12 data for scan #27 of orbit 05386 on March 12th 2003 (red triangles). Also plotted is the coincident CFC-12 data from MIPAS-STR measurements 42 to 47 (01_01092 to 01_01168 respectively) for the same day (squares). The polar winter climatology of Remedios [1999] is also shown (blue squares) for comparison.

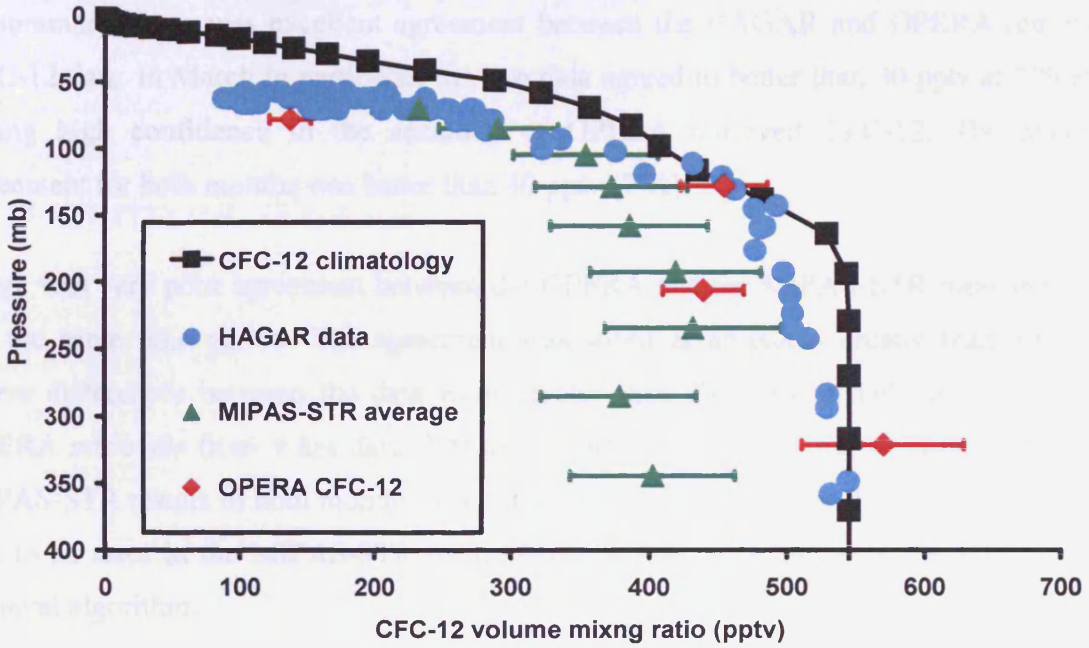

Figure 5.33 Retrieved OPERA CFC-12 data for scan #28 of orbit 05386 on March 12th 2003 (red triangles). Also plotted is the coincident CFC-12 data from MIPAS-STR measurements 31 to 36 (01_00898 to 01_00972 respectively) for the same day (squares). The polar winter climatology of Remedios [1999] is also shown (blue squares) for comparison.

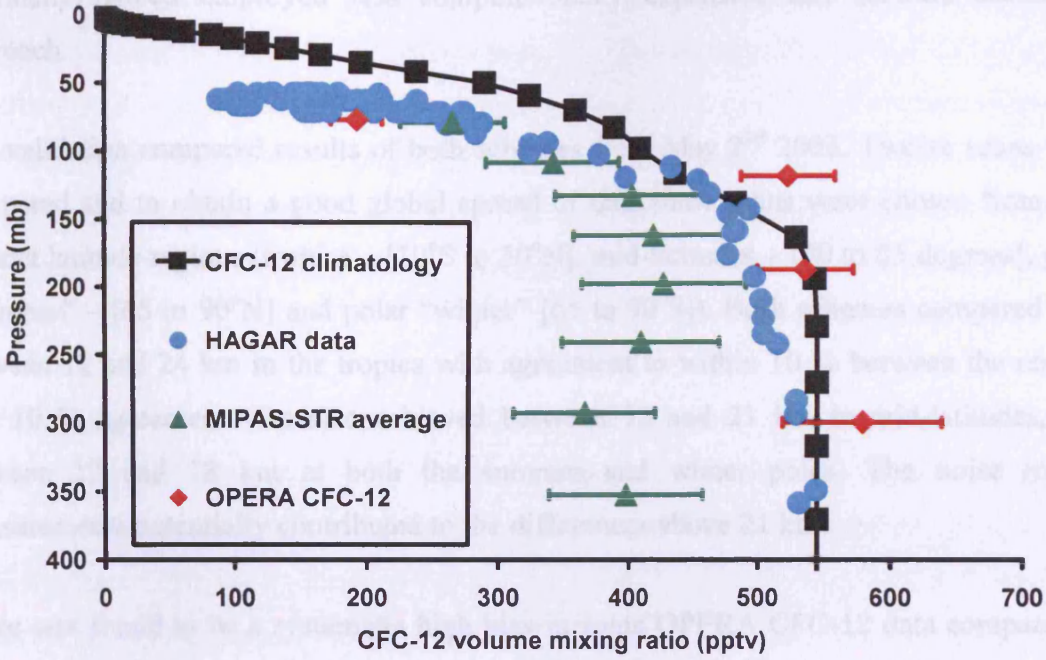

Figure 5.34 Retrieved OPERA CFC-12 data for scan #29 of orbit 05386 on March 12th 2003 (red triangles). Also plotted is the coincident CFC-12 data from MIPAS-STR measurements 6 to 11 (01_00541 to 01_00612 respectively) for the same day (squares). The polar winter climatology of Remedios [1999] is also shown (blue squares) for comparison.

In summary, there was excellent agreement between the HAGAR and OPERA retrieved CFC-12 data. In March in particular, the two data agreed to better than 30 pptv at 300 mb, giving high confidence in the accuracy of OPERA retrieved CFC-12. The average agreement for both months was better than 40 pptv (7 %).

There was very poor agreement between the OPERA and the MIPAS-STR measurements for the same time period. The agreement was worst at pressures greater than 300 mb, where differences between the data were greater than 200 pptv in February 2003. The OPERA retrievals from 9 km data (300 to 320 mb) tended to be higher compared to the MIPAS-STR results in both months. The most likely explanation for these differences was due to an error in the MIPAS-STR instrument, the measurement, or in the MIPAS-STR retrieval algorithm.

5.5 Summary

This chapter has compared retrieved CFC-12 results obtained by the OPERA scheme from MIPAS-E spectra with results using a scheme developed at a research institute in Juelich

(Germany) which employed less computationally expensive fast forward modelling approach.

The validation compared results of both schemes from May 2nd 2003. Twelve scans were compared and to obtain a good global spread of data three scans were chosen from four distinct latitude regions (tropics – [30°S to 30°N], mid-latitudes – [30 to 65 degrees], polar "summer" – [65 to 90°N] and polar "winter" [65 to 90°S]). Both schemes compared well between 12 and 24 km in the tropics with agreement to within 10 % between the results. The 10 % agreement was also achieved between 12 and 21 km in mid-latitudes, and between 12 and 18 km at both the summer and winter poles. The noise in the measurements potentially contributed to the differences above 21 km.

There was found to be a systematic high bias in some OPERA CFC-12 data compared to those retrieved from the Juelich scheme. This occurred chiefly when OPERA retrieved CFC-12 vmrs were below 400 pptv in the tropics, 200 pptv in mid-latitudes, 300 pptv at the summer pole (Arctic) and below 150 pptv at the winter pole (Antarctica).

Aerosol comparisons showed very good agreement in general shape between both schemes but there was poor agreement quantitatively, with some Juelich aerosol profiles high biased compared to OPERA profiles by up to 100 %. At extinctions greater than 10^{-4} km^{-1} the average of three profiles showed very good agreement giving some confidence to the OPERA aerosol retrievals. At lower extinctions, the profiles were similarly shaped but with a systematic bias between them.

This chapter has validated OPERA retrieved HCFC-22 and CFC-12 vmrs from MIPAS-E data by tracer-tracer comparisons with operationally retrieved N_2O version 4.61 data from May 2nd 2003. MIPAS-E N_2O data have been measured to within 10 % precision and a zonal comparison with the version 3.1 reference atmospheres of Remedios [1999] showed less than a 10 % difference to the climatology in the tropics between 9 and 21 km. In mid-latitudes the agreement was better than 8 % below 21 km. Results from the Arctic (polar summer) agree to within 7 % between 9 and 15 km. In the Antarctic (polar winter), the profile shapes between the climatology N_2O and MIPAS-E N_2O are very different and there was a high bias of MIPAS-E data by between 25 and 70 %. Therefore it was shown that the MIPAS-E data between 9 and 15 km in particular gave similar behaviour to the N_2O climatology and could be used in tracer-tracer correlations with some confidence.

There was a positive bias in the global MIPAS-E N_2O and OPERA CFC-12 correlation compared to the expected relationship from the climatology files. This could not be explained by changes of atmospheric concentration of either gas since the climatology was produced and is explained by a slight high bias in the MIPAS-E N_2O or up to 30 pptv low bias in the CFC-12. For HCFC-22, the global atmospheric increase of 20 pptv expected from surface observations since the climatology was produced, was realised in the comparison.

A close agreement was found between ATMOS CFC-12 and OPERA CFC-12 and there was an indication that the OPERA retrieved results fitted the trend expected since the ATMOS measurements were made as estimated from surface measurements and age of air considerations. The comparison between ATMOS HCFC-22 and OPERA retrieved HCFC-22 showed an average increase in HCFC-22 global concentrations of approximately 7 pptv/yr since ATMOS. This was higher than that estimated from surface measurements but lower than that derived from ACE data in 2004. Indications are that HCFC-22 could be accurate to 15 pptv (better than 10 %).

Validation of OPERA retrieved CFC-12 data with measurements from the HAGAR instrument flown onboard the Geophysica aircraft in late Northern Hemisphere winter (February 28th and March 12th 2003) were also performed. Here consolidated level 2 data (version 4.61), including pressure, temperature, water vapour, ozone and nitric acid, were incorporated in the forward modelling and not the near real time products (version 4.57). CFC-12 data were compared over the 9 to 18 km range. There was excellent agreement between the HAGAR and OPERA retrieved CFC-12 data. In March in particular, the two data agreed to better than 30 pptv (6 %) at 300 mb, giving high confidence in the accuracy of OPERA retrieved CFC-12. The mean difference for both months between OPERA and HAGAR was better than 40 pptv (7 %).

There was found a low bias of MIPAS-STR CFC-12 compared to the polar winter climatology used by 80 to 170 pptv throughout the 9 to 18 km range. Although OPERA CFC-12 was also generally low biased compared to the same climatology, especially at 9 and 12 km, the differences were less than 90 pptv. The mean OPERA CFC-12 profile from the five scans was high biased compared to the mean MIPAS-STR profile by between 50 and 135 pptv in the lower stratosphere, although at approximately 21 km the mean

MIPAS-STR CFC-12 concentration was greater than OPERA CFC-12 by 60 pptv. It was likely that the MIPAS-STR data were in error.

The good results in CFC-12 in conjunction with the indirect validation for HCFC-22 lend some confidence to the quality of the OPERA HCFC-22 and CFC-12 data. The following chapter shows results of using the OPERA scheme to retrieve volume mixing ratios of both CFC-12 and HCFC-22 (and aerosol) in the upper troposphere and lower stratosphere from the four seasons in 2003 and investigates distribution of the gases over time and space.

Chapter 6

6 Seasonal halocarbon measurements

6.1 HCFC-22

In chapter 1 it was noted that the distribution of hydrochlorofluorocarbon-22 (HCFC-22) throughout the troposphere and lower stratosphere and the trend over time is important to quantify its contribution as an efficient greenhouse gas. If transported to the stratosphere, it also plays an important role in stratospheric chemistry through the release of chlorine which consequently reacts with ozone and destroys the ozone layer protecting life on Earth from ultraviolet radiation from the sun.

Global average surface measurements from stations as part of the American based National Oceanic and Atmospheric Administration (NOAA) Earth System Research Laboratory (ESRL) determined a mean surface concentration of HCFC-22 of 158 pptv in 2003, increasing at approximately 5 pptv/yr. These estimates were based on surface data that were available publicly from http://www.cmdl.noaa.gov/hats/. The method used by ESRL to produce these global surface data and early results were first presented in Montzka *et al.*, [1993] and a brief description was given in chapter 1. Further HCFC-22 data were presented in Montzka *et al.*, [1996] and Montzka *et al.*, [1999]. Results from ESRL Northern Hemisphere HCFC-22 data in 2003 were also published by Rinsland *et al.*, [2005a].

The tropospheric lifetime of HCFC-22 is 11.8 years [IPCC, 2001], inferring the gas should be well-mixed although not necessarily completely uniform, and so it can be inferred from the surface data that the mean tropospheric concentration of HCFC-22 in 2003 was 158 pptv. This, combined with routine surface measurements of HCFC-22, mean that tropospheric levels can be estimated as a function of time. In the lower stratosphere, HCFC-22 has a strong vertical gradient due to its stratospheric lifetime and high static stability of the layer. The distribution of the gas spatially and temporally is not well known and has to be inferred from infrequent balloon and aircraft measurements.

The aims of this section were therefore twofold. The first aim was to measure the tropospheric concentration of HCFC-22 from MIPAS-E measurements to confirm that, within errors, the OPERA scheme could retrieve tropospheric HCFC-22. The second aim and the initial aim of the thesis overall, was to measure HCFC-22 in the lower stratosphere and in particular to examine the zonal and temporal distribution of the gas. It was discovered (section 2.5.3) that the vertical extent to which HCFC-22 could be measured from MIPAS-E was limited by the low signal to noise above 15 km. Stratospheric information, however, might be present in the mid-latitudes and poles at 15 km and below.

6.1.1 Retrieval periods

To investigate the temporal and zonal distribution of HCFC-22 from MIPAS-E measurements, data were chosen and analysed from each of the four seasons in 2003. One month was chosen from each season to represent the "mid" season and from each month one week of MIPAS-E data was chosen with the largest number of data (Table 6.1 to Table 6.4). The analysis could not be extended to include more than one week from each season due to computational constraints. One week of data was sufficient, however, for two reasons. Firstly, as a global average, the gas is fairly well-mixed throughout the whole troposphere. Secondly, although strong vertical gradients are likely to exist in the lower stratosphere because of high static stability, the mean features of the distribution are likely to be well-represented by the global coverage with one week of data.

DATE	8/1/03	9/1/03	10/1/03	11/1/03	12/1/03	13/1/03	14/1/03	TOTAL
orbits	12	10	5	9	11	14	11	72
profiles	379	314	118	300	341	440	305	2197

Table 6.1 The number of orbits and profiles with reprocessed level 1b (version 4.62) and corresponding level 2 (version 4.62) data from January 8th to 14th 2003 inclusive.

DATE	15/4/03	16/4/03	17/4/03	18/4/03	19/4/03	20/4/03	21/4/03	TOTAL
orbits	9	9	12	8	9	10	10	67
profiles	174	156	228	142	187	168	225	1280

Table 6.2 The number of orbits and profiles with reprocessed level 1b (version 4.62) and corresponding level 2 (version 4.62) data from April 15th to 21st 2003 inclusive.

For 2003, January, April, July and October were chosen as suitable months, all providing MIPAS-E measurement data. For each month, data were cloud screened by the cloud index (CI) technique introduced in section 4.1.2.4.1 using a threshold of 1.8. October provided the largest dataset for the week, containing the greatest number of orbits (83) and from that the largest number of cloud screened and converged profiles (2212). Each day between the 15th and 21st October provided converged data for more than 243 scans and up to 356.

DATE	8/7/03	9/7/03	10/7/03	11/7/03	12/7/03	13/7/03	14/7/03	TOTAL
orbits	11	11	13	10	8	9	12	74
profiles	64	95	107	86	87	89	174	702

Table 6.3 The number of orbits and profiles with reprocessed level 1b (version 4.61) and corresponding level 2 (version 4.61) data from July 8th to 15th 2003 inclusive.

DATE	15/10/03	16/10/03	17/10/03	18/10/03	19/10/03	20/10/03	21/10/03	TOTAL
orbits	11	13	11	11	11	13	13	83
profiles	243	308	309	321	325	350	356	2212

Table 6.4 The number of orbits and profiles with reprocessed level 1b (version 4.61) and corresponding level 2 (version 4.61) data from July 8th to 15th 2003 inclusive.

6.1.2 Global and Seasonal means

This section analyses the vertical distribution of measured HCFC-22 from OPERA globally and also in four distinct zonal regions, the tropics (30°S to 30°N), mid-latitudes (30 to 65 degrees) and both poles (65 to 90°S and 65 to 90°N).

Globally, the HCFC-22 retrievals from MIPAS-E data were expected (section 4.2.3) to produce, on average, more information from the measurements than the *a priori* at three levels (9, 12 and 15 km levels), when retrievals were performed between 9 and 21 km. This was found for most seasons and most regions although some variation occurred with season for certain latitudes, most notably for the Antarctic winter season (July). This was most likely caused by the onset of the Antarctic vortex which introduces very cold temperatures (often below -80°C) and relatively "clean" air containing low halocarbon amounts from higher up in the stratosphere into the polar lower stratosphere.

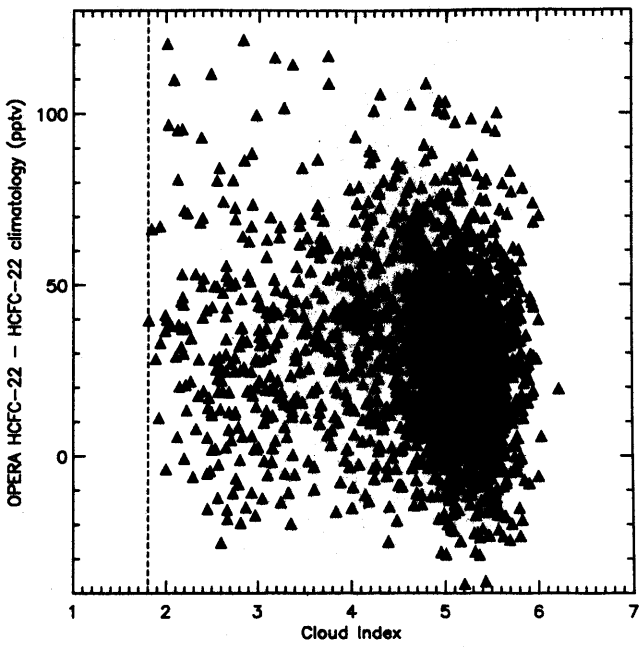

Figure 6.1 OPERA retrieved HCFC-22 data plotted against cloud index (CI) at approximately 9 km (MIPAS-E scan height 15). The plot includes all converged data for January 8th-14th 2003. The HCFC-22 data have been differenced with the HCFC-22 climatology to remove any bias within the retrieved data.

Firstly, to confirm that the OPERA retrieved HCFC-22 volume mixing ratios were independent of cloud, the difference between the retrieved HCFC-22 volume mixing ratios and the HCFC-22 climatology were plotted as a function of cloud index (CI) at 9 km (Figure 6.1). The lack of any strong correlation between the data (the associated correlation coefficient was -0.162) confirmed that the OPERA scheme performed HCFC-22 retrievals with no dependence on aerosol or cloud contamination in the measured spectrum, at least where the CI was greater than or equal to 1.8.

The most obvious place for comparison to surface measurements is the tropics at the lowest altitudes where air is clearly tropospheric in character. The mean of all four seasons measured at 9 km in the tropics is 187 pptv which is 29 pptv (34 %) greater than the surface mean measurement for 2003.

Outside the tropics 9 km altitude is likely to be in the uppermost troposphere in mid-latitudes. At the poles, 9 km may be in the upper troposphere or lowermost stratosphere depending on the season. Comparing the global average at 9 km, for all seasons (Table 6.5), it was shown that within measurement error there was agreement between average global ESRL surface measurements in all three months. The mean agreement was better than 15 %.

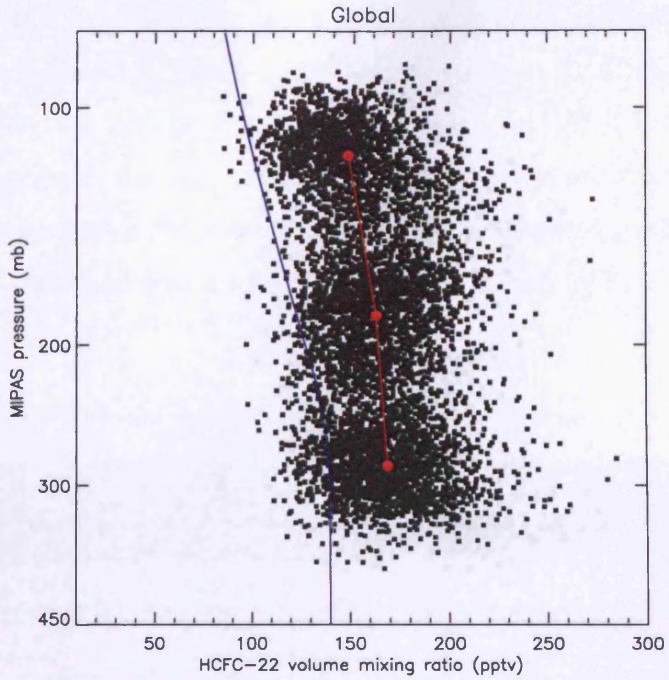

Figure 6.2 OPERA retrieved HCFC-22 data (black squares) from MIPAS-E level 1b (version 4.62) data between the 8th to 14th January 2003 (orbits 04480 to 04579). Mean HCFC-22 data (red circles) are shown at an average pressure for each level (Table 6.5). The solid blue line displays the HCFC-22 *a priori* climatology profile used in OPERA [Remedios, 1999].

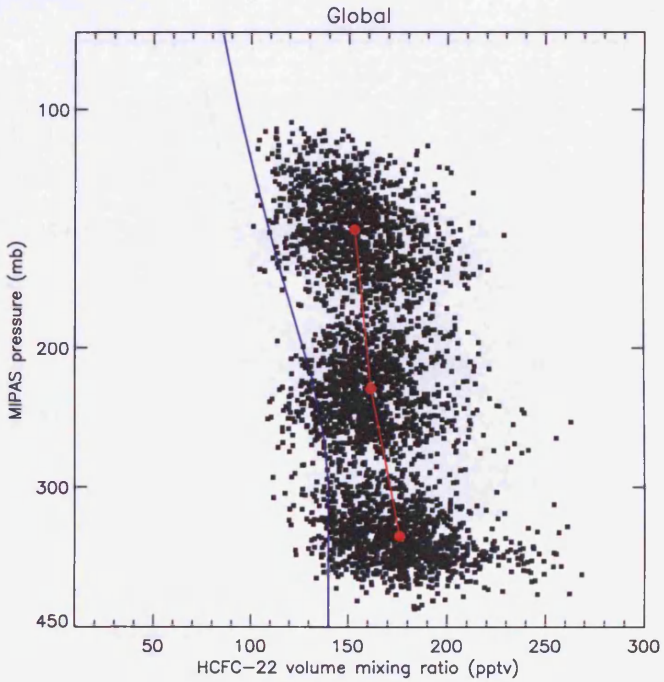

Figure 6.3. Retrieved HCFC-22 data (black squares) from MIPAS-E level 1b (version 4.61) data between the 15th to 21st April 2003 (orbits 05868 to 05967). Mean HCFC-22 data (red circles) are shown at an average pressure for each level (Table 6.5) by red circles. The solid blue line displays the HCFC-22 *a priori* climatology profile used in OPERA [Remedios, 1999].

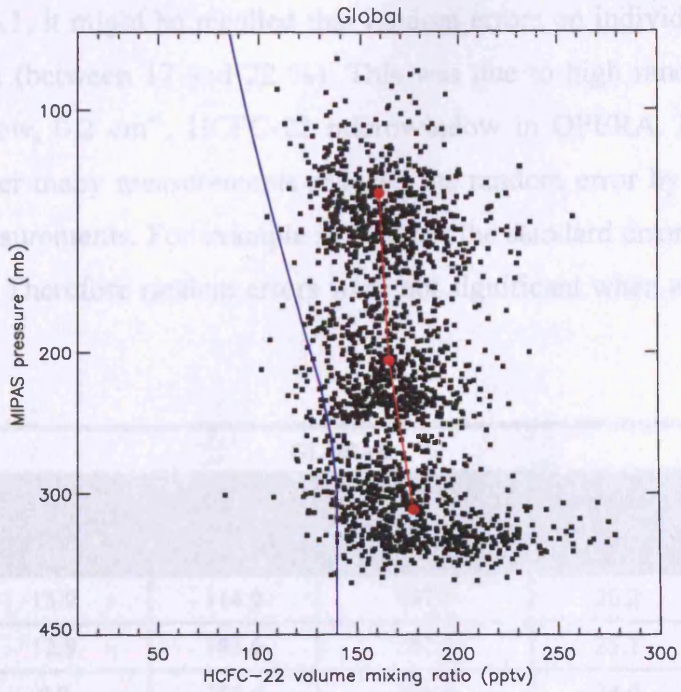

Figure 6.4. Retrieved HCFC-22 data (black squares) from MIPAS-E level 1b (version 4.61) data between the 8th to 15th July 2003 (orbits 07070 to 07170). Mean HCFC-22 data (red circles) are shown at an average pressure for each level (Table 6.5) by red circles. The solid blue line displays the HCFC-22 *a priori* climatology profile used in OPERA [Remedios, 1999].

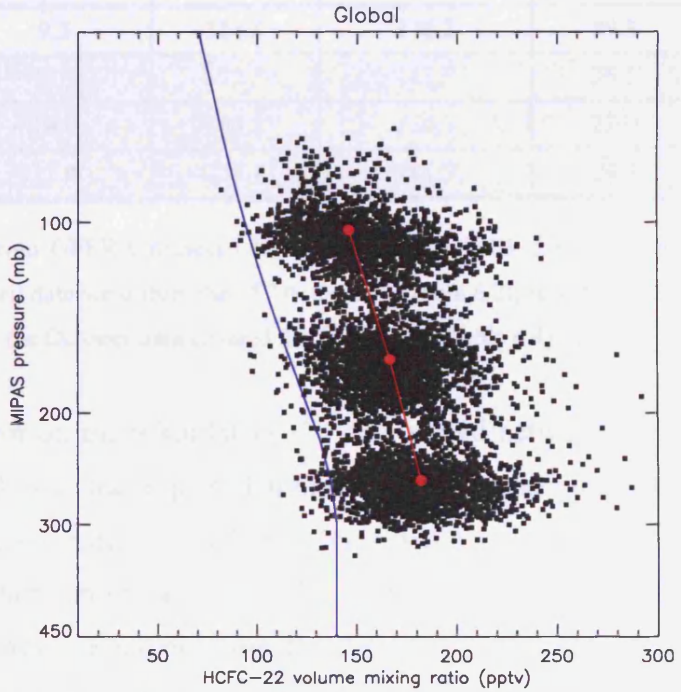

Figure 6.5. Retrieved HCFC-22 data (black squares) from MIPAS-E level 1b (version 4.61) data between the 15th to 21st October 2003 (orbits 08488 to 08587). Mean HCFC-22 data (red circles) are shown at an average pressure for each level (Table 6.5) by red circles. The solid blue line displays the *a priori* climatology profile of HCFC-22 used [Remedios, 1999].

From section 4.2.6.1, it might be recalled that random errors on individual HCFC-22 data at 9 km were high (between 17 and 22 %). This was due to high random retrieval error from using a narrow, 0.2 cm^{-1}, HCFC-22 microwindow in OPERA. From global mean data, averaging over many measurements reduced the random error by the square root of the number of measurements. For example in October the standard error on the 9 km mean was only 0.5 pptv. Therefore random errors were not significant when analysing data from each week.

GLOBAL					
month (2003)	**Mean altitude (km)**	**Mean Pressure (mb)**	**MEAN HCFC-22 volume mixing ratio (pptv)**	**standard deviation (pptv)**	**Standard Error on mean (pptv)**
January	15.9	114.9	147.5	26.2	0.6
	12.9	183.6	162.3	23.1	0.5
	9.9	283.5	169.0	24.0	0.5
April	14.5	141.7	152.9	21.9	0.6
	11.5	225.4	160.9	21.0	0.6
	8.5	346.0	175.9	25.1	0.7
July	15.4	127.0	160.1	24.7	0.9
	12.4	205.0	166.0	21.7	0.8
	9.5	314.5	178.2	29.3	1.1
October	16.9	102.7	145.7	26.5	0.6
	14.0	164.8	166.1	22.0	0.5
	11.0	255.7	181.5	24.7	0.5

Table 6.5. Statistics from OPERA retrieved HCFC-22 data for 2003. January data covered the 8th to 14th period (Table 6.1), April data were from the 15th to the 21st (Table 6.2), July data were from the 8th to the 14th (Table 6.3) and finally the October data covered the 15th to 21st (Table 6.4) period.

The systematic error on the 9 km HCFC-22 data varied between 7 % at the summer pole and increased to 11 % in the tropics, dominated by spectroscopic error introduced from the HITRAN cross-section data, although gain error was also important. Systematic error on a measurement can not simply be reduced by increasing the number of measurements. For example the HITRAN line and cross-section data were identical for every OPERA retrieval and so each retrieval would be affected identically, making the error source wholly systematic. Including the systematic error terms, the highest global mean data at 9 km in October (181.5 ± 18 pptv) still agrees with the indirect surface measurement within the error limits.

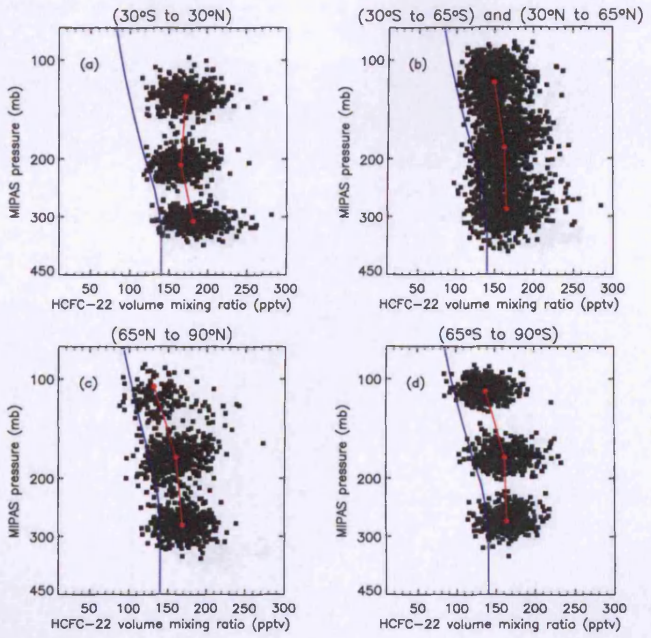

Figure 6.6 OPERA retrieved HCFC-22 data (black squares) from MIPAS-E level 1b (version 4.62) data between 8th to 14th January 2003 (orbits 04480 to 04579). The data are identical to those in Figure 6.2 but divided into four regions, depending on latitude. Mean HCFC-22 data (red circles) are shown at an average pressure for each level (Table 6.6 to Table 6.9). The solid blue line displays the version 3.1 climatology profile of HCFC-22 from Remedios [1999].

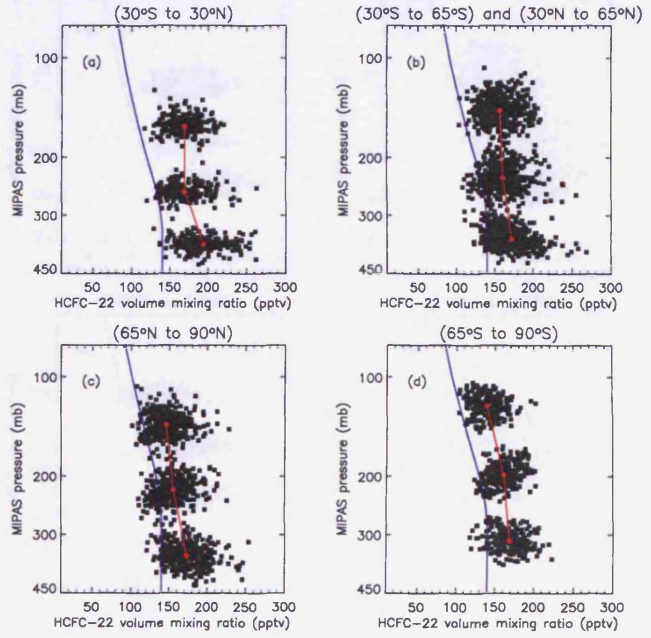

Figure 6.7. OPERA retrieved HCFC-22 data (black squares) from MIPAS-E level 1b (version 4.61) data between 15th to 21st April 2003 (orbits 05868 to 05967). The data are identical to those in Figure 6.3 but divided into four regions, depending on latitude. Mean HCFC-22 data (red circles) are at an average pressure for each level (Table 6.6 to Table 6.9). The solid blue line displays the version 3.1 climatology profile of HCFC-22 from Remedios [1999].

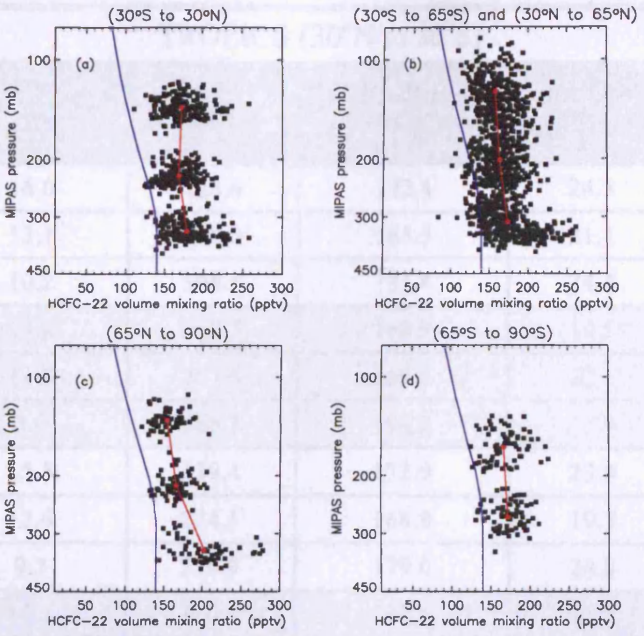

Figure 6.8. OPERA retrieved HCFC-22 data (black squares) from MIPAS-E level 1b (version 4.61) data between 8th to 14th July 2003 (orbits 07070 to 07170). The data are identical to those in Figure 6.4 but divided into four regions, depending on latitude. Mean HCFC-22 data (red circles) are shown at an average pressure for each level (Table 6.6 to Table 6.9). The solid blue line displays the version 3.1 climatology profile of HCFC-22 from Remedios [1999].

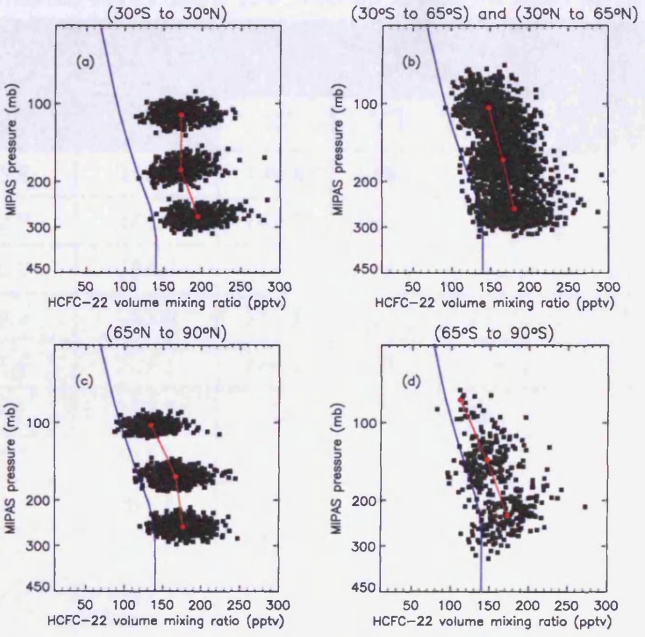

Figure 6.9. OPERA retrieved HCFC-22 data (black squares) from MIPAS-E level 1b (version 4.61) data between 15th to 21st October 2003 (orbits 08488 to 08587). The data are identical to those in Figure 6.4 but divided into four regions, depending on latitude. Mean HCFC-22 data (red circles) are shown at an average pressure for each level (Table 6.6 to Table 6.9). The solid blue line displays the version 3.1 climatology profile of HCFC-22 from Remedios [1999].

TROPICS (30°N to 30°S)					
month (2003)	**Mean altitude (km)**	**Mean Pressure (mb)**	**MEAN HCFC-22 volume mixing ratio (pptv)**	**standard deviation (pptv)**	**Standard Error on mean (pptv)**
January	16.0	128.6	172.4	24.3	1.2
	13.1	208.0	165.5	21.1	1.0
	10.2	308.5	181.4	24.4	1.2
April	14.8	160.5	168.9	19.5	1.3
	11.8	253.6	169.0	22.1	1.4
	8.9	366.3	194.2	27.4	1.8
July	15.5	139.4	172.9	23.9	1.7
	12.6	224.1	168.8	19.7	1.4
	9.7	330.9	179.0	24.8	1.8
October	17.4	110.6	172.9	23.3	1.1
	14.5	180.4	172.6	21.7	1.0
	11.7	273.9	195.0	24.4	1.2

Table 6.6 Statistics from OPERA retrieved HCFC-22 data in the tropics (30°S to 30°N). For each season, data covered the periods described in section 6.1.1.

MID-LATITUDES (30°S to 65°S and 30°N to 65°N)							
month (2003)	**Mean altitude (km)**	**Mean Pressure (mb)**	**MEAN HCFC-22 volume mixing ratio (pptv)**			**standard deviation (pptv)**	**Standard Error on mean (pptv)**
			All	NH	SH		
January	15.8	116.9	149.8	148.6	151.5	22.1	0.8
	12.9	184.4	162.8	161.6	164.8	23.6	0.8
	10.0	284.0	165.3	158.1	176.2	26.1	0.9
April	14.6	143.6	157.1	157.0	157.2	20.2	1.0
	11.6	229.5	160.9	163.5	158.3	21.6	1.0
	8.6	352.2	172.1	177.0	167.2	23.4	1.1
July	15.5	125.3	158.5	168.1	153.1	22.9	1.2
	12.5	201.8	164.2	171.6	160.1	23.1	1.2
	9.5	311.5	174.6	198.7	161.2	30.5	1.6
October	17.0	103.6	148.0	152.1	141.1	21.0	0.7
	14.1	164.7	166.4	167.8	164.0	20.9	0.7
	11.2	254.3	180.4	177.7	185.0	25.1	0.8

Table 6.7 Statistics from OPERA retrieved HCFC-22 data in the mid-latitudes (30 to 65 degrees). For each season, data covered the periods described in section 6.1.1.

NORTHERN HEMISPHERE POLAR (65°N to 90°N)					
month (2003)	**Mean altitude (km)**	**Mean Pressure (mb)**	**MEAN HCFC-22 volume mixing ratio (pptv)**	**standard deviation (pptv)**	**Standard Error on mean (pptv)**
January	14.9	105.6	131.7	22.5	1.0
	11.9	172.1	160.3	24.8	1.1
	8.9	276.2	168.9	20.5	0.9
April	13.6	139.5	146.3	19.8	1.0
	10.5	219.7	155.7	20.0	1.0
	7.5	346.4	173.2	22.9	1.2
July	14.1	135.4	154.1	17.2	2.1
	11.1	213.9	166.0	16.9	2.1
	8.0	337.5	202.8	32.7	4.1
October	16.1	102.4	134.5	18.7	0.7
	13.1	161.9	166.9	20.8	0.8
	10.2	253.5	176.7	19.8	0.8

Table 6.8. Statistics from OPERA retrieved HCFC-22 data in the Northern Hemisphere polar latitudes (65°N to 90° N). For each season, data covered the periods described in section 6.1.1.

SOUTHERN HEMISPHERE POLAR (65°S to 90°S)					
month (2003)	**altitude (km)**	**Pressure (mb)**	**MEAN HCFC-22 volume mixing ratio (pptv)**	**standard deviation (pptv)**	**Standard Error on mean (pptv)**
January	16.7	108.8	137.9	19.2	0.9
	13.7	172.3	162.2	21.7	1.0
	10.7	267.8	164.0	19.1	0.9
April	15.4	122.2	138.8	17.3	1.1
	12.3	197.7	160.4	17.4	1.1
	9.3	313.1	168.2	19.4	1.3
July	13.0	164.2	168.4	22.4	2.6
	10.0	267.3	172.7	18.7	2.2
October	16.9	102.7	145.7	26.5	1.9
	14.0	164.8	166.1	22.0	1.6
	11.1	255.7	181.5	24.7	1.8

Table 6.9. Statistics from OPERA retrieved HCFC-22 data in the Southern Hemisphere polar latitudes (65°S to 90°S). For each season, data covered the periods described in section 6.1.1.

Measurements at 15 km, were lower than the 9 km data for all seasons. The difference in the global mean was least for July (18 pptv) and largest for October 2003 (36 pptv).

Globally, the systematic errors were on average 5.9 % at 15 km, compared to 8.5 % at 9 km, but the difference in error was only expected to contribute to maximum of 4 pptv (section 4.2.6). Although there was an average difference of 2.6 % between the 9 km and 15 km errors, this was calculated to be less than a 4 pptv difference in vmr. This suggests that the OPERA retrieved HCFC-22 data has distinguished a vertical profile from data from all four seasons of 2003. The gradient of HCFC-22 decrease with height was steepest in October 2003 data.

The global average data is most likely affected by the high tropical value between 9 and 15 km (Table 6.6). The tropical troposphere generally extends to altitudes of 15 and 18 km [Holton, 1995] so it were likely that all tropical data in Table 6.6 were measured in the troposphere. The data confirm this as although the average HCFC-22 vmrs at 15 km were lower in all four seasons than that at 9 km, the systematic error at 15 km was 7 % lower than at 9 km. Therefore, variations between the two heights were probably due to differences in systematic error.

For the mid-latitudes, the HCFC-22 data showed excellent agreement at 9 km within 20 pptv (13 %) of the ESRL surface data throughout the year. The 9 km data also show an increase throughout the year, in every season, increasing from 165.3 pptv at 10 km in January to 180.4 pptv in October. A change in HCFC-22 concentration with height was also measured in the mean mid-latitude data. Although the systematic error at 15 km was 2.6 % less than the error at 9 km, it was not likely that the difference would have accounted for the 14-22 pptv differences observed. Therefore, the mid-latitudes show there is a significant gradient in the vertical profile. This also implies that 15 km data at least contains a component of stratospheric air.

The 9 km Northern Hemisphere polar data showed good agreement with surface measurements in January, April and October to within 15 %. The agreement was poorer in July and the mean OPERA HCFC-22 vmr of 202.8 pptv was almost 44 pptv (45 %) greater than the surface average. The difference can not be explained by the calculated errors and it was again likely, as for the tropics, that inaccuracies in MIPAS-E water vapour measurements were likely propagating into the retrieval. The presence of semi-persistent cirrus in the Arctic was confirmed in the aerosol extinction data (section 6.3.3.2), and although the scheme can potentially retrieve thin cirrus it was unable to account for inaccuracies in water vapour. If there was a problem unique to July 2003, the data for the

other three months showed an increase from 168.9 pptv in January 2003 to 176.7 pptv in October, an increase slightly lower than observed in the mid-latitude data.

As for both the mid-latitudes and Arctic data at 9 km, the Southern Hemisphere polar HCFC-22 data showed an increasing of HCFC-22 vmr throughout the year that was probably not attributable simply to changes in pointing of the instrument. The 9 km data agreed to better than (14 %) with surface observations.

One semi-permanent feature of the mid-latitude and polar data appears to be the observation in this limited vertical range of data of a vertical profile which shows a decrease of HCFC-22 vmr with height. In Antarctica, the systematic errors were lowest (due mainly to the low contribution of water vapour to the signal in the Antarctic upper troposphere) and comparable at both 9 km (7.6 %) and 15 km (6.4 %). The difference between the 9 km and 15 km data was up to 36 pptv (over 25 %) giving credence to the measurement of a vertical profile and the results were not simply due to errors within the measurements. Furthermore, it is expected that 15 km data is, on average, likely to be stratospheric air.

In summary, the HCFC-22 data showed interesting behaviour despite the limited vertical range over which useful information could be gained from the MIPAS-E measurements. In mid-latitudes and at both poles a decrease of HCFC-22 with height was measured; this was independent of season. The results in the tropics were different. The tropical measurements shown between 9 and 15 km were probably tropospheric and as such, HCFC-22 vmrs were expected to be well-mixed. This was shown in the results for each season and explains the lack of a decrease of HCFC-22 with height between 9 and 15 km in the tropics.

Although the joint retrieval approach has largely removed effects of thin cloud effects in the HCFC-22 retrieval, there was evidence that in July 2003, the data at the Northern pole were contaminated (section 6.3.3.2) with many cirrus clouds. The mean MIPAS-E HCFC-22 profile (including total error) was more than 40 pptv greater than the average surface value in July 2003. One possible reason is that there were likely very high (greater than 20 %) inaccuracies in the operational retrieval of water vapour with the MIPAS-E operational processor which led to an overestimation in HCFC-22.

6.1.3 Zonal behaviour

Section 6.1.2 investigated the seasonal distribution of HCFC-22 globally and in four broad latitude regions. This section investigates the zonal distribution of the results from 2003 on a global scale with particular reference to analysis of the local behaviour of HCFC-22 in the lower stratosphere.

In Figure 6.10 to Figure 6.13 data from each season were binned into a 12 degree x 4 pressure level grid (144 "bins") depending on the pressure and latitude of the data. Latitude bins were centred at 84°S, 72°S, 60°S, etc and continued in 12 degree intervals until 84°N. In terms of pressure, the bins were centred at 325 mb, 250 mb, 175 mb and 100 mb. For example the bin centred at 84°S and with a central pressure of 325 mb contained all data between 78°S to 90°S and between 362.5 mb and 287.5 mb (37.5 mb either side of the central pressure).

In January 2003 (Figure 6.10), the highest HCFC-22 vmrs were found in the tropics, predominantly in the Southern Hemisphere tropics at pressures above 250 mb, between the equator and 30°S and extending towards the Southern Hemisphere mid-latitudes up to 40°S.

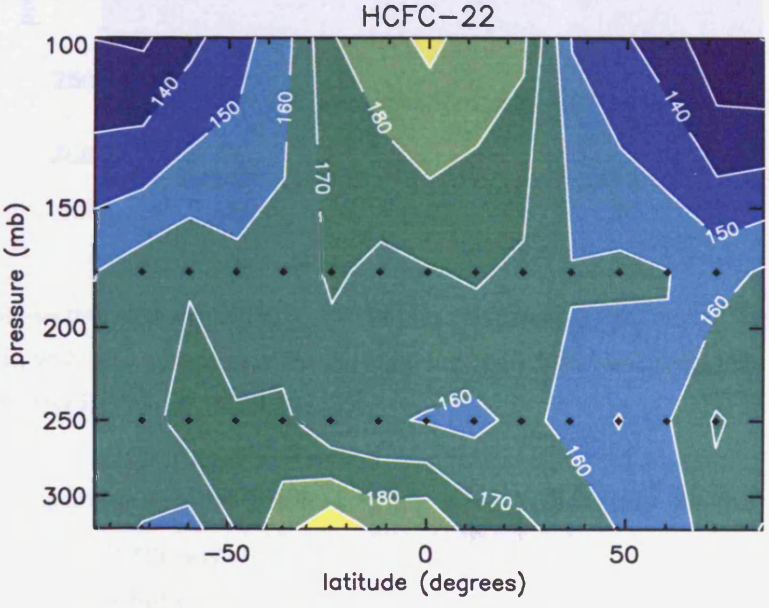

Figure 6.10. A cross-section of retrieved HCFC-22 data (in pptv) from the 8th to 14th January 2003. Data were gridded into 60 bins, with the centre of each bin shown in the figure with black diamonds. The dimensions of each bin were 12 degrees latitude by 75 mb pressure.

A region of high HCFC-22 vmrs at 100 mb was also observed, centred on the equator, but extending towards the edge of the tropics. This feature was dominant in the other three seasons. From the synthesised retrieval tests performed in section 4.2.1 it was shown that between 18 and 21 km (approximately coincident with the 100 mb data) tropical OPERA data were high biased. That is the concentrations at 18 and 21 km in the retrieved state vector were up to 20 % higher than the known HCFC-22 profile. It appears that this feature is also apparent in retrievals from MIPAS-E spectra.

At latitudes higher than 50 degrees, in both Hemispheres and at pressures below 175 mb, there was a rapid decline in HCFC-22 vmr with latitude. Comparing both Hemispheres, lower vmrs were found towards the Northern Hemisphere pole in January 2003, most likely due to descent and mixing of HCFC-22 depleted air from the upper stratosphere within the polar vortex.

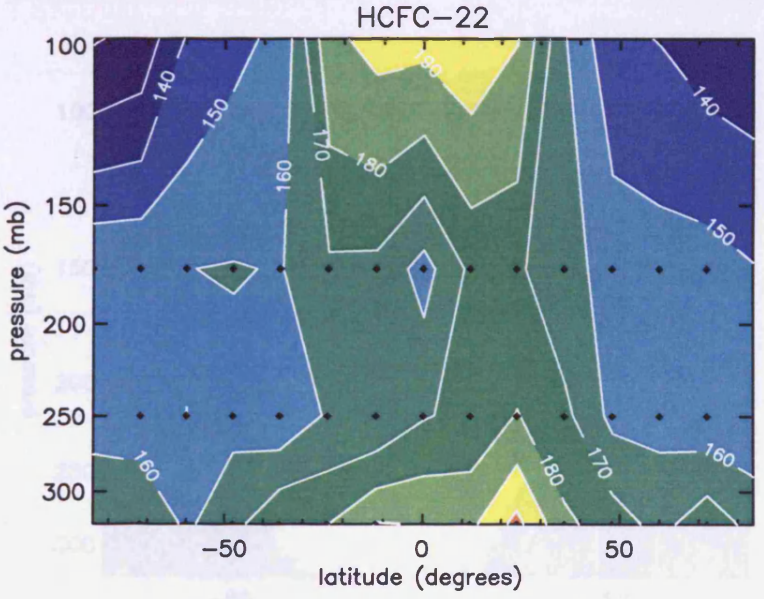

Figure 6.11. A cross-section of retrieved HCFC-22 data (in pptv) from the 15th to 21st April 2003. Data were gridded into 60 bins, with the centre of each bin shown in the figure with black diamonds. The dimensions of each bin were 12 degrees latitude by 75 mb pressure.

In April 2003, Figure 6.11, the highest vmrs were still found in the tropics both at pressures above 250 mb and around 100 mb, although unlike in January of 2003 the two regions were "linked" at 20°N and vmrs were generally high (above 160 pptv) throughout the whole tropics and extending to around 30°N.

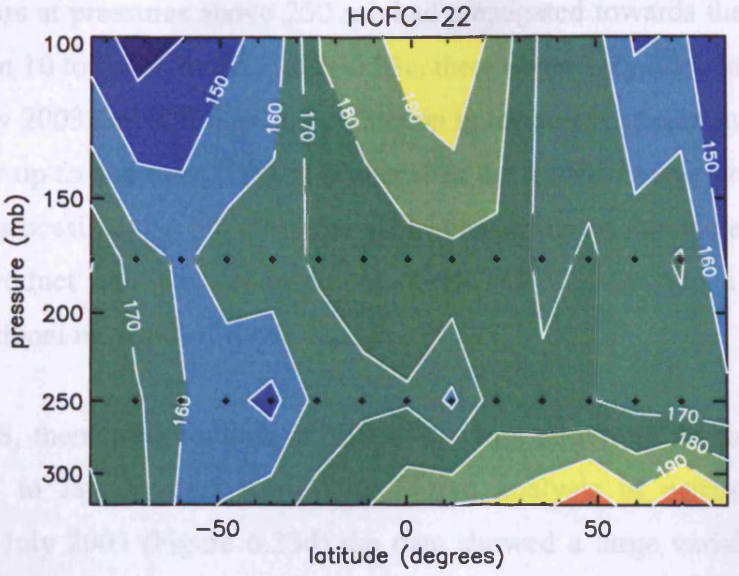

Figure 6.12. A cross-section of retrieved HCFC-22 data (in pptv) from the 8th-14th July 2003. Data were gridded into 60 bins, with the centre of each bin shown in the figure with black diamonds. The dimensions of each bin were 12 degrees latitude by 75 mb pressure.

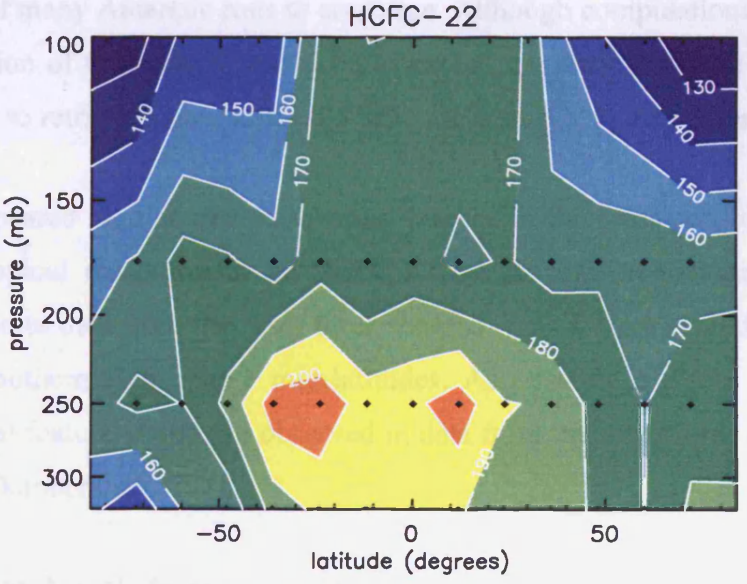

Figure 6.13. A cross-section of retrieved HCFC-22 data (in pptv) from the 15th-21st October 2003. Data were gridded into 60 bins, with the centre of each bin shown in the figure with black diamonds. The dimensions of each bin were 12 degrees latitude by 75 mb pressure.

The July 2003 cross-section of data (Figure 6.12) shows a large variability with both latitude and pressure and although some features were consistent with those observed in both January and April 2003 others were not. The permanent high HCFC-22 feature centred near the equator at 100 mb was still apparent in the data, although at pressures above 250 mb, there were not the high concentrations observed in the January and April

data. Highest vmrs at pressures above 250 mb had propagated towards the North Pole and extended between 10 to 90°N. From Figure 6.23c, there was a very high frequency of polar cirrus during July 2003 and although the extinction in the Arctic and in many mid-latitude was enhanced by up to and over 1000 % higher than the *a priori* value and was measured by OPERA it was possible that the polar cirrus had contaminated the operational MIPAS-E water vapour product and the enhancement of HCFC-22 vmr was a product of the inaccurate operational retrieval of water vapour.

Poleward of 65°S, there were regions of HCFC-22 vmrs that were up to 20 pptv (15 %) larger compared to January and April 2003. From analysis of aerosol extinctions in Antarctica from July 2003 (Figure 6.23d) the data showed a large variability with many data with extinctions greater than 10^{-3} km^{-1}. It was likely that these data were PSCs, not necessarily at the altitude they appeared to be measured at, but within the line of sight of the measurement, above 21 km (6.3.3.2). The incorrect aerosol retrieval affected the accuracy of the HCFC-22 data leading to high variability within the HCFC-22 data and also the failure of many Antarctic runs to converge. Although computationally expensive, a future modification of the scheme would be to extend the retrieval range up to 30 km in regions sensitive to retrieve higher altitude PSCs, for example, at the winter pole.

October data appeared high compared to other seasons in the cross-section (Figure 6.13). There was a tropical enhancement of HCFC-22 by 20 pptv at pressures greater than 230 mb compared to data from the other three seasons. This feature extended into both the Northern and Southern Hemisphere mid-latitudes. As possibly a direct result, the high HCFC-22 tropical feature at 100 mb observed in data from the other three seasons was not as strong in the October data.

At latitudes higher than 50 degrees, in both Hemispheres and at pressures below 175 mb, the rapid decline in HCFC-22 vmr with latitude that was seen in January and April data was replicated again for October. Comparing both Hemispheres, lower vmrs were found towards the Northern Hemisphere pole in October 2003, most likely due to the beginning of descent and mixing of HCFC-22 depleted air from the upper stratosphere within the onset of the winter polar vortex.

In summary, zonal data have been plotted incorporating retrieved HCFC-22 data in January, April, July and October 2003. Although the cross-sections from each season appear quite noisy, there is clear evidence from each mean plot of variations of HCFC-22

with pressure and latitude. In particular, it appears that stratospheric air is sampled, particularly at the poles. July had the "noisiest" data although it appears that PSCs in the line of sight above the uppermost retrieval height caused high variability in the Antarctic HCFC-22 data. July also contained the lowest number of retrieved number of data reducing the spread of data.

6.2 CFC-12

CFC-12 data were calculated to exhibit the capabilities of OPERA to retrieve vmr data with higher information content in the MIPAS-E measurements. It was also to show the high accuracy of the retrievals that can be produced.

It was known that global average surface measurements in 2003 were 536 pptv, increasing at 0.6 pptv/yr (section 1.2). In the lower stratosphere, the CFC-12 volume mixing ratio has vertical gradients due to the high static stability suppressing vertical transport. Measurements of CFC-12 have previously been made sporadically throughout the upper troposphere and the lower stratosphere (UTLS) by the MIPAS-B instrument (the balloonborne version of the MIPAS). It has also been shown in chapter 5 of this thesis that retrieval of CFC-12 from MIPAS-E spectra is possible to a mean accuracy of 7 %. Stratospheric measurement CFC-12 has also been previously possible both by in-situ sampling and remote sensing techniques from the Geophysica aircraft (for example Keim *et al.*, 2004 and Baehr *et al.*, 2004).

This section shows CFC-12 vmr retrievals from MIPAS-E data between 9 and 30 km to indicate good performance of the instrument and retrievals, and to provide support for the HCFC-22 analysis. From the simulation tests performed in section 4.2.3, the MIPAS-E can measure CFC-12 at up to seven out of the eight nominal heights between 9 and 30 km, giving important profile information and it will be shown that the OPERA CFC-12 results in the upper troposphere agree well with surface measurements and the concentrations in the stratosphere decrease with altitude as expected.

6.2.1 Retrieval Periods

Data were chosen from the same four weeks as analysed for HCFC-22 (section 6.1.1) although due to the longer computation time needed for the processing of CFC-12 data,

only one day from each week was chosen, a day with the largest number of coincident MIPAS-E level 1b and level 2 data. The 13th January provided the most data for one day (295 profiles from 14 orbits) with the total number of converged profile data for the four days of 878.

DATE	13/1/03	21/4/03	14/7/03	21/10/03	TOTAL
orbits	14	10	12	13	49
profiles	295	213	154	216	878

Table 6.10. The number of orbits and retrieved profile data from each day from the four seasons in 2003

6.2.2 Seasonal behaviour

Although CFC-12 is well mixed in the troposphere it was expected (for example from measurements by Toon *et al.*, 1999) that in the lower stratosphere vertical gradients would exist and would be measurable from the MIPAS-E data. This section analyses in particular the vertical distribution of measured CFC-12 from OPERA and change over the course of one year.

Firstly, as for HCFC-22, it was examined whether the CFC-12 retrievals were affected by spectra containing thin cloud by investigating whether the OPERA retrieved CFC-12 data were independent of cloud index. Figure 6.14 shows the result of comparing retrieved CFC-12 with cloud index at 9 km and it was confirmed that retrieved CFC-12 vmrs were indeed independent of the cloud index, as the correlation between the two data was only −0.167

The CFC-12 data measured at the lowest retrieval height could be considered as tropospheric for the tropics and potentially the mid-latitudes. It was also likely that polar air at the lowest retrieval altitude contained a component of tropospheric air. It was found that (Table 6.11) the data measured below 10 km were all higher than the average 2003 surface concentration (ESRL) by between 18 and 25 pptv (3 to 5 %). The differences were not significant, however, considering the systematic error on the MIPAS-E measurements was an average of 8.4 % (up to 46 pptv).

only one day from each week was chosen, a day with the largest number of coincident MIPAS-E level 1b and level 2 data. The 13th January provided the most data for one day (295 profiles from 14 orbits) with the total number of converged profile data for the four days of 878.

DATE	13/1/03	21/4/03	14/7/03	21/10/03	TOTAL
orbits	14	10	12	13	49
profiles	295	213	154	216	878

Table 6.10. The number of orbits and retrieved profile data from each day from the four seasons in 2003

6.2.2 Seasonal behaviour

Although CFC-12 is well mixed in the troposphere it was expected (for example from measurements by Toon *et al.*, 1999) that in the lower stratosphere vertical gradients would exist and would be measurable from the MIPAS-E data. This section analyses in particular the vertical distribution of measured CFC-12 from OPERA and change over the course of one year.

Firstly, as for HCFC-22, it was examined whether the CFC-12 retrievals were affected by spectra containing thin cloud by investigating whether the OPERA retrieved CFC-12 data were independent of cloud index. Figure 6.14 shows the result of comparing retrieved CFC-12 with cloud index at 9 km and it was confirmed that retrieved CFC-12 vmrs were indeed independent of the cloud index, as the correlation between the two data was only −0.167

The CFC-12 data measured at the lowest retrieval height could be considered as tropospheric for the tropics and potentially the mid-latitudes. It was also likely that polar air at the lowest retrieval altitude contained a component of tropospheric air. It was found that (Table 6.11) the data measured below 10 km were all higher than the average 2003 surface concentration (ESRL) by between 18 and 25 pptv (3 to 5 %). The differences were not significant, however, considering the systematic error on the MIPAS-E measurements was an average of 8.4 % (up to 46 pptv).

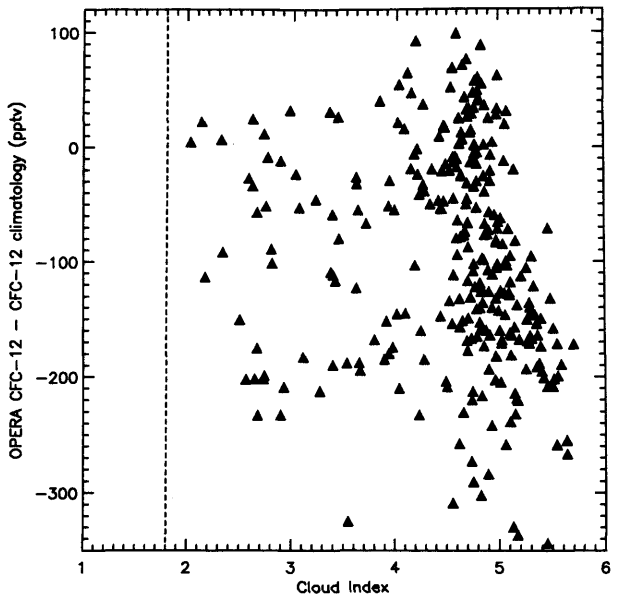

Figure 6.14. OPERA retrieved CFC-12 data plotted against cloud index (CI) at approximately 9 km (MIPAS-E scan height 15). The plot includes all converged data for January 13th 2003. The CFC-12 data were differenced with the CFC-12 reference atmosphere to remove any bias within the retrieved data.

The systematic error on the 9 km CFC-12 data was the highest of all the vertical levels, varying between 7 % at both poles and up to 11 % in the tropics. It was dominated by spectroscopic and temperature errors. However, between 12 and 21 km (18 km in the polar winter) the systematic errors were similar at between 4 and 5 %. Comparing the globally retrieved data between the 12 km data and that at 21 km shows that the 21 km CFC-12 vmrs were always lower than the 12 km vmrs by between approximately 170 pptv and 230 pptv (47 to 75 %) and considering the similar systematic errors the result was significant. It is clear that the OPERA retrieved global mean data for each season has a distinct profile in the upper troposphere and lower stratosphere with the highest concentrations at 12 km and decreasing to 21 km. This trend is likely to extend above 21 km.

The tropical data gave profile information from MIPAS-E measurements for up to six heights between 9 and 30 km. From the tropical results, it was clear that on average the tropical troposphere extended up to between 15 and 18 km (consistent with expectations) as the results showed no distinct profile shape (Table 6.12 and Figure 6.15 to Figure 6.18) or change in concentration with height when both the average concentration and errors were considered on the data. Above 18 km, the data were more variable about the mean with the standard error on the data in April and July of over 10 %, but more vertical variations were expected in the stratosphere.

GLOBAL					
Month (2003)	**Mean Altitude (km)**	**Mean Pressure (mb)**	**MEAN CFC-12 volume mixing ratio (pptv)**	**Standard deviation of data (pptv)**	**Standard error on mean (pptv)**
January	21.8	48.7	340.8	112.5	6.6
	18.9	77.2	449.1	93.9	5.5
	15.9	125.2	507.6	54.4	3.2
	13.0	199.1	547.6	45.1	2.6
	10.0	302.5	554.9	72.9	4.2
April	20.4	56.6	333.8	107.6	7.4
	17.5	90.0	441.5	97.9	6.7
	14.5	145.3	500.9	61.4	4.2
	11.4	231.0	544.0	43.3	3.0
	8.5	353.5	557.8	64.2	4.4
July	21.2	50.9	364.4	104.4	8.4
	18.3	81.0	472.9	90.3	7.3
	15.3	133.2	515.0	50.0	4.0
	12.3	213.6	533.2	43.1	3.5
	9.4	323.7	553.9	51.6	4.2
October	22.6	41.0	298.6	121.9	8.3
	19.6	64.9	391.3	96.4	6.5
	16.7	105.0	466.9	62.2	4.2
	13.8	167.5	531.2	36.7	2.5
	10.9	258.4	561.1	53.0	3.6

Table 6.11 Statistics from OPERA retrieved CFC-12 data for 2003 including the mean (and associated standard error) and median at each level calculated at an average altitude and pressure. The standard deviation of the data at each level is also included. For each month the average global data were calculated from only one day of data, the days were listed in Table 6.10.

From the mid-latitude mean (Table 6.13), although the tropospheric data at the 9 km retrieval level were all higher than the surface mean by between 20 and 30 pptv (4 and 6 %) there was very good agreement within the total error. The data showed a more distinct vertical profile than for the tropics with decreases observed at heights above 12 km and as the systematic errors between 12 and 21 km were similar (4 to 5 %) this proved further the ability of OPERA to measure the vertical change in CFC-12 concentration with altitude in the stratosphere. An interesting feature of data from all regions was that above 15 km, Figure 6.15 to Figure 6.18, the OPERA measured CFC-12 was lower

systematically than the reference atmosphere data, implying that the profile of CFC-12 in the reference atmosphere may need updating as it underestimates the decrease of CFC-12 with height.

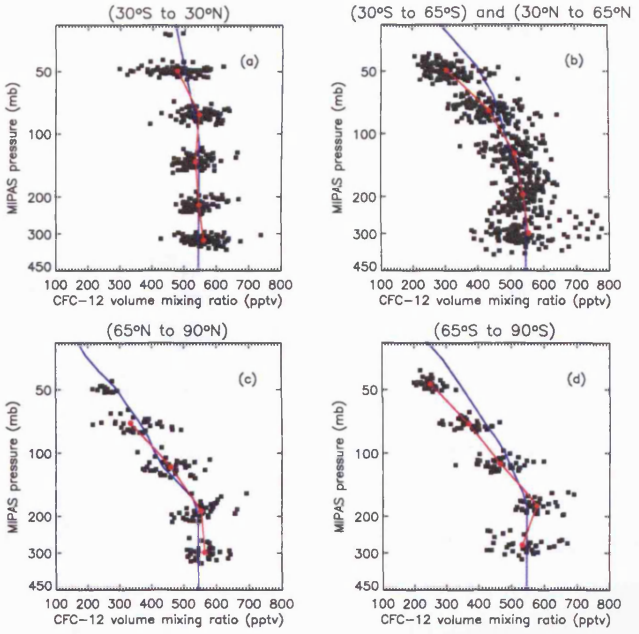

Figure 6.15 OPERA retrieved CFC-12 data (black squares) from MIPAS-E level 1b data (version 4.62) data on the 13th January 2003 (orbits 04551 to 04565). The data were divided into four regions (a) tropical - 30°S to 30°N, (b) mid-latitudes - 30 to 65 degrees in either Hemisphere, (c) Arctic data - north of 65°N (d) Antarctic data - south of 65°S. Mean CFC-12 data (red circles) are shown at an average pressure for each level (Table 6.12 to Table 6.15). The solid blue line displays the version 3.1 reference atmosphere profiles of CFC-12 from Remedios [1999].

The mid-latitude data showed distinct differences between Northern Hemisphere and Southern Hemisphere data although there was no evidence from this fairly small dataset that there were any systematic differences. The data at 9 km were very variable making comparisons to surface measurement difficult and in particular the Southern Hemisphere data ranged between 542 pptv in July up to 606 pptv in January. Although the mean Southern Hemisphere January data agreed to within 9 pptv of the average surface measurement, the mean July data was over 73 pptv (14 %) different. It was thought that high variability in the operational MIPAS-E temperature data were the most likely cause of this. Northern Hemisphere 9 km data also showed some variability about the mean but the mean value itself compared better to the Northern Hemisphere mean surface data. Indeed, agreement with surface measurements was between 12 and 32 pptv (2 to 6 %) and certainly within the calculated error on the mean.

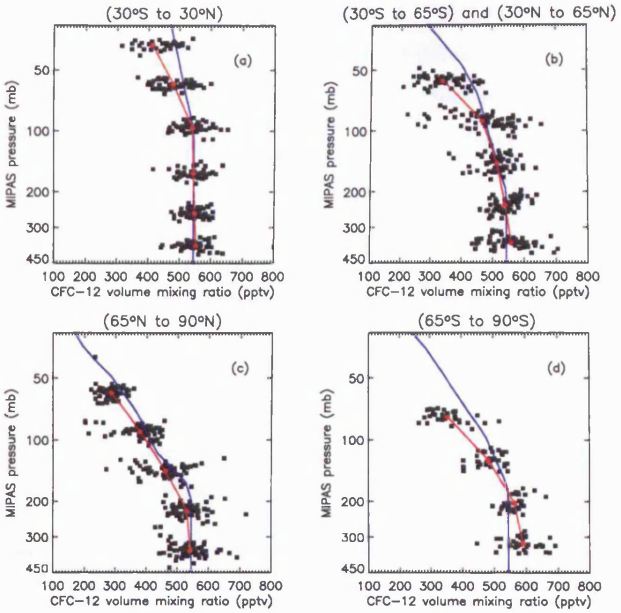

Figure 6.16 OPERA retrieved CFC-12 data (black squares) from MIPAS-E level 1b data (version 4.61) data on the 21st April 2003 (orbits 05954 to 05967). The data were divided into four regions; (a) tropical - 30°S to 30°N, (b) mid-latitudes - 30 to 65 degrees in either Hemisphere, (c) Arctic data - north of 65°N (d) Antarctic data - south of 65°S. Mean CFC-12 data (red circles) are shown at an average pressure for each level (Table 6.12 to Table 6.15). The solid blue line displays the version 3.1 reference atmosphere profiles of CFC-12 from Remedios [1999].

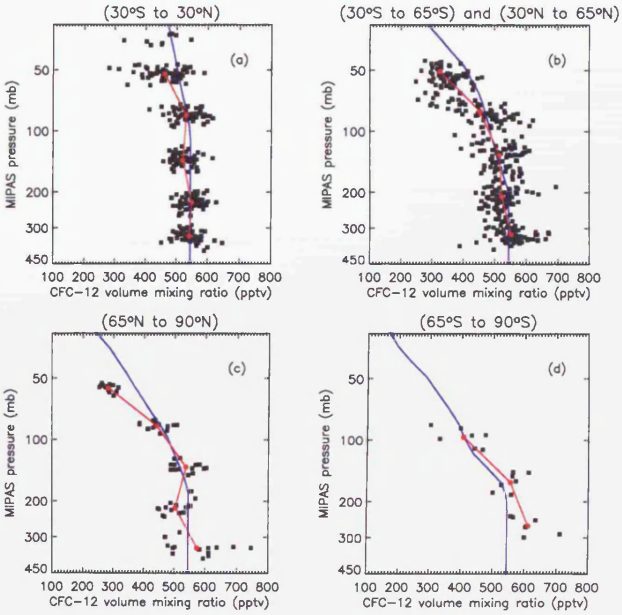

Figure 6.17 OPERA retrieved CFC-12 data (black squares) from MIPAS-E level 1b data (version 4.61) data on the 14th July 2003 (orbits 07158 to 07170). The data were divided into four regions; (a) tropical - 30°S to 30°N, (b) mid-latitudes - 30 to 65 degrees in either Hemisphere, (c) Arctic data - north of 65°N (d) Antarctic data - south of 65°S. Mean CFC-12 data (red circles) are shown at an average pressure for each level (Table 6.12 to Table 6.15). The solid blue line displays the version 3.1 reference atmosphere profiles of CFC-12 from Remedios [1999].

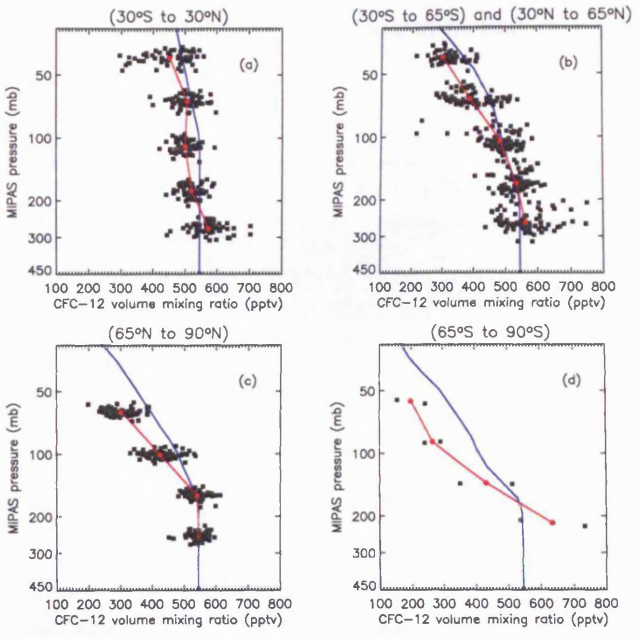

Figure 6.18 OPERA retrieved CFC-12 data (black squares) from MIPAS-E level 1b data (version 4.61) data on the 21st October 2003 (orbits 08574 to 08587). The data were divided into four regions; (a) tropical - 30°S to 30°N, (b) mid-latitudes - 30 to 65 degrees in either Hemisphere, (c) Arctic data - north of 65°N (d) Antarctic data - south of 65°S. Mean CFC-12 data (red circles) are shown at an average pressure for each level (Table 6.12 to Table 6.15). The solid blue line displays the version 3.1 reference atmosphere profiles of CFC-12 from Remedios [1999].

Northern polar data provided more information from the MIPAS-E measurements at between four and five levels and was season dependent. The mean polar tropospheric MIPAS-E measurements were in agreement to surface measurements by better than 33 pptv (excluding the July data which only included 12 data points). The agreement was significant as in the January, April and October data the means were within the 7 % systematic error expected for the OPERA data.

Southern polar data provided very few data to analyse in both July and October, although more data were obtained in January and April. The likely cause of the lack of data in July and October was the contamination of the line of sight with PSCs. From these results, although the presence of cirrus in the tropical data did not dramatically reduce the number of converged OPERA data compared to the HCFC-22 data, the fact that only two profiles converged in October was significant. Most likely, the effect of a PSC in the CFC-12 microwindow was minimal and the linear increase response expected from an increase in extinction does not appear valid for the CFC-12 microwindow. Future work would have to look at the effect of PSCs at different levels and different extinctions, perhaps by a single

aerosol retrieval from OPERA, and compare measured and modelled spectra in greater detail

TROPICS (30°S to 30°N)					
Month (2003)	**Mean Altitude (km)**	**Mean Pressure (mb)**	**Mean CFC-12 volume mixing ratio (pptv)**	**Standard deviation of data (pptv)**	**Standard error on mean (pptv)**
January	24.8	31.3	398.2	77.3	8.1
	21.8	49.5	477.7	63.7	6.7
	18.9	80.9	545.8	44.7	4.7
	16.0	135.5	534.6	37.2	3.9
	13.1	218.4	545.5	35.6	3.8
	10.3	321.4	561.2	45.5	4.8
April	23.5	37.5	411.4	72.0	10.1
	20.6	58.8	478.9	53.1	7.4
	17.6	96.3	541.0	42.7	6.0
	14.7	161.4	543.8	39.6	5.5
	11.8	254.6	549.1	34.7	4.9
	8.8	368.7	553.2	53.7	7.5
July	24.2	33.2	407.9	78.2	10.3
	21.3	52.1	461.3	62.2	8.2
	18.4	83.8	531.9	41.6	5.5
	15.5	139.2	520.9	31.8	4.2
	12.6	224.1	549.6	33.0	4.3
	9.7	329.9	543.1	36.5	4.8
October	26.0	26.3	369.2	66.3	8.5
	23.0	41.4	451.5	67.6	8.7
	20.1	66.7	506.4	39.5	5.1
	17.2	110.0	500.3	30.9	4.0
	14.4	178.8	519.4	30.9	4.0
	11.6	271.7	572.7	47.9	6.1

Table 6.12. Statistics from the tropical (30°S to 30°N) OPERA retrieved CFC-12 data for 2003 including the mean (and associated standard error) and median at each level calculated at an average altitude and pressure. The standard deviation of the data at each level is also included. For each month the average tropical data were calculated from only one day of data, the days were listed in Table 6.10.

For the Southern Polar data that did converge, the tropospheric January mean data showed agreement with the mean surface value of better than 1 pptv. Agreement for April was not as good and was no better than 58 pptv (11 %). This high variability of Southern Polar data between seasons and compared to surface measurement gives less confidence in the data

G

for this region. Further investigation of the causes of the variability would need to be investigated as it was unlikely that the variability could be attributed to operational temperature data used in the forward modelling.

MID-LATITUDES (30°S to 65°S and 30°N to 65°N)							
			All	NH	SH		
January	21.8	49.5	308.2	323.6	286.2	56.1	4.9
	18.9	77.3	437.9	445.5	426.9	65.5	5.7
	15.9	124.1	514.2	512.4	516.8	48.7	4.3
	12.9	194.8	538.9	542.1	534.4	45.4	4.0
	10.0	298.1	553.8	517.1	606.2	94.5	8.3
April	20.7	56.8	339.9	347.6	334.9	70.8	8.9
	17.7	90.1	469.1	426.7	496.3	94.4	11.8
	14.8	146.0	516.4	487.0	535.3	50.0	6.3
	11.8	233.4	541.8	537.5	544.6	40.3	5.0
	8.8	357.9	560.2	545.9	569.4	74.3	9.3
July	21.3	50.6	327.0	366.2	290.8	63.3	7.0
	18.3	80.2	454.0	513.1	399.5	84.2	9.4
	15.3	131.2	516.4	528.5	505.2	50.1	5.6
	12.4	210.0	524.0	517.5	530.0	45.6	5.1
	9.4	321.6	553.1	565.1	542.1	50.4	5.6
October	22.8	41.7	300.4	300.7	299.9	51.5	5.9
	19.8	65.7	389.6	403.4	366.2	62.2	7.2
	16.9	105.4	485.0	493.6	470.3	62.6	7.2
	13.9	167.5	534.9	531.9	540.0	40.4	4.7
	11.0	258.2	562.7	547.0	589.3	67.4	7.8

Table 6.13. Statistics from the mid-latitude (30 to 65 degrees) OPERA CFC-12 data for 2003 including the mean (and associated standard error) and median at each level calculated at an average altitude and pressure. The data were also analysed for the mid-latitudes in both the Southern Hemisphere (SH) and Northern Hemisphere (NH). The standard deviation of the data at each level is also included. For each month the average mid-latitude data were calculated from only one day of data, the days were listed in Table 6.10.

In summary, although the OPERA retrieved CFC-12 data were limited to only one day from every season in 2003, the results still provided very interesting profile information for the gas. For most instances the tropospheric data could be directly compared to surface measurements and in the tropics and mid-latitudes the agreement between these data was better than 30 pptv (6 %). Agreement was more variable towards the poles and future

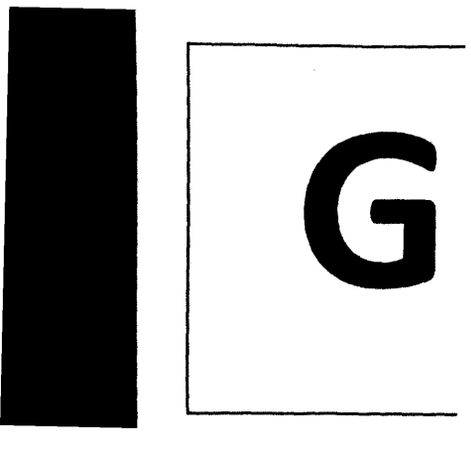

investigation is required to determine the exact cause of the variability of the polar data and in particular the lack of polar data during seasons with likely high PSC occurrence.

NORTHERN POLAR (65°N to 90°N)					
January	17.9	72.2	334.5	75.6	12.4
	14.9	116.9	460.9	55.7	9.2
	11.9	188.7	554.1	52.9	8.7
	8.9	298.9	565.6	35.5	5.8
April	19.6	58.9	287.2	28.1	3.5
	16.6	91.1	379.5	59.3	7.3
	13.6	141.7	461.3	66.3	8.2
	10.5	223.1	531.9	52.2	6.4
	7.4	351.7	542.8	60.5	7.4
July	20.2	55.9	281.8	19.3	5.2
	17.2	85.8	441.3	37.6	10.0
	14.2	136.4	537.4	40.6	10.9
	11.1	215.3	503.1	41.2	11.0
	8.1	339.3	574.5	84.1	22.5
October	18.9	62.7	301.0	41.3	4.9
	16.0	100.8	423.7	45.8	5.3
	13.0	158.8	539.8	28.0	3.2
	10.0	248.5	547.4	26.7	3.1

Table 6.14. Statistics from the Arctic (65°N to 90°N) OPERA CFC-12 data for 2003 including the mean (and associated standard error) and median at each level calculated at an average altitude and pressure. For each month the average Northern Hemisphere high latitude data were calculated from only one day of data, the days were listed in Table 6.10.

Accounting for the agreement to within 1 % of the systematic errors between 12 and 21 km it was shown that OPERA measured a decreasing concentration of CFC-12 with altitude. The smallest mean difference between 12 and 21 km, in effect the shallowest gradient of change with height, was in the tropics during January and October 2003 at 68 pptv (13 %). The most rapid decrease with height was during January 2003 with a difference between the 12 and 18 km data of 245 pptv (85 %) coincident with the winter Arctic vortex bringing air "clean" of halocarbons into the lower stratosphere from higher altitudes. The effect in Antarctica of the vortex could not be measured by the current version of OPERA.

With the processing of more data in the future the OPERA results could be used to determine trends, with most information found in the tropics and mid-latitudes based on the current version of the scheme.

SOUTHERN POLAR (65°S to 90°S)					
Month (2003)	**Mean Altitude (km)**	**Mean Pressure (mb)**	**Mean CFC-12 volume mixing ratio (pptv)**	**Standard deviation of data (pptv)**	**Standard error on mean (pptv)**
January	22.8	47.0	250.4	27.5	4.5
	19.8	72.6	367.9	41.6	6.8
	16.8	112.5	465.5	55.3	9.1
	13.7	177.6	577.1	44.6	7.3
	10.8	275.5	532.9	64.0	10.5
April	18.4	77.4	355.5	58.3	10.3
	15.4	125.9	483.4	42.2	7.5
	12.4	204.9	565.3	32.2	5.7
	9.3	324.2	591.0	54.4	9.6
July	16.0	97.3	406.2	66.7	25.2
	13.0	161.4	556.2	35.6	13.5
	10.0	262.4	611.1	50.9	19.2
October	20.8	56.6	198.9	62.2	44.0
	17.8	88.6	266.6	35.5	25.1
	14.8	140.1	433.3	112.5	79.5
	11.9	216.8	635.6	138.3	97.8

Table 6.15. Statistics from the Antarctic (65°S to 90°S) OPERA CFC-12 data for 2003 including the mean (and associated standard error) and median at each level calculated at an average altitude and pressure. For each month the average Southern Hemisphere high latitude data were calculated from only one day of data, the days were listed in Table 6.10.

6.3 Total particle extinction

As a concomitant benefit of the joint retrieval approach, OPERA retrieves extinctions throughout the whole of the UTLS as well as vmr information from the target gas. As noted in section 2.5.6, what is retrieved here is a total particle extinction which could be from "thin clouds" or from "aerosol" associated with biomass burning, volcanic emissions or industrialised nations. It is re-iterated that only "thin" clouds here refers to a measured CI such that $4>CI>1.8$. Retrievals were not performed on scans where $CI<1.8$ in the profile due to masking and/or saturation effects. Section 6.3.1 shows the aerosol results from the

joint retrieval with HCFC-22 between 9 and 21 km (unless otherwise stated) and explores some of the most interesting features from the results themselves. Unlike the HCFC-22 data where there was only significant information at three of the five levels used in the retrieval, there was aerosol information at up to five levels.

6.3.1 Seasonal means

It was expected that the global aerosol extinction would be closely related to CI. As the calculated CI decreased (indicating increased particle opacity in the MIPAS-E line of sight), the aerosol extinction was expected to rise. Plotting the global aerosol extinction at 9 km as a function of calculated CI (Figure 6.19), showed a close relationship between the parameters with high aerosol extinction coincident with a low CI.

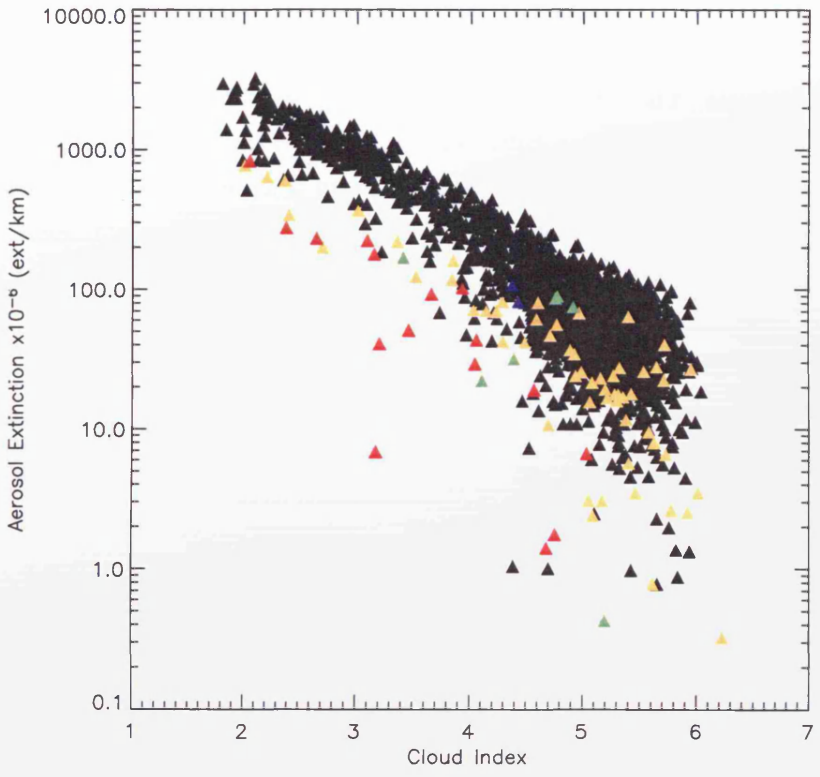

Figure 6.19 Total particle extinction data plotted against cloud index (CI) at 9 km (MIPAS-E scan height 16) from joint HCFC-22 retrieval (January 8th-14th 2003). Black triangles represent extinctions where CI above 9 km was more than 0.5 greater than the CI value at 9 km. Orange triangles indicate extinction data where 0 < CI(12 km)-CI(9 km) < 0.5. Red triangles indicate extinction data where the CI(12 km) < CI(9 km). Green triangles display extinction data where CI(15 km) < CI(9 km). Blue triangles indicate extinction data where CI(18 km) < CI(9 km).

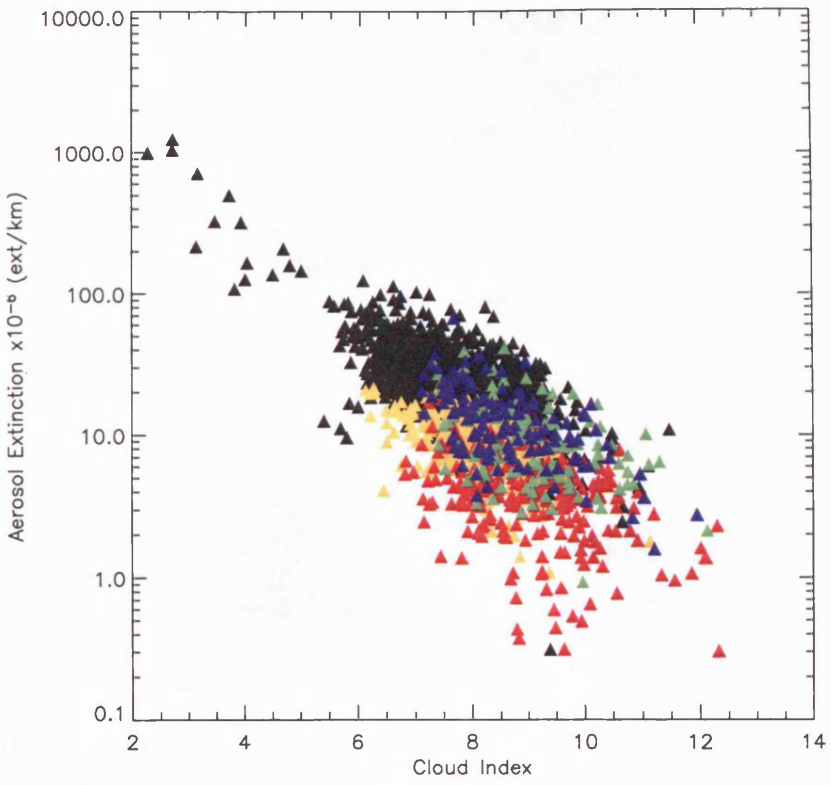

Figure 6.20 Aerosol extinction data plotted against cloud index (CI) at approximately 18 km (MIPAS-E scan height 12) from the joint HCFC-22 retrieval. The plot includes all converged data for January 8th to 14th 2003. Black triangles represent extinctions where CI above 18 km was more than 0.5 greater than the CI value at 18 km. Orange triangles indicate where 0 < CI(21 km)-CI(18 km) < 0.5. Red triangles indicate where CI(21 km) < CI(18 km). Green triangles display where CI(24 km) < CI(18 km). Blue triangles indicate where CI(27 km) < CI(18 km).

Cloud contamination in layers above 9 km will tend to increase the variability within the relationship since they affect the values of CI. Where the CI was lower at 12 km than the value at 9 km (red triangles in Figure 6.19), the retrieved extinction at 9 km appeared lower than where this was not the case. Where the 9 km and 12 km CI values were comparable (0 < CI(12 km)-CI(9 km) < 0.5, orange triangles) the retrieval again appeared lower than where the difference was greater than 0.5. Both of these lower than expected extinctions are due to the imperfect nature of CI as a measure of cloud opacity at a given altitude compared to the retrieval which determines a better representation of the vertical profile of aerosol. A second minor cause of the remaining variability could be due to polar stratospheric clouds (PSCs) towards Northern Hemisphere high latitudes. However, it was found that they have no effect in the Arctic but some evidence was found in the Antarctic.

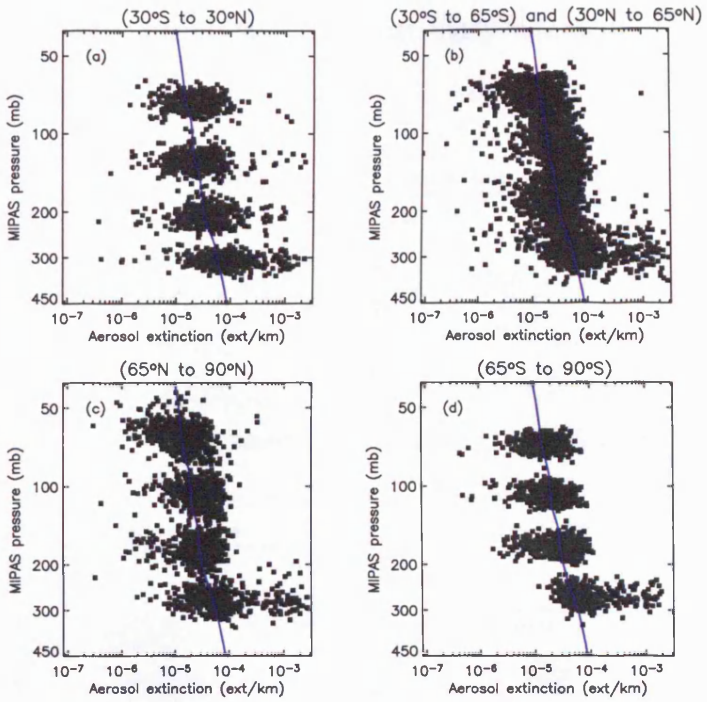

Figure 6.21 Retrieved aerosol data (black squares) from the joint retrieval of HCFC-22 from 8th to 14th January 2003 (from orbits 04480 to 04579 where both level 1b calibrated spectra (version 4.62) and level 2 data (version 4.61) were available). The aerosol data are divided into four regions, depending on latitude. The solid blue line displays the *a priori* climatology profile of aerosol extinction used [Remedios, 1999].

At 18 km (Figure 6.20), the relationship between extinction and CI was also observable in these data, particularly in the largest extinctions above 10^{-4} km^{-1}. The highest extinctions at 18 km occurred where $1.8 < CI < 5$.

In January 2003, high total particle extinctions greater than 10^{-3} km^{-1} could be found globally (Figure 6.21) at around 300 mb (or approximately 9 km). At both poles, these high extinctions were most likely caused by thin polar cirrus in the uppermost troposphere. Another interesting feature was that the April Arctic data included measured extinctions greater than 10^{-3} km^{-1} at pressures between 200 mb and 300 mb (approximately 12 km). Further investigation of the distribution of the 9 km polar data is presented in section 6.3.3.2.

Similar to the 300 mb data, the Arctic data in January 2003 (Figure 6.24c) also had retrieved extinctions exceeding 1000 % of the *a priori* between 50 and 70 mb (approximately 18 km). January was the only month in the year that total extinctions exceeding 10^{-4} km^{-1} were measured in the Arctic at this altitude. The time of year was coincident with the Northern Hemisphere winter where polar stratospheric cloud (PSC) formation can occur in the Arctic stratosphere. These data are further investigated in

section 6.3.3.2 and it was found that the most likely cause of this feature was PSC formation.

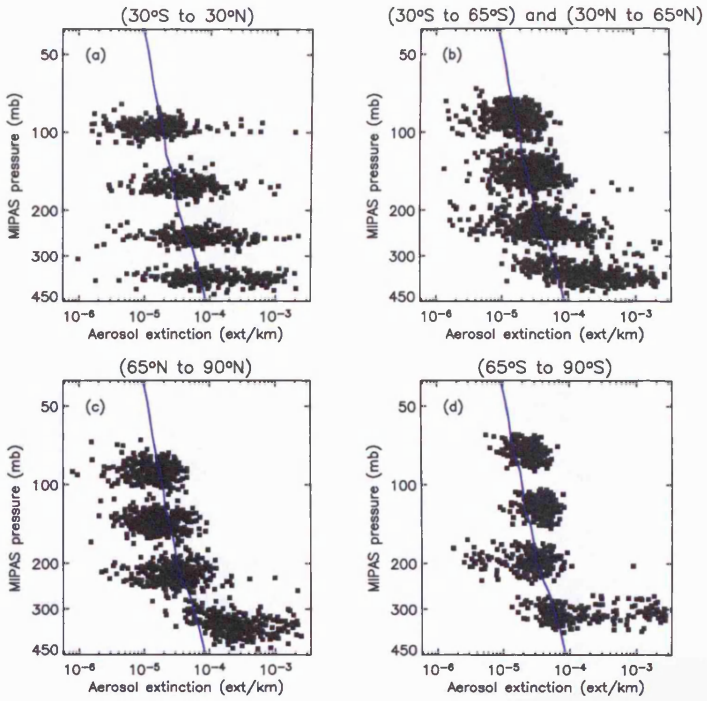

Figure 6.22. Retrieved aerosol data (black squares) from the joint retrieval of HCFC-22 from 15th to 21st April 2003 (from orbits 05868 to 05967 where both level 1b calibrated spectra (version 4.61) and level 2 data (version 4.61) were available). The aerosol data are divided into four regions, depending on latitude. The solid blue line displays the *a priori* climatology profile of aerosol extinction used [Remedios, 1999].

Conversely in the January Antarctic data extinctions greater than 10^{-3} km^{-1} were confined to pressure greater than 230 mb. It is known [Fahey *et al.*, 1989] that the occurrence of PSCs is confined to the winter and early spring seasons of both polar regions, explaining why January 2003 saw no Antarctic PSCs. As expected in July 2003 that PSC formation was measured from Antarctic MIPAS-E data. Extinctions above 10^{-4} km^{-1} were measured up to pressures below 50 mb. July Antarctic HCFC-22 data showed a high variability within the data compared to other seasons. It was thought that this may be due to PSCs in the line of sight and above the uppermost retrieval level. Further analysis of July Antarctic data in section 6.3.3.2 confirm this.

The tropical data were very interesting throughout the year and in the January to July data, extinctions greater than 10^{-4} km^{-1} were measured throughout the datasets at pressures down to 70 mb. A combination of thin cloud formation and biomass burning were likely sources for these enhancements. This requires further work beyond the scope of this thesis. By October, extinctions greater than 10^{-4} km^{-1} were only measured down to 100 mb, but this

still represented a region of high extinctions measured between approximately 9 and 15 km.

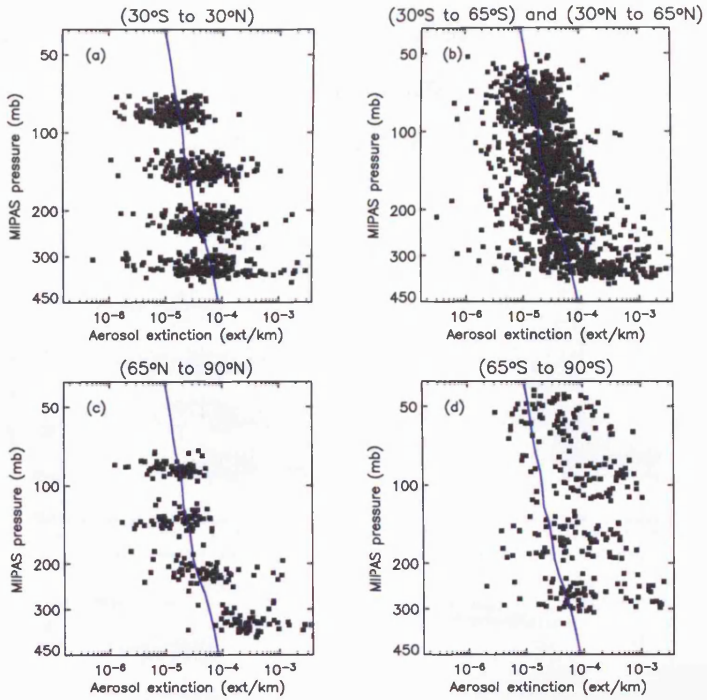

Figure 6.23. Retrieved aerosol data (black squares) from the joint retrieval of HCFC-22 from 8th-14th July 2003 (from orbits 05868-05967 where both level 1b calibrated spectra (version 4.61) and level 2 data (version 4.61) were available). The aerosol data are divided into four regions, depending on latitude. The solid blue line displays the *a priori* climatology profile of aerosol extinction used [Remedios, 1999].

The mid-latitude total extinction data showed some high extinctions (greater than 10^{-3}) at 9 km. The most interesting feature was at pressures below 200 mb where total extinctions of up to 10^{-3} km^{-1} were found in all seasons. These data were measured at pressures corresponding to altitudes above 12 km, rather high for cirrus formation in extratropical cyclones. The reasons for these enhanced extinctions were not clear.

In summary, the likely cirrus feature at approximately 300 mb (or 9 km), was a semi-permanent feature throughout the whole of 2003. As well as identifying the feature and although future work is required to attempt to validate these data, the evidence from 2003 data shows that the scheme has managed to identify potential cloud extinction in the polar and mid-latitude upper troposphere. As mentioned previously, this quantity is very important for climate studies as cirrus is known to both reflect incoming solar radiation and also absorb long-wave radiation emitted from the surface. Which effect dominates is still open to much uncertainty.

The OPERA scheme has also identified and quantified instances of high extinctions in the polar atmospheres, particular in the winter hemisphere. Further analyses of these data are performed in section 6.3.3.2 and suggest that these were likely to be PSCs. It was found that sometimes the instances of "high" extinctions measured were not necessarily at the height measured. The cause of this was contamination (particularly in the winter pole) of PSCs within the measurement line of sight above the uppermost 21 km retrieval altitude.

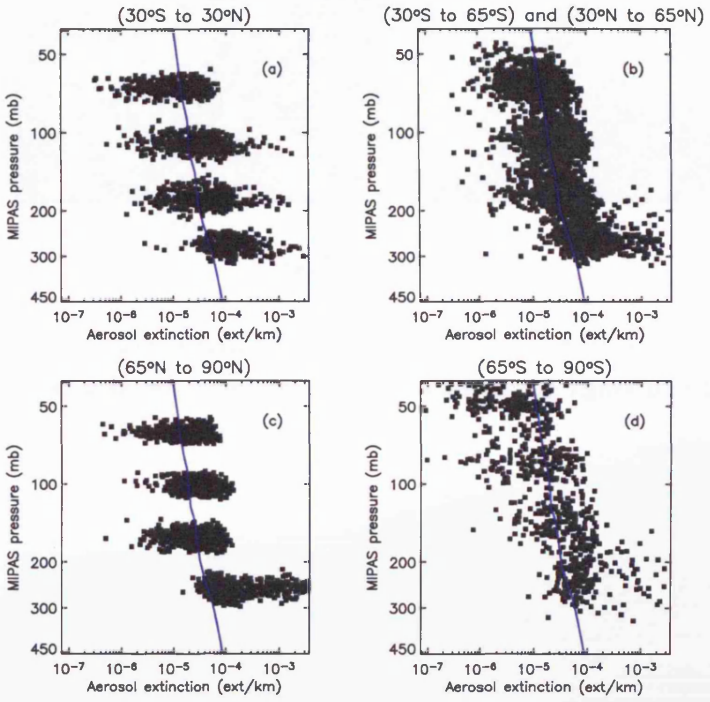

Figure 6.24 Retrieved aerosol data (black squares) from the joint retrieval of HCFC-22 from 15th to 21st October 2003 (from orbits 08488 to 08587 where both level 1b calibrated spectra (version 4.61) and level 2 data (version 4.61) were available). The aerosol data are divided into four regions, depending on latitude. The solid blue line displays the *a priori* climatology profile of aerosol extinction used [Remedios, 1999].

6.3.2 Zonal behaviour

Section 6.3.1 investigated the seasonal distribution of the measured aerosol extinctions in four broad latitude regions. This section investigates the zonal distribution of the results from 2003 on a global scale with particular reference to analysis of the local behaviour of aerosol/clouds in the lower stratosphere. As for section 6.1.3, the zonal plots in Figure 6.25 to Figure 6.28 were constructed by the same method as outlined in section 6.1, separated into identical pressure and latitude "bins".

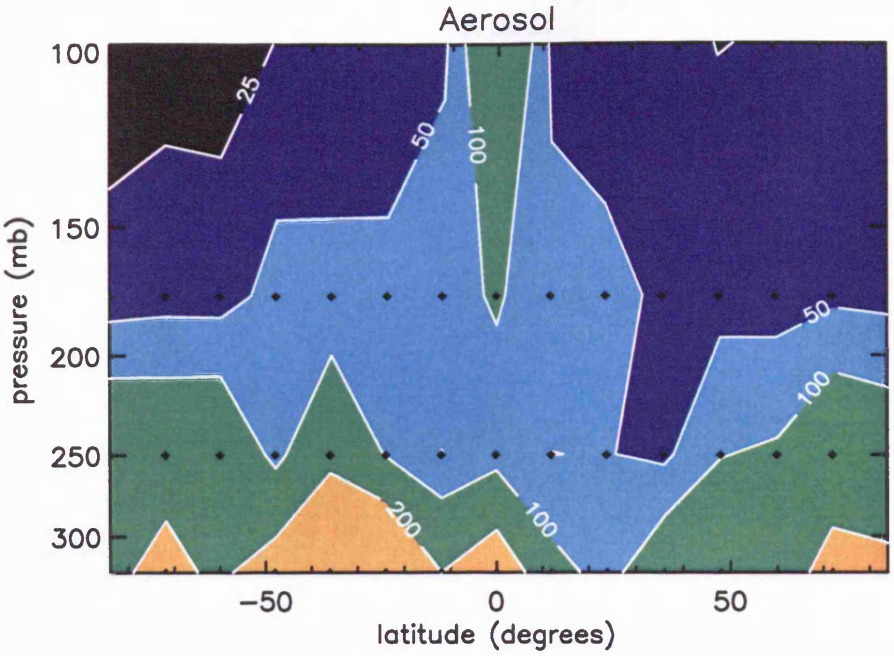

Figure 6.25 A cross-section of retrieved total extinction data (x10^{-6} km^{-1}) from the 8th-14th January 2003. Data were gridded into 60 bins, with the centre of each bin shown in the figure with black diamonds. The dimensions of each bin were 12 degrees latitude by 75 mb pressure.

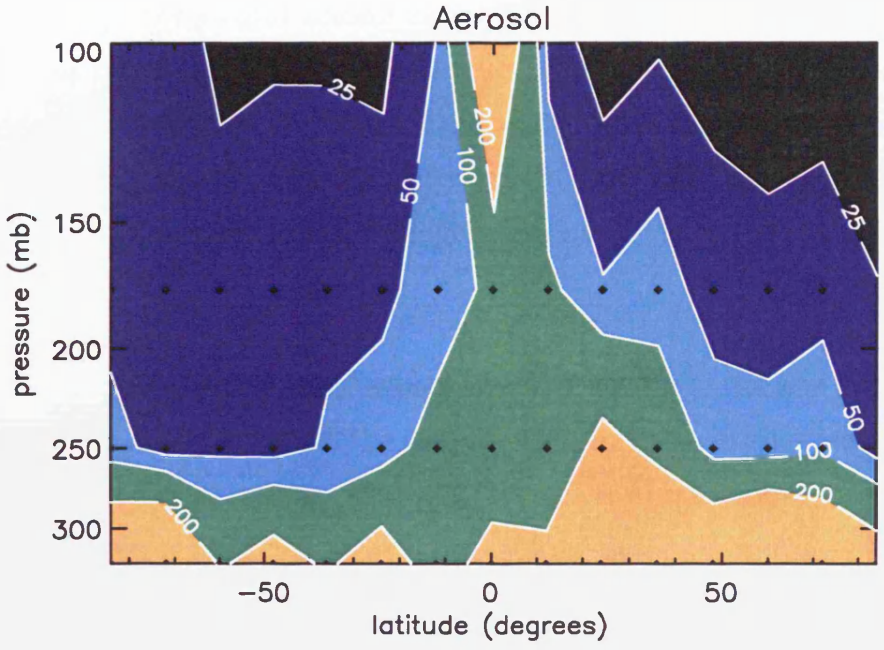

Figure 6.26 A cross-section of retrieved total extinction data (x10^{-6} km^{-1}) from the 15th-21st April 2003. Data were gridded into 60 bins, with the centre of each bin shown in the figure with black diamonds. The dimensions of each bin were 5 degrees latitude by 75 mb pressure.

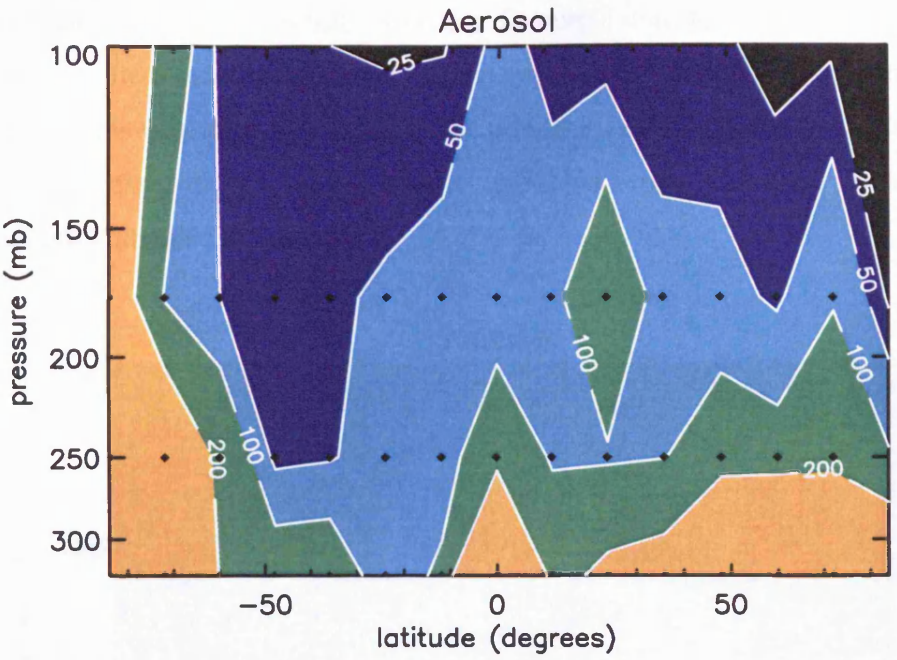

Figure 6.27 A cross-section of retrieved total extinction data ($x10^{-6}$ km^{-1}) from the 8^{th}-14^{th} July 2003. Data were gridded into 60 bins, with the centre of each bin shown in the figure with black diamonds. The dimensions of each bin were 12 degrees latitude by 75 mb pressure.

Figure 6.25 displays the gridded aerosol extinction data from January 2003. The highest extinctions were found between 325 and 250 mb, with very little variation of extinction with latitude. Below pressures of 150 mb, there was a strong zonal variation of extinction with the highest extinctions in the tropics between 15°S and 15°N at over 10^{-3} km^{-1} .These data decreased towards the poles, with the highest decrease (and lowest extinction) towards Antarctica.

By April 2003 (Figure 6.26) the zonal pattern was very similar to January. Little variation was again shown in data at 325 and 250 mb up to 50°N. Poleward of this latitude the April data show a distinct enhancement. This time period was consistent with the onset of Northern Hemisphere summer and an increase in tropopause height. It was likely that in the measurements between 325 and 250 mb in the Northern Hemisphere high latitudes some data were of tropospheric air and therefore more likely to contain cloud. The lowest extinctions were also found towards the North Pole above 70°N and at pressures below 250 mb.

Progressing into July (Figure 6.27), the Antarctic data showed a strong increase of extinctions poleward of 65 S between 100 and 300 mb, compared to the previous data in the year with extinctions in many cases greatest than in the tropics. July is coincident with

the mid-point of the Antarctic winter and is a favoured time for PSC formation. These results show that there was an apparent enhancement of extinction throughout the lower stratosphere and this was most likely due to the presence of PSCs in the line of sight of the measurement (section 6.3.1). The feature persisted into October Antarctic data (Figure 6.28) and extended towards 60°S.

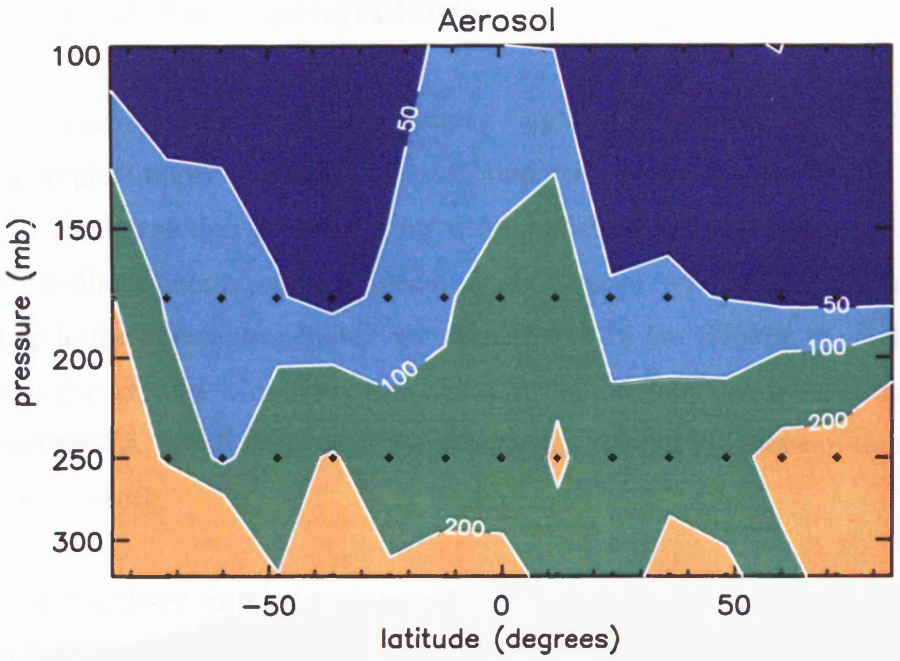

Figure 6.28. A cross-section of retrieved total extinction data ($x10^{-6}$ km^{-1}) from the 15th-21st October 2003. Data were gridded into 60 bins, with the centre of each bin shown in the figure with black diamonds. The dimensions of each bin were 12 degrees latitude by 75 mb pressure.

Some high July extinctions were also found between 45 and 90°N in the upper troposphere. The exact reason for these high extinctions is unclear, and further investigation is required. This feature in the data was short lived after July as by October (Figure 6.28), Arctic extinctions between 250 and 325 mb had almost returned to levels measured in January of the same year.

In summary, the zonal aerosol extinction data for 2003 showed some interesting features throughout the year. The highest total extinctions were generally at 300 mb and decreased towards 100 mb although the fine structure within the data yielded some interesting zonal results. In particular, measurements poleward of 65°S in July highlighted very high extinctions throughout the whole measurement range. The feature was semi-persistent throughout the year and was also observed in April and October data. The Arctic data also

highlighted regions of very high extinction between 250 and 325 mb in April and July 2003.

6.3.3 Regional behaviour

6.3.3.1 Tropical enhancements

It was of particular interest to examine regions of "high" total extinction. For example, thin cirrus in the tropical upper troposphere has an important effect on the energy balance of Earth due to the interaction between long wave radiation originating from the Earth's surface and by direct interaction with incoming short wave solar radiation. These clouds can extend up to the tropical tropopause between 15 and 18 km (Holton *et al.,* 1995). This section shows that regions with likely thin cloud or high aerosol can be both detected and measured by OPERA. A full analysis of the results was beyond the scope of this thesis and is possible future work.

One drawback of only performing retrievals from MIPAS-E spectra that were "cloud-free", i. e. not inclusive of optically thick cloud (CI greater than 1.8) between 9 and 21 km inclusive, was that the scheme would likely not retrieve extinctions from cirrus formed at the top of cumulonimbus clouds (which accounts for around a third of all cirrus formed in the tropics; [Luo and Rossow, 2004]). Fortunately, in terms of OPERA measurements, typical tropical cirrus systems can last for 19 to 30 ± 16 hours [Luo and Rossow, 2004] and can consequently advect by between 600 and 100 km during their lifetime. The advantage from a remote sensing perspective when cloud contaminates the spectra at lower altitudes is that the same cirrus system can be measured by more than one MIPAS-E pass.

To look at regions of high extinctions, the extremes of 9 and 18 km data are examined. Figure 6.29 shows tropical (30°S to 30°N) extinction data at 9 km from the 8th to 14th January 2003 period for data where the extinctions shown were greater than one standard above the mean tropical extinction at that level.

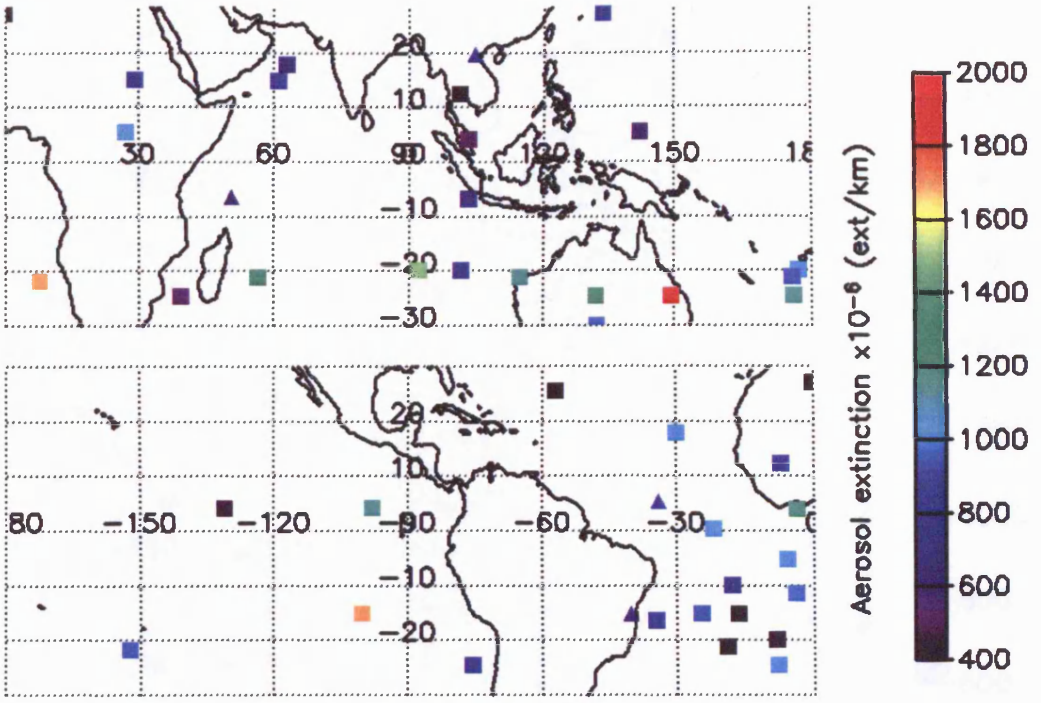

Figure 6.29 Tropical aerosol extinctions (30°S to 30°N) at 9 km between the January 8th to 14th 2003 period where the data were above the one standard deviation limit of the mean aerosol extinction (for the tropics). Triangles represent extinctions with thin cloud in a layer above (1.8<CI<4), squares no thin cloud.

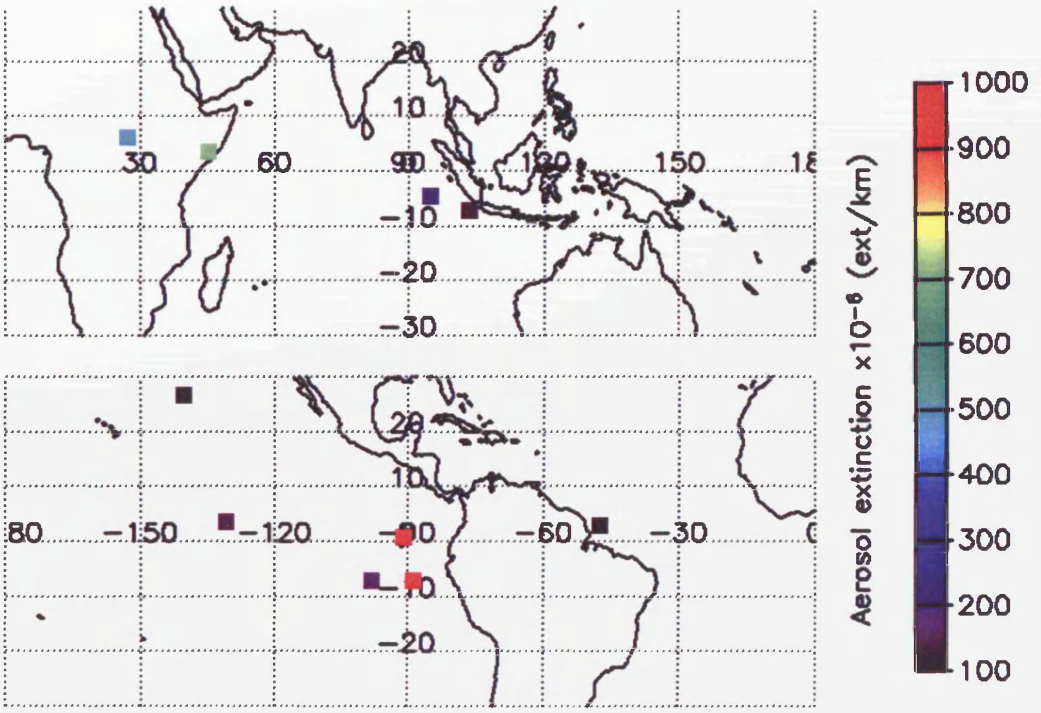

Figure 6.30 Tropical total extinctions (30°S to 30°N) at 18 km between the January 8th to 14th 2003 period where the data were above the one sigma limit of the mean aerosol extinction (for the tropics).

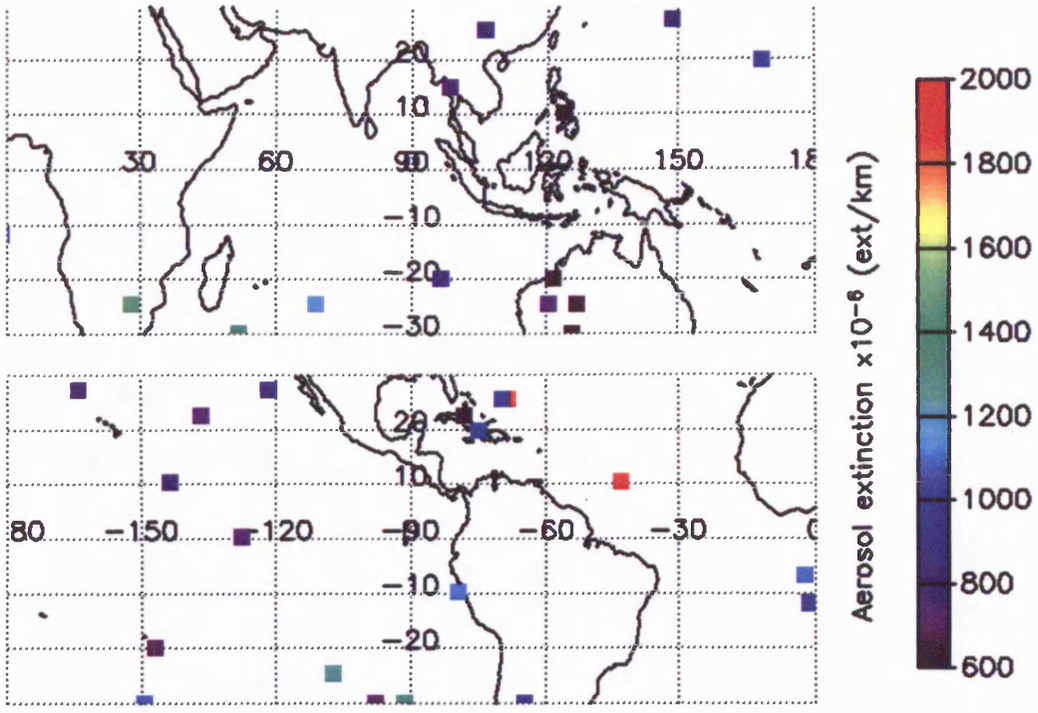

Figure 6.31 Tropical total extinctions (30°S to 30°N) at 9 km between the April 15th to 21st 2003 period where the data were above the one standard deviation limit of the mean aerosol extinction (for the tropics).

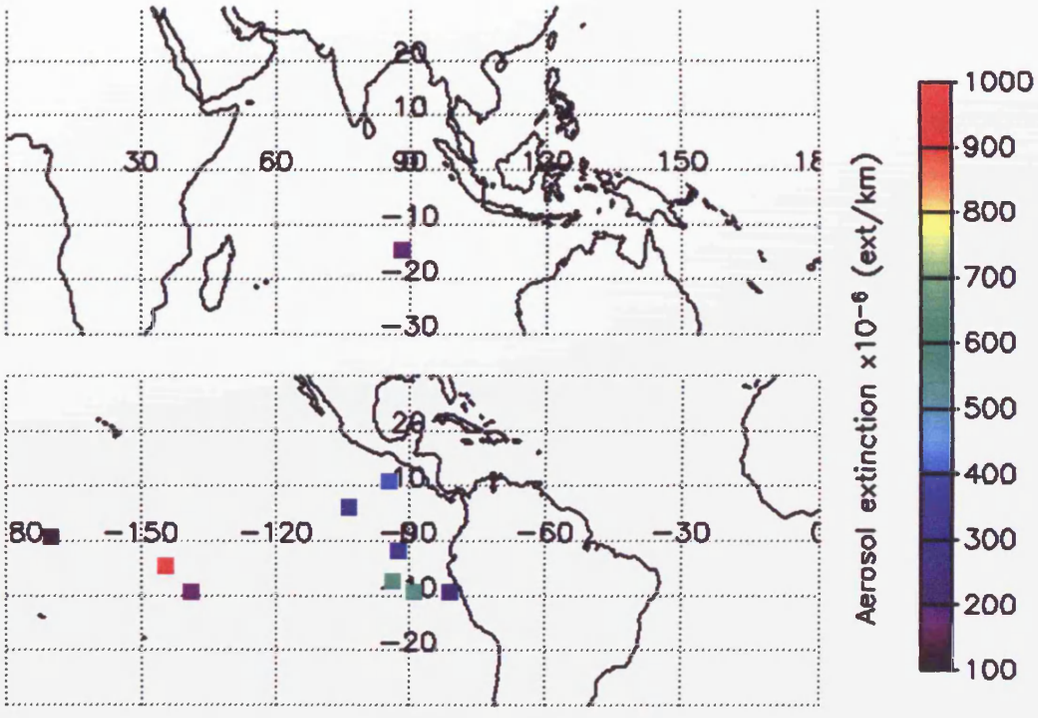

Figure 6.32 Tropical total extinctions (30°S to 30°N) at 18 km between the April 15th to 21st 2003 period where the data were above the one standard deviation of the mean extinction (for the tropics).

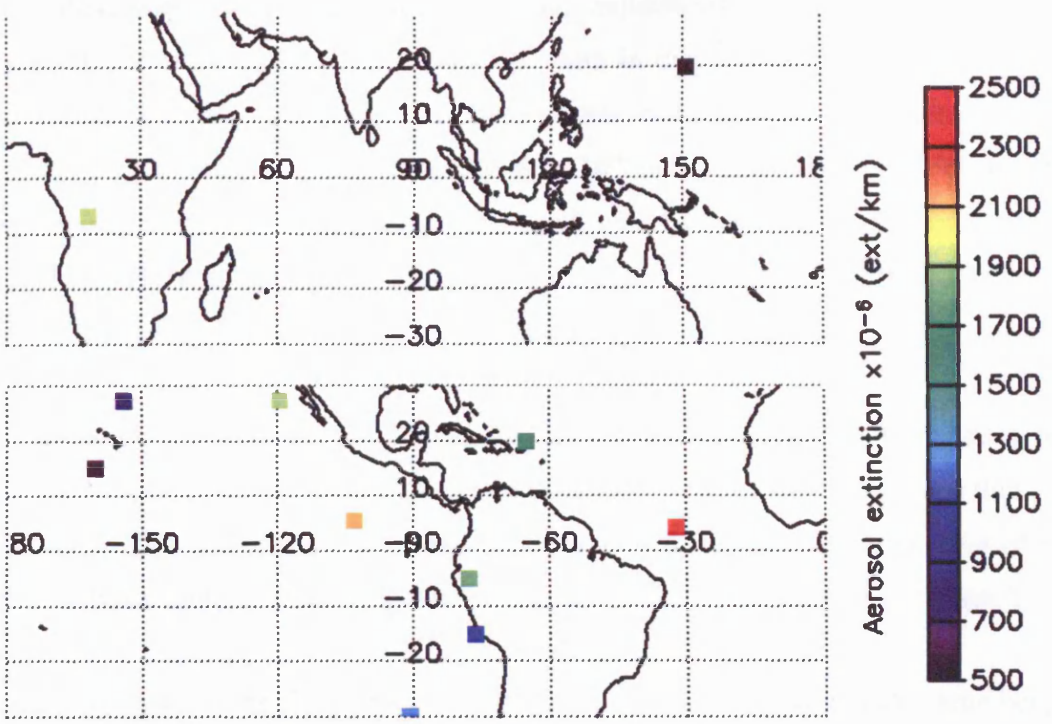

Figure 6.33 Tropical total extinctions (30°S to 30°N) at 9 km between the July 8th to 14th 2003 period where the data were above the one standard deviation limit of the mean extinction (for the tropics).

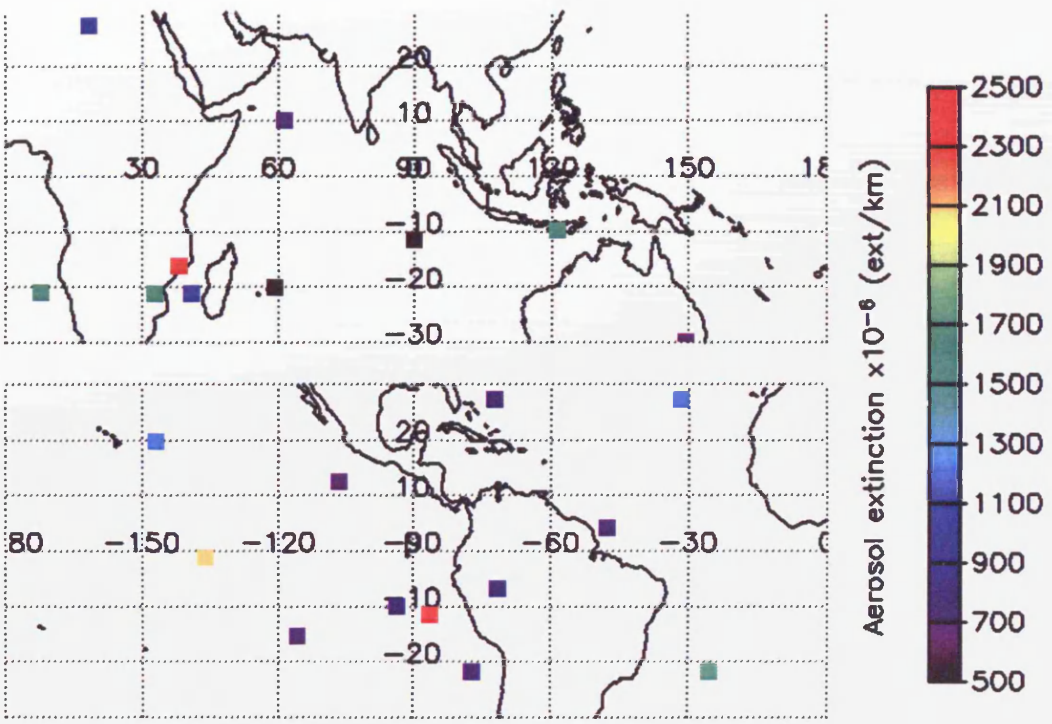

Figure 6.34 Tropical total extinctions (30°S to 30°N) at 9 km between the October 15th to 21st 2003 period where the data were above the one standard deviation limit of the mean extinction (for the tropics).

At 9 km, there was a fairly broad spread of high extinctions throughout the whole of the tropics for January 8th to 14th 2003, but little data in the north-eastern extending to the western Pacific Ocean. The highest data density was in the Southern Atlantic Ocean with extinction ranging between approximately 6 x 10^{-4} and 1.2 x 10^{-3} km^{-1}, although the highest extinction was not measured here and was found over Eastern Australia at 2 x 10^{-3} km^{-1}. By April, Figure 6.31, there were very few high extinction data over the South Atlantic Ocean, a feature also seen in the July and October data.

Cirrus formation is likely to occur towards higher altitudes near the tropopause in the tropics. At 18 km, Figure 6.30, the highest extinctions were likely to be from thin cirrus. From January 2003 data high extinctions were found off the north-western coast of South America with two independent measurements of an extinction of up to 2 x 10^{-4} km^{-1}.

At 18 km, Figure 6.32, the data were comparable to those for January at the same height as high extinctions were measured mainly over the Peru Basin with little data coverage over the rest of the tropics. Although a full analysis was not performed as part of this thesis, the high extinctions observed during both January and April could be due to residual cirrus formed within deep convective clouds over the Amazon. Once the short lived cumulus cell has died, the cirrus potentially remained in the atmosphere for up to 36 hours and may have been transported westwards from the source region by the tropical trade winds.

Of course, the findings of this section were limited to the week from each season covered. For further analysis of particular regions such as the tropics to investigate long-lived features throughout the month, it would be desirable to retrieve a whole month of data. However, from this analysis it has been shown that at 9 km there were a number of data points with thin clouds or aerosol in distinct regions. Future work would involve understanding the origins of these regions and their evolution over time.

6.3.3.2 Polar enhancements

Cloud and aerosol particles can also exist in the polar upper troposphere (as polar cirrus) and the lowermost stratosphere (as PSCs). Polar cirrus could form all year round but PSCs only form in the cold polar winter of each hemisphere. A detailed characterisation of polar cirrus clouds (and PSCs) is beyond the scope of this thesis but an improved understanding of cirrus formation and distribution in the polar region is needed. OPERA could be used in

future studies to expand on the results shown here to investigate other months to produce comprehensive seasonal datasets.

From Figure 6.21, there were numerous instances in January where the extinction between 65°N to 90°N was over 1000 % larger than the "climatology" value suggesting the presence of cirrus clouds. Figure 6.35 displays the Arctic extinction data for the 8th to 14th January 2003 period, showing only data that were more than one standard deviation greater than the Arctic extinction mean. As the December to March period is likely to be associated with a very cold polar stratosphere, the cold temperatures allow the formation of polar stratospheric clouds (PSCs) between about 15 and 30 km. To remove Arctic extinction data that may be contaminated by PSCs, data were removed if the cloud index of a scan was below 4 at any height between 15 and 30 km (the value 4 chosen from the PSC detection method in MIPAS-E data described by Spang *et al.*, 2005). It was found, however, no January data with high extinctions at 9 km were contaminated by PSCs above 21 km.

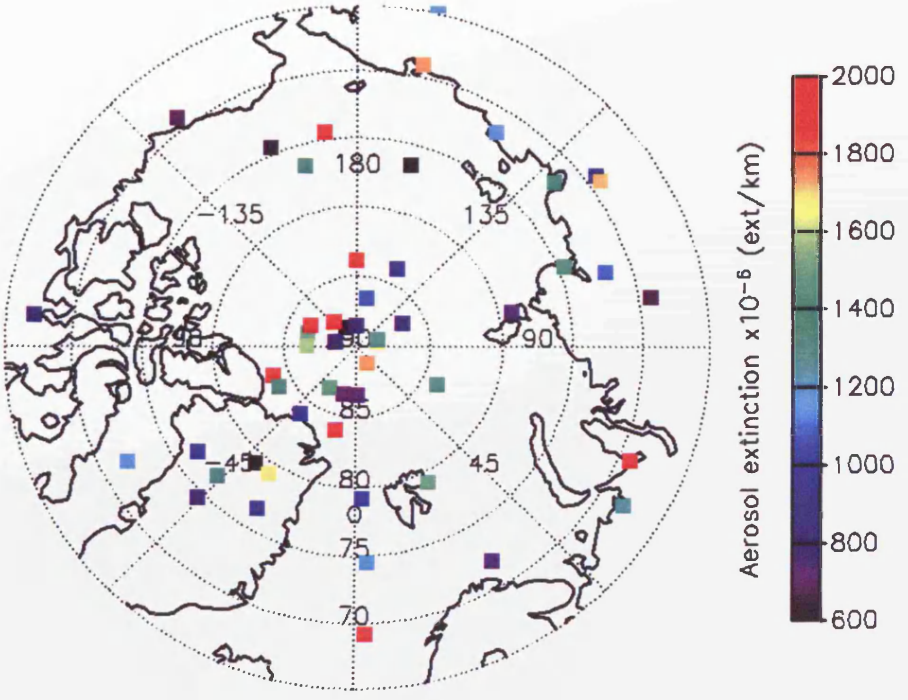

Figure 6.35 Northern Hemisphere polar extinctions (65°N to 90°N) at 9 km between the January 8th to 14th 2003 period where the data were above the one standard deviation limit of the mean aerosol extinction (for the Arctic).

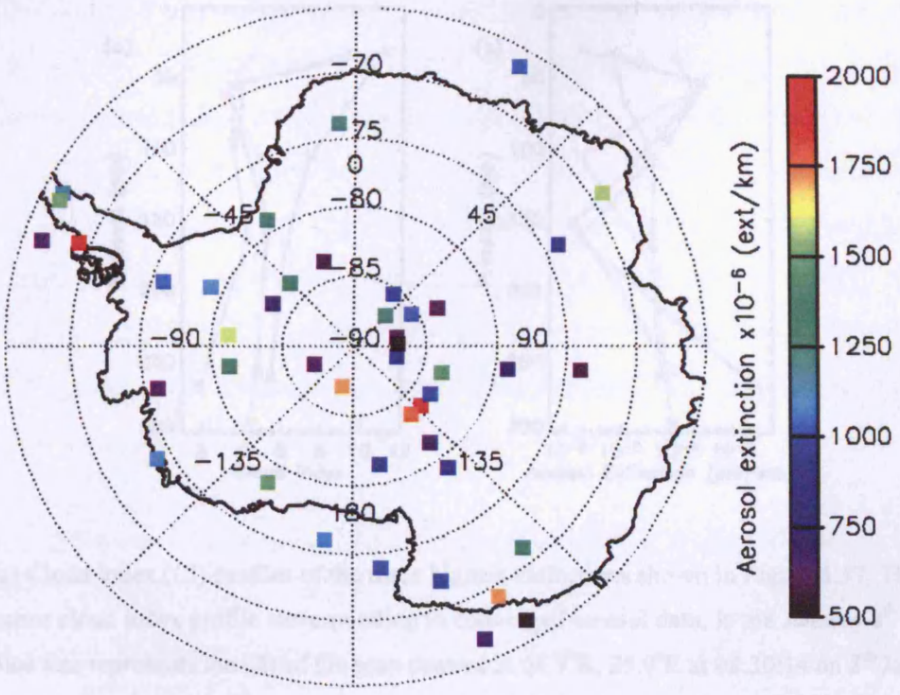

Figure 6.36 Southern Hemisphere polar extinctions (65°S to 90°S) at 9 km between the January 8th to 14th 2003 period where the data were above the one standard deviation limit of the mean aerosol extinction (for the Antarctic).

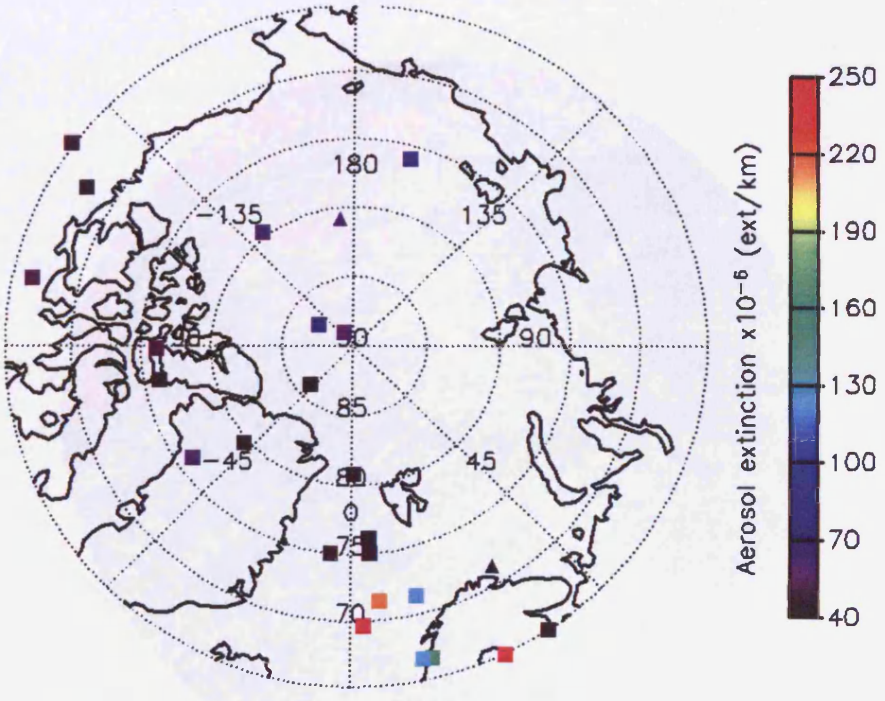

Figure 6.37 Northern Hemisphere polar extinctions (65°N to 90°N) at 18 km between the January 8th to 14th 2003 period, only including data that were above the one standard deviation limit of the mean aerosol extinction (for the Arctic). Triangles represent extinctions with a thin cloud in a layer above (1.8<CI<4), squares no thin cloud.

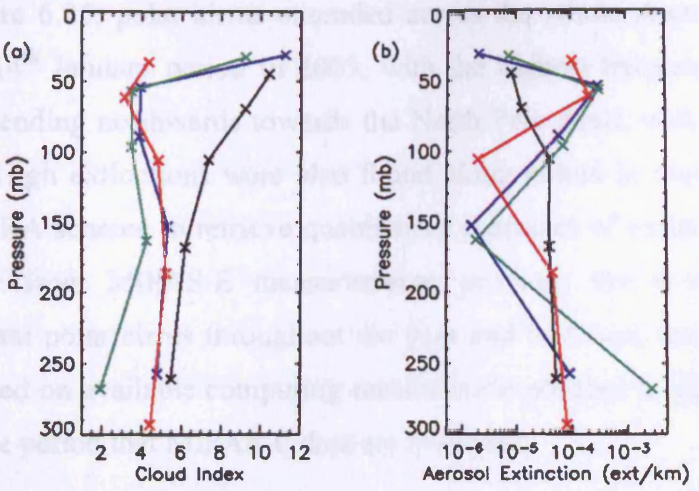

Figure 6.38 (a) Cloud index (CI) profiles of the three highest extinctions shown in Figure 6.37. The black line displays the mean cloud index profile corresponding to converged aerosol data, in the January 8th to 14th 2003 period. The blue line represents the CIs of the scan centred at 64.9°N, 25.9°E at 08:30:14 on 8th January 2003. The green line indicates the CIs of the scan centred at 69.9°N, 2.5°E at 10:08:28 on 8th January 2003. The red line displays the CIs of the scan centred at 71.4°N, 6.2°E at 21:41:31 on 8th January 2003. (b) Aerosol extinction profiles of the three scans from the 8th to 14th January 2003 period with the highest extinction at 18 km. The solid black line represents the mean aerosol extinction profile from January 8th to 14th. The other three profiles correspond to the same scans as shown in (a).

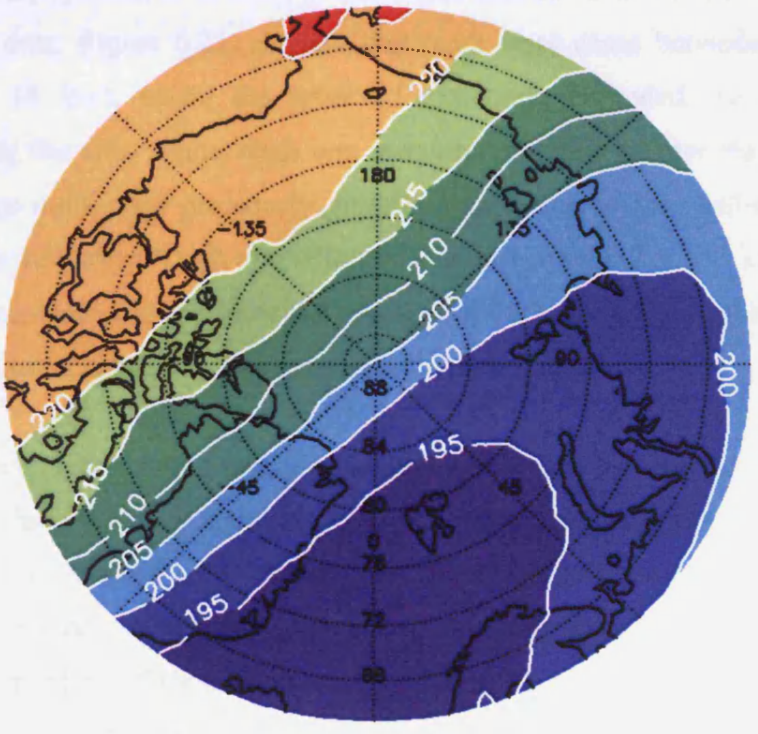

Figure 6.39 ECMWF temperatures (in Kelvin) at 55 mb at 18z on January 8th 2003.

As shown in Figure 6.35, polar cirrus extended across the whole Arctic region at 9 km during the 8th to 14th January period in 2003, with the highest frequency over Northern Greenland and extending northwards towards the North Pole itself, with extinctions of up to 2 x 10^{-3} km^{-1}. High extinctions were also found along points in northern Russia. The ability of the OPERA scheme to retrieve quantitative estimates of extinctions in the polar upper troposphere from MIPAS-E measurements, provides the potential to monitor radiatively important polar cirrus throughout the year and in future work the scheme has the capability (based on available computing resources) to produce a climatology of polar cirrus for the whole period that MIPAS-E data are available.

In Antarctica, there was also a large frequency of polar cirrus, at approximately 9 km, over the seven day period and these are displayed in Figure 6.36. The data were concentrated mainly above the Antarctic land mass itself with few data over the Southern Ocean. Extinctions were similar to the Arctic for the same time period as they peaked at up to 2 x 10^{-3} km^{-1}. Again, the ability of the OPERA scheme to measure and quantify cloud extinctions has been demonstrated by results from Antarctic data.

Although the aerosol extinction data were only available up to 21 km for the whole of the 8th to 14th January period, it is known that PSCs can form at 18 km and below. The Northern polar data, Figure 6.21, showed that there were cases between 60 and 70 mb (approximately 18 km), where the retrieved extinction exceeded the climatology by 1000 %. Plotting the data greater than one standard deviation greater than the mean and cloud filtering as mentioned previously, highlights a region to the northwest of Norway where there was a cluster of high extinction values exceeding 1.2 x 10^{-4} km^{-1}, exceptional for this height compared to the other data measured during the same week. These points were likely to constitute one or maybe several PSC formations.

The three highest 18 km Arctic extinctions were investigated further. It was known that these highest extinctions all occurred on January 8th 2003. Plotting the whole cloud index (CI) profile between 9 and 21 km from each of these points, Figure 6.38a, shows that the lowest CI was coincident with the high extinction (Figure 6.38b) between 50 and 60 mb. It is also known that type 1 PSCs (believes to be nitric acid and water mixtures, [Fahey *et al.*, 1989]) only form at temperatures of below approximately 195 K [Voigt *et al.*, 2000] which is just above their frost point. From analysis of ECMWF assimilated temperatures at 55 mb (the level of high extinction) it has been shown in Figure 6.39 that the areas of high

extinctions were in a "cold pool" of air with temperatures at or below 195 K. It was therefore likely that at least the data on January 8th were PSCs.

OPERA did not measure any 18 km January 2003 Antarctic extinctions exceeding the climatology by 1000 %. This result was consistent with expectations as Antarctic PSCs only form from late May to the end of October. The Antarctic data were therefore not shown. In summary, it has been shown that OPERA retrievals can be used to measure and quantify PSC extinctions in the lower stratosphere from MIPAS-E data.

Figure 6.40 displays the 9 km Arctic extinction data for the 15th to 21st April 2003 period, again plotting only data that were more than one standard deviation greater than the Arctic extinction mean. Polar cirrus extended across the whole Arctic region, but unlike in January where there was a high data density over Northern Greenland and extending northwards towards the North Pole, no clustering occurred. The highest extinction, however, did occur over the Greenland land mass with aerosol extinction just over 2.4 x 10^{-4} km^{-1}.

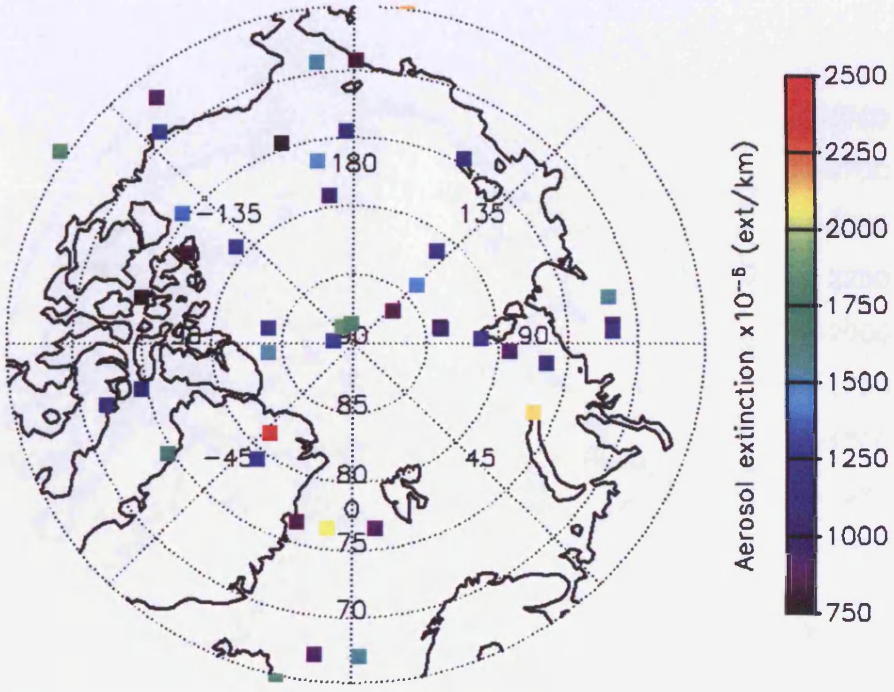

Figure 6.40 Northern Hemisphere polar extinctions (65°N to 90°N) at 9 km between the April 15th to 21st 2003 period where the data were above the one standard deviation limit of the mean aerosol extinction (for the Arctic).

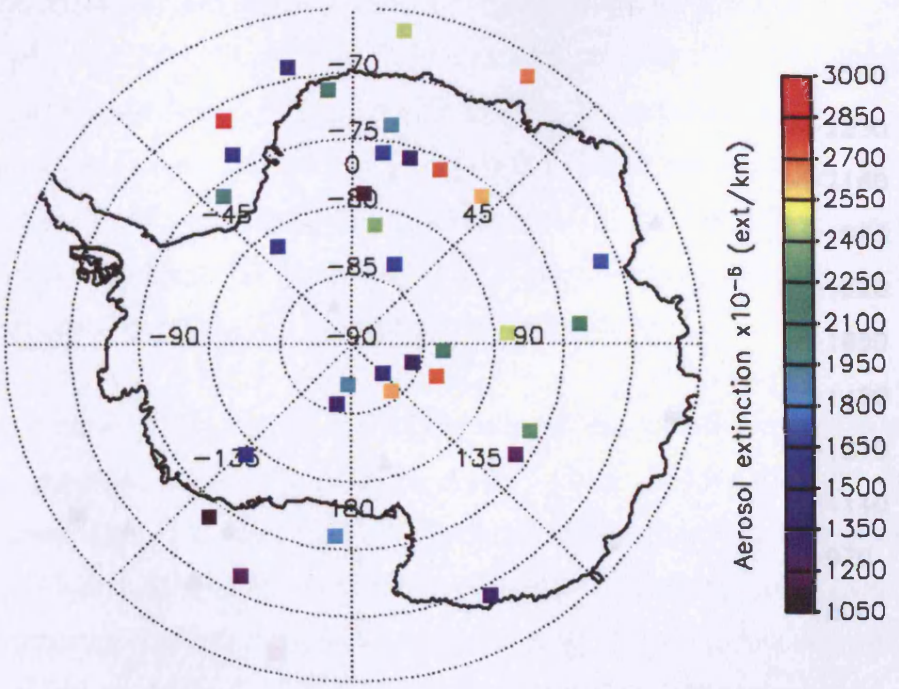

Figure 6.41 Southern Hemisphere polar extinctions (65°S to 90°S) at 9 km between the April 15th to 21st 2003 period where the data were above the one standard deviation limit of the mean aerosol extinction (for Antarctica).

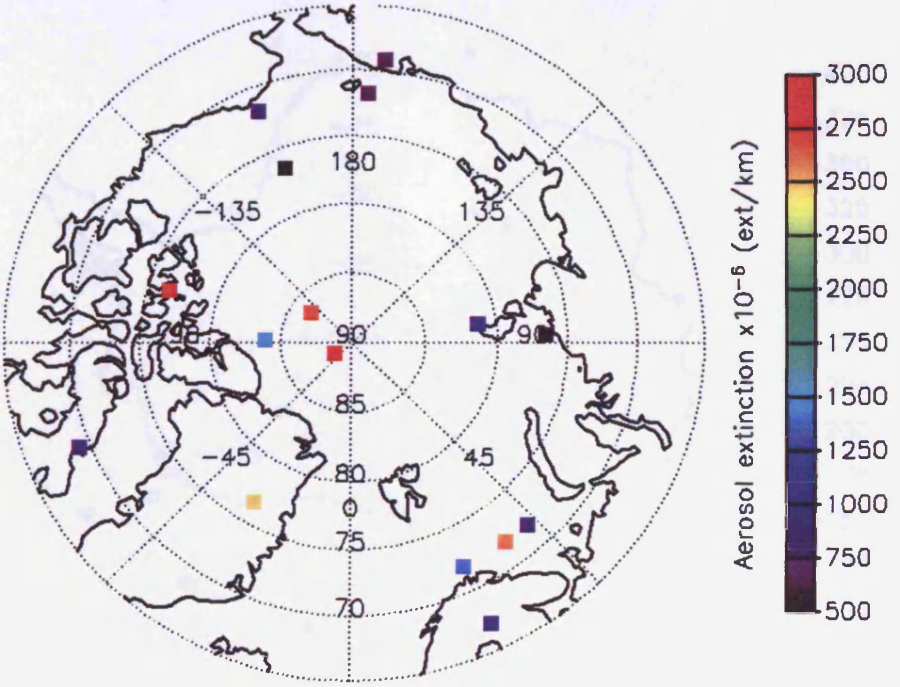

Figure 6.42 Northern Hemisphere polar extinctions (65°N to 90°N) at 9 km between the July 8th to 14th 2003 period where the data were above the one standard deviation limit of the mean aerosol extinction (for the Arctic).

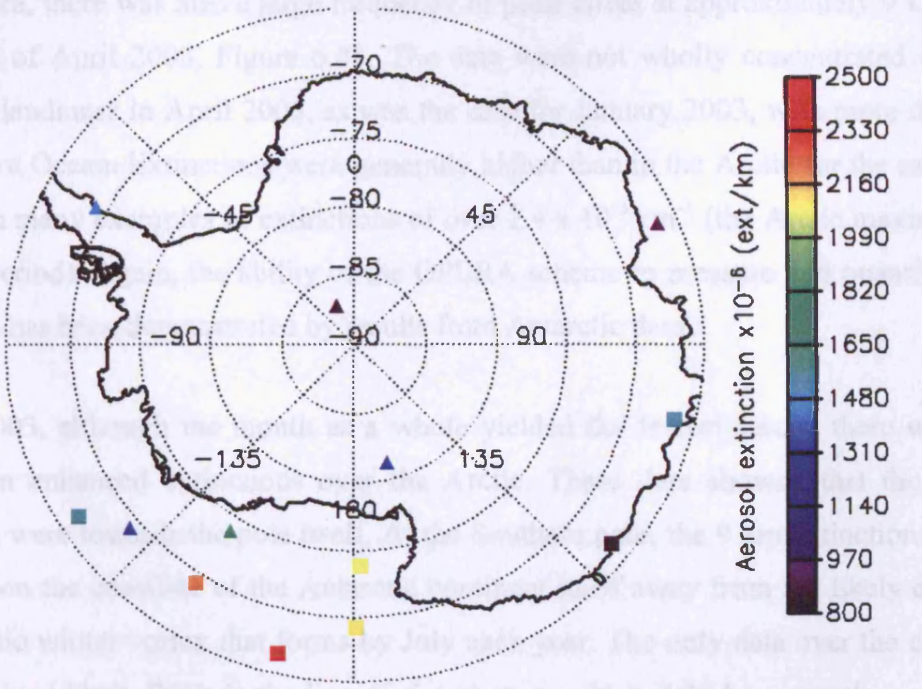

Figure 6.43 Southern Hemisphere polar extinctions (65°S to 90°S) at 9 km between the July 8th to 14th 2003 period where the data were above the one standard deviation limit of the mean extinction (for Antarctica). Triangles represent extinctions with thin cloud in a layer above (1.8<CI<4), squares no thin cloud.

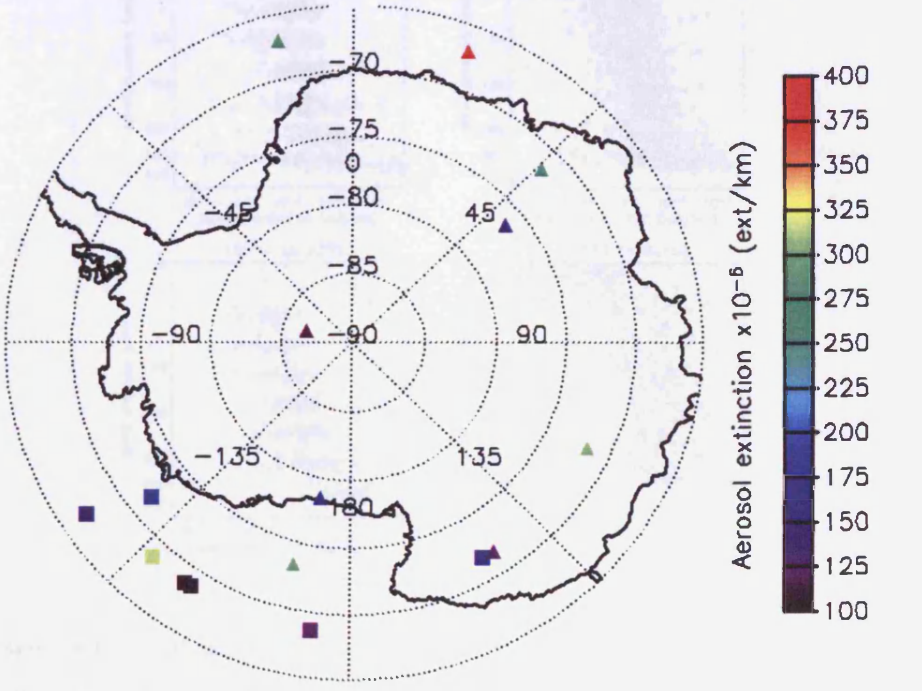

Figure 6.44 Southern Hemisphere polar extinctions (65°S to 90°S) at 18 km between the July 8th to 14th 2003 period, only including data that were above the one standard deviation limit of the mean extinction (for Antarctica). Triangles represent extinctions with thin cloud in a layer above (1.8<CI<4), squares no thin cloud.

In Antarctica, there was also a large frequency of polar cirrus at approximately 9 km in the third week of April 2003, Figure 6.41. The data were not wholly concentrated over the Antarctica landmass in April 2003, as was the case for January 2003, with more data over the Southern Ocean. Extinctions were generally higher than in the Arctic for the same time period with many examples of extinctions of over 2.4 x 10^{-3} km^{-1} (the Arctic maximum for the same period). Again, the ability of the OPERA scheme to measure and quantify cloud extinctions has been demonstrated by results from Antarctic data.

By July 2003, although the month as a whole yielded the fewest results there were still some 9 km enhanced extinctions over the Arctic. These data showed that the highest extinctions were towards the pole itself. At the Southern pole, the 9 km extinction data lay outside or on the coastline of the Antarctic continent itself away from the likely centre of the Antarctic winter vortex that forms by July each year. The only data over the continent itself contained likely PSCs in the line of sight between 21 and 30 km, over the uppermost retrieval level.

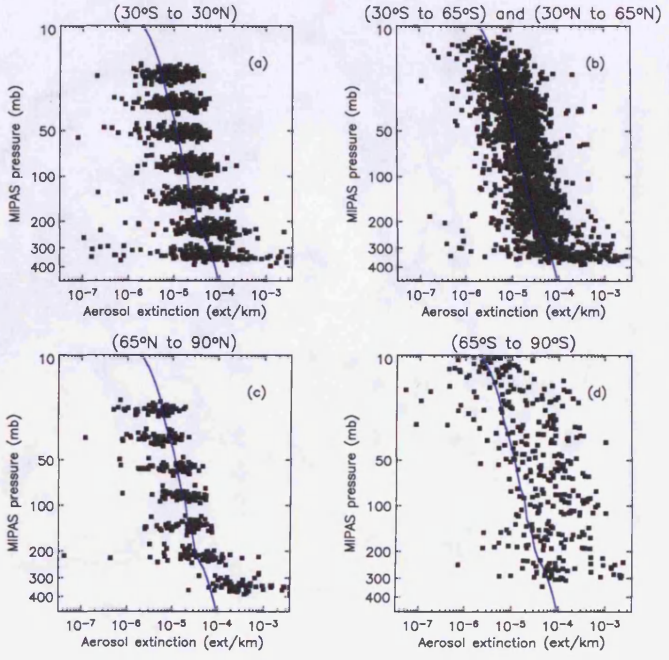

Figure 6.45. Retrieved aerosol data (black squares) from the joint retrieval of CFC-12 from 8th to 14th July 2003 (from orbits 07070 to 07170 where both level 1b calibrated spectra (version 4.61) and level 2 data (version 4.61) were available). The aerosol data are divided into four regions, depending on latitude. The solid blue line displays the *a priori* climatology profile of HCFC-22 used (Remedios, 1999).

July Antarctic data at 18 km were again contaminated by likely PSCs that lay above the retrieval range but within the measurement line of sight. The only data not affected by

higher altitude PSCs were at the edge of or away from the Antarctic continental landmass. The CFC-12 retrieval was run for the week from July 8th to 14th 2003 between 9 and 30 km. The jointly retrieved total extinctions are shown in Figure 6.45 and confirm that OPERA has measured very high extinctions, likely PSCs, at pressures up to 10 mb (approximately 27 km). The CFC-12 data from July still measured high extinctions between 300 and 100 mb, similar to HCFC-22 data, so it was likely that there were still PSCs/cirrus measured between 9 and 18 km.

In summary, total extinction results that were jointly retrieved with HCFC-22 for the 2003 show that OPERA can be used to measure and attempt to quantify both polar cirrus and PSC extinctions throughout the polar lower stratosphere from MIPAS-E data. Future work is needed to determine the potential for PSC extinction retrieval at higher altitudes due to the reduction of MIPAS-E signal to noise. It does appear possible from the CFC-12 joint retrieval that in likely PSC formation seasons that PSCs could be measurable up to 27 km.

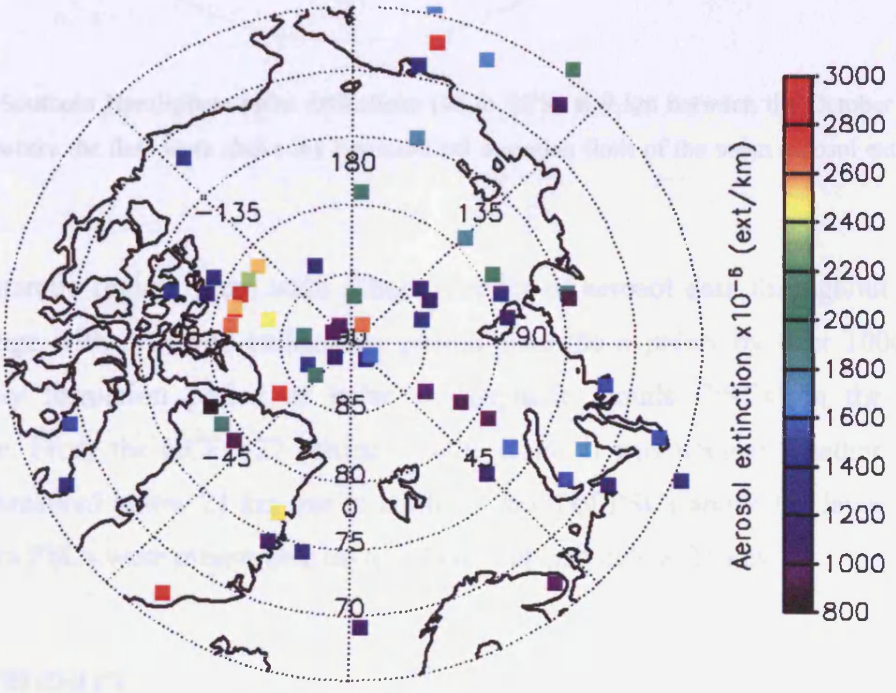

Figure 6.46 Northern Hemisphere polar extinctions (65°N to 90°N) at 9 km between the October 15th to 21st 2003 period where the data were above the one standard deviation limit of the mean aerosol extinction (for the Arctic).

Likely Arctic PSCs in January 2003 over Northern Scandinavia at 18 km were confirmed by comparison with the temperatures for the same period. The temperatures showed that the region was at or below 195 K, the temperature at which type 1 PSCs form. This result

provides extra confidence that the Arctic results at 18 km were not simply noisy data and PSC events were measured in at least three different scans.

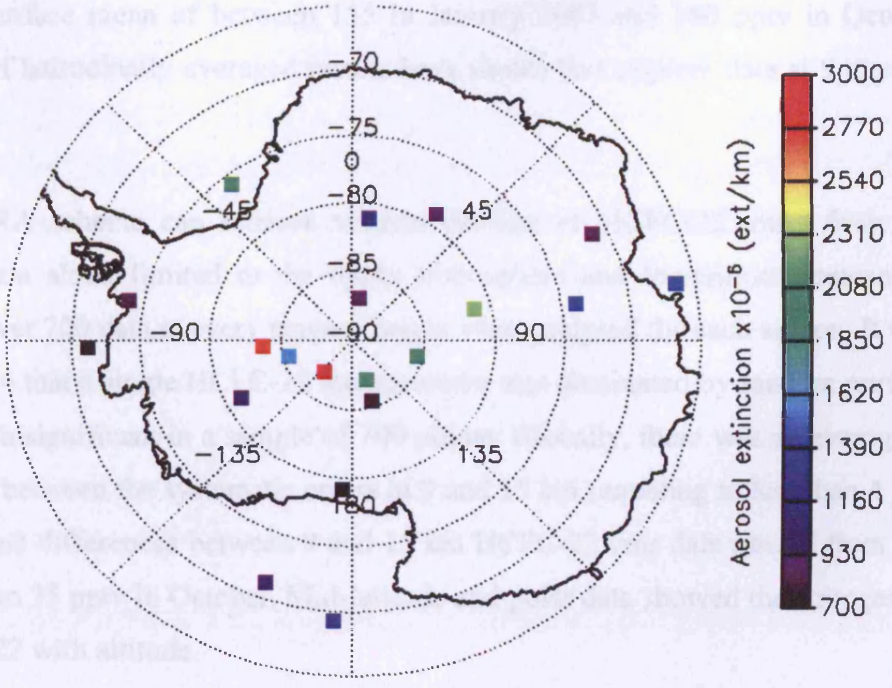

Figure 6.47. Southern Hemisphere polar extinctions (65 to 90°S) at 9 km between the October 15th to 21st 2003 period where the data were above the one standard deviation limit of the mean aerosol extinction (for Antarctica).

For the Antarctic region, there were a high number of aerosol data throughout the 30 to 400 mb range with retrieved extinctions greater than the *a priori* by over 1000 %. July marks likely formation period of polar stratospheric clouds (PSCs) in the Antarctic stratosphere. From the HCFC-22 aerosol results alone, it was unclear whether any PSCs had been measured below 21 km due to contamination of PSCs above the layer. From the CFC-12 data PSCs were measurable up to 27 km and also below 21 km.

6.4 Summary

This thesis project has aimed to explore the potential for measurement of primarily HCFC-22 volume mixing ratios (vmrs), but also CFC-12, in the UTLS by the limb-viewing spectrometer MIPAS-E onboard the ENVISAT satellite. The evidence presented in this chapter strongly indicates that the 829 cm^{-1} Q-branch feature of HCFC-22 can be successfully used to retrieve HCFC-22 volume mixing ratios in the upper troposphere and lowermost stratosphere from MIPAS-E spectral measurements.

Results have been shown from a week of data from each of the four seasons from 2003. It has been shown, via indirect validation with ESRL globally averaged surface measurements, that global mean MIPAS-E data at 9 km agree to within 22 pptv (15 %) with the surface mean of between 155 in January 2003 and 160 pptv in October 2003, Analysis of latitudinally averaged results have shown that tropical data at 9 km dominated this mean.

The OPERA scheme can retrieve vertical profiles of HCFC-22 vmrs from MIPAS-E spectral data albeit limited to the upper troposphere and lowermost stratosphere (9 to 15 km). Over 700 data at every tangent height were analysed for each season. It was shown in chapter 4 that a single HCFC-22 measurement was dominated by random retrieval error, but this is insignificant in a sample of 700 points. Globally, there was an average of 2.6 % difference between the systematic errors at 9 and 15 km (equating to less than 4 pptv vmr). Global mean differences between 9 and 15 km HCFC-22 vmr data ranged from 18 pptv in July 2003 to 35 pptv in October. Mid-latitude and polar data showed the strongest decrease of HCFC-22 with altitude.

Cross-sections of HCFC-22 vmr data appeared noisy but there was clear evidence that HCFC-22 vmrs decreased with both decreasing pressure but also with increasing latitude (i.e. a poleward decrease in vmr). It was found that PSCs above 21 km (outside the retrieval range for the HCFC-22 and total extinction joint retrieval) contaminated the July Antarctic data.

To demonstrate the ability of OPERA to retrieve volume mixing ratios of a gas with a higher concentration in the UTLS, it was also decided to retrieve CFC-12 vmrs. Due to the extension of the retrieval range between 9 and 30 km only one day of data from each season was analysed. Agreement between the global mean 9 km CFC-12 vmr data to a global mean surface CFC-12 vmr was better than 5 % (25 pptv) for every season. This was within the mean systematic error at 9 km on the MIPAS-E data of 8.4 %. The global mean data CFC-12 vmr also exhibit a distinct profile of decreasing CFC-12 vmrs with height between 12 and 21 km.

Total particle extinction results from the joint retrieval with HCFC-22 (and CFC-12) showed a very compact relationship between total particle extinction and cloud index (CI) in both the 9 km and 18 km data. A decrease in CI was coincident with an increased extinction. There were many instances of potential cirrus cloud measured at 300 mb

(approximately 9 km) which was a semi-permanent feature throughout 2003. In the tropics, there were a number of points containing thin clouds/high aerosol between 9 and 18 km. Future work is required to understand their origin.

Evidence was presented which showed that PSC extinctions were measured at altitudes up to 24 km in the joint CFC-12 and total particle extinction retrievals. This was most evident in the July 2003 data in the Antarctic. There were also likely Arctic PSCs in January 2003 measured over Northern Scandinavia which were indirectly confirmed by comparison with temperatures from the same period. Type I PSCs form at temperatures below 195 K and for January 8th 2003 the region of PSC measurements was coincident with a cold pool of air with a temperature below 195 K.

Chapter 7

7 Conclusions and Future Work

This chapter summarises the work undertaken in this thesis and the conclusions drawn from its results. In addition, possible future work will be identified related to the potential retrieval of other halocarbons in the upper troposphere and lower stratosphere (UTLS) using a retrieval scheme developed as part of this project.

To retrieve halocarbon volume mixing ratios (vmrs), this thesis developed the OPtimal Estimation Retrieval Algorithm (OPERA), specifically designed to invert spectral measurements from remotely sensed MIPAS-E data to concentrations. The scheme performed a joint retrieval of the target gas (for example HCFC-22) and aerosol. The scheme yielded positive results for HCFC-22, and also quantified the extinction of aerosol/thin clouds at 9 km and polar stratospheric clouds (PSCs) above 15 km.

In this thesis, HCFC-22 vmrs have been globally retrieved between 9 and 21 km at three kilometre intervals. From information content analysis, Rodgers [2000], more information was obtained from the MIPAS-E measurements compared to the *a priori* at three of these five intervals. Data were only shown for these three levels (9, 12 and 15 km). Due to the MIPAS-E utilising limb infrared emission as a measurement source, retrieval of HCFC-22 vmrs was possible independently of time of day.

A validation of HCFC-22 data was performed by comparison with indirect surface measurements. The HCFC-22 results at 9 km showed agreement in January 2003 of better than 8 %. The mean agreement with surface measurements for 2003 was within 15 % for all four seasons. The accuracy of these results was limited by the operationally retrieved MIPAS-E temperature and water vapour used in OPERA.

CFC-12 retrievals were also performed from the same spectral dataset between 9 and 30 km to both demonstrate the retrieval scheme and perform a consistency check on the likely accuracy of HCFC-22 data. These data were also validated against independent measurements. In particular the mean 9 km CFC-12 data agreed with global average surface data to better than 5 %.

These brief conclusions are now summarised further in the following sections.

To the author's knowledge, this thesis has presented the first retrievals of aerosol/cloud extinction profiles from MIPAS-E. The OPERA scheme provided a means of measuring the extinction due to cirrus and polar stratospheric clouds (PSCs). In particular it has been shown that three measurements from January 2003 at 18 km over Northern Scandinavia, had extinctions exceeding 10^{-4} km^{-1} (over one order of magnitude higher than expected). These data were consistent with temperatures below 195 K, which is the threshold for type I PSCs [Voigt *et al*, 2000].

7.1 The OPtimal Estimation Retrieval Algorithm (OPERA)

A retrieval scheme based on the optimal estimation approach to inverting spectral measurements [Rodgers, 2000] was developed as part of this thesis. The OPtimal Estimation Retrieval Algorithm (OPERA) performed radiometric retrievals and was particularly suited to the retrieval of halocarbon compounds which have no distinct line structure. The scheme performed a joint retrieval with aerosol to both aid convergence and increase the number of retrievals from spectra containing "thin" clouds.

HCFC-22 and CFC-12 were detected in MIPAS-E spectral data at up to 30 km and 21 km respectively. Microwindows from 828.95 to 829.15 cm^{-1} for HCFC-22 and 921.4 to 924.4 cm^{-1} for CFC-12 were selected as optimum regions containing information on the gases. The aerosol microwindow was between 832.3 and 834.4 cm^{-1}.

To represent average atmospheric conditions in OPERA the version 3.1 reference atmospheres of Remedios [1999] were used. It was though that by 2003, these data may underestimate the tropospheric HCFC-22 by up to 20 pptv so a high 100 % *a priori* covariance was assumed in the scheme. The CFC-12 data were known to a better accuracy so a lower 25 % *a priori* covariance was assumed. Little was known about the expected accuracy of the aerosol profile. A very high 1000 % *a priori* covariance was assumed on these data.

From simulated retrievals it was found that to both maximise the accuracy of the results whilst also minimising the iteration time the number of gases and the resolution of the fine mesh calculation with the ILS could be reduced in the forward model. For HCFC-22 and

CFC-12 it was still possible to retrieve known profiles with an accuracy of better than 10 %. The gases that should be included for the HCFC-22 window are HCFC-22, CFC-11, H_2O, CO_2, O_3, HNO_3, $ClONO_2$, C_2H_6 and aerosol. For the CFC-12 window it was decided to include CFC-12, H_2O, CO_2, HNO_3, CFC-113 and aerosol. The aerosol microwindow should include H_2O, CO_2, O_3, HNO_3, C_2H_6, CFC-11, HCFC-22, $ClONO_2$ and aerosol. The fine mesh resolution can be reduced to 0.01 cm^{-1} with no great effect on the accuracy of HCFC-22 and CFC-12 data.

From degrees of freedom for signal analysis (Rodgers, 2000), it was found that significant HCFC-22 information was gained from MIPAS-E measurements at an average of three heights between 9 and 30 km. It was decided therefore to save further iteration time by reducing the HCFC-22 retrieval range to 9 to 21 km. Only data with more information arising from the measurement than the *a* priori information are shown. "New" data at up to three levels was obtained (9, 12 and 15 km). For CFC-12 significant information was measured at up to seven heights in the tropics between 9 and 30 km (eight measurement levels). This decreased to four levels at the winter pole.

7.2 Error analysis

Expected errors on both HCFC-22 and CFC-12 were calculated from the approach presented in Rodgers, 2000. Both random errors (including retrieval and model parameter) and systematic errors (including model parameter, spectroscopic and instrument gain and offset) were evaluated and a total error on each measurement calculated.

Random retrieval errors for individual MIPAS-data were calculated from simulated spectra between 9 and 30 km. This error is lowest for both HCFC-22 and CFC-12 at 9 km (less than 25 % and 4 % respectively). The error increases with altitude for both gases. The random error on the total extinction for the tropics, mid-latitudes and polar summer is always better than 40%. In the polar winter this error is better than 50 %.

For HCFC-22 the lowest total random errors were at 9 km in mid-latitudes (16 %) and increasing globally up to 100 % by 30 km. Single profile HCFC-22 data were dominated by random retrieval error throughout the whole profile.

For CFC-12, the lowest total random error was 4 % globally at 12 km, increasing up to 25 % at 30 km in the winter pole. The highest total random error was found in the tropics at 9 km (40 %), due to both random retrieval errors and MIPAS-E temperature and water vapour uncertainties.

Systematic errors were less variable than the random component. For HCFC-22, the error ranged from a low 4 % in the tropics at 12 km, up to 22 % at 27 km at the summer pole. For heights where most information comes from the measurement (i.e. 9 to 15 km) the systematic error was less than 11 %.

The lowest systematic component for CFC-12 was in the tropics at 3 % between 21 and 27 km. At altitudes where more information came from the MIPAS-E measurement, the highest error was at 9 km in the tropics, due to instrument gain, spectroscopic and MIPAS-E temperature uncertainties.

The total error for a single HCFC-22 measurement was dominated by random error and to obtain useful information from the single profiles, many data had to be averaged. The error increased for all regions with height but was less than 25 % for 9 km data and increasing with altitude. By 21 km, errors were globally no better than 70 %.

For CFC-12, the total error on a single measurement varied between 6 and 14 % in the tropics between 12 and 27 km. Tropical 9 km data had an associated error of 41 % due to large temperature, gain and spectroscopic uncertainties. In mid-latitudes and the summer pole, the total error was better than 10 % between 12 and 21 km giving very good accuracy for single profile retrievals. At 9 km both the mid-latitude and polar data had an error of 17 % and 20 % respectively. Polar winter retrievals below 18 km had a total error of less than 14 %.

7.3 Validation of retrieved data

Comparison of OPERA retrieved CFC-12 data and results from a fast forward modelling scheme were compared between 12 and 30 km. Twelve scans with a global spread were chosen and agreement between the profiles was better than 10 % between 12 and 18 km. There was a systematic high OPERA bias above for CFC-12 data below 400 pptv in the tropics. The same bias was also observed in mid-latitude data below 200 pptv, the summer

pole below 300 pptv and at the winter pole below 150 pptv. There was good agreement in profile shape in the aerosol comparison, but poor quantitative agreement as OPERA was high biased by up to 100 %.

Tracer-tracer correlations with MIPAS-E N_2O were used to validate CFC-12 and HCFC-22 data. There was a positive bias in the global MIPAS-E N_2O and OPERA CFC-12 correlation compared to the expected relationship from the climatology files. This could not be explained by changes of atmospheric concentration of either gas since the climatology was produced and is explained by a slight high bias in the MIPAS-E N_2O or up to 30 pptv low bias in the CFC-12. For HCFC-22, the global atmospheric increase of 20 pptv expected from surface observations since the climatology was produced, was realised in the comparison.

A close agreement was found between ATMOS CFC-12 and OPERA CFC-12 and there was an indication that the OPERA retrieved results fitted the trend expected since the ATMOS measurements were made as estimated from surface measurements and age of air considerations. The comparison between ATMOS HCFC-22 and OPERA retrieved HCFC-22 showed an average increase in HCFC-22 global volume mixing ratios of approximately 7 pptv/yr since ATMOS. This was higher than that estimated from surface measurements but lower than that derived from ACE data in 2004. Indications are that HCFC-22 could be accurate to 15 pptv (better than 10 %).

Validation of OPERA retrieved CFC-12 data with measurements from the HAGAR instrument flown onboard the Geophysica aircraft in late Northern Hemisphere winter (February 28th and March 12th 2003) were also performed. Here consolidated level 2 data (version 4.61), including pressure, temperature, water vapour, ozone and nitric acid, were incorporated in the forward modelling and not the near real time products (version 4.57). CFC-12 data were compared over the 9 to 18 km range. There was excellent agreement between the HAGAR and OPERA retrieved CFC-12 data. In March in particular, the two data agreed to better than 30 pptv (6 %) at 300 mb, giving high confidence in the accuracy of OPERA retrieved CFC-12. The mean difference for both months between OPERA and HAGAR was better than 40 pptv (7 %).

Retrieved CFC-12 data were compared to MIPAS-STR measurements taking over Northern Scandinavia between 9 and 18 km during February and March 2003. There was a low MIPAS-STR bias in the mean profile compared to the reference atmosphere of

between 80 and 170 pptv. The mean OPERA profile was also low biased to the reference climatology but by less than 90 pptv. These results suggested that there were likely problems with the MIPAS-STR measurements at the lower altitudes.

7.4 Seasonal measurements

OPERA retrieved HCFC-22 and CFC-12 results from MIPAS-E level 1b spectral data (version 4.61 and 4.62) were presented from the four seasons in 2003. One week of data from each season were processed for HCFC-22 and one full day of data from each season for CFC-12. HCFC-22 retrievals were performed between 9 and 21 km, CFC-12 retrievals between 9 and 30 km. Prior to retrieval, MIPAS-E spectra containing optically thick cloud were identified and the whole scan removed (applying the technique of Spang *et al.*, [2002] and a cloud index of less than 1.8). From the remaining spectra it was confirmed from the retrieved results that both OPERA CFC-12 and HCFC-22 measurements were independent of thin cloud (which had a cloud index of between 1.8 and 4).

The global HCFC-22 mean data at 9 km agreed to within 15 % of the measured mean surface value for all four seasons. Agreement in January was better than 8 %. These results show that within errors, OPERA results at the lowest retrieval altitude were comparable to expected vmrs based on an indirect comparison with average surface measurements.

The 15 km HCFC-22 vmrs were lower in the global mean than those at 9 km, for all seasons. This suggested that the data exhibited a vertical profile. This was shown by comparison of the systematic error terms at 9 and 15 km. The systematic difference between these heights was globally less than 3 % (equating to less than 5 pptv). Therefore, there is confidence therefore that OPERA can measure global mean HCFC-22 vertical profiles from MIPAS-E data.

A global tropospheric HCFC-22 increase of around 5 pptv during 2003 was expected from surface observations (first published in Montzka *et al.*, [1993]). However differences of HCFC-22 of 15 pptv were measured at 9 km between the mean mid-latitude data, averaged from both hemispheres. It was clear that although the standard error on the mean mid-latitude data was less than 2 pptv for each season, the variability within the operationally retrieved temperature or water vapour data at 9 km were the most likely cause of this high seasonal mid-latitude HCFC-22 variation.

For CFC-12, the agreement between the 9 km global data and indirect surface observations were better than 5 %. Retrievals extended up to 30 km and also provided information on the profile variability of CFC-12. In the global data, a vertical profile of CFC-12 was measured between 12 and 21 km with 21 km vmrs between 170 and 230 pptv (50 to 75 %) lower than at 12 km. Systematic errors were similar between 12 and 21 km, varying between 4 and 5 %, inferring that the changes in concentration with height was real. Above 21 km, the systematic error increased sharply so although a profile in CFC-12 is expected, the differences in vmrs between levels could also be explained by variations in the systematic error.

When analyzed zonally, there were many interesting findings. The mid-latitude CFC-12 data above 15 km (below 100 mb) showed an offset compared to the climatology profile for all seasons of over a 50 pptv decrease. It was likely that either the CFC-12 climatology profile was too high or the results indicated a decrease of CFC-12 above 15 km. It was likely that the age of air at 15 km in 2003 originated from troposphere two to three years previously. This period was coincident with a rise of tropospheric CFC-12 by between 1 and 4 pptv/yr. It is therefore unlikely that CFC-12 levels should be observed to have fallen at 15 km since the climatology was produced.

Aerosol data were also analysed from each season as the joint retrieval approach yielded profiles of thin cloud and aerosol extinctions in the upper troposphere and lower stratosphere. Both tropical and polar tropospheric clouds were observed, together with PSCs at the winter pole.

It was shown that a close relationship existed between cloud index (the measure of the "cloudiness" of a spectrum) and high OPERA retrieved extinctions in both the 9 km and 18 km aerosol data from the joint retrieval with HCFC-22.

Potential cirrus or other aerosol particles with an extinction exceeding 10^{-3} km^{-1} were measured globally at 9 km for each season.

In January 2003, extinctions exceeding 10^{-4} km^{-1} were measured in the Arctic between 50 and 70 mb. The highest extinctions for this month were over Northern Scandinavia and coincided with stratospheric temperatures below 195 K (the temperature at which PSCs can form, [Voigt *et al.*, 2000]).

In July 2003, the Antarctic data contained a high number of measured extinctions exceeding 10^{-4} km^{-1} between 40 and 200 mb. Comparison of the aerosol data from the HCFC-22 retrieval with the joint retrieval with CFC-12 showed that likely PSCs were measured above 21 km. The high extinctions measured below 21 km in the aerosol data from the joint retrieval with HCFC-22 were due to the clouds being present within the line of sight of the measurement, but above the uppermost retrieval altitude.

In the tropics, there were a number of points containing thin clouds/high aerosol between 9 and 18 km. Future work is required to understand their origin.

7.5 Future work

Future work is expected to have three components: 1) extension of the OPERA retrieval to other important halocarbons, 2) further refinement of the OPERA scheme and methods for reducing iteration time and finally 3) application of the current dataset to other seasons/years of MIPAS-E data.

Halocarbons are important greenhouse gases and stratospheric ozone destroying compounds. Tropospheric concentrations of other halocarbons are growing rapidly and although they are not currently measurable from MIPAS-E their future growth may mean that species such as HCFC-141b or HCFC-142b may be detectable from MIPAS-E before the end of the lifetime of MIPAS-E. To do this a full feasibility study to characterise target gases is required. Likely objectives would include:

- Detection limits for detection above the MIPAS-E NESR level from synthesised data at MIPAS-E altitudes in the upper troposphere and lower stratosphere.

- A full characterisation of potential microwindow regions for the retrieval of the halocarbon. This would include measuring the contribution to signal from interfering gases and the likely errors caused by inaccuracies in the climatology/other data used to model these gases.

The OPERA scheme currently performs joint radiometric gas retrievals with aerosol extinction from MIPAS-E level 1b spectra over a user-defined altitude range, incorporating user-defined microwindow ranges. The scheme also incorporates MIPAS-E

level 2 data for the operational products to use in the forward modelling of spectra. The computation of limb emission spectra has been found to be computationally expensive using resources available at the time of this thesis. To decrease the iteration time, the scheme could be adapted to incorporate pre-computed "look-up" tables which contain "exact" line by line calculations of transmittance for pressure, temperature and gas concentrations over a range of atmospheric conditions. A full expected error analysis of the forward modelling error from using this approach would need to be carried out.

To increase the number of retrievals from each day, OPERA could be modified at retrieve halocarbons above cloudy spectra. This would be most advantageous for CFC-12 retrievals based on results from this thesis work as information was obtainable from MIPAS-E measurements at least up to 30 km.

Further updates of the HITRAN spectroscopic data for HCFC-22 (and to an extent CFC-12) would be desirable as spectroscopic error was a major contributor to the total error.

The 9 km errors were generally dominated by MIPAS-E temperature (and in the tropics and mid-latitudes water vapour) uncertainties. The possibly improved accuracy of using other sources of information for this data (such as from the ECMWF) would need to be investigated.

The quality of OPERA retrieved data shown in this thesis for CFC-12, HCFC-22 and aerosol extinction could be exploited further in the future. Although limited HCFC-22 profile information was obtained from MIPAS-E measurements given current levels, the further exploitation of MIPAS-E data to measure trends in OPERA retrieved HCFC-22 data between 9 and 15 km should be utilised. For CFC-12, there is clearly potentially future exploitation to extend the retrieval range (given adequate computational resources).

The OPERA extinction data has provided some fascinating information for the temporal and spatial variability of aerosol/thin clouds/PSCs in the UTLS, and has quantified the extinction observed. After further validation of the current data against independent aerosol measurements the ability of OPERA to quantify UTLS extinction should be further exploited. This should be done by extending analysis to other seasons (particularly in the tropics) and other years (in the case of the PSCs in polar winter).

Bibliography

Abrams, M. C., Chang, A. Y., Gunson. M. R., et al. On the assessment and uncertainty of atmospheric trace gas burden measurements with high resolution infrared solar occultation spectra from space by the ATMOS experiment. *Geophys. Res. Letts,* 23, no. 17, 2337-2340, 1996.

Allen, G.: The Infrared Remote Sensing of Peroxyacetyl Nitrate in the Upper Troposphere, DPhil thesis, *University of Leicester*, 2003.

Armstrong, B. H.: Spectrum Line Profiles: The Voigt Function. *J. Quant. Spectrosc. Radiat. Transfer* 7, 61-88, 1967.

Ballard, J., Knight, R. J., Newnham, D. A., Vander Auwera, J., Herman, M., Lonardo, G., Masciarelli, G., Nicolaisen, F. M., Beukes, J. A., Christensen, L. K., McPheat, R., Duxbury, G., Freckleton, R., and Shine, K. P.: An inter-comparison of laboratory measurements of absorption cross-sections and integrated absorption intensities for HCFC-22, *J. Quant. Spect. Radiat. Trans.*, 66 (2), 109-128, 2000.

Baray, J. L., V. Daniel, G. Ancellet, and B. Legra, Planetary-scale tropopause folds in the southern subtropics, *Geophys. Res. Lett.*, 27, 353-356, 2000.

Beer, R: TES Scientific Objectives & Approach, Goals & Requirements *Revision 6.0*, JPL document: D-11294, April 14, 1999.

Bernath, P. F., Infrared Fourier Transform Emission Spectroscopy, *Chem. Soc. Rev.*, 25, 111-115, 1996.

Blom, C. E., C. Camy-Peyret, V. Catoire, K.Chance, H. Oelhaf, J. Ovarlez, S. Payan, M. Pirre, c. Piesch, G. and Wetzel, Validation of MIPAS temperature profiles by stratospheric balloon and aircraft measurements, *Proc. ACVE-2 meeting*, 3-7 May 2004, Frascati, Italy, ESA SP-562, 2004.

Blom, C. E., et al., MIPAS- STR: ein Fernerkundungsinstrument für Stratosphärenflugzeuge.". Nachrichten - Forschungszentrum Karlsruhe, 35(2003) S.46-50, 2003

Browning, K. E., Organisation of clouds and precipitation in extra-tropical cyclones, in *Extratropical Cyclones-The Erik Palmen Memorial Volume*, pp 129-153, *Am. Meteorol. Soc.*, Boston, Mass., 1990.

Butler, J. H. et al. 1999: A record of atmospheric halocarbons during the twentieth century from polar firn air. *Nature*, 399, 749-755.

Camy-Peyret, C., G. Dufour, S. Payan, H. Oelhaf, G. Wetzel, G. Stiller, Th. Blumenstock, C.E. Blom, T. Gulde, N. Glatthor, A. Engel, M. Pirre, V. Catoire, G. Moreau, M. De Mazière, C. Vigouroux, E. Mahieu, U. Cortesi, F. Mencaraglia, Validation of MIPAS N2O profiles by stratospheric balloon, aircraft and ground based measurements, *Proc. ACVE-2 meeting, 3-7 May 2004, Frascati, Italy,* 2004.

Carli, B, Alpaslan, D., Calotti, M., and Castelli, S.: First results of MIPAS/ENVISAT with operational Level 2 code, *Adv. Space. Res.,* 2004.

Carli, B., et al., Airborne polar experiment geophysica aircraft in Antarctica (APE_GAIA). *Sparc newsletter*, 2000.

Chang, A. Y., et al., A comparison of measurements from ATMOS and instruments aboard the ER-2 aircraft: Halogenated gases, *Geophys. Res. Letts.*, 23, 2393-2396, 1996.

Clerbaux, C., R. Colin, P. Simon, and C. Granier, Infrared cross sections and global warming potentials of 10 alternative hydrohalocarbons, *J. Geophys. Res.*, 98, 10,491-10,497, 1993.

Dudhia, A., V. L. Jay and C. D. Rodgers. Microwindow selection for high-spectral resolution sounders. *Appl. Optics.*, 41, 18, 3665-3673, 2002.

Dudhia, A.: MIPAS Micro-window Processing Scheme (MWPROC), ESA contract No. 11886/96/NL/GS, 2001.

Dudhia, A.: A multi-layer Technique for Micro-window Selection, ESA Contract No. 11886/96/NL/GS, 1999.

Dudhia, A. RFM software user's manual. Technical report, ESTEC, Noordwijk, Netherlands. ESA Document PO-MA-OXF-GS-0003, 1997. http://www.atm.ox.ac.uk/RFM/sum.html.

Ebel, A., H. Hass, H. J. Jakobs, M. Laube, M. Memmesheimer, A. Oberreuter, H. Geiss, and Y.-H., Kuo, 1991: Simulation of ozone intrusion caused by a tropopause fold and cut-off low. *Atmos. Environ.,* 25A, 2131-2144.

Fabian, P., R. Borchers, Growth of Halocarbon Abundances in the Stratosphere between 1977 and 1999, *Adv. Space. Res.*, 28, No. 7, 961-964, 2001.

Fahey, D.W., K.K. Kelly, S.R. Kawa, A.F. Tuck, M. Loewenstein, K.R. Chan, and L.E. Heidt, Observations of denitrification and dehydration in the winter polar stratospheres, *Nature*, 344, 321, 1990.

Farman, J. C., B. G. Gardiner and J. D. Shanklin, Large losses of the total ozone in Antarctica reveal seasonal ClO_x/NO_x interaction, *Nature,* 315, 207-210, 1985.

Finkbeiner, M. et al., Reaction between HO_2 and ClO: product formation between 210 and 300 K, *J. Phys. Chem.*, 99, 16264-16275, 1995.

Finlayson-Pitts, J.: Chemistry of the upper & lower atmosphere. *Academic press,* 2000.

Fischer, H., and H. Oelhaf, Remote sensing of vertical profiles of atmospheric trace constituents with MIPAS limb-emission spectrometers, *Appl. Opt.*, 35, 2787-2796, 1996.

Flaud, J.-M., Piccolo, C., Carli, B., A spectroscopic database for MIPAS. *Proceedings of the ENVISAT validation workshop*, ESRIN, Italy, 2002.

Freckleton, R., E. Highwood, K. Shine, O. Wild, K. Law, and M. Sanderson, greenhouse gas radiative forcing: effects of average and inhomogeneities in trace gas distribution, *Q. J. R. Meteorol. Soc*, 124, 2,099-2,127, 1998.

Goody R. M., and Y. L. Yung. Atmospheric Radiation, Theoretical Basis. *Oxford University Press.* Second Edition, 1989.

Greenhough J., J. J. Remedios and H. Sembhi. Cloud detection and distributions from MIPAS infra-red limb observations. *Advances in Space Research*, in press , 2004.

Gulde, T., et al., Validation of MIPAS-ENVISAT profiles for CH_4 and N_2O with data from the MIPAS-STR instrument onboard the GEOPHYSICA, *ENVISAT & ERS symposium*, Salzburg, Austria, Sep. 6-10, 2004.

Gunson, M. R., Abbas, M. M., Abrams, M. C., et al.The Atmospheric Trace Molecule Spectroscopy (ATMOS) experiment: Deployment on the ATLAS Space Shuttle missions, *Geophys. Res. Lett.*, 23, 2333-2336, 1996.

Highwood, E. J., and B. J. Hoskins, The tropical tropopause, *Q. J. R. Meteorol. Soc.*, 124, 1579-1604, 1998.

Hoffmann, L., R. Spang , M. Kaufmann, and M. Riese, Retrieval of atmospheric trace constituents from Envisat MIPAS observations by means of rapid radiative transfer calculations, Adv. Space Res., 2004, in print.

Hollas, J. M.: Modern Spectroscopy, Third edition. *John Wiley & sons*, Chichester, UK. 1997.

Holton, J. R., Haynes, P. H., McIntyre, M. E., Douglass, A. R., Rood, R. B., and Pfister, L.: Stratosphere-Troposphere Exchange, *Rev. Geophys.*, 33, 403-439, 1995.

Holton, J. R., Meridional distribution of stratospheric trace constituents, *J. Atmos. Sci.*, 43, 1238-1242, 1986.

Houghton J. T., F. W. Taylor, and C. D. Rodgers, Remote Sounding of Atmospheres, *Cambridge University Press*, 1984.

IPCC. Climate Change 2001: The Scientific Basis. Contribution of Working Group I to the Third Assessment Report of the Intergovernmental Panel on Climate Change (IPCC) [J.

T. Houghton, Y. Ding, D.J. Griggs, M. Noguer, P. J. van der Linden and D. Xiaosu (Eds.)] Cambridge University Press, UK. pp 944, 2001.

IPCC, : Climate Change 1995: *The Science of Climate Change. Contribution of Working Group I to the Second Assessment Report of the Intergovernmental Panel on Climate Change* [Houghton, J.T., L.G. Meira Filho, B.A. Callander, N. Harris, A. Kattenberg, and K. Maskell (eds.)]. Cambridge University Press, Cambridge, United Kingdom and New York, NY, USA, 572 pp, 1996.

IPCC, : Climate Change 1994: *Radiative Forcing of Climate Change and an Evaluation of the IPCC IS92 Emission Scenarios* [Houghton, J.T., L.G. Meira Filho, J. Bruce, H. Lee, B.A. Callander, E.F. Haites, N. Harris, and K. Maskell (eds.)]. Cambridge University Press, Cambridge, United Kingdom and New York, NY, USA, 1994.

IPCC, : Climate Change 1990: *The Intergovernmental Panel on Climate Change Scientific Assessment* [Houghton, J.T., B.A. Callander, and S.K. Varney (eds)]. Cambridge University Press, Cambridge, United Kingdom and New York, NY, USA, 1990.

Jay, V.: Remote sounding of the atmosphere by high-resolution spectroscopy, DPhil thesis, *Oxford University*, 2000.

Jones, R. L. and A. J. Pyle, Comparisons of SAMS methane and nitrous oxide with model calculations, *Q. J. Roy. Astron. Soc.*, 25, 322, 1984.

Kanakidou, M., F. J. Dentener and P. J. Crutzen. A global three-dimensional study of the fate of HCFCs and HFC-134a in the troposphere. *J. Geophys. Res.*, 100, 18781-18801, 1995.

Kerridge, B. J., et al., MIPAS ozone validation by satellite intercomparisons, *Proc. ACVE-2 meeting*, 3-7th May, Frascati, Italy, 2004.

Kiehl, J. T. and K. E. Trenberth. Earth's annual global mean energy budget. *Bull. Amer. Meteor. Soc.*, 78, 197-208.

Kleinert, A. Gain and offset analysis of level 1 data November 2003, MIPAS: Quality Working Group meeting (QWG#3), March 2004.

Lambert, A., R. G. Grainger, C. D. Rodgers, F.W. Taylor, J. L Mergenthaler, J. B. Kumer, S. T. Massie, Global evolution of the Mt. Pinatubo volcanic aerosols observed by the infrared limb-sounding instruments CLAES and ISAMS on the Upper Atmosphere Research Satellite, *J. Geophys. Res.*, 102, p1495, 1997.

Lahoz, W., et al. Modelling and assimilation: evaluation of MIPAS water vapour data, *Proc. ACVE-2 meeting*, 3-7th May, Frascati, Italy, 2004.

Lipson, J. B., et al., Temperature dependence of the rate constant and branching ratio for the OH+ClO reaction, *J. Chem. Soc., Faraday. Trans.*, 93, 2665-2673, 1997.

Lopez-Puertas, M. and F. W. Taylor. Non-LTE radiative transfer in the atmosphere. *World Scientific*, 2001.

Luo, Z., and W.B. Rossow, Characterizing tropical cirrus life cycle, evolution, and interaction with upper-tropospheric water vapor using Lagrangian trajectory analysis of satellite observations. *J. Climate,* 17, 4541-4563, doi:10.1175/3222.1, 2004.

McIlveen, J.F.R, Fundamentals of weather and climate, *Chapman and Hall*, London, 1992.

Mantovani, R.: Envisat MIPAS technical note, ESA document: ENVI-SPPA-EOPG-TN-05-0012, 2003.

Marshall, T.B., L.L. Gordley and D.A. Chu, Bandpak: Algorithms for modeling broadband transmissions and radiance, *JQSRT,* 52 (1994), 581-599.

Marks, C. J. and C. D. Rodgers. A retrieval method for atmospheric composition from limb emission measurements. *J. Geophys. Res.*, 98, 14939-14953.

Molina, M.J. and F.S. Rowland, Stratospheric sink for chlorofluoromethanes-chlorine atom catalyzed destruction of ozone. *Nature,* 249, 810-812, 1974.

Montreal protocol, Protocol on Substances That Deplete the Ozone Layer, treaty signed on Sept. 16, 1987.

Montzka, S. A., Butler, J. H., Elkins, J. W., Thompson, T. M., Clarke, A. D., and Lock, L. T.: Present and future trends in the atmospheric burden of ozone-depleting halogens, *Nature*, 398, 690-694, 1999.

Montzka, S.A., et al., Decline in the tropospheric abundance of halogen from Halocarbons: implications for stratospheric ozone depletion, *Science*, 272, 1318-1322, 1996.

Montzka, S. A., R. C. Myers, J. H. Butler, J. W. Elkins, and S. O. Cummings, Global tropospheric distribution and calibration scale of HCFC-22, *Geophys. Res. Lett.*, 20, 703-706, 1993.

Murphy, D. M. and D. W. Fahey, An estimate of the flux of stratospheric reactive nitrogen and ozone into the troposphere, *J. Geophys. Res.*, 99, 5325-5332, 1994.

Naik, V., A. Jain, K. Patten, and D. Wuebbles, Consistent sets of atmospheric lifetimes and radiative forcings on climate for CFC replacements: HCFCs and HFCs, *J. Geophys. Res.*, 105, 6,903-6,914, 2000

Nett, H., Frerick, J., Paulsen, T., and Levrini, G.: The atmospheric instruments and their applications: GOMOS, MIPAS and SCIAMACHY. ESA Bulletin – European Space Agency, 106, 77-87, 2001.

Norton, R. H., and Beer, R.: New apodising functions for Fourier spectrometry, *J. Opt. Soc. A. 66,* 259, 1976.

Norton, R. H., and Beer, R.: New apodising functions for Fourier spectrometry – Erratum. *J. Opt. Soc. A.*, 67, 419, 1977.

Oelhaf, H., T. Blumenstock, M. De Mazière, S. Mikuteit, C. Vigouroux, S. Wood, G. Bianchini, R. Baumann, C. Blom, U. Cortesi, G.Y. Liu , H. Schlager, C. Camy-Peyret, V. Catoire, M. Pirre, K. Strong, G. Wetzel, Validation of MIPAS-ENVISAT version 4.61 HNO3 operational data by stratospheric balloon, aircraft and ground-based measurements, *Proc. ACVE-2 meeting, 3-7 May 2004, Frascati, Italy,* 2004a.

Oelhaf, H., A. Fix, C. Schiller, K. Chance, W. Gurlit, J. Ovarlez, J.-B. Renard, S. Rohs, G. Wetzel, T. von Clarmann, M. Milz, D.-Y. Wang, J.J. Remedios, and A.M. Waterfall,

Validation of MIPAS-ENVISAT version 4.61 operational data with balloon and aircraft measurements: H2O, *Proc. ACVE-2 meeting, 3-7 May 2004, Frascati, Italy,* 2004b.

Oelhaf, H., F. Friedl-Vallon, A. Kleinert, A. Lengel, G. Maucher, M. Höpfner, H. Nordmeyer, G. Wetzel, G. Zhang, and H. Fischer, Validation of Envisat chemistry instruments with MIPAS-B observation, *Proc. Quadr. Ozone Symp., 1-8 June 2004, Kos, Greece*, p. 591, 2004c.

Offermann, D., K.-U. Grossmann, P. Barthol, P. Knieling, M. Riese and R. Trant, Cryogenic Infrared Spectro-meters and Telescopes for the Atmosphere (CRISTA) experiment and middle atmosphere variability, J. Geophys. Res., 104, 16311-16326, 1999.

Peixoto , J. P, and A. H, Oort, Physics of Climate, *American Institute of Physics*, New York, p157,158.

Perron, G.: NESRT verification, MIPAS: Quality Working Group meeting (QWG#3), Frascati, March 2003.

Plumb, R.A., A "tropical pipe" model of stratospheric transport, *J. Geophys. Res.*, 101, 3957 - 3972, 1996.

Plumb, R. A., and M. K. W. Ko, Interrelationships between mixing ratios of long lived stratospheric constituents, *J. Geophys Res.*, 97, 10145-10156, 1992.

Remedios, J.J. and R. Spang, Detection of cloud effects in MIPAS spectral data and implications for the MIPAS operational processor, Proceeding of the ENVISAT Calibration Review, 9-13 September 2002, ESTEC, Noordwijk, The Netherlands, 2002.

Remedios, J. J.: Extreme atmospheric constituent profiles for MIPAS, *Proceedings of the European Symposium on atmospheric measurements from space,* Vol. 2, ESTEC, Nordwijk, Netherlands, 20-22nd Jan, 779-783, 1999.

Ridolfi, M., Carli, B., Carlotti, M., von Clarmann, T., Dinelli, B. M., Dudhia, A., Flaud, J-M., Hopfner, M., Morris, P. E., Raspollini, P., Stiller, G., and Wells, R. J.: Optimised

forward modelling and retrieval scheme for MIPAS near-real-time data processing, *Applied Optics*, 39, 1323-1340, 2000.

Riediger, O., U. Schmidt, M. Strunk, and C. M. Volk, HAGAR: A new in-situ instruments for stratopsheric balloons and high altitude aircraft, In *Stratospheric Ozone 1999, Proceedings of the fifth European symposium, Air Pollut. Rep.,*, 73, edited by N. R. P. Harris et al., Eur. Comm., Brussels, 2000.

Rinsland, C. P., Chiou, L. S., Goldman, A., et al. Long-term trend in CHF2Cl (HCFC-22) from high spectral resolution infra red solar absorption measurements and comparison with in situ measurements. *J. Quant. Spectrosc,* 90 (3-4): 367-375, 2005a.

Rinsland, C. P. et al. Trends of HF, HCl, CCl_2F_2, CCl_3F, $CHClF_2$ (HCFC-22), and SF_6 in the lower stratosphere from Atmospheric Chemistry Experiment (ACE) and Atmospheric Trace Molecule Spectroscopy (ATMOS) measurements near 30°N latitude, *Geophys. Res. Letts.,* 32, 10.1029/2005GL022415,2005b.

Roche, A. E. et al., The cryogenic limb array etalon spectrometer CLAES on UARS: experiment description and performance, *J. Geophys. Res,* 98, 10763-10775, 1993.

Rodgers, C. D.: Inverse methods for atmospheric sounding: Theory and practice (Series on atmospheric, oceanic and planetary physics). *World Scientific Publishing*, 2000.

Rodgers, C. D. Information content and optimisation of high spectral resolution remote measurements. *Adv. Space. Res.*, 21, 361-367, 1998.

Rodgers, C. D. Characteristaion and error analysis of profiles retrieved from remote sounding measurements. *J. Geophys. Res.*, 95, 5587-5595, 1990.

Rodgers, C. D. Retrieval of Atmospheric Temperature and Composition from remote measurements of thermal radiation. *Reviews of Geophysics and Space Physics*, 14, 609-624, 1976.

Rothman, L. S., Barbe, A., Benner, D.C., Brown, L. R., Camy-Peyret, C., Carleer, M. R., K. Chance, K, Clerbaux, C., Dana, V., Devi, V. M., Fayth, A. Flaud, J.M., Gamache, R. R., Goldman, A., Jacquemart, D., Jucks, K. W., Lafferty, W. J., Mandin, J.-Y., Massie, S.

T., Nemtchinov, V., Newnham, D. A., Perrin, A., Rinsland, C. P., Schroeder, J., Smith, K. M., Smith, M. A. H., Tang, K., Toth, R. A., Vander Auwera, J., Varanasi, P., and Yoshino, K.: The HITRAN molecular spectroscopic database: edition of 2000 including updates through 2001. *J. Quant. Spect.*, 82(1-4): 5-44, 2003.

Rothman, L. S., C. P. Rinsland, A. Goldman, S. T. Massie, D. P. Edwards, J.-M Flaud, A. Perrin, C. Camy-Peyret, V. Dana, J.-Y Mandin, J. Schroeder, A. McCann, R. R. Gamache, R. B. Wattson, K. Yoshino, K. V. Chance, K. W. Jucks, L. R. Brown, V. Nemtchinov, and P. Varanasi, The HITRAN Molecular Spectroscopic Database and HAWKS (HITRAN Atmospheric Workstation), *Special Issue of the Journal of Quantitative Spectroscopy and Radiative Transfer.*, 60, 665 – 710, 1998.

Seo, K. H. and K. P. Bowman, A climatology of isentropic cross-tropopause exchange, J. Geophys. Res., 106, 28159 – 28172, 2001.

Shannon. C. E., and W. Weaver. The mathematical theory of communication, *University of Illinois Press.*, eighth edition, 1949.

Sihra, K., Hurley, M. D., Shine, K. P., and Wallington, T. J.: Updated radiative forcing estimates of 65 halocarbons and nonmethane hydrocarbons. *J. Geophys. Res.*, 106(D17), 2001.

Smith,H.J.P. et al, 1978. FASCODE - Fast Atmospheric Signature Code. AFGL-TR-0081. Air Force Geophysics Laboratory, Hanscom AFB MA 01731.

Spang, R., Remedios, J. J., Kramer, L. J., et al. Polar stratospheric cloud observations by MIPAS on ENVISAT: detection method, validation and analysis of the Northern Hemisphere winter 2002/2003. *Atmos. Chem. Phys.*, 5, 679-692, 2005.

Spang, R., J. Remedios, and M. Barkley Colour indices for the detection and differentiation of cloud types in infra-red limb emission spectra, Adv. Space Res, 33,1041-1047, 2004

Spang, R.; Remedios, J. J. Observations of a distinctive infra-red spectral feature in the atmospheric spectra of polar stratospheric clouds measured by the CRISTA instrument Geophysical research letters, 30 (2003), 16, 1875, 10.1029/2003GL017231

Spang, R., G. Eidmann, M. Riese, D. Offermann, P. Preusse, L. Pfister and P. H. Wang, CRISTA observations of cirrus clouds around the tropopause, *J. Geophys. Res.*, *107*(D23), 8174, doi:10.1029/2001JD000698, 2002.

Spang, R., M. Riese, and D. Offermann, CRISTA-2 observations of the south polar vortex in winter 1997: A new dataset for polar process studies ,*Geophys. Res. Lett.*, 28, 3159-3162, 2001.

Stohl, A. *et al.* Stratosphere-troposphere exchange: A review and what we have learned from STACCATO. *J. Geophys. Res.*, 108, 8516, 10.1029/2002JD002490.

Toon, G. C., et al., Comparison of MkIV balloon and ER-2 aircraft measurements of atmospheric trace gases, *J Geophys. Res.*, 104, 26779-26790, 1999.

United Nations Environment Programme (UNEP), 1998. Environmental Effects of Ozone Depletion, 1998 Assessment, *Journal of Photochemistry and Photobiology B: Biology*, 46, 1-4, Published by Elsevier Science.

U. S. Standard Atmosphere. National Oceanic and Atmospheric Administration, National Aeronautics and Space Administration, U. S. Air Force, *U. S. Government printing office*, Washington D. C.

Varanasi, P., Z. Li, V. Nemtchinov and A. Cherukuri, Spectral Absorption-Coefficient Data on HCFC-22 and Sf6 for Remote-Sensing Applications, J. Quant. Spectrosc. Radiat. Transfer, 52, 323 – 332, 1994.

Varanasi, P. and V. Nemtchinov, Thermal infrared absorption coefficients of CFC-12 at atmospheric conditions. *Journal of Quantitative Spectroscopy & Radiative Transfer*, 51, 679-687, 1994.

Varanasi, P., Absorption coefficients of CFC-11 and CFC-12 needed for atmospheric remote sensing and global warming studies, *Journal of Quantitative Spectroscopy & Radiative Transfer,*48, 205-219, 1992a.

Varanasi, P., Absorption spectra of HCFC-22 around 829 cm^{-1} at atmospheric conditions, J. Quant. Spectrosc. Radiat. Transfer, 47, 251 – 255, 1992b.

Voigt, C., et al., Nitric Acid Trihydrate (NAT) in Polar Stratospheric Clouds, *Science*, 290, 1756-1758, 2000.

Von Clarmann, T., Glatthor, N., Grabowski, U., et al.: Retrieval of temperature and tangent altitude pointing from limb emission spectra recorded from space by the Michelson Interferometer for Passive Atmospheric Sounding (MIPAS), *J. Geophys. Res.*, 108(D23), 4736, doi:10.1029, 2003.

Von Clarmann, T. and Echle, G.: Selection of optimized micro-windows for atmospheric spectroscopy, *Applied Optics*, 37, 7661-7669, 1998.

Waterfall, A. M.: Measurement of organic compounds in the upper troposphere using remote sensing, DPhil thesis, *Oxford University*, 2003.

Wayne, R.P.: *Chemistry of Atmospheres, 2nd Ed.*, Oxford University Press, Oxford, 1991.

Weber, M., Overview of validation of MIPAS H_2O vapour by comparison with independent satellite measurements, *Proc. ACVE-2 meeting*, 3-7th May, Frascati, Italy, 2004.

World Meteorological Organisation. Scientific Assessment of Ozone Depletion: 2002. *Global Ozone Research and Monitoring Projects,* Geneva, 2003.

World Meteorological Organization (WMO), Scientific Assessment of Ozone Depletion: 2002, *Global Ozone Res. and Monitor. Proj., Rep.47*, 498 pp., Geneva, Switzerland, 2002.

World Meteorological Organization (WMO), Scientific assessment of ozone depletion: 1998, Rep. 44, *Global Ozone Res. and Monit. Project*, Geneva, 1999.

World Meteorological Organization (WMO), Guide to Meteorological instruments and methods of observation, 6th edition, WMO Rep.8, *World. Meteorol. Organ.*, Geneva, Switzerland, 1996.

Zander, R., et al., Potential of the NDSC in Support of the Montreal Protocol: Examples from the station Jungfraujoch, Switzerland, in non-CO greenhouse gases (NCGG-3): Scientific understanding, control options, and policy aspects, in *Proceedings of the 3rd International Symposium, Maastrict, the Netherlands, 21–23 Jan. 2002*, edited by J. van Ham et al., pp. 305–310, Millpress, Rotterdam, Netherlands, 2002.

Zander, R., C. P. Rinsland, C. B. Farmer, R. H. Norton, Infrared Spectroscopic Measurements of Halogenated Source Gases in the Stratosphere with the Atmos Instrument, J. Geophys. Res., 92, 9836 – 9850, 1987.